HIGH RESOLUTION ION MOBILITY SPECTROMETRY WITH INCREASED ION TRANSMISSION: EXPLORING THE ANALYTICAL UTILITY OF PERIODIC-FOCUSING DC ION GUIDE DRIFT CELLS

A Dissertation

by

RYAN CHRISTOPHER BLASE

Submitted to the Office of Graduate Studies of
Texas A&M University
in partial fulfillment of the requirements for the degree of

DOCTOR OF PHILOSOPHY

December 2010

Major Subject: Chemistry

HIGH RESOLUTION ION MOBILITY SPECTROMETRY WITH INCREASED ION TRANSMISSION: EXPLORING THE ANALYTICAL UTILITY OF PERIODIC-FOCUSING DC ION GUIDE DRIFT CELLS

A Dissertation

by

RYAN CHRISTOPHER BLASE

Submitted to the Office of Graduate Studies of
Texas A&M University
in partial fulfillment of the requirements for the degree of

DOCTOR OF PHILOSOPHY

Approved by:

Chair of Committee,	David H. Russell
Committee Members,	David Church
	Simon W. North
	Gyula Vigh
Head of Department,	David H. Russell

December 2010

Major Subject: Chemistry

ABSTRACT

High Resolution Ion Mobility Spectrometry with Increased Ion Transmission: Exploring the Analytical Utility of Periodic-Focusing DC Ion Guide Drift Cells. (December 2010)

Ryan Christopher Blase, B.S., Truman State University

Chair of Advisory Committee: Dr. David H. Russell

Drift tube ion mobility spectrometry (IMS) is a powerful, post-ionization separation that yields structural information of ions through an ion-neutral collision cross section. The ion-neutral collision cross section is governed by the collision frequency of the ion with the neutral drift gas. Consequently, ions of different size will have different collision frequencies with the gas and be separated in the drift cell. A significant challenge for IMS, however, is to separate ions with very similar collision cross sections, requiring higher resolution ion mobility spectrometers. Resolution in IMS is of utmost importance for the separation of complex mixtures, e.g. crude oil samples, proteolytic digests, positional isomers, and ion conformers. However, most methods employed to increase mobility resolution significantly decrease ion transmission through the mobility device.

Herein, a periodic-focusing DC ion guide drift cell (PDC IG) is presented to display its potential capabilities for higher mobility resolution with increased ion transmission. The PDC IG utilizes unique electrode geometry compared to the conventional uniform field electrode design. Electrode geometry can be defined by the

electrode inner diameter (*d*), thickness (*t*), and spacing (*s*). Specifically, the ratio of $d : t : s$ is equal to, or very near, 1:1:1. The PDC IG electrode design creates a non-uniform (fringing) electric field-especially near the electrode walls. The design also causes variations in the radial electric field which provides an effective RF as ions move through the device and a radially confining effective potential that improves ion transmission through the device.

In this dissertation the analytical utility of the PDC IG drift cell for ion mobility separations will be explored. The radial focusing properties of the device will be presented along with studies of electrode geometry and its effect on ion mobility resolution and ion transmission through the drift cell. PDC IG drift cell length is also examined to determine its effect on mobility resolution and ion transmission. Finally, the PDC IG drift cell device is coupled to an orthogonal-acceleration time-of-flight mass spectrometer as well as a modular, PDC IG drift cell being adapted to a commercial qTOF mass spectrometer for IM-MS experiments.

DEDICATION

This dissertation must be dedicated to a slew of individuals. First, and foremost, I would like to dedicate this dissertation to my parents, David and Betty Blase. They have seen me through so much in life and taught me everything I know about hard work, efficient work, and diligence. Without their example in my life, I never would have been able to accomplish this dissertation and become Dr. Ryan Christopher Blase.

I must also dedicate this dissertation to my wife, Erica, who has been patient with me and dealt with the long hours I have been away from home to complete all of the research contained within this dissertation. I must also thank her for the countless hours she has spent at home with our son, Maverick. She is truly my helpmate in life and I wouldn't have accomplished this without her.

I would also like to dedicate this dissertation to my brother, Jason Blase, who has sacrificed much of himself serving in the United States Navy. In fact, during my education, from high school through my doctoral degree, he has been serving the United States of America.

Finally, I dedicate this dissertation to Maverick, who gives me inspiration to be the best Dad I can be.

ACKNOWLEDGEMENTS

I would like to thank my committee chair, Dr. David H. Russell, for his guidance through my graduate career. I would also like to thank him for allowing me to have the creative freedom in graduate school to build instruments in the group. This was a sometimes frustrating, but always rewarding experience.

I would also like to thank my committee members, Dr. David Church, Dr. Simon W. North, and Dr. Gyula Vigh, for their guidance and support.

Thanks also to past and present members of the Russell Research Group for being mentors to me and teaching me in the early years of my graduate career. Specifically, I would like to thank past members Dr. Kent J. Gillig, Dr. Jody C. May, and Dr. Wenjian Sun for their valuable knowledge in scientific instrumentation. I would also like to thank Dr. Brad J. Williams (Brady) and Dr. Stephanie Cologna for their encouragement through my graduate career and especially the encouragement to get this dissertation written.

Thanks must also be sent out to the ‘Neanderthals’, as I once called our Friday morning meeting group. This group kept me going through graduate school. They were also co-authors on many publications. Thanks go out to Dr. Chaminda Gamage, Kevin Kmiec, Joshua Silveira, Junho Jeon, Kyle Fort, and Dr. Francisco Fernandez-Lima.

Finally, thanks to Will Seward and Carl Johnson in the Texas A&M University Chemistry Machine Shop for precision machining of scientific instrumentation and Greg Matthijetz for his expertise in electronics.

NOMENCLATURE

CI	Chemical Ionization
CID	Collision-Induced Dissociation
d	drift electrode inner diameter
DMA	Differential Mobility Analyzer
DMS	Differential Mobility Spectrometer
$E_{0,r}$	Radial Electric Field Amplitude
$E_{0,z}$	Axial Electric Field Amplitude
E_c	Central Electric Field
E_r	Radial Electric Field
E_r(r)	Radial electric field in the radial direction / Radial E-field as function of r
E_r(z)	Radial electric field in the axial direction / Radial E-field as function of z
E_z	Axial Electric Field
E_z(r)	Axial electric field in the radial direction / Axial E-field as function of r
E_z(z)	Axial electric field in the axial direction / Axial E-field as function of z
ECD	Electron Capture Dissociation
EI	Electron Ionization
ETD	Electron Transfer Dissociation
FAIMS	High-Field Asymmetric Waveform Ion Mobility Spectrometry
FT-ICR MS	Fourier Transform Ion-Cyclotron Resonance Mass Spectrometry
GC	Gas Chromatography

IMS	Ion Mobility Spectrometry
IM-MS	Ion Mobility-Mass Spectrometry
K	Ion mobility constant
K_0	Reduced ion mobility constant
LIT	Linear Ion Trap
MALDI	Matrix Assisted Laser Desorption/Ionization
MCP	Microchannel Plate
m/z	mass-to-charge ratio
oa-TOF-MS	orthogonal acceleration Time-of-Flight Mass Spectrometry
PD	Photodissociation
PDC IG	Periodic-Focusing DC Ion Guide
QIT	Quadrupole Ion Trap
r	radial position or displacement
s	drift electrode spacing
SID	Surface-Induced Dissociation
t	drift electrode thickness
T_{eff}	Effective ion temperature
TDC	Time-to-Digital Converter
TOF	Time-of-Flight
TOF-MS	Time-of-Flight Mass Spectrometry
TW IMS	Traveling Wave Ion Mobility Spectrometry
$V^*(r)$	Effective potential in the radial direction, often denoted simply as V^*

v_d	drift velocity
V_z	Ion axial velocity
z	Axial position or displacement

TABLE OF CONTENTS

Page

Page

LIST OF FIGURES

Page

Page

Page

Page

Page

Page

Page

Page

LIST OF TABLES

Page

Page

1. INTRODUCTION: BACKGROUND OF ION MOBIILTY SPECTROMETRY AND MASS SPECTROMETRY

1.1 Ion Mobility Spectrometry

Ion Mobility Spectrometry (IMS) is a gas-phase separation technique that separates ions in terms of their size, specifically their ion-neutral collision cross section [1]. Drift tube IMS uses the accelerating force of an electric field, *E*, to accelerate ions while a neutral drift gas acts as an opposing force to the resulting ion motion. Ions are then separated by their collisional frequency with the neutral drift gas molecules.

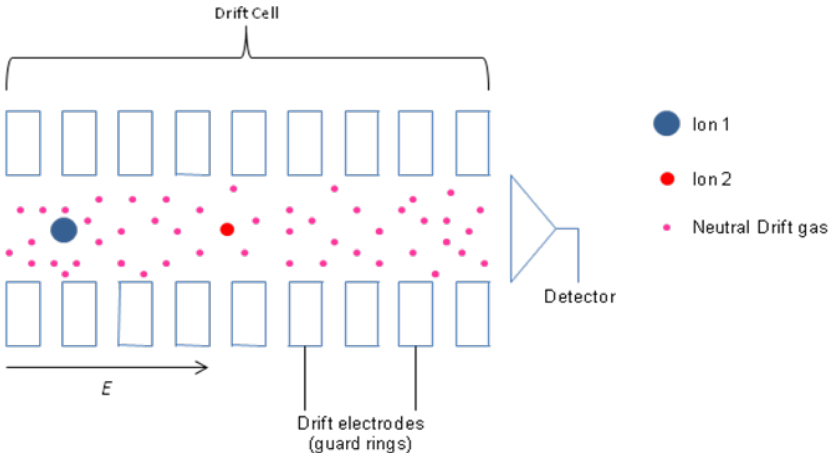

Figure 1. The basic operation of a drift tube ion mobility spectrometer.

This dissertation follows the style of the International Journal of Mass Spectrometry.

For ions of the same *m/*z, larger ions (ion 1 in Figure 1) have a greater collision frequency and therefore experience longer drift times while small ions (ion 2 in Figure 1) have a lower collision frequency resulting in shorter drift times. The time it takes an ion to traverse the drift cell until detection is referred to as the ion drift time, t_d. This time can be converted to a drift velocity, v_d, as the ion drift time is measured and drift cell length, L_d, is known from construction of the apparatus. The drift velocity is used to determine the ion mobility which is defined by the equation

$$v_d = K * E \tag{1.1-1}$$

where K is the ion mobility and E is the applied electric field. The earliest measurements of drift velocities in gases, the first ion mobility experiments, were done by Rutherford and Thomson [2] followed by Zeleny [3].

The ion mobility, *K*, is dependent on the identity of the drift gas in which the separation takes place [4]. Thus, an ion's mobility will be different in He, Ar, N_2, etc. It is also important to note that mobilities are converted to reduced mobilities for direct comparison of results taken under different experimental conditions. The reduced mobility is defined by the equation

$$K_0 = K \frac{p}{p_0} \frac{T_0}{T} \tag{1.1-2}$$

where p is the experimental drift gas pressure, T is experimental drift gas temperature, and T_o and p_o are standard temperature and pressure. Ion mobility data taken from different ion mobility spectrometers and different laboratories can be compared when reduced mobility values in the same drift gas are used.

1.2 Measurement of the Ion-Neutral Collision Cross Section

The mobility of an ion can be used to obtain important ion structural information. The ion mobility is inversely proportional to the ion-neutral collision cross section (K α $1/\Omega$). Specifically, the Mason-Schamp equation (1.2-1) illustrates this inverse relationship [1].

$$\Omega_T = \frac{3ze}{16N}\left(\frac{2\pi}{\mu k_B T_{eff}}\right)^{1/2}\left(\frac{1}{K}\right) \tag{1.2-1}$$

In the above equation, z and e are number of charges and elementary charge, N is number gas density, μ is reduced mass, k_B is Boltzmann's constant, T_{eff} is the effective temperature of the ion, and K is the ion mobility. Notice that the ion-neutral collision cross section, Ω_T, is dependent on ion temperature. Most ion-neutral collision cross section measurements are taken in the low-field regime where the value of the electric field over the pressure (E/p) or the electric field over the gas number density (E/N, known as the Townsend) is low and thus an approximation is made where T_{eff} simply reduces to the drift gas temperature. This is important because if the E/p value is high, the ion may gain an excess of internal energy from the applied electric field and this approximation should not be used.

The Mason-Schamp equation can be expanded based on the relationship of the reduced mobility of the ion with the drift velocity and electric field. Remember from equation 1.1-2 that the reduced mobility can be determined from the equation

$$K_0 = K\frac{p}{760}\frac{273}{T} \tag{1.2-2}$$

This equation is rearranged and substituted in the Mason-Schamp equation above to yield the equation

$$\Omega = \frac{(18\pi)^{1/2}}{16}\frac{ze}{(k_B T)^{1/2}}\left[\frac{1}{m_g}+\frac{1}{m_i}\right]^{1/2}\frac{t_d E}{L}\frac{760}{p}\frac{T}{273}\frac{1}{N_0} \qquad (1.2\text{-}3)$$

where m_g and m_i are the masses of the drift gas and ion, t_d is the drift time, E is the applied electric field, L is drift cell length, p is drift gas pressure, and T is drift gas temperature. To obtain accurate ion-neutral collision cross section measurements, multiple experiments are performed at different E/p ratios. The experimenter can vary either the applied electric field or the drift gas pressure to change experimental conditions. Varying the electric field is usually the easier of the two as waiting for equilibration of a power supply is much faster than the equilibration of a gas pressure even with a precise flow controller.

Another important parameter to remember is drift gas purity. For confident ion-neutral collision cross section measurements, collisions of the ion with the neutral drift gas must be as pure as possible. If the drift gas is not pure, the impurities will have a different collisional body (changing μ) and perhaps a different interaction potential with the ion resulting in errors of the ion-neutral collision cross section measurement. The purity of the drift gas is not limited to issues of the purity of the dewar or bottle used, but also the vacuum of the instrument. If any flanges of the system contain leaks, especially those near the mobility cell, atmospheric air as well as water from humid air can contaminate the drift cell and lead to errors in the measurement of the ion-neutral collision cross section. This becomes a greater issue as the length of the mobility cell

increases. As ion drift times increase so do the numbers of ion-neutral collisions and therefore a greater likelihood of collisions with impurities in the drift cell.

1.3 Types of Ion Mobility Spectrometers

1.3.1 Drift Tube IMS

The most common ion mobility spectrometer is the drift tube, or drift time, IMS (DT IMS) [5]. Ions drift under the influence of an electric field and separation of different size ions occurs as a result of the collision frequency with a neutral drift gas (as is described in section 1.1). The early history of ion mobility centered on drift tube IMS instruments and the determination of atomic ion mobilities in a variety of drift gases [1, 6-14]. In fact, all of the theoretical work that is still widely used and accepted today was based on work with atomic ions.

Drift tube IMS has remained relevant through the years owing to its simplistic operation and its first-principles calculation of ion-neutral collision cross section values. Ion mobility, K, is independent of the electric field under low-field conditions and is inversely proportional to ion-neutral collision cross section, Ω. For this reason, DT IMS is commonly used for determining ion-neutral collision cross section values providing more information of ion structure-especially peptides and proteins.

1.3.2 Traveling Wave IMS (TW IMS)

Traveling Wave IMS can be considered a variant of drift tube IMS where the electric field applied across the drift electrodes is replaced by a pulse across a set of six pairs (12) adjacent electrodes creating a localized electric field [15]. After a finite amount of time, a second pulse is applied across adjacent electrodes further down the

IMS cell. For improved ion transmission, a superimposed RF voltage is applied to the ring electrodes providing increased ion transmission via radial focusing of ions through the device. The operation of the Synapt HDMS traveling wave IMS is depicted in Figure 2.

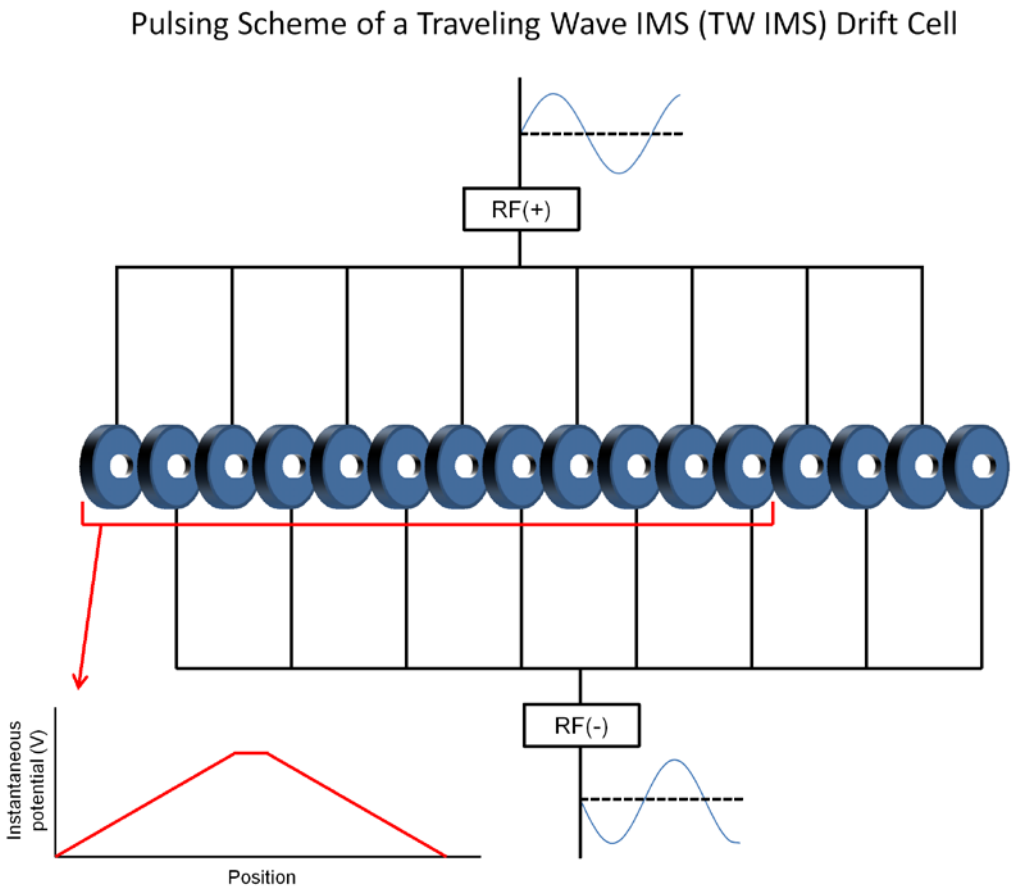

Figure 2. Schematic of the basic operation of the Synapt HDMS traveling wave IMS. The superimposed RF on the electrodes is shown while the pulsed instantaneous potential on a set of six pairs of electrodes (bracketed in red) shows one DC pulse of the DC traveling wave.

The pulsing frequency of the electrodes can be varied as well as the amplitude of the traveling wave (instantaneous DC potential). Variation of the pulsing frequency provides a change in the speed of the traveling wave, *c*, while variation of the amplitude provides an increased magnitude, localized electric field. A low velocity wave through the traveling wave IMS results in faster separation times as the localized electric field is applied for a longer period of time resulting in increased displacement of ions prior to pulsing the next set of electrodes. Likewise, a high velocity wave results in slower separation times (slower drift times) as the localized electric field is applied for a shorter period of time and thus ion displacement in the localized region is decreased. Variation of the speed of the wave can be optimized to separate two ions as one ion can surf the wave while another ion will fall behind the wave.

Traveling wave IMS provides high ion transmission owing to the superimposed RF voltage on the drift electrodes. The frequency and amplitude of the RF voltage creates an "effective potential" that confines ions near the central axis of the drift cell [16]. Descriptions of the "effective potential" produced from inhomogeneous RF fields have been described previously [17-18] and its role in the TW IMS as well as the traveling wave ion guides (TW IGs) preceding and following the TW IMS [16].

The Waters Synapt and Synapt G2 HDMS have exploded into laboratories around the world owing to their commercial availability, outstanding sensitivity and limit of detection, and high mass resolution W-reflectron TOF. However, ion mobility separation on the traveling wave IMS can be complicated as the ion separation does not depend solely on the mobility constant, *K*, but rather K^2. Moreover, mobility separation

depends on the ratio of the drift velocity (*K*E*) to the speed of the wave, *c*. Ions can travel ahead of the wave or can fall over the crest of the wave depending on the ratio of drift velocity to wave speed. Furthermore, ions can experience turn-around events in the traveling wave IMS that cause the ion to traverse a longer length than the established drift length. All of these issues make ion-neutral collision cross section calculations difficult. There has been a great deal of effort put forth into developing methods for calculating ion-neutral collision cross sections of ions with known calibrants previously established from DMA or DT IMS separations [19-21].

1.3.3 Differential Mobility Analyzer (DMA)

A good analogy to demonstrate the operation of the differential mobility analyzer (DMA) is a flowing river with boats of varying size at a docking point at one river bank. A second docking point on the opposite bank is placed downstream from the original docking point. The boats then leave the docking point with the same acceleration but different velocities, according to their size, heading straight for the opposite bank. A boat of certain size, correct velocity to the counter flow of the river current, will reach the second docking point while others will land upstream or downstream from their intended docking point destination.

The DMA is a scanning mobility technique where ions are accelerated by an electric field created by two parallel plates with a neutral drift gas flow orthogonal to the electric field [22-23]. The ions are introduced into the DMA through a small entrance slit in one plate and a similar exit slit is placed at the opposite plate slightly downstream from the entrance slit. Ions of certain mobility will be focused to the exit slit based on

the gas flow conditions and electric field (Figure 3). The separation conditions of the DMA, gas flow or electric field, can be scanned to allow all ions to be sampled.

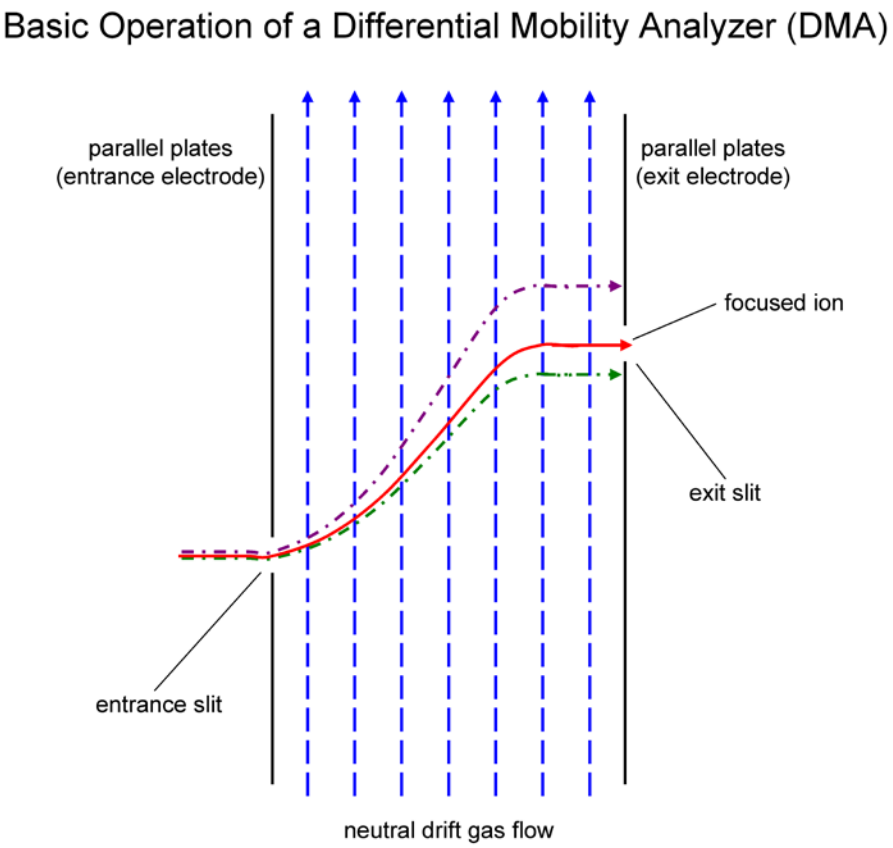

Figure 3. A schematic drawing showing the basic operational principles of a differential mobility analyzer (DMA).

The scanning properties of the DMA are advantageous when used with a continuous ionization source as ions will be analyzed individually based on the DMA voltage. Differential mobility analysis was commercialized and one such commercial instrument is referred to as the GEMMA [24-27] (gas-phase electrophoretic mobility molecular analysis), where a condensation particle counter or evaporative light scattering detector

[28-29] is used for detection of nanometer sized particles [30]. The DMA has been used to analyze particle diameters of large biomolecules [24, 31] that are more difficult to analyze by traditional drift tube IMS coupled with mass spectrometry.

Recently, a differential mobility analyzer has been coupled with an ABI Sciex QSTAR XL mass spectrometer to analyze ionic liquid nanodrops [32]. The two-dimensional DMA-MS separation provides information of *m/z* versus DMA voltage which makes it a powerful platform for a continuous ionization source with mobility selection and subsequent mass analysis of a mobility selected ion. The same instrument was used to investigate protein and protein cluster ions and presented at the 2010 American Society for Mass Spectrometry Conference [33].

1.3.4 Differential Mobility Spectrometry

A differential mobility spectrometer (DMS) is another scanning mobility technique that utilizes asymmetric waveforms of high and low electric fields between two parallel plates orthogonal to a neutral gas flow [34]. A schematic of the basic operational principles of the DMS are shown in Figure 4. As ions traverse the DMS, the magnitude and direction of the electric field change over time. Furthermore, more complicated asymmetric waveforms have been employed, providing an asymmetric saw-tooth instantaneous potential profile. During application of the high field the ion mobility, *K*, changes and the mobility differences between high- and low- fields adds to the dynamic of the ion separation. Specifically, ion trajectories through the DMS are dependent on the ratio of the ion mobility constant at high-field, K_h, compared to the ion mobility constant, *K*, at low-field conditions [35]. From Figure 4, it can be seen that one

ion will maintain stability through the DMS. To detect every ion in a mixture, the magnitude of the high and low fields can be changed or the duration of the high and low field application.

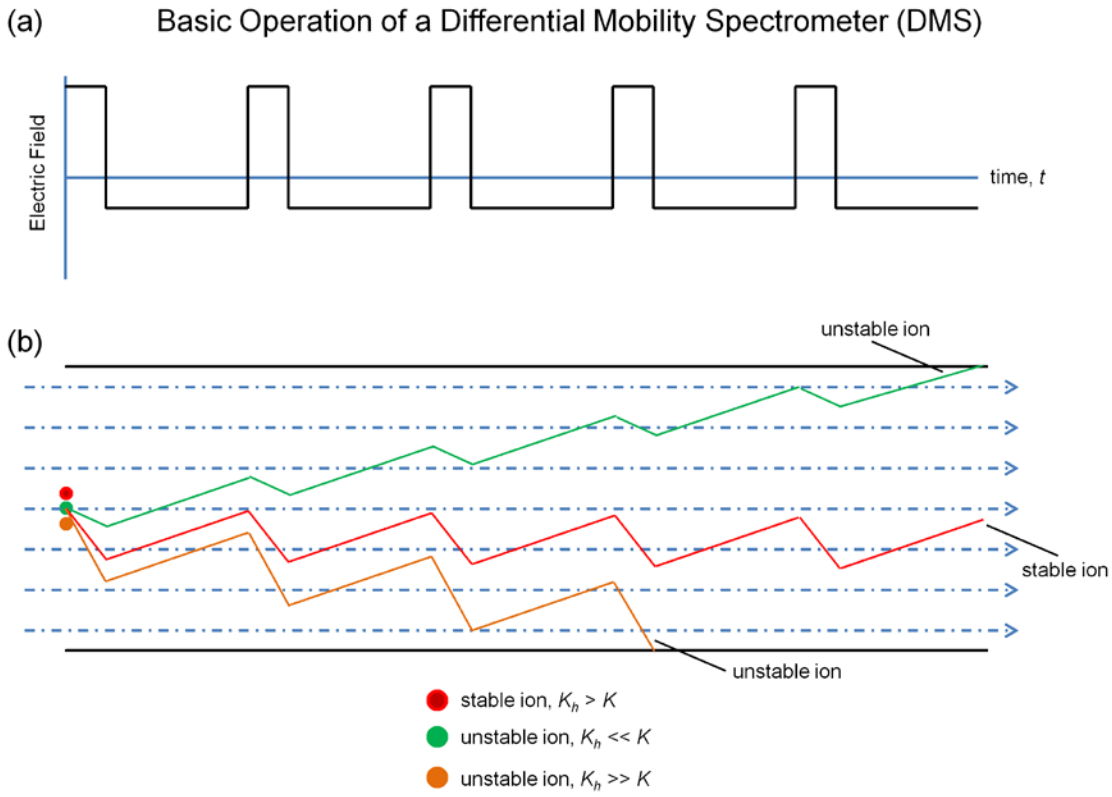

Figure 4. Schematic showing the asymmetric electric field waveform as a function of time (a) and ion trajectories through the DMS according to ion mobilities at high- and low-field conditions (b).

Differential mobility spectrometry has also been termed high-field asymmetric waveform ion mobility spectrometry, or FAIMS [36]. FAIMS has been commercialized by Thermo Electron Corporation and can be adapted to a variety of their mass spectrometers. In the FAIMS device, the voltage on the lower plate of Figure 4 is

referred to as the compensation voltage and the detection of ions as a function of compensation voltage provides compensation voltage spectra.

1.4 Types of Mass Spectrometers

1.4.1 Magnetic, Electrostatic, and Hybrid Electromagnetic Sector Instruments

Perhaps the most common mass spectrometer in the last century was the sector mass spectrometer. Sector instruments can be composed of a magnetic field, an electrostatic field, or a hybrid with both magnetic and electrostatic field portions of the instrument. Briefly, each type of sector instrument will be explained.

In a magnetic sector instrument, ions are deflected in their motion through a magnetic field. The amount of deflection in the magnet is determined by ion momentum. The first consideration of the experiment regarding ion momentum is the kinetic energy of the ions received from the accelerating voltage in the source region. The kinetic energy of the ion is determined through equation 1.4.1-1

$$qV = \frac{1}{2}mv^2 \qquad (1.4.1\text{-}1)$$

where q is equal to the product of number of charges and elementary charge, V is accelerating voltage, m is ion mass, and v is ion velocity. As ions move through the magnetic field, they are deflected owing to the force exerted by the magnetic field on a moving charged particle. This is represented by equation 1.4.1-2.

$$\frac{mv}{r} = qB \qquad (1.4.1\text{-}2)$$

where r is the arc radius of the deflected ion beam and B is the magnitude of the magnetic field strength. Substituting equation 1.4.1-2 for the velocity term in equation 1.4.1-1 yields equation 1.4.1-3.

$$\frac{m}{q} = \frac{B^2 r^2}{2V} \tag{1.4.1-3}$$

Equation 1.4.1-3 reveals that if the magnetic field and accelerating voltage are held constant then ions of the same charge state but different mass will have different arc radii through the magnet [37]. The arc radii of ions in relation to mass are shown in Figure 5 with lower mass ions experiencing greater deflection through the magnetic field.

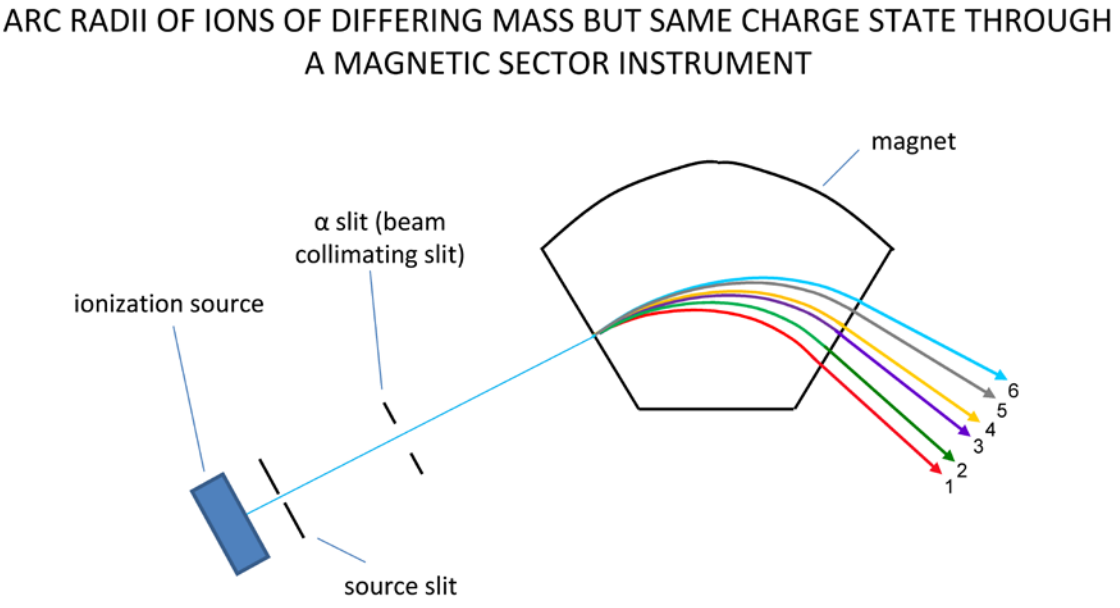

Figure 5. A schematic diagram of a magnetic sector instrument showing ion trajectories of ions of the same charge state but differing in mass. Ion 1 has the lowest mass and is therefore deflected to the greatest degree in the magnet while ion 6 has the greatest mass and is deflected to the least degree.

One advantage of a magnetic sector instrument is the directional, or angular, focusing it provides. If a divergent ion beam enters the magnetic field, it will come out of the magnet as a convergent beam and will be collected at the detector. This angular focusing increases sensitivity, however, magnetic sector instruments have no energy focusing component. Hence, ions of differing kinetic energies will arrive at the detector at different times, leading to broadening of the ion signal.

Electrostatic sector instruments provide energy focusing that is lacking in the magnetic sector instrument [37]. The source region is very similar to the magnetic sector in that ions are accelerated from the ionization source through a slit and then enter an electrostatic analyzer, two curved electrodes with a potential difference between the two electrodes to create an electric field. Ions with greater kinetic energy, and thus higher velocity, will be less deflected through the electrostatic sector and will travel closer to the outside wall of the analyzer. On the other hand, ions with less kinetic energy, and thus lower velocity, will experience greater deflection and will travel near the inner wall of the analyzer. Ion trajectories according to kinetic energy differences for ions of the same *m/z* are depicted in Figure 6. Different ion trajectories through the electrostatic sector allow for detection of ions with slight differences in kinetic energy either through a scanning method or with multiple detectors positioned at different points after a multi-slit exit. The electrostatic sector is a great platform for determining kinetic energy spreads of ions from different ionization conditions, especially in the case of electron ionization (EI) and chemical ionization (CI).

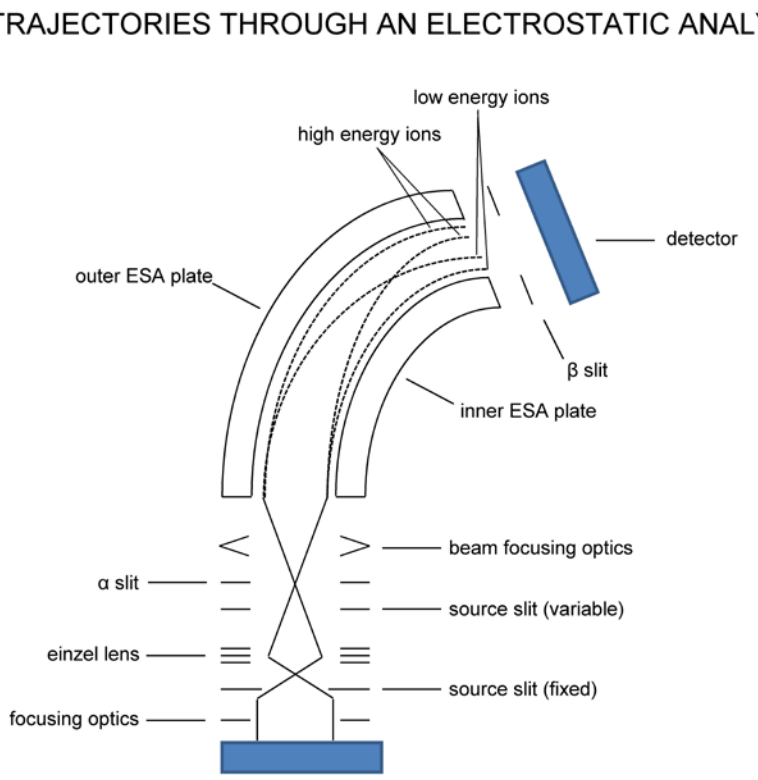

Figure 6. Ion trajectories through an electrostatic analyzer owing to kinetic energy differences of ions of the same mass-to-charge (*m/z*).

Hybrid sector instruments, also known as double-focusing instruments, are much more powerful owing to ion focusing both energetically and directionally. Early double-focusing instruments were introduced by Dempster [38], Bainbridge [39], Nier [40-41], and Mattauch [42]. To date, double-focusing instruments are referred to as double-focusing forward or double-focusing reverse geometry. In the double-focusing forward geometry the electrostatic analyzer is placed before the magnet whereas the magnet is placed first in a double-focusing reverse geometry. Double-focusing sector instruments were the 'workhorses' of mass spectrometry until major improvements were made in quadrupole mass spectrometry and time-of-flight mass spectrometry.

1.4.2 Time-of-Flight Mass Spectrometers

In 1946, W.E. Stephens developed the first time-of-flight mass spectrometer at the University of Pennsylvania [43]. He noticed that pulsing ions from a low voltage ion source and letting them travel down a vacuum tube resulted in a separation of ions of different *m/z* in space owing to differences in velocities. This phenomenon could be explained rather simply by the equation for kinetic energy.

$$KE = \frac{1}{2}mv^2 \qquad (1.4.2\text{-}1)$$

He also predicted that such a mass spectrometer would have utility for rapid analysis and portable use. While most time-of-flight mass analyzers are not portable, the rapid analysis provided by time-of-flight mass spectrometers has impacted a variety of research areas for 60 years.

In 1948, the idea developed by Stephens was followed with the development of an instrument called an *ion velocitron* [44]. The instrument consisted of an electron impact (EI) ionization source where ions were continually extracted from the ion source towards a 3.17 meter flight tube. Ions were gated into the flight tube by pulsing a set of deflection plates at the flight tube entrance. The ions were only accelerated to 500 eV of kinetic energy, resulting in a broad distribution at the detector. A similar instrument was reported that also accelerated ions to constant energy [45]. Owing to constant energy acceleration, ion velocity, *v*, and ion flight time, *t*, can be calculated in a straightforward fashion from the equations

$$v = \left(\frac{2KE}{m} \right)^{1/2} \tag{1.4.2-2}$$

$$t = \left(\frac{m}{2KE} \right)^{1/2} d \tag{1.4.2-3}$$

where *m* is ion mass, *d* is flight distance, and *KE* is ion kinetic energy. The ion kinetic energy can be determined by the product of the accelerating voltage and charge of the ion. A different type of acceleration scheme was also developed in which ions receive the same momentum, termed constant momentum acceleration [46]. In this design, the pulse of the extraction field is turned off before ions exit the source region. The idea of constant momentum acceleration has garnered some attention since its inception but has not been as popular as constant energy acceleration.

In 1955, Wiley and McLaren published groundbreaking work pertaining to both focusing of ions with spatial and kinetic energy distributions from the initial ionization process [47]. The design utilized a dual-stage, pulsed extraction field where the electric field in each stage could be manipulated. Ions were formed by electron impact ionization in a field free region and then extracted after a slight time delay in the first stage of the TOF source by a low voltage pulse. The formation of ions in a field free region was done by Katzenstein and Friedland [48], but the idea of varying the time delay and an elaborate description of the spatial and kinetic energy focusing of such a source design was termed *time-lag focusing* by Wiley and McLaren [47]. The time delay allowed for ions to be better energy focused as ions with different initial velocities (kinetic energies) in the source region could move freely to different points in the source

region prior to extraction. In addition, the dual-stage extraction source allowed for manipulation of the space-focus plane, meaning ions extracted from the source are in focus at a point in space. A brief explanation on the spatial and energy focusing of ions from a TOF extraction source are given below.

A single-stage extraction source consists of two electrodes, a backing plate and grid that serve to extract ions. In a continuous extraction field, there would be a continuous electric field applied to the plates to extract ions and the space focus plane would be defined by the equation

$$d = 2s \tag{1.4.2-4}$$

where s is the distance of the source region. The distance of the source region is governed by the type of ionization source used. For EI, CI, and other continuous ionization sources this would be wherever the ions are born in the source region whereas in desorption methods like LDI and MALDI [49-50] the source of ion birth can be considered the back plate of the source. In a continuous extraction mode, there is no energetic focusing of ions with different initial kinetic energies, so ions focused in space at the space focal plane may not be focused as expected owing to initial kinetic energy distributions. The space-focus plane is independent of ion mass and the applied electric field in the source region. Figure 7(a) displays a single-stage, continuous extraction source and the space focus plane.

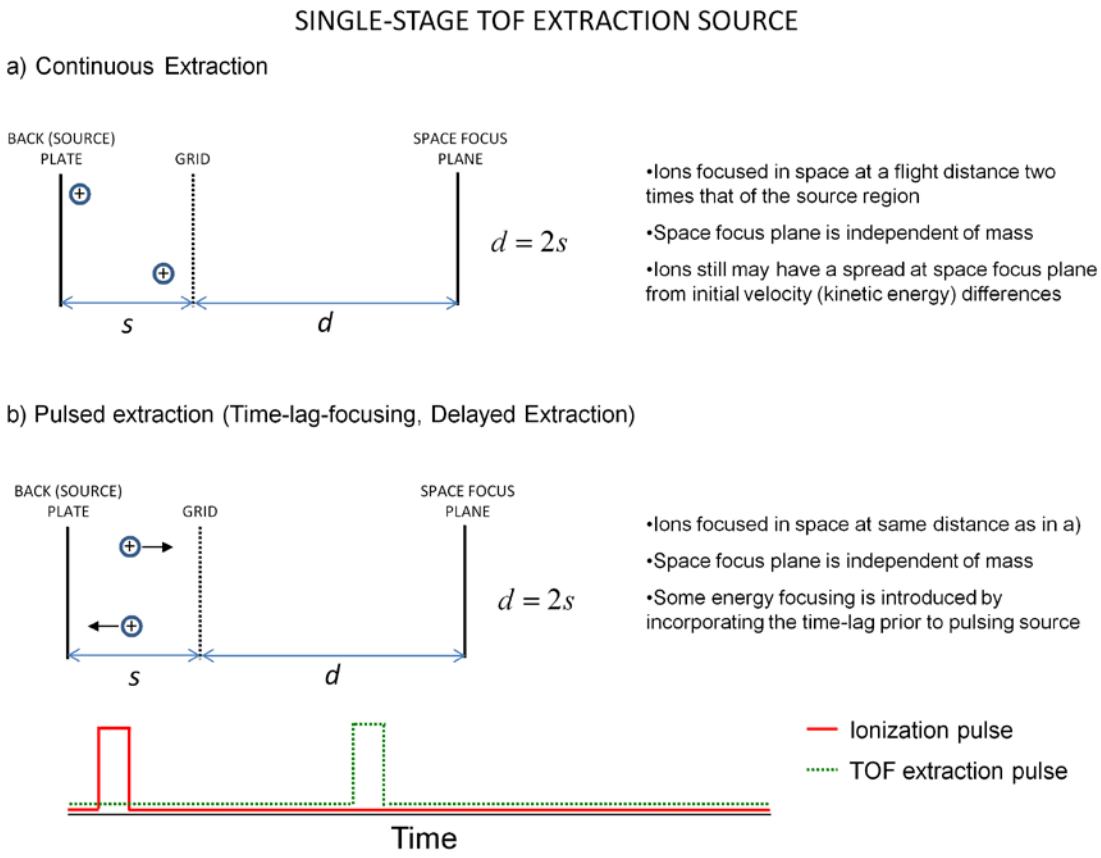

Figure 7. A schematic diagram of a single-stage time-of-flight extraction source showing both continuous extraction mode (a) and a pulsed extraction mode (b) taking advantage of *time-lag focusing*, also known as *delayed extraction*.

Figure 7(b) displays a single-stage extraction source that employs *time-lag focusing* for energy focusing of initial kinetic energy distributions in the extraction source. In this design, the space focus plane is still defined by the distance of the source region, however, before ions are extracted they are allowed to move in a field-free source region to different points governed by their initial velocities prior to extraction. The utility of *time-lag focusing* can be seen in an example where two ions of the same

*m/*z formed at the same point in the source region have equal, but opposite velocities (same magnitude but opposite direction). If a constant extraction field would be applied these ions would not be focused at the space focus plane owing to differences in initial kinetic energies resulting in different final kinetic energies of the extracted ions. If a pulsed extraction with a slight time delay is used then the ions are allowed to move to different positions in the source prior to extraction. Now, an ion with an initial velocity in the direction of the source back plate will move toward the plate while an ion with opposite velocity in the direction of the grid and subsequent field-free TOF region will move in the opposite direction. After a short time period (hundreds of nanoseconds to microseconds) the extraction field is pulsed. The ion that has now moved back toward the source back plate will receive a greater amount of kinetic energy than it would have in its initial position with a continuous extraction field. Likewise, the ion that has moved toward the grid will receive less kinetic energy upon extraction than in its initial position. The final kinetic energies of the ions upon extraction from the TOF source will be much closer to uniform when *time-lag focusing* is employed and hence ions are better focused at the space focus plane. The idea of *time-lag focusing* was revisited in the mid 1990s and was termed *delayed extraction* [51-55]. The advantages of *time-lag focusing*, or *delayed extraction*, were now better realized from improvements in TOF mass analyzers.

A dual-stage extraction source consists of three electrodes employing two different accelerating field regions. The dual-stage extraction source was introduced by Wiley and McLaren and the ratio of the electric fields in the two regions can be used to

manipulate the distance of the space focus plane from the extraction source region. The distance of the space focus plane from the exit of the extraction region in a dual-stage extraction TOF source is defined by the equation

$$d = \frac{2\left(s_0 + \frac{E_1}{E_0} s_1\right)^{3/2}}{s_0^{1/2}} \qquad (1.4.2\text{-}5)$$

where variables s_0 and s_1 are the distances of the two regions of the extraction source and E_0 and E_1 are the magnitude of the electric fields in the two source regions. Wiley and McLaren utilized a much higher magnitude electric field in the second region of the extraction source shifting the space focus plane further from the TOF extraction source exit (Figure 8). This is advantageous in that as flight distance is increased the separation of ions of different *m/z* values in space, and therefore time, is increased. The increase in flight distance increases the dynamic range as ions of higher *m/z* values can now be better separated. Prior to the publication by Wiley and McLaren, Wolff and Stephens and Katzenstein and Friedland reported time-of-flight mass spectrometers with the capability to resolve masses up to 20 Daltons and 75 Daltons, respectively [46, 48]. The dual-stage, pulsed extraction source introduced by Wiley and McLaren increased mass resolution and allowed for complete separation of ions over 100 Daltons and adequate mass resolution up to 300 Daltons.

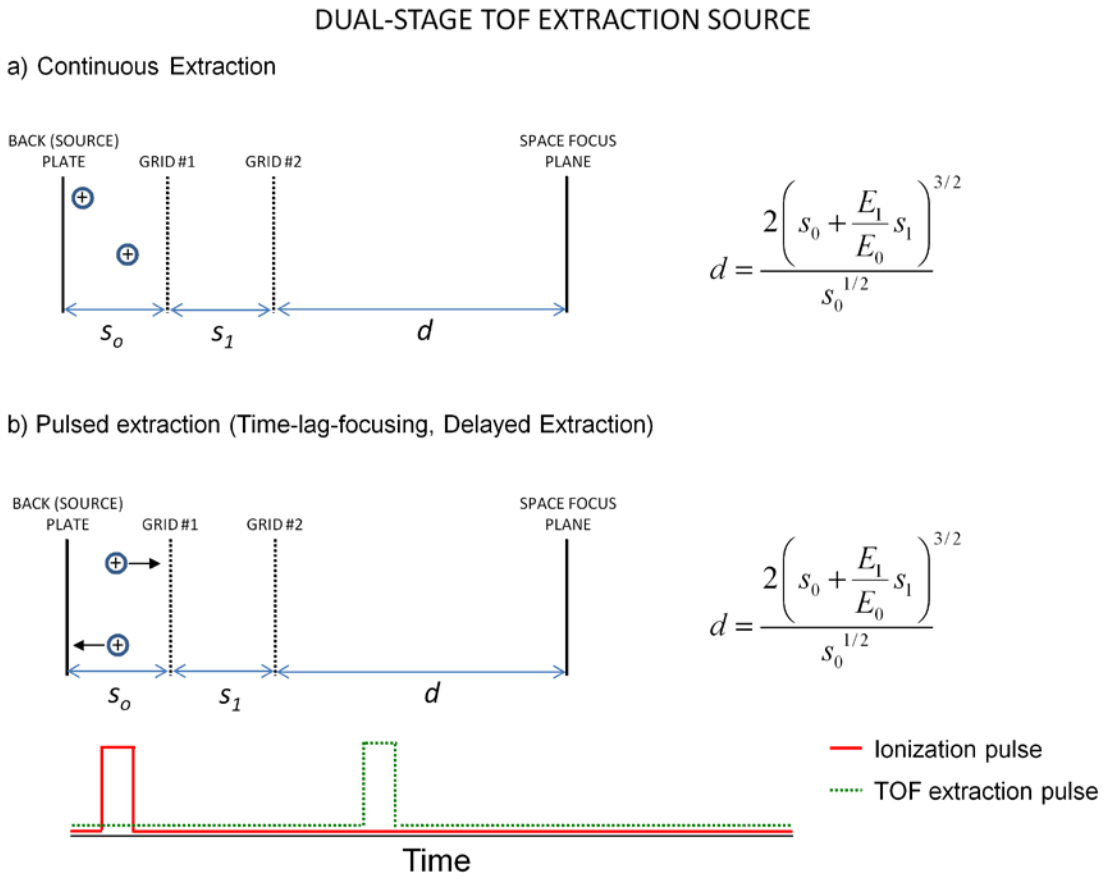

Figure 8. A schematic diagram of a single-stage time-of-flight extraction source showing both continuous extraction mode (a) and a pulsed extraction mode (b) taking advantage of *time-lag focusing*, also known as *delayed extraction*.

Major increases in mass resolution owing to energy focusing were introduced by Mamyrin in 1973 with the reflectron [56]. This device was used to decelerate ions, after initial acceleration and separation in a field-free region, in two retarding electric field regions. The first region decelerates the ions to approximately one-third of their initial kinetic energy and the second retarding electric field serves to decelerate the ions completely (instantaneous velocity and kinetic energy of zero) and then turn the ions around by reaccelerating them to their initial kinetic energy upon exiting the reflectron.

The advantage is that ions with very broad initial kinetic energy distributions would be corrected by the different penetration depths, or flight lengths, in the reflectron. Consider three ions extracted from the same spatial plane in a time-of-flight extraction source (Figure 9). Ion 1 has a negative initial kinetic energy, $-KE_i$, (a velocity with direction away from the extraction source exit and field-free region), ion 2 has zero initial kinetic energy, and ion 3 has a positive initial kinetic energy, KE_i (a velocity with direction toward the extraction source exit). If these ions were extracted with the same acceleration energy, KE_A, to a linear time-of-flight detector, the order of arrival at the detector would be ion 3, ion 2, and ion 1 resulting in a broad distribution at the detector. However, if these ions are extracted towards the Mamyrin reflectron, the ions would penetrate a different depth of the reflectron resulting in a shorter flight path for ion 1 and a longer flight path for ion 3 in relation to ion 2. The ions would then be reaccelerated to different kinetic energies as a function of their position and would be focused at the detector, thereby improving energy focusing and mass resolution.

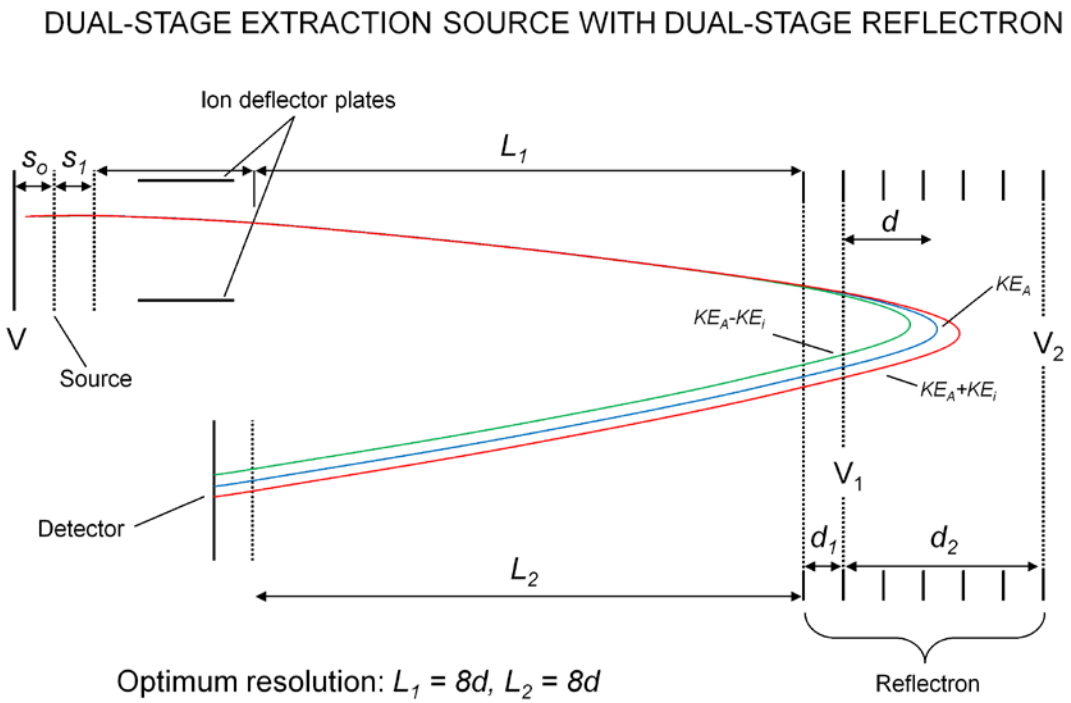

Figure 9. A schematic diagram of a dual-stage TOF extraction source with a dual-stage reflectron. The diagram shows ions 1, 2, and 3 described in the text as the green, blue, and red trajectories, respectively.

In 1987, Standing *et al.* introduced the single-stage reflectron, or ion mirror. The single-stage reflectron uses a single, shallow retarding electric field [57]. The optimum mass resolution for this instrument, as implied by Standing, is when ions spend an equal amount of time in the field-free regions and the reflectron (Figure 10) [58]. This is accomplished when the sum of L_1 and L_2 (field free region) is equal to four times the ion penetration depth in the reflectron (d). Thus, maximum resolution occurs when equation 1.4.2-6 is met.

$$L_1 + L_2 = 4d \qquad (1.4.2\text{-}6)$$

In order to meet the requirements of equation 1.4.2-6 a longer reflectron is needed to achieve the same mass resolution as a dual-stage reflectron. However, the operation of a single-stage reflectron is much simpler in terms of mass calibration and determination of product ions from metastable fragmentation of precursor ions.

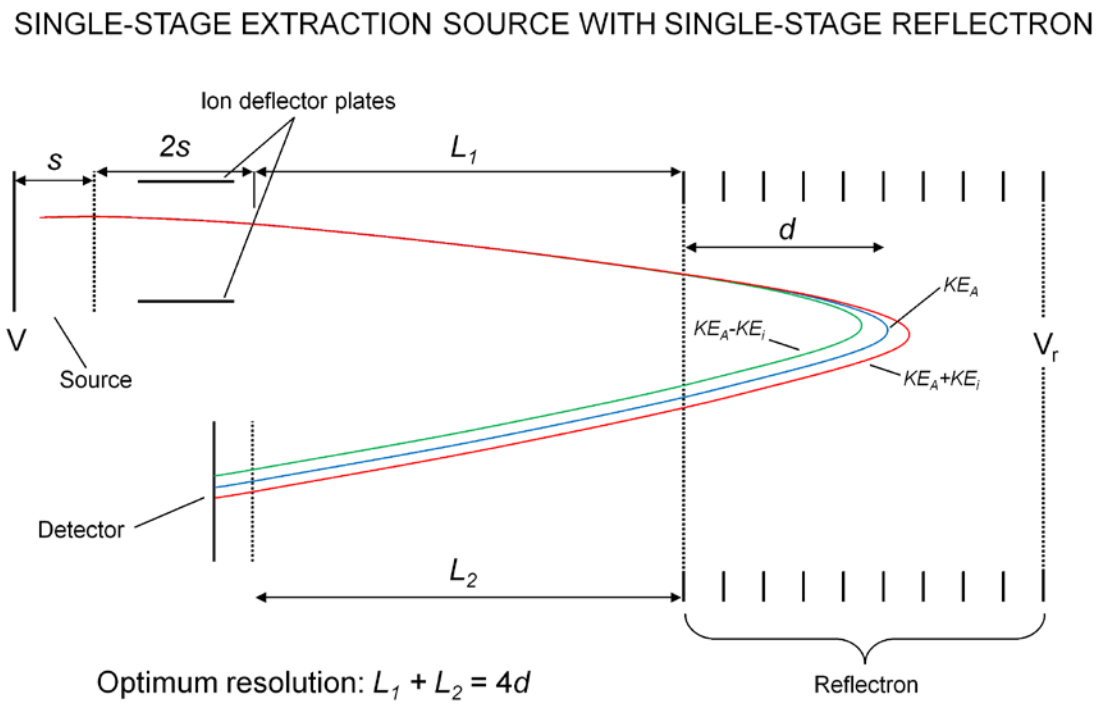

Figure 10. A schematic diagram of a single-stage TOF extraction source with a single-stage reflectron. The diagram shows ions 1, 2, and 3 once again previously described in the text for the dual-stage reflectron as the green, blue, and red trajectories, respectively.

The determination of metastable fragment ions and the precursor ions from whence they came can be established from a linear time-of-flight and therefore mass relationship.

1.4.3 Quadrupole Mass Spectrometry

Quadrupole mass spectrometry is an electrodynamic mass spectrometric technique that uses four parallel rods in a concentric circle with a combination of DC and RF voltages to create a quadrupolar field. Studies on the electrodynamic quadrupole field and its applicability to ion motion was introduced by Wolfgang Paul [59]. Opposite rods are connected to have the same applied DC potential and the same amplitude and phase RF voltage (time-varying waveform) (Figure 11).

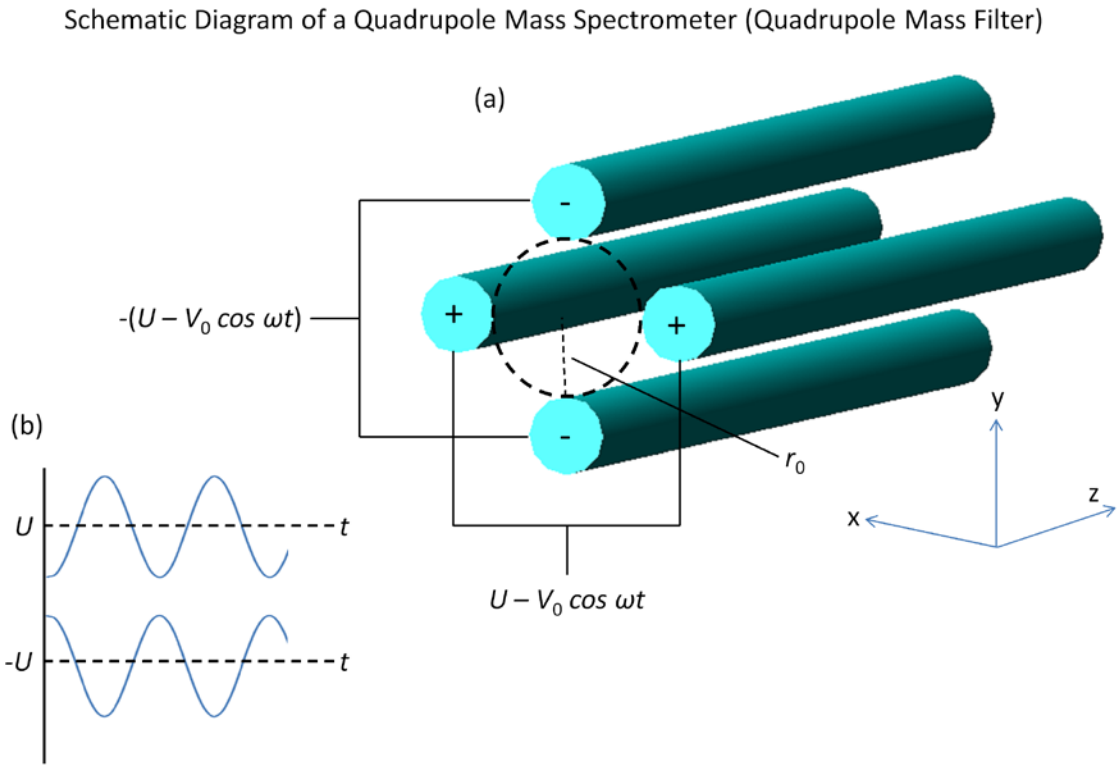

Figure 11. Schematic showing the basic operation of a quadrupole mass spectrometer (a) and the instantaneous potential on the quadrupole rod sets as a function of time (b).

The positive rods have a positive DC potential, *U*, applied as well as the RF voltage, $-V_0 \cos \omega t$. The negative rods have a negative DC potential, *-U*, applied along with the same amplitude RF voltage, $-V_0 \cos \omega t$, but 180 degrees out of phase with the positive rods. The instantaneous potential difference, V_{inst}, between an adjacent set of rods is then defined by the equation

$$V_{inst} = 2(U + V \cos \omega t) \qquad (1.4.3\text{-}1)$$

Consider positively charged ions of varying *m/z* travelling through a quadrupole mass spectrometer. The positive and negative DC biased rods affect ion motion differently for ions of different *m/z*. The positive rods, in the x-z plane, will have a greater impact on low mass ions as ion motion will oscillate in phase with the RF frequency. High mass ions remain relatively unaffected by the RF frequency and remain near the center of the quadrupole. Ion motion for high mass ions is impacted by the negative rods, in the y-z plane, owing to the negative DC potential bias on the rods. High mass ions are drawn toward the rods while low mass ions can be corrected back toward the center of the quadrupole by the RF voltage. Thus, the x-z plane acts as a high-mass pass filter while the y-z plane acts as a low-mass pass filter for positive ions [60].

Soon after, Paul introduced the quadrupole mass filter and its ability to select a specific *m/z* value based on ion stability through the device [61-62]. Ion stability, according to *m/z*, through the quadrupole is established by the DC and RF voltage amplitude and the RF frequency applied to the rods. The ion stability can be defined by the Mathieu equation

$$\frac{d^2u}{d\xi^2} + \left(a_u - 2q_u \cos 2\xi\right)u = 0 \qquad (1.4.3\text{-}2)$$

where u is displacement in the x- or y- dimension, ξ is equal to $\omega t/2$, and a_u and q_u are trapping parameters of the DC and RF voltages, respectively, that apply a force to the ions in the x- and y- directions. The values of a_u and q_u are defined by the following equations

$$a_u = a_x = -a_y = \frac{8eU}{m\omega^2 r_0^2} \qquad (1.4.3\text{-}3)$$

$$q_u = -q_x = q_y = \frac{4eV}{m\omega^2 r_0^2} \qquad (1.4.3\text{-}4)$$

where m is ion mass and r_0 is the circumscribed radius inside the quadrupole rods. From equation 1.4.3-2, it can be seen that ion stability through the quadrupole as a function of mass can be varied by either changing the values of U and V or by changing the RF frequency, ω. Depending on the a_u and q_u values selected, a Mathieu stability diagram can be constructed to determine *m/z* ions that maintain a stable trajectory through the quad. The quadrupole mass filter can also be scanned to generate a mass spectrum by either scanning U and V with a fixed ratio of U/V and fixed RF frequency or by scanning the RF frequency while fixing the values of U and V. If the U value on the quadrupole rods is set to zero (RF only mode) the quadrupole will pass all *m/z* ions, acting as an ion guide [60].

1.4.4 Fourier-Transform Ion Cyclotron Resonance Mass Spectrometry

Fourier-Transform Ion Cyclotron Resonance Mass Spectrometry was first introduced in 1949 when Hipple measured the cyclotron resonance frequency of protons in a magnetic field [63]. FT-ICR MS utilizes a permanent magnetic field to impart a force on an ion moving in the presence of said magnetic field to create a cyclotron motion of the ion. The force on the ion moving through the magnetic field can be defined by the following equation

$$F = ma = m\frac{dv}{dt} = qv \times B \tag{1.4.4-1}$$

where *q*, *m*, and *v* are ion charge, mass, and velocity and *B* is the magnetic field. The resulting force yields a cyclotron motion of the ion where the direction of motion depends on ion charge meaning positive and negative ions orbit the z-axis (are displaced in the x-y plane) in different directions. The acceleration term in equation 1.4.4-1 can be converted to angular acceleration to give the equation

$$\frac{m{v_{xy}}^2}{r} = qv_{xy}B_0 \tag{1.4.4-2}$$

Angular velocity defined by the equation

$$\omega = \frac{v_{xy}}{r} \tag{1.4.4-3}$$

can be substituted into equation 1.4.4-2 to give

$$m\omega^2 r = qB_0\omega r \tag{1.4.4-4}$$

Equation 1.4.4-4 can be reduced to the ion cyclotron frequency equation

$$\omega = \omega_c = \frac{qB_0}{m} \qquad (1.4.4\text{-}5)$$

The ion cyclotron frequency is dependent on the mass and charge of the ion and the magnetic field, B_0, in tesla. Ions of the same *m/z* will have the same cyclotron frequency regardless of ion velocity while ions of different *m/z* will have different cyclotron frequencies in a given magnetic field. An ion packet with a specific cyclotron frequency can be excited to larger radial position (increased cyclotron path) by an RF voltage on a set of excitation plates. As the ions are excited to larger cyclotron paths, their current can be detected by current detection plates as a function of time and through the use of Fourier Transforms, the *m/z* can be detected [64].

FT-ICR MS is an expensive technique but very popular owing to its ultrahigh mass resolution capabilities. The coupling of IMS with FT-ICR MS has been limited, however, and for this reason FT-ICR MS will not be addressed much in this dissertation.

1.5 Ion Mobility/Mass Spectrometry

The first IM-MS instrument was a drift tube IMS coupled with a magnetic sector analyzer in 1962 [65]. Ions eluting the drift cell were accelerated through the magnetic sector mass analyzer to measure the *m/z* of the ion. The acceleration energy was scanned to detect ions of different *m/z* in the magnetic sector. Shortly after, drift tube IMS was coupled with quadrupole mass spectrometers and proved to be a simpler hyphenated instrument [66-67]. With IMS-q-MS designs, mobility-selected ions can be mass analyzed or the quadrupole can be scanned to detect different *m/z* ions as they elute the drift cell. Another advantage is the high sensitivity as nearly all ions eluting the drift cell will be transferred to the quadrupole mass spectrometer, maintaining In addition,

IMS-q-MS designs also allow for ions to be accumulated and trapped prior to tandem MS or MS^3 analyses [68-69]. The enrichment of ions in the trap prior to analyses increases the sensitivity of low abundance ions. One detrimental aspect of IMS-q-MS, however, is the scan time of the quadrupole. A scan speed of ~5000 Da s^{-1} can be accomplished while maintaining sufficient mass resolution [60]. This corresponds to scanning or detecting one Dalton (*m/z*) increments every 0.2 milliseconds (200 μs). If a complex mixture, such as a tryptic protein digest, is separated by IMS the numbers of ion signals of different *m/z* eluting the drift cell over a 0.2 millisecond (200 μs) window is quite high and thus some ions would not be detected owing to the scan time of the quadrupole. Scanning speeds of the quadrupole can be increased in an attempt to overcome this problem but at the expense of mass resolution.

Ion mobility-orthogonal acceleration time-of-flight mass spectrometry (IM-oa-TOF-MS) was introduced in 1963 [70-72]. At the time, oa-TOF-MS suffered from low mass resolution and therefore IM-q-MS remained the standard for IM-MS until higher mass resolution TOF-MS was made available through the reflectron [56] and the resurgence of oa-TOF-MS [73-74]. Ion mobility-orthogonal acceleration time-of-flight mass spectrometry (IM-oaTOF-MS) is attractive to a variety of mass spectrometry applications owing to their experimental compatibility. The time scales of the two separations are compatible as IMS separations are on the order of hundreds of microseconds to tens of milliseconds and time-of-flight mass spectrometry (TOFMS) separations occur in tens to hundreds of microseconds [75]. This means that in the time frame of a single mobility separation, hundreds of mass spectra can be recorded. The

other aspect of TOFMS that is quite appealing for coupling to IMS is the Fellgett advantage [76], or the acquisition of the entire mass range of ions present in every TOF mass spectrum. Another advantage of oa-TOFMS is that high mass resolution can still be obtained with an ion packet with initial spatial and kinetic energy spreads since only a slice of the distribution is extracted orthogonally for mass analysis. For this reason, IM-oaTOF-MS has become the workhorse of IM-MS for the past 20 years.

The separation of IMS enriches the content of the MS experiment by providing additional information on the physical characteristics of the ions. In the first dimension, IMS, ions are separated according to their ion-neutral collision cross section, or ion size. The second dimension, MS, separates ions by their mass-to-charge (*m/z*) ratio. Data from both separation dimensions can be plotted simultaneously to construct a two-dimensional mobility-mass plot that correlates ion mobility arrival time with ion time-of-flight. Interpretation of the two-dimensional plot yields information about ion structure. For instance, a group of ions from the same chemical family should have similar structures and ion signals in the two-dimensional plot should fall along a “trend line” indicative of that chemical family [75, 77]. Multiple reports have looked at these trend lines and the ability of IM-MS to differentiate distinct chemical families by looking at where ion signals fall in the two-dimensional plots. Moreover, studies can be done on single families of ions, *i.e.* carbohydrates, peptides, nucleic acids. Within a specific chemical family, experiments can be done to see if there are structural differences in ions according to their deviation from an expected trend line [78-79].

1.6 Ion Mobility Spectrometry Employing Different Ionization Sources

Ionization sources play a role in the mobility experiment as some ionization sources produce a distribution of ion charge states while some ionization sources produce only single-charged ions. Electrospray ionization (ESI) [80] has shown great analytical utility in the analysis of large biomolecules. The acidity of the electrospray solvent can be manipulated [81-83], or supercharging solvents can be added [84-87], to achieve different distributions of ion charge states to be analyzed. This allows for studies of changes in ion mobility and ion-neutral collision cross section as a function of ion charge state.

Furthermore, some ionization sources impart internal energy exceeding that which is required for ionization which results in activation and dissociation of the ion. Thus, the parent ion and subsequent fragment ions would be analyzed. Ion activation and dissociation occurs in high energy electron impact ionization and matrix assisted laser desorption/ionization (MALDI) [49-50] at high laser fluence as well as high velocity electrons in electron ionization (EI). The deleterious effect of ion dissociation is decreased sensitivity owing to parent ion population depletion and complication of the ion mobility spectrum.

Another consideration of ion sources to be coupled with ion mobility spectrometry is whether the ion source is pulsed or continuous. A continuous ion source such as ESI, EI and chemical ionization (CI) produces a constant stream of ions. This becomes detrimental to the mobility experiment as ions with different mobilities produced at different times will elute from the mobility cell at the same time, causing an

overlap of ions admitted to the drift cell at different times. In other words, the resulting mass spectrum cannot be correlated with the mobility spectrum since the ion signals from the mass spectrum are not introduced to the mobility cell at the same time. To overcome this challenge, a method must be developed to stop the continuous flow of ions and intermittently introduce them into the mobility drift cell.

The most popular methods for introducing ions to the drift cell from a continuous ion source is through the use of a Bradbury-Nielsen gate [88] or an ion trapping device such as a quadrupole ion trap (QIT) [89], linear ion trap (LIT) [90-93], or an RF ion funnel [94-96]. A Bradbury-Nielsen gate is the simplest of these devices and utilizes a series of parallel wires. The parallel wires are strung orthogonal to the direction of the ion flight path. When the gate is closed, adjacent wires are held at opposite polarity potentials to create an electric field. The electric field created between the wires causes ions to be deflected from their normal flight path and thus are not transmitted to the ion mobility drift cell. When the gate is open all wires are held at the same potential, creating a field free region which allows ions to pass through. Ion gates are normally pulsed open for a finite amount of time that will define the initial ion packet width introduced to the drift cell.

Multiplexing methods have been employed with ion gates to increase the number of ions introduced to the drift cell in a finite amount of time, thereby increasing the instrumental duty cycle [97-98]. The multiplexing process is made possible by a binary S-matrix produced by a pseudorandom sequence of events [99]. The number of events, or elements, denoted in the matrix is defined by the equation (1.6-1)

$$n = \sqrt{2n-1} \tag{1.6-1}$$

where n is the total number of elements in the matrix determined by the product of the number of rows and columns.

Ion trapping devices provide a similar introduction of ions to the drift cell but also provide a means of ion accumulation to increase the number of ions admitted to the drift cell in a finite amount of time, resulting in greater sensitivity. Quadrupole ion traps (QIT) [100-103], linear ion traps (LIT) [104-106], and RF ion funnels [107-110] have been employed utilizing their ion trapping capabilities to accumulate ions over a period of time followed by axial ejection of the ions into the drift cell. The LIT has a great advantage over a QIT in terms of trapping capacity, making it more amenable for analyses of low concentration species [60]. Furthermore, LITs provide capabilities for trapping and admitting all ions produced from the ion source in an RF only operating mode, or can be used in an ion selection mode where only one ion maintains stability in the quadrupole before injection to the ion mobility drift cell. This allows for a complex sample to be analyzed initially and the presence of an ion signal of interest may then be mass selected in the quadrupole for an isolated analysis.

1.7 Drift Tube Ion Mobility Spectrometry at Pressures of 1-10 torr

One experimental variable of considerable interest in ion mobility separations is drift gas pressure. As mentioned in section 1.1, the electric field, *E* (*V/L* where *V* is applied voltage and *L* is drift length), is the accelerating force in the separation. For a fixed drift cell length, the voltage that can be applied is a function of pressure and the distance between two electrodes (1.7-1)

$$V = f(pd) \tag{1.7-1}$$

Paschen conducted a study over 100 years ago to determine electrical breakdown voltages between two electrodes spaced at a certain distance apart as a function of pressure [111]. The curve shows that at high vacuum (low pressure), 6 x 10^{-5} torr, 40 kV can be applied across two electrodes spaced 1 inch apart. The same voltage can be applied across the electrodes at atmospheric pressure, but at pressures of 1-10 torr, electrical breakdown occurs at 900 V, respectively. Thus, the applied voltage can be increased at elevated pressures.

Second, diffusion of ions in the drift cell is mitigated at higher pressures. Diffusion of ions is dependent on ion flux, described by Fick's first law (1.7-2)

$$J = -D\nabla n \tag{1.7-2}$$

where J is ionic flux density, n is ion number density, and D is the diffusion coefficient which is a joint property of the ion and drift gas. As the drift gas pressure increases the diffusion coefficient decreases resulting in a less diffuse ion packet. This leads to a narrower mobility peak width and a less radially diffuse packet of ions.

There are challenges, however, associated with running mobility separations at elevated pressures. The first of these challenges is the need for increased differential pumping when high pressure ion mobility spectrometry is interfaced with a mass spectrometer. High speed vacuum pumps and a conductance limit on the gas flow from the mobility cell are required to achieve the pressures needed for mass analysis. To achieve the gas flow conductance limit, a small aperture plate is normally positioned at the mobility cell exit. The diameter of the aperture ranges from hundreds of microns to a

few millimeters. Larger apertures require higher speed vacuum pumps than do smaller apertures. At high pressures, smaller aperture diameters must be used.

A compounding problem of utilizing small apertures is the transmission of ions through the ion mobility drift cell. While traversing the drift cell an ion cloud diffuses in the drift gas in all directions away from the initial density of the ion packet; in the direction of the negative concentration gradient. This means that ions diffuse both in the longitudinal dimension of the drift cell and the radial dimension. As the pressure or drift cell length is increased, ion transmission through the drift cell decreases and the sensitivity of the experiment is greatly reduced.

A second challenge associated with high pressure ion mobility spectrometry is drift gas purity. The mobility of an ion, *K*, is directly related to the drift gas used in the separation. The ion mobility would change if a different drift gas [4, 112], or mixture of drift gases, was used. This phenomenon can be explained by the different atomic sizes of different drift gases and different interaction potentials between the ion and neutral drift gas. As the drift gas pressure is increased the gas purity becomes a greater factor for the experiment as the probability for a collision of an ion with a neutral contaminant is increased. The interaction of an ion with a neutral contaminant has the potential to be very different than the interaction potential with the selected drift gas. Thus, the measured ion mobility may change if the collision frequency with a contaminant is too high.

The major advantage of performing ion mobility separations at lower pressure is the faster separation time allowing for higher repetition rate ion sources and thus higher

throughput. Consider an ion mobility experiment where the drift cell voltage and length are fixed and the pressure is varied. Hypothetically speaking, if a peptide mixture is separated in the drift cell at atmospheric pressure and the drift time of the ion with the largest collision cross section is 10 milliseconds. To ensure that all ions are detected prior to introducing the next ion packet to the mobility cell, a time period of 10 milliseconds is required in order to avoid convoluted data owing to correlation of the timing of introduction of the ions to the drift cell and subsequent detection. To put it simply, in IM-TOF-MS hundreds to thousands of TOF spectra can be summed over the course of a mobility separation but each TOF extraction must be correlated with the introduction of ions to the mobility cell; a reference to start the time clock. Thus, in the example above a pulsed ion source, normally a MALDI laser, cannot exceed a frequency of 100 Hz. As the pressure in the drift cell is decreased the laser frequency can be increased to higher repetition rates. A mobility drift time of 5 milliseconds corresponds to 200 Hz and a mobility drift time of 1 millisecond increases the repetition rate to 1 kHz.

The higher throughput is realized when one considers the number of ions that can be introduced over a time period of one second with the three experimental parameters mentioned above. A MALDI N_2 laser (λ = 337 nm) has been reported to produce around 10^5 ions per laser shot [113]. Over the course of one second of data acquisition, the numbers of ions introduced to the mobility cell and for subsequent detection is summarized in Table 1.

Table 1. A representation of ion drift times limiting the laser pulse frequency and thus the throughput of the IM-MS experiment. The number of ions per laser shot is assumed to be 10^5.

Ion Drift Time (ms)	Laser Pulse Frequency (Hz)	# Ions·s^{-1}	# Ions·min^{-1}
10	100	1×10^7	6×10^8
5	200	2×10^7	1.2×10^9
1	1000	1×10^8	6×10^9

As can be seen from Table 1, the number of ions introduced to the mobility cell per second is increased by an order of magnitude from 100 Hz to 1000 Hz, or 1 KHz. Although merely stating, "an order of magnitude," it does not demonstrate the large increase in the number of ions introduced. The exact increase in the number of ions from 100 Hz to 1 KHz in a time span of one second is 90 million. Over a one minute interval, this number increases to 5.4 billion. Thus, ion mobility separations at lower pressure offer the advantage of higher throughput.

1.8 High Resolution Ion Mobility Spectrometry

High-resolution ion mobility spectrometry is very appealing to mass spectrometry as IMS is capable of separating ions, *i.e.* isobaric ions, peptide positional isomers, disaccharide carbohydrates with different branched linkages, which are inseparable by mass spectrometry alone. All of the examples given above would have the same mass and if containing the same number of charges would have the same mass-to-charge (*m/z*) ratio. Therefore, in a mass spectrum the ion signals would overlap as no mass spectrometer would be able to differentiate ions of the same *m/z*. However, in the

hyphenated method of IM-MS the ion signals could be separated on the condition that they have differences in ion structure, or ion-neutral collision cross sections.

The main challenge associated with high-resolution IMS is that most methods employed to increase mobility resolution decrease ion transmission and thus sensitivity. Most experiments to increase mobility resolution in drift tube IMS have centered around increasing the applied electric field. In order to increase the electric field and maintain low *E/p* separation conditions as well as electrical breakdown through the drift gas, drift gas pressure or drift length must be increased. Either of these adjustments leads to longer residence time of ions in the drift cell and thus increased radial diffusion. As a result, ion transmission through the drift cell is low owing to the fact that radially diffuse ions will not be transmitted through the drift cell. The problem of ion transmission becomes magnified when higher pressure or long-length drift tube IMS separations are coupled to mass spectrometry.

To overcome problems of low ion transmission through an IMS drift tube a variety of radial focusing mechanisms have been employed. The radial focusing devices employed have been a segmented quadrupole for IMS separations [114], an RF ion funnel [94-96], and the combination of DC and RF fields applied to the drift electrodes of an IMS device [15-16, 115] (see Section 2 for more discussion on the following devices). All of these devices use an RF field that creates a confining effective potential [17] which continually focuses ions in the radial dimension throughout each device. The main difference in the devices is the steepness of the effective potential, or effective potential decay, as a function of radial position. In the segmented quadrupole design, the

radial effective potential is proportional to r^2 whereas the ring electrode designs (RF ion funnel and combination DC/RF on drift electrodes) produce a radial effective potential that is proportional to e^r [17, 60]. The quadrupole field creates a less steep radial effective potential with an electric field minimum only at the center of the device. The ring electrode design creates a steep radial effective potential with a broad electric-field free region in the center. Therefore the segmented quadrupole design confines ions closer to the central axis of the device while the ring electrode design allows for increased space charge capacity.

In this dissertation, we present the periodic-focusing DC ion guide drift cell for high resolution IMS with markedly improved ion transmission (focusing properties similar to the RF ion funnel and DC/RF combination on drift electrodes). The PDC IG employs unique electrode geometry with a DC-only voltage gradient across the device. The unique electrode geometry (similar dimensions of electrode thickness, spacing, and inner diameter) creates a non-uniform axial electric field which in turn creates variations in the radial electric field, an effective RF frequency for ions moving through the device (a position varying waveform), and a confining effective potential produced from the radial electric field and effective RF frequency in the device (see Section 2 for more detailed discussion).

2. PERIODIC-FOCUSING DC ION GUIDE THEORY: RADIAL FOCUSING PROPERTIES OF THE DEVICE

2.1 Introduction

Conventional uniform field ion mobility spectrometry separates ions based on their mobilities through a drift gas under the influence of a weak electric field. Ion packets pulsed into the drift cell are allowed to separate and elute from the drift cell for detection. IMS usually suffers from poor sensitivity owing to the low duty cycle of gating ions into the drift cell as well as radial diffusion of ions in the drift cell resulting in ion packet dimensions that are much larger than sampling apertures used at the mobility cell exit to interface with a mass spectrometer. The frequency of ion injection into the drift cell can be increased with multiplexing methods or by performing mobility separations at lower pressures while overcoming issues of radial diffusion need to be addressed by incorporating radial focusing devices into the mobility separation.

Radial ion focusing can be accomplished in a quadrupole utilizing the RF quadrupole field. Depending on the frequency and amplitude of the RF and the DC rod bias, ions of certain *m/z* will be confined near the center axis of the quadrupole rods. The idea of radial ion confinement utilizing a quadrupole field in IMS was introduced by Javahery and Thomson [114]. In their design, a modified PE-Sciex API 300 triple quadrupole mass spectrometer was used for measurements of ion-neutral collision cross sections. A segmented quadrupole was inserted in place of the Q_2 collision quadrupole. The ten segments of the segmented quadrupole are connected by 20 MΩ resistors and an

electric field is applied across the segments along with the RF field for radial ion confinement. The authors estimate that ion beams traveling through the segmented quadrupole are confined to the central 30 percent of the quadrupole field.

Perhaps the most popular radial ion focusing mechanism is the RF ion funnel developed in Dick Smith's laboratory in 1997. The RF ion funnel utilizes a set of ring electrodes with tapered down inner diameters to focus radially diffuse ions back to the instrument central axis to improve ion transmission. A DC voltage gradient is applied across the electrode stack to provide an axial electric field while the RF voltage is applied 180 degrees out of phase to adjacent electrodes to focus ions through the radial electric field and confining effective potential produced from the radial electric field [95]. Originally, the design was implemented after electrospray ionization sources to increase ion transmission from the source into a mass spectrometer [94-96]. In 2001, the first RF ion funnel was used to accumulate and trap ions prior to injecting them into an ion mobility drift tube [116]. The first publication to take advantage of the radial focusing of the RF ion funnel to correct ion trajectories of radially diffuse ions at the end of a mobility drift tube and increase ion transmission was reported by Tang [108]. After the publication by Tang, the use of RF ion funnels for improving ion transmission in DT IMS has become very prevalent [107, 117-119]. Increased length uniform field drift cells have employed multiple RF ion funnels dividing the overall drift length into multiple drift regions [110, 120] allowing for multiple radial focusing events to increase ion transmission as well as the introduction of IMS-IMS platforms [121-123].

Similar to the idea of ion mobility separations in a segmented quadrupole is the idea of the combination of a DC field for axial ion motion along with a superimposed RF voltage for radial ion confinement on individual drift electrodes. The idea of using both DC and RF fields on the electrodes of a DT IMS device was proposed by Thalassinos *et al*. on a modified Waters UK "Ultima" Q-TOF instrument [115]. The drift cell consists of ring electrodes that are grouped into sets of four connected by a resistor chain and then connected via another resistor to the next set of four electrodes. This design provides a non-uniformity in the potential gradient, providing a non-uniform electric field much like in the PDC IG while the RF fields serve to confine ions as they traverse the mobility drift cell. In the same year, Giles introduced a similar design utilizing an RF stacked ring ion guide (SRIG) with a traveling DC voltage wave through the SRIG (termed a TWIG). Detailed descriptions of the effective potentials produced from the SRIG and their role in radial ion focusing is presented as well as the potential for a SRIG with a traveling DC voltage wave (TWIG) for ion mobility separations [16]. This paper proved to be the prelude to the Waters Synapt HDMS [15] and its newly improved model, the Waters Synapt G2 HDMS.

Here, we present the radial focusing properties of a dispersive IMS device that we have termed a periodic-focusing DC ion guide (PDC IG) drift cell. The drift cell utilizes a unique electrode geometry in terms of electrode thickness, spacing, and inner diameter that create a non-uniform (fringing) axial electric field. The non-uniform axial electric field also creates variations in the radial electric field, ion axial velocity, and ultimately leads to a position varying waveform that creates an effective RF field in the

device. The effective RF field in the device also creates confining effective potentials from the edges of the electrodes that can be seen as a slow drift motion of ions toward the drift cell central axis.

2.2 Experimental

2.2.1 SIMION simulations

SIMION version 8.0 (SIS; Ringoes, NJ) simulations were used for calculating the axial electric field, equipotential lines, and radial electric field in the PDC IG drift cell with dimensions of thickness, spacing, and inner diameter of 6 millimeters. Ion trajectories provided herein are for the radical cation of C_{60}, *m/z* 720 Daltons, with an ion-neutral collision cross section of 124 $Å^2$. A user program, collision_hs1.lua, is employed to simulate ion-neutral collisions with He drift gas using hard-sphere collisions.

2.3 Results and Discussion

To first analyze the differences between a uniform field drift tube IMS and periodic-focusing DC ion guide (PDC IG) IMS design, it is important to look at the equipotential lines provided by each design. In a uniform field drift tube, thin electrodes with large inner diameters are used to eliminate end effects or protruding electric field lines causing a non-uniform electric field (Figure 12(a)). This means that ions traveling down the drift cell axis will feel the same potential drop over a fixed distance anywhere on the *z*-axis of the drift cell. Figure 12(a) shows that non-linear (non-uniform) electric

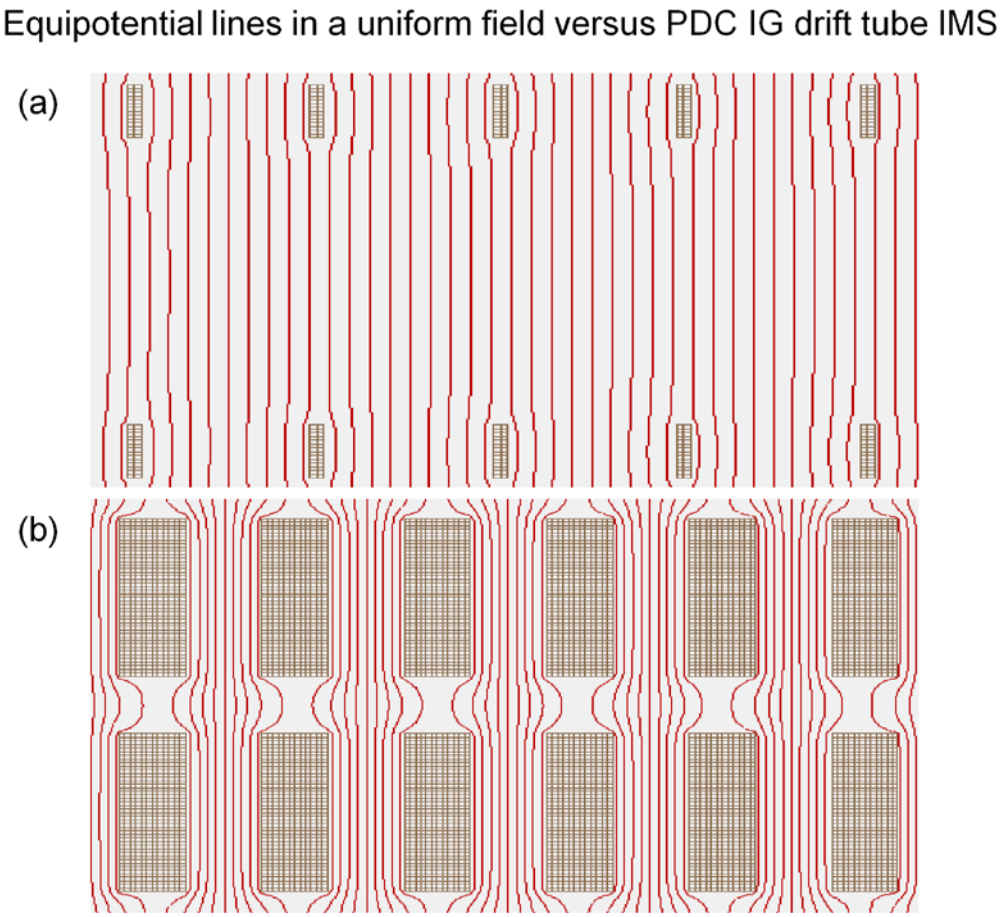

Figure 12. Equipotential lines shown for a uniform field drift tube IMS and a PDC IG drift tube IMS design. The electrode dimensions were drawn to be approximately 6 mm thick, 6 mm spacing, and 8 mm inner diameter for the PDC IG.

fields only exist near the electrode walls. In the PDC IG, thick electrodes are used with much smaller inner diameters to create a non-uniform electric field experienced by ions as they travel down the *z*-axis of the drift cell (Figure 12(b)). This means that ions experience a different magnitude electric field according to their *z*-position in the drift cell. The highest magnitude electric field is experienced in between two adjacent electrodes and the lowest magnitude electric field is experienced inside of an electrode.

The non-uniform electric field provided by the PDC IG design plays an integral role in the radial focusing properties of the device.

The effect of the non-uniform electric field in the PDC IG and its general effect on ion transmission can be seen from a comparison of two SIMION simulation results. Figure 13 displays the ion trajectories from simulations on a uniform field and PDC IG drift cell 40 centimeters in length. The important mobility parameters are the same for each separation. The electric field for the separation is 30 Vcm^{-1} with a Helium drift gas pressure of 1 torr resulting in an *E/p* value for the separation of 30 $Vcm^{-1}torr^{-1}$. The ion used in both simulations is $C_{60}^{\bullet+}$, with an *m/z* of 720 Daltons and a defined ion-neutral collision cross section of 124 $Å^2$. Ion transmission is determined by counting the number of ions that pass by a physical boundary, the aperture plate, and continue to the detector. The ions are counted in a data recording program in SIMION.

In Figure 13(a), the radial diffusion of ions can be seen from the off-axis ion trajectories and low ion transmission, specifically 2 percent. The lack of a radial focusing mechanism in the uniform field design leads to low ion transmission. For uniform field IMS ion transmission continues to decrease as drift length is increased, causing great limitations in sensitivity. Figure 13(b), however, shows a dramatic increase in ion transmission through a PDC IG drift cell. The ion transmission through this device improves twenty-fold to 40 percent.

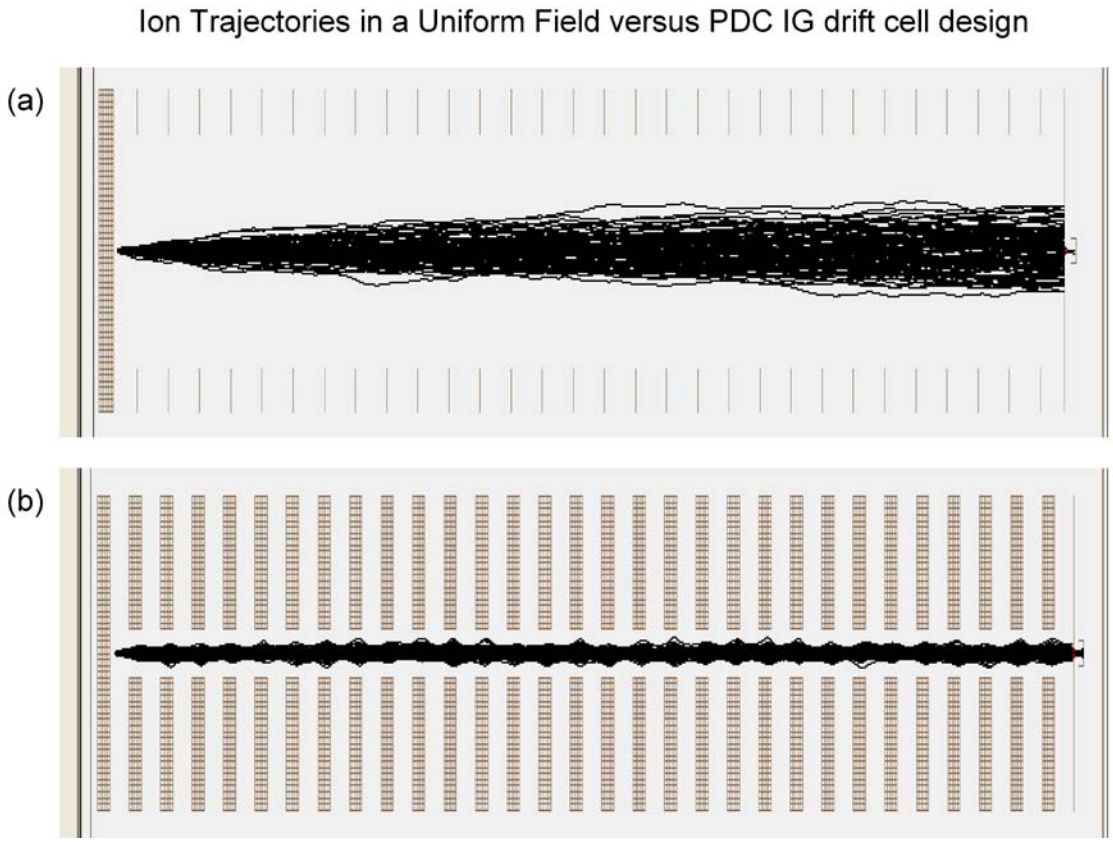

Figure 13. Ion trajectories in a 40 centimeter uniform field drift tube IMS (a) and PDC IG drift tube (b) design.

The radial diffusion of ions is corrected for and ion trajectories are maintained near the central drift cell axis. Generally, the ion trajectories seem to follow the equipotential lines (shown in Figure 12(b)) much like ions through an Einzel lens system in vacuum, however, there is much more involved in the radial focusing of ions in the PDC IG drift cell that must be explained in detail.

The first detail of importance in the PDC IG is the non-uniform axial electric field, E_z. The axial field varies as a function of axial position (z) in the drift cell and actually oscillates and may be described by a sinusoidal wave. The sinusoidal oscillation as a function of axial position (z) is shown in Figure 14. The applied electric field in the example in Figure 14 is 25 $Vcm^{-1}torr^{-1}$. The axial electric field, E_z, oscillates from a maximum of approximately 40 $Vcm^{-1}torr^{-1}$ to a minimum of ~8 $Vcm^{-1}torr^{-1}$, with an overall central electric field, E_c, of approximately 25 $Vcm^{-1}torr^{-1}$ for an ion traveling down the central drift axis, z. The oscillating electric field provides a variable ion axial velocity as it traverses the PDC IG drift cell. The ion would still attain an overall average axial velocity through the drift cell but the local velocity of the ion is changing with respect to axial position, z, in the drift cell.

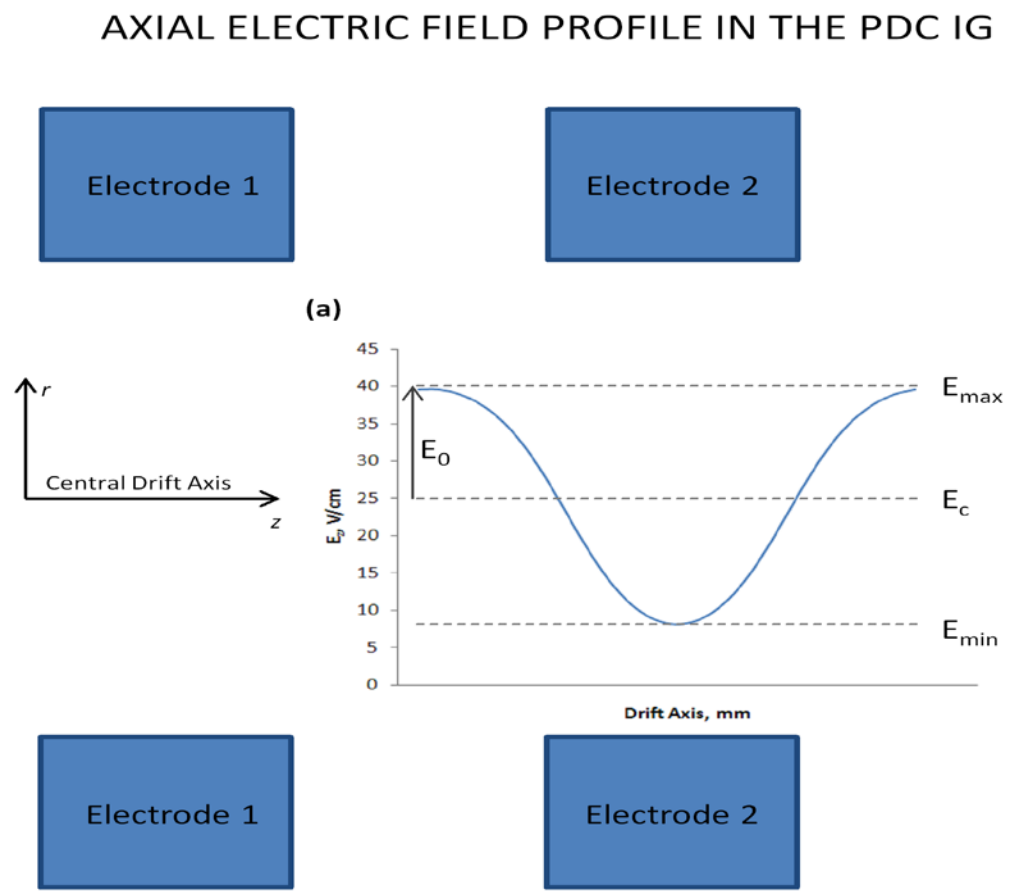

Figure 14. The non-uniform axial electric field, E_z, profile in the periodic-focusing DC ion guide in relation to electrode position.

The oscillating electric field as a function of *z*-position leads to what can be considered a position-varying waveform. A more familiar concept is a time-varying waveform which is utilized in quadrupole and linear ion traps through the use of RF fields to radially confine ions. A descriptive term for the wiggle motion of a charged particle in an RF field is given by the effective potential. The effective potential, *V**, in an RF field is given by the equation [17]

$$V^*(r) = \frac{q^2 E_{0,r}{}^2}{4m\Omega^2} \tag{2.3-1}$$

where q is ion charge, $E_{0,r}$ is the radial electric field amplitude, m is ion mass, and Ω is the RF frequency. The force,Δ V^*, from the radial electric field serves to confine the ion.

The concept of effective potentials in a DC-only device was introduced by Guan and Marshall [124]. In their design adjacent electrodes have the same amplitude but opposite polarity voltages applied to create an oscillating DC field, which they called a stacked-ring DC ion guide. The oscillating DC field acts as an effective RF field for an ion moving through the electrode stack with an axial velocity. The effective RF amplitude is determined by the amplitude of the applied voltage on the rings and the effective RF frequency is determined by the periodicity, or geometry, of the device along with the ion axial velocity, V_z, of the ion. To put it more simply, the periodicity of the stacked-ring DC ion guide is determined by the thickness and spacing between three adjacent electrodes, representing one period of the RF cycle. The effective RF frequency, ν_{eff}, in Hertz is then determined from the ion axial velocity of the ion and the periodicity of the electrode stack

$$\nu_{eff} = \frac{V_z}{\pi z_0} \tag{2.3-2}$$

where V_z is the ion axial velocity and z_0 is the length of one electrode. The effective RF frequency, Ω_{eff}, in radians per second can then be determined by equation 2.3-3.

$$\Omega_{eff} = 2\pi\nu_{eff} = \frac{2V_z}{z_0} \tag{2.3-3}$$

The effective RF frequency (equation 2.3-3) can then be inserted into equation 2.3-1 to yield the equation

$$V^*(r) = \frac{q^2 E_{0,r}{}^2 z_0{}^2}{16 m V_z{}^2} \tag{2.3-4}$$

where z_0 is the periodicity of the electrode geometry and V_z is the axial velocity of the ion.

Analogous to the DC IG, the effective RF frequency and effective potentials in a DC field have been applied to the periodic-focusing DC ion guide. One of the subtle differences between the stacked ring DC ion guide and the PDC IG is the thickness of the electrodes. The PDC IG utilizes thick electrodes which causes radial electric field variations at both the front edge and back edge of the electrode. The period of the radial electric field in the PDC IG is actually equal to the thickness (t) of an electrode plus half the spacing (s) between adjacent electrodes on either side.

$$\lambda = t + s \tag{2.3-5}$$

The radial electric field, E_r, oscillates as a sine wave as a function of position in relation to the electrode subunits. A depiction of the oscillation of the radial electric field as a function of position is shown in Figure 15. As can be seen from the figure, the radial electric field is in the direction away from the central axis (-r direction) of the drift cell as ions enter an electrode. On the other hand, the radial electric field is in the direction toward the central axis (+r direction) of the drift cell as ions leave an electrode. This can be confirmed by looking at a potential energy diagram showing one electrode of a PDC IG (shown in Figure 16). According to the potential energy diagram, a convex saddle is

present as ions approach the front edge of an electrode. As a result, ion trajectories start to diverge from the central axis of the drift cell until they reach a position near the middle of an electrode where the axial electric field approaches a minimum and the amplitude of the radial electric field approaches zero. When exiting the electrode, a concave saddle is present which serves to focus ions back to the central axis of the drift cell.

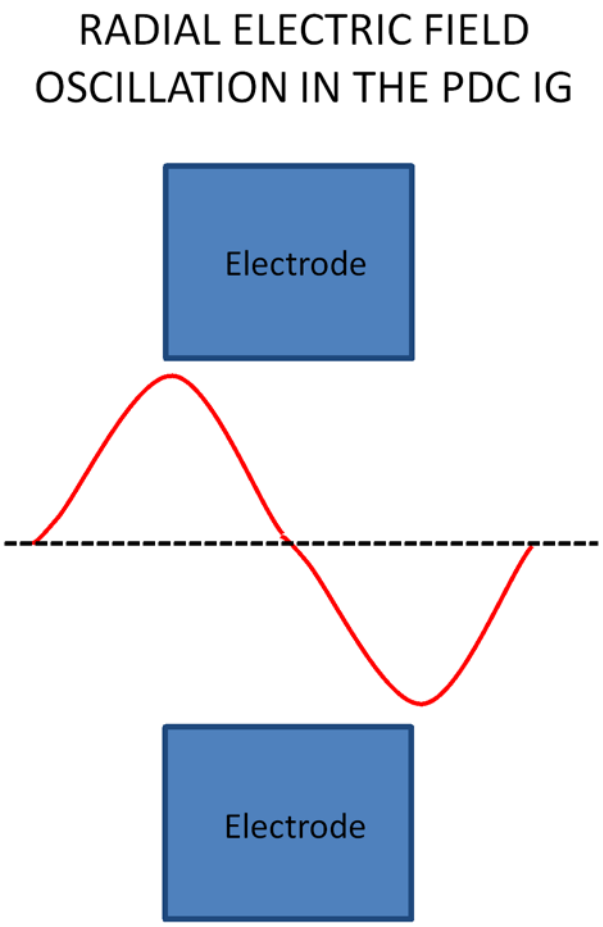

Figure 15. Radial electric field oscillation in the PDC IG representing one period in relation to an electrode.

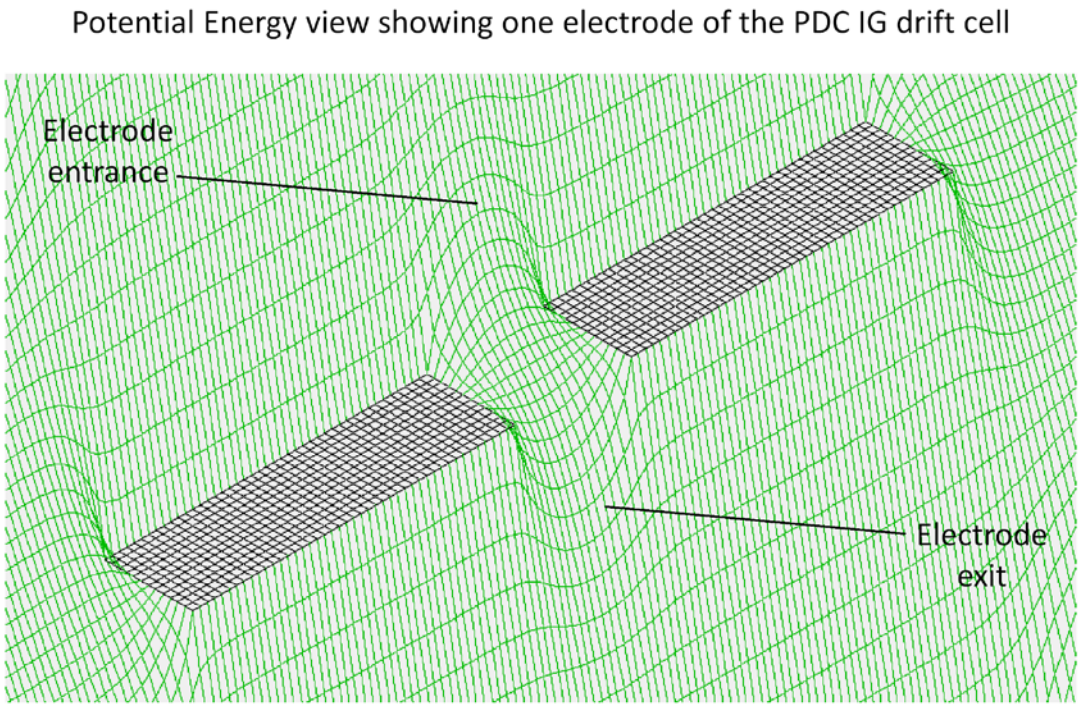

Figure 16. Potential energy view showing one electrode of a periodic-focusing DC ion guide drift cell.

The radial ripple motion is a convoluted product of both the axial electric field and the radial electric field and the effective RF frequency is in the kHz to hundreds of kHz range in the PDC IG. If only the radial electric field were considered then ion motion, or ion displacement, would be governed by the force provided from the radial electric field (Figure 15). To help understand ion displacement in a radial electric field, consider the example of an ion moving with a constant velocity with harmonic motion changing in time. The force from the radial electric field can be defined by

$$F_r = ma_r = qE_r = qE_{0,r}\sin\left(\Omega_{eff}t\right) \tag{2.3-6}$$

where q is ion charge, E_r is the radial electric field, $E_{0,r}$ is the radial electric field amplitude as a function of radial position, m is ion mass, and a_r is acceleration in the radial direction. Rearrangement of equation 2.3-6 yields an expression for the radial acceleration.

$$a_r = \frac{qE_r}{m} = \frac{q}{m} E_{0,r} \sin\left(\Omega_{eff} t\right) \tag{2.3-7}$$

In equation 2.3-6 and 2.3-7, the radial electric field, E_r, is converted to the amplitude of the radial wave, E_0, and the sinusoidal oscillation of the radial electric field, $\Omega_{eff}t$. The term Ω_{eff} is defined by the periodicity of the electrode design according to equation 2.3-8

$$\Omega_{eff} = \frac{2\pi V_z}{\lambda} \tag{2.3-8}$$

where V_z is ion axial velocity and λ is equal to the sum of the distance of one period of motion. Substitution of 2.3-8 for Ω_{eff} yields the following equation [125]

$$a_r = \frac{q}{m} E_{0,r} \sin\left(\frac{2\pi V_z t}{\lambda}\right) \tag{2.3-9}$$

Integration of equation 2.3-9, radial ion acceleration, with respect to t yields the radial velocity term plus the initial radial velocity $V_{r,i}$ given in the following equation [125].

$$V_r = -\frac{q}{m} E_{0,r} \left(\frac{\lambda}{V_z 2\pi}\right) \cos\left(\frac{2\pi V_z t}{\lambda}\right) + V_{r,i} \tag{2.3-10}$$

Likewise, integration of equation 2.3-10, the radial ion velocity, with respect to time (t) yields the expression for the radial displacement of the ion [125].

$$r = -\frac{q}{m} E_{0,r} \left(\frac{\lambda}{V_z 2\pi}\right)^2 \sin\left(\frac{2\pi V_z t}{\lambda}\right) + V_{r,i} t + r_i \tag{2.3-11}$$

From equation 2.3-11, the radial displacement of the ion in the DC IG is dependent on the ion axial velocity. If ion axial velocity is high then the radial displacement of the ion from an initial position is small. On the other hand, if ion axial velocity is low then the magnitude of radial displacement of the ion increases.

In the PDC IG, however, ions experience collisions as they traverse an intermediate pressure region ($\geq$ 1 torr) where ion axial velocity changes as a function of *z*-position and ion motion is also dependent on the mobility, *K*, of an ion. For this reason, ion motion through the PDC IG is different than in the DC ion guide

To demonstrate, consider an ion of varying axial velocity through one electrode where the variation in velocity is asymmetric in relation to the electrode geometry, or periodicity (Figure 17). The axial velocity minimum occurs toward the back edge of the electrode as a result of a higher magnitude axial electric field (E_z = 30 $Vcm^{-1}torr^{-1}$ for example shown in Figure 17(b)). Let us define an initial ion radial displacement of $r \neq 0$, meaning an initial position that is off-axis from the central drift axis. The ion moves forward owing to the dominating force from the axial electric field but moves to a further radial position ($r \neq 0$) from the radial electric field force and the declining force from the axial electric field. Similar to equations 2.3-10 and 2.3-11 the radial velocity of the ion and radial ion displacement in the PDC IG varies with ion axial velocity. In the PDC IG, ions experience collisions with the neutral drift gas and therefore radial ion velocity can be approximated by the drift velocity in the following equation [125].

$$V_r = KE_{0,r} \sin\left(\frac{2\pi v_z t}{\lambda}\right) \tag{2.3-12}$$

Integration of 2.3-12 with respect to *t* gives the radial ion displacement in the PDC IG. Specifically, the amplitude, *A*, of the radial ion displacement can be defined by [125]

$$A = -\frac{q}{m} E_{0,r} \left(\frac{\lambda}{V_z 2\pi} \right)^2 \tag{2.3-12}$$

As the ion begins to enter the back-edge region of the electrode, the force from the radial electric field is in the direction of the central drift axis and the ion axial velocity approaches a minimum. Thus, the amplitude of the radial ion displacement is increased at the back edge of the electrode and strongly focuses the ion toward the central drift axis prior to entering a subsequent period of the PDC IG.

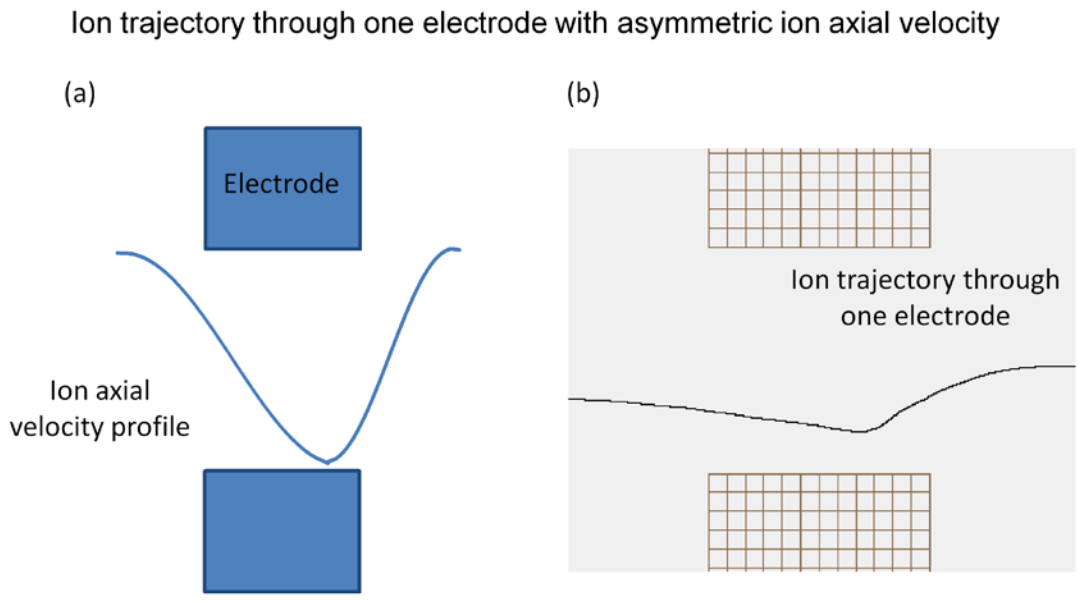

Figure 17. Ion trajectory through the PDC IG with an asymmetric ion axial velocity in relation to the periodicity of the electrode design (a). The ion trajectory provided by SIMION is shown in (b).

Next, consider the case where ion axial velocity through one period of the PDC IG is symmetrical (Figure 18). The symmetric axial velocity scenario is accomplished by applying a lower magnitude axial electric field (E_z = 15 $Vcm^{-1}torr^{-1}$ for example in Figure 18(b)) which results in decreased force from the axial electric field. Thus, the amplitude of radial ion displacement at the front edge of the electrode is increased resulting in an increased radial position ($r \neq 0$) of the ion in the center of the electrode (middle of electrode orifice). Furthermore, the ion axial velocity minimum occurs in the center of the electrode making the axial velocity profile symmetric in relation to the electrode design (Figure 18(a)). Consequently, ion motion exiting the electrode would also be symmetric which should result in an equivalent radial ion displacement toward the central axis of the electrode. However, the magnitude of the radial ion displacement at the back edge of the electrode is asymmetrical when compared to displacement at the front edge of the electrode (Figure 18(b)). Ion motion through one period of the PDC IG cannot be explained completely by radial ion displacement provided by the force of the radial electric field.

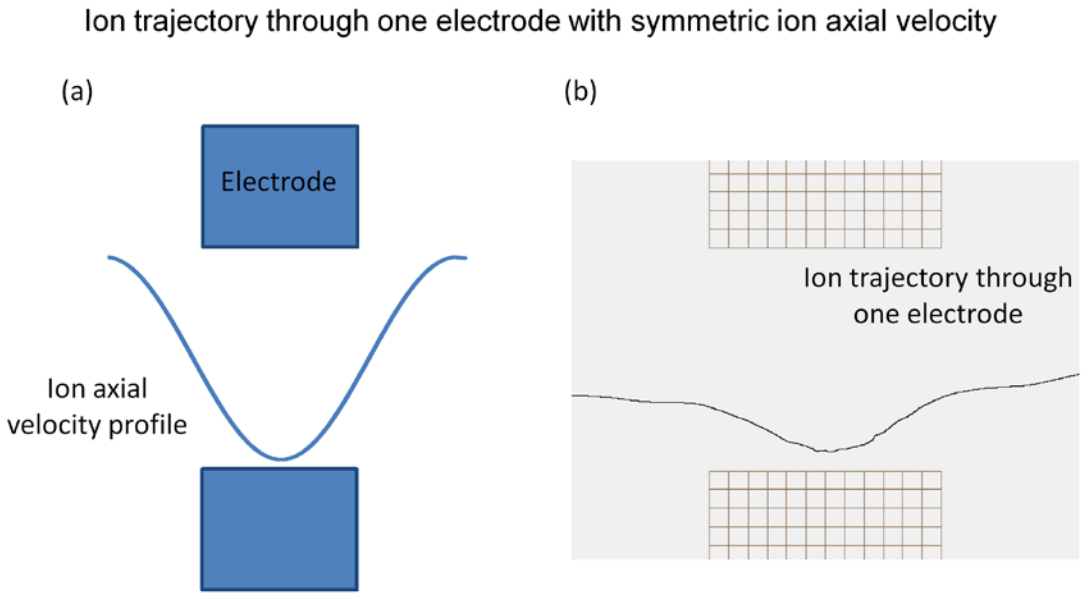

Figure 18. Ion trajectory through the PDC IG with a symmetric ion axial velocity in relation to the periodicity of the electrode design (a). The ion trajectory provided by SIMION is shown in (b).

In order to fully understand ion motion through the PDC IG, effective potentials produced by variations in the radial electric field and ion axial velocity must be considered. The effective potential was presented in equation 2.3-4 and its magnitude depends on the magnitude of the radial electric field as a function of radial position and the axial velocity of the ion through the PDC IG drift cell (Figure 19).

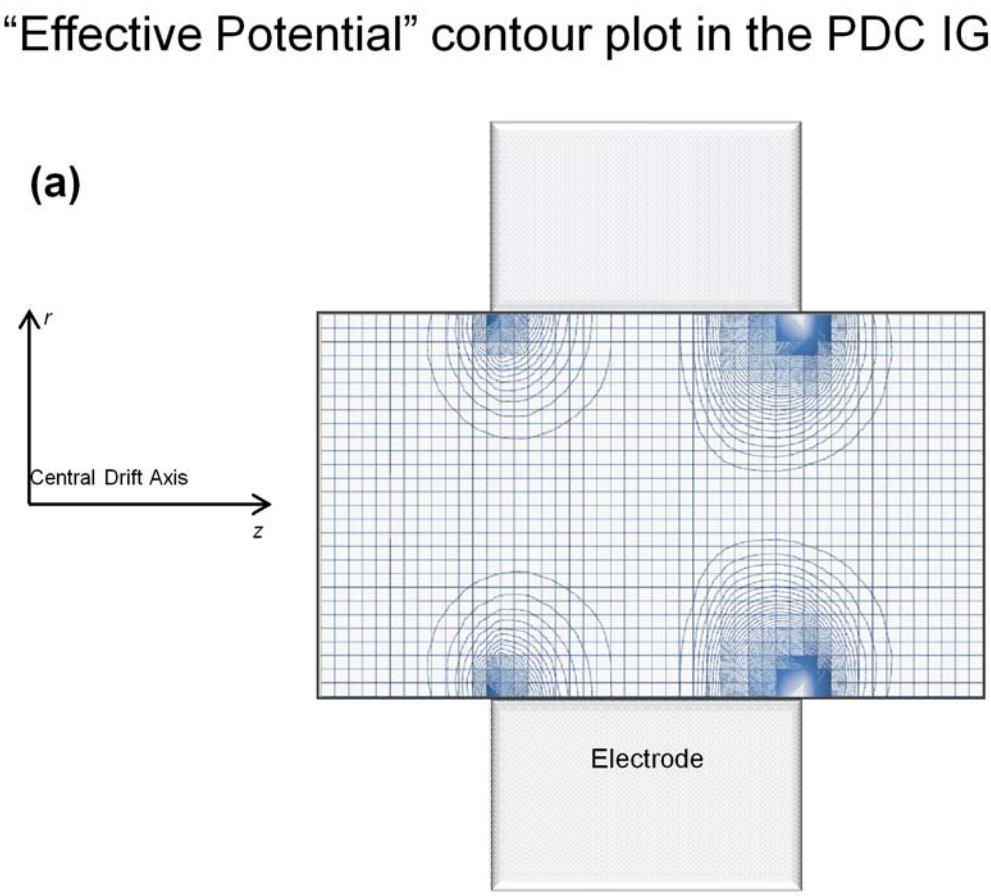

Figure 19. A contour plot showing the calculated "effective potentials" in the 6 mm inner diameter PDC IG.

As an ion approaches the front edge of an electrode, the axial velocity is high and thus the magnitude of the effective potential is low. In fact, ion motion is dominated by the axial electric field and the radial ion displacement from the central drift axis is a direct result of the radial electric field while the front edge effective potential has minimal effect on ion trajectory. At the back edge of an electrode, however, the ion axial velocity is at a minimum and thus the ion trajectory is less affected by the axial electric field; rather, ion trajectories are mainly governed by the radial electric field and effective

potentials. The effective potentials produced at the back edges of the electrode are higher in magnitude owing to decreased ion axial velocity. Therefore, the slow drift of ions toward the central axis of the drift cell can be described by the effective potential model, specifically the increased magnitude effective potentials at the electrode back edge. To further illustrate this point, consider the scenario of the symmetric ion axial velocity through one period of the PDC IG. As an ion reaches the center of the electrode (an ion axial velocity minimum), the ion moves to a larger radial, *r*, position. Upon exiting the electrode, the ion trajectory is radially corrected by the increasing magnitude effective potentials near the electrode surface. The effective potential magnitude increase near the electrode surface can be explained from the increasing $E_{0,r}$ term in equation 2.3-4.

2.4 Conclusion

The periodic-focusing DC ion guide utilizes its unique electrode geometry to radially focus ions to improve ion transmission in DT IMS. The small inner diameter and widened electrode thickness produce variations in the radial electric field that produce both an effective RF frequency (position varying waveform) as ions move through the PDC IG and a confining effective potential that can be seen as the slow drift of ions toward the central axis of the drift cell. The amplitude of radial ion displacement from the radial electric field and effective potential magnitude is asymmetric due to axial electric field variations causing oscillations in the ion axial velocity through the device. The ion velocities at the back edge of the electrode are much lower than at the front edge

of the electrode, resulting in increased magnitude effective potentials thereby increasing the radial focusing of ions through the device.

3. THE DESIGN OF A PERIODIC-FOCUSING DC ION GUIDE DRIFT CELL*

3.1 Introduction

Ion mobility spectrometry (IMS) separates gas-phase ions on the basis of ion-neutral collision cross section [1, 126], which when combined with molecular modeling can be used to augment structural information obtained by using other techniques, *i.e.*, fragmentation chemistry from tandem mass spectrometry and H/D exchange experiments [75, 79]. The obstacles to increasing the experimental capabilities of IMS are ion transmission, *viz.* transmission of ions through the IMS device, and resolution. Increasing the mobility resolution increases peak capacity and allows for separation of ions that have similar collision cross sections.

IMS is already capable of separating different chemical families in conformation space and are easily detected in two-dimensional plots provided by IM-MS [75, 77]. The need for higher resolution IMS centers on the potential capability for separating closely related species that are inseparable by mass spectrometry alone. For example, ions of similar mass may only be identified with a high resolution mass spectrometer, while isobaric ions will never be separated by any mass spectrometer, however if said ions have different collision cross sections, they will be separated by IM-MS. To illustrate this point, consider isomers that contain small structural differences but identical molecular weights. For example, oligosaccharides possess different structures

*Reprinted with permission from "Increased ion transmission in IMS: A high resolution, periodic-focusing DC ion guide ion mobility spectrometer" by R.C. Blase, J.A. Silveira, K.J. Gillig, C.M. Gamage, D.H. Russell, 2010. *International Journal of Mass Spectrometry*, doi:10.1016/j.ijms.2010.08.016, [2010] by Elsevier.

owing to linkage or branch isomers and stereoisomers of asymmetric carbons on a single sugar [127]. Another example would be peptides which are optically-isomeric, one peptide altered by insertion of a single d-amino acid substitution compared to the same peptide without the substitution [117].

Peptide positional isomers, identified by different arrangements of the amino acid sequence within a peptide, and their effect on the ion-neutral collision cross section has also been of significant interest. This is evident in investigations of metalated tyrosine tripeptides YGG and GGY, [128]and separation owing to collision cross section differences of $[M+2H]^{+2}$ ions of SDGRG and GRGDS; termed inverse peptides [117, 129]. It should be noted that cross sectional differences for these smaller peptides may be more pronounced than amino acid rearrangements in larger peptide systems [130]. For example, the cross sectional difference for the doubly charged inverse pentapeptides listed above is about 5 percent while no significant difference is seen for the singly charged species. For larger peptide systems, the deviation in size would be less pronounced as charge sites are better solvated by residues along the peptide backbone and coulombic repulsion energies associated with multiple charged sites is decreased as well. For this reason, increasing ion mobility resolution is imperative to detect ions that would normally go undetected in low mobility resolution instruments.

Finally, separation of different conformations of the same ion have been reported previously by IM-MS coupled with H/D exchange studies [131] and high resolution IMS [132-134]. A continued investigation to increasing resolution in IMS should increase the

already high peak capacity [135-136] in IM-MS leading to advances in ion structure analyses and ion-neutral collision cross section calculations.

The resolution in drift tube IMS is mainly limited by longitudinal diffusion of ions in the drift gas. An equation for diffusion-limited resolution has been defined by [137]

$$R_d = \left(\frac{ELez}{16 k_b T \ln 2} \right)^{1/2} \tag{3.1-1}$$

where E and L are electric field and drift cell length, e and z are electronic charge and number of charges, respectively, K_b is Boltzmann's constant, and T is temperature of the drift gas. As one can see from the equation, resolution can be increased by increasing applied voltage or ion charge state or decreasing the drift gas temperature. Much of the research in high resolution IMS have centered on these three experimental variables [132, 138-140]. This work will focus mainly on the applied electric field and drift cell length and their effect on ion mobility resolution.

In order to increase the applied voltage in drift tube IMS, the length of the drift cell must be increased. Lengthening the drift cell decreases the electric field, E, to avoid entering the high-field limit as well as decreasing the possibility of an electrical discharge through the drift gas. To date, most experiments utilize conventional uniform field electrodes to achieve high resolution measurements. The ion transmission of these experiments is low owing to the main challenge associated with IM-MS being the different pressure regimes at which the two separations must be operated. Ion mobility separations are performed at pressures of a few torr to atmospheric pressure, while mass

spectrometry detection is done in the range of 10^{-5} to 10^{-7} torr. In order to achieve high vacuum conditions needed for mass spectrometry, differential pumping of the ion mobility-mass spectrometry interface is required. This is accomplished by placing a small aperture at the mobility exit followed by a region evacuated by a high speed turbomolecular, or diffusion, pump prior to mass spectrometry analyses. The size of the aperture determines the gas flow conductance limit and thus smaller apertures will decrease the gas load and amount of differential pumping required for MS analyses. The expense of using small apertures is the decrease in ion transmission. As ions traverse the drift cell they diffuse in the drift gas and only a portion of the initial ion population that remains within the radial dimension of the aperture from the central axis of the cell will be transmitted for detection. As drift cell length increases, the number of transmitted ions decreases. The focusing of radially diffuse drifting ions to increase ion transmission without a detrimental effect on resolution is desired to improve ion mobility separation efficiency.

One solution for increasing the ion transmission in IMS-MS was the introduction of an RF ion funnel at the mobility cell exit [108]. The ion funnel is constructed with a series of decreasing inner diameter electrodes to which DC and RF fields are applied to focus diffuse ions back to a tight ion packet for increased ion transmission to the mass spectrometer. A 2.89 meter drift cell built in David Clemmer's laboratory utilizes three ion funnels that segment the drift cell into 3 distinct regions [110, 120-121]. The ion funnel does have some limitations in its coupling with ion mobility separations. First, the funnel must compose a small length compared to the overall drift cell length. This is

because the time the ion spends in the funnel must be negligible compared to the drift time of the ion since the ion transit through the funnel is much different than the ion transit in the drift cell. Secondly, the DC and peak-to-peak RF voltages of the funnel must not be too high or ion heating and possibly ion activation and dissociation in the funnel region could be detrimental to the experiment.

Herein lies the main advantage of the PDC IG drift cell. The simplistic design, utilizing DC fields, eliminates the RF fields used in ion funnels while still increasing ion transmission. The focusing properties of the PDC IG have been described previously [141]. Briefly, the differences in focusing between the PDC IG and conventional uniform field electrodes can be explained by simple electrode geometries. Periodic electrodes have small electrode inner diameters while uniform field electrodes have large inner diameters. The large electrode inner diameters of uniform field electrodes create a linear electric field where the voltage drop that the drifting ions experience is constant (except for at the electrode wall) regardless of radial position in the drift cell. The homogeneity of the electric field provides high resolution [142], but low ion transmission. On the other hand, small inner diameters of the PDC IG create a non-uniform, periodic-field where the voltage drop seen by the ions is dependent on their radial position in the drift cell. Radially diffuse ions are continually refocused to the center of the drift cell by the PDC IG, thus increasing ion transmission.

The increase in ion transmission provided by RF ion funnels and PDC IG drift cells slightly degrade mobility resolution owing to ion trajectory corrections of ions at different radial positions in the drift cell. This problem cannot be overcome since higher

ion transmission is desired, but the extent of resolution degradation must be limited. For PDC IG drift cells, this can be established by altering drift cell variables and examining their effects on resolution.

This work will focus on the performance of a 63 cm PDC IG drift cell; specifically the effect of the PDC IG on mobility resolution and ion transmission. To our knowledge, these are the first experiments investigating drift cell length, applied electric field, and electrode geometry on resolution and ion transmission of a PDC IG drift cell.

3.2 Experimental

3.2.1 Chemicals

A fullerene mixture, C_{60} (MW = 720 Da) and C_{70} (MW = 840 Da), was purchased from Sigma-Aldrich (St. Louis, MO). The peptide Val-4-Angiotensin I (MW = 1208.4 Da), amino acid sequence NRVVIHPFNL, and Glu-Fibrinopeptide B (MW = 1569.6 Da) were purchased from American Peptide Company, Inc. (Sunnyvale, CA) and used without further purification. A suspension of fullerene in benzene was deposited on the stainless steel MALDI probe target and allowed to dry prior to analysis. The peptides were dissolved in distilled water at a concentration of 1 mg ml^{-1} and mixed 1:1 (v:v) with 5 $mgml^{-1}$ alpha-cyano-4-hydroxycinnamic acid in 60% acetonitrile, 38% distilled water, 1% (10%) trifluoroacetic acid solution, and 1% 1M ammonium phosphate. The mixture of peptide and matrix was then spotted on the MALDI target.

3.2.2 Instrumentation

The schematic drawing of the MALDI-IMS instrument used in these studies is contained in Figure 20. Samples are spotted on a stainless steel probe that is inserted into the drift cell between the first and second electrode. The ions formed by MALDI (nitrogen laser, λ = 337 nm (Stanford Research Systems; Sunnyvale, CA)) drift through a 63 cm drift cell composed of 50 individual electrodes (see section *2.3*) operated at pressures between 1-3 torr. The electrodes are connected by 1 MΩ high precision resistors (Mouser Electronics; Mansfield, TX) to establish a linear voltage drop across the drift cell. Ions exit the drift cell through a 500 μm aperture which provides a vacuum differential between the drift cell and the ion detector region. The aperture plate is connected to ground through a high-precision 2.88 MΩ resistor (Mouser Electronics, Mansfield, TX), and the resulting voltage drop serves to accelerate the ions toward the detector (Galileo Channeltron electron multiplier (CEM)) detector (Burle Electro-Optics, Inc.; Lancaster, PA).

3.2.3 Electrodes

The electrode dimensions (inner diameter (*d*), thickness (*t*) and spacing between the electrodes (*s*)) define the periodic-focusing drift field. Here, we examine two different electrode aspect ratios: electrode configuration A where *d*, *t*, and *s* are 6.35 mm (aspect ratio 1:1:1) and electrode configuration B where d is 8 mm while t and s are 6.35 mm (aspect ratio approximately 4:3:3). These two electrodes were used to estimate the effects of the electrode design on both resolution and ion transmission compared with

uniform field electrodes. For the uniform field electrodes, *d* is 50 mm and *t* and *s* are 6.35 mm.

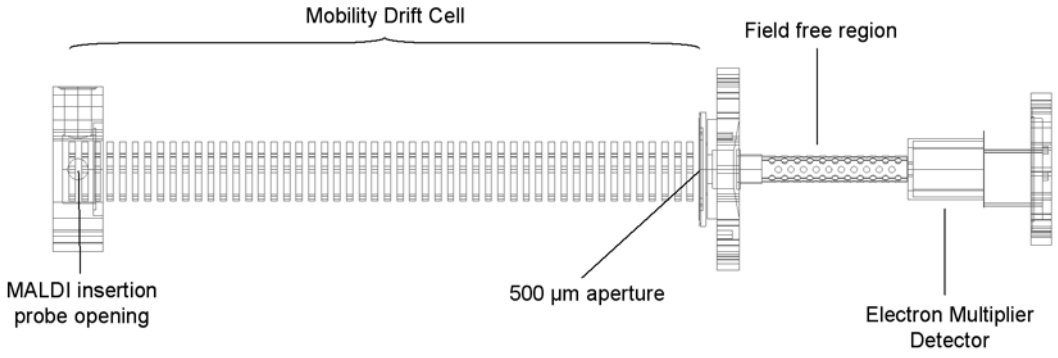

Figure 20. A schematic of the MALDI-IMS instrument. The periodic-focusing DC ion guide (PDC IG) is composed of 50 electrodes with a total drift length of 63 cm.

3.2.4 SIMION Simulations

SIMION version 8.0 (SIS; Ringoes, NJ) simulations were performed for $C_{60}^{\bullet+}$, with an ion-neutral collision cross section of 124 $Å^2$, to investigate resolution and ion transmission for different drift cell electrodes. Ion-neutral collisions were simulated using Helium as the drift gas with the collision_hs1.lua user program provided with SIMION employing a hard-sphere collision model.

3.3 Results and Discussion

The PDC IG was developed in our laboratory for increased ion transmission IMS [141]. Briefly, the device consists of a series of stacked, thick electrodes that radially confine ions to the center of the drift axis, thereby increasing overall ion transmission.

This design takes advantage of the nonlinear electric fields at the edges of each electrode when an electrical potential is applied across the electrode stack. These conditions are very different from those typically employed for uniform field IMS drift cells. For example, the inner diameter of the electrodes used for uniform field drift cells is large relative to the electrode thickness, whereas the inner diameter for the PDC IG is smaller and approximately equivalent to that of the electrode thickness. The geometry (diameter, thickness and spacing) of the electrodes is critical to the focusing properties of the device. Ion focusing occurs as a result of radial variations in the electric field, which generate a confining "effective potential" or "pseudopotential" that extends from the edges of the electrodes (Figure 21(a)). Furthermore, the axial electric field and drift gas pressure determine the drift velocity of the ions which also influences the ion focusing. Clearly ions having different radial position with respect to the electrode

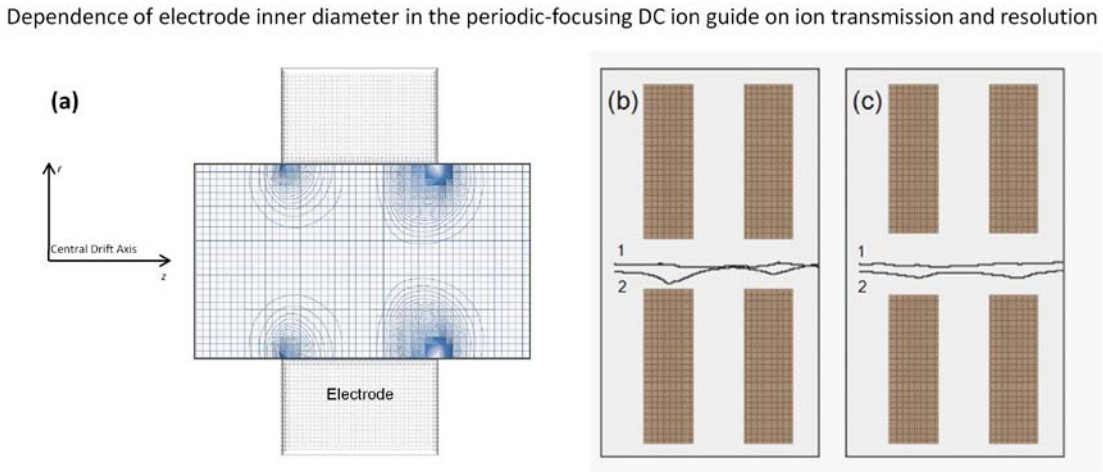

Figure 21. "Effective potential" contours considering axial velocity and radial electric field variations for the 6.35 mm inner diameter drift cell (a). Cross-section of two electrodes from the 6.35 mm inner diameter (b) and 8 mm inner diameter (c) drift cell showing two representative ion trajectories at 29 $Vcm^{-1}torr^{-1}$ ((E/N) = 90 Td).

surface experience different magnitude effective potentials (Figure 21(b) and (c)). As ions diffuse to increased radial positions ($r \neq 0$) they experience greater magnitude effective potentials and are refocused toward the central drift axis ($r = 0$) upon exiting an electrode. After exiting an electrode all ions experience a relatively large potential drop and are accelerated by the electric field. We previously showed that under these conditions the mobility separation corresponds to low-field conditions for large molecule ions, *i.e.*, peptides of the size examined in this study [143]. A more rigorous theoretical treatment of the focusing mechanism, which includes consideration of the effective ion temperature (T_{eff}), of the PDC IG is presented elsewhere [144].

Figure 22 contains theoretical plots of resolution and percent ion transmission versus pressure for the molecular ion $C_{60}^{\bullet+}$ (molecular weight = 720 Da) for three electrode geometries. These simulations were performed for a drift length of 61 cm, an applied voltage of 3500 V and a 1 mm aperture at the exit of the drift cell (results from simulations also tabulated in Table 2). The slight variation in drift length compared to the instrumental drift length and the aperture is due to the millimeter to grid unit ratio in SIMION.

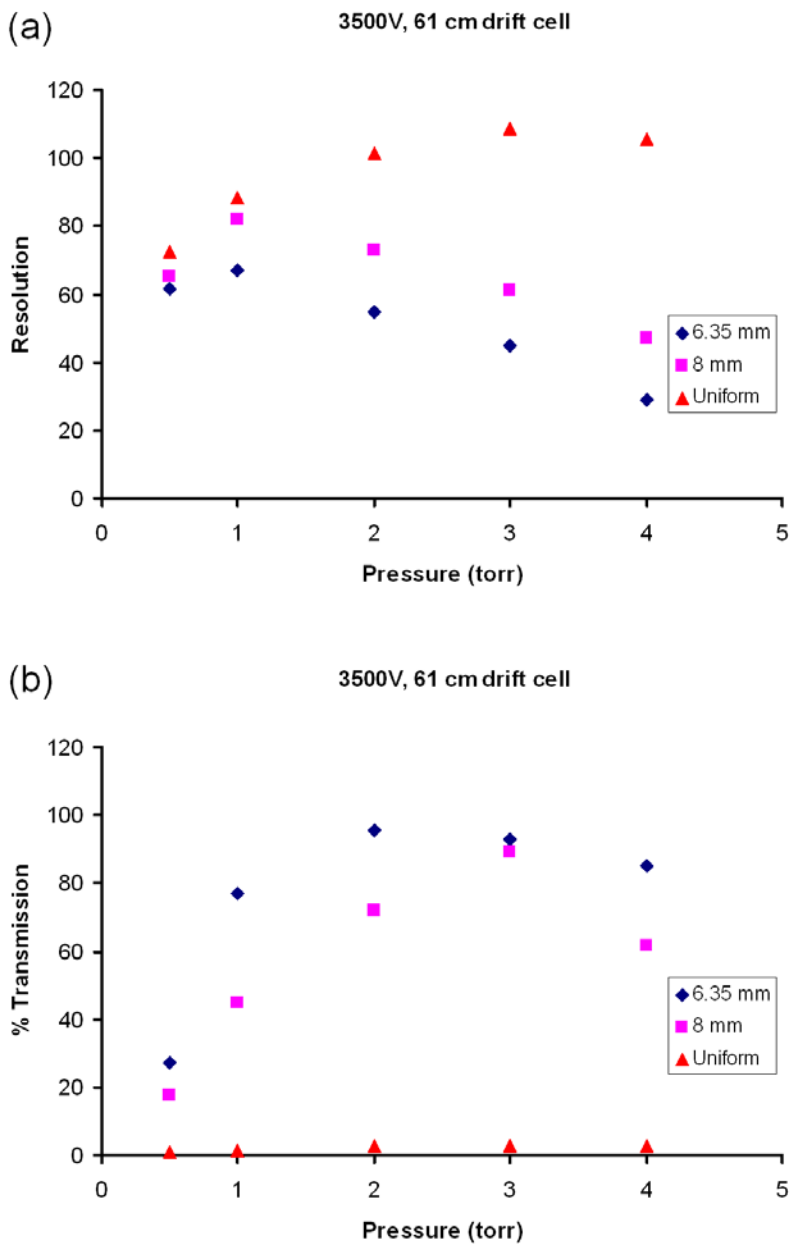

Figure 22. SIMION simulation results depicting resolution (a) and percent transmission (b) as a function of pressure for two PDC IG geometries and a uniform field drift cell 61 cm in length with an applied voltage of 3500 V.

Table 2. SIMION simulation results of electrode configuration A (6.35 mm i.d.) and electrode configuration B (8 mm i.d.) comparing mobility resolution for a 61 cm PDC IG drift cell. Simulation results are also provided for uniform field electrodes for comparison of resolution and percent ion transmission with the PDC IG.

Simulated Resolution and Percent Transmission for 61 cm drift cells

Electrode Inner Diameter	Pressure (torr)	Simulated Resolution	Simulated Percent Ion Transmission	Ion Transmission Increase over Uniform Field Electrodes
6.35 mm	0.5	61.61	27.00	33.75
	1	66.99	76.80	64.00
	2	54.58	95.40	36.69
	3	44.66	93.00	33.21
	4	28.95	85.20	30.43
8 mm	0.5	65.33	17.70	22.13
	1	81.87	45.00	37.50
	2	72.78	72.20	27.77
	3	61.2	89.20	31.86
	4	47.14	61.40	21.93
Uniform Field Electrode	0.5	72.45	0.80	N/A
	1	88.49	1.20	N/A
	2	101.22	2.60	N/A
	3	108.83	2.80	N/A
	4	105.53	2.80	N/A

As illustrated by Figure 22(a), the uniform field drift cell yielded the highest resolution but the overall ion transmission is extremely low. For example, the simulations suggest that the ion transmission is less than 3 percent for all pressures investigated for the uniform field. This value can be compared to that of electrode configuration A, which refocuses radially diffusing ions to the center of the cell, and provides a 40-fold increase in ion transmission versus uniform field electrodes. This focusing effect becomes more pronounced with decreasing inner diameter due to an increase in the effective potentials felt by an ion at an equivalent radial position [144]. This is evident from the increased ion transmission of electrode configuration A compared to electrode configuration B. On the other hand, smaller inner diameter electrodes produce a larger difference in drift length for on- and off-z axis ($r \neq 0$) ion trajectories, which ultimately broadens the ion packet and degrades mobility resolution (Figure 21(b) and (c)). This is evident by the higher resolution of electrode

configuration B versus electrode configuration A (a maximum resolution increase of 22 percent over configuration A for all pressures investigated). A comparison to uniform field electrodes reveals that configuration B decreases resolution by only 10 percent at pressures of 1-2 torr. Although the larger inner diameter of configuration B leads to a slight decrease in ion transmission when compared to configuration A, the increase in ion transmission of configuration B compared to uniform field electrodes is still significant—approximately 28 times.

The two periodic-focusing electrode geometries, configuration A (d=6.35 mm) and configuration B (d=8 mm) were also tested experimentally for resolution at different pressures. Simulations suggest that the maximum resolution for configuration A and configuration B are between pressures of 1 and 2 torr with 3500 V applied across the cell. This was also found experimentally in that the highest resolution measurements at approximately 3500 V were at pressures of 1.42 torr for configuration A and 1.82 torr for configuration B, respectively. Multiple field strengths are also investigated for each of the electrodes at the respective pressures to illustrate the proportionality of electric field and resolution presented in equation 1 (Figure 23(a)). A more complete set of data investigating ion mobility resolution as a function of field strength at varying pressures can be found in Appendix A.

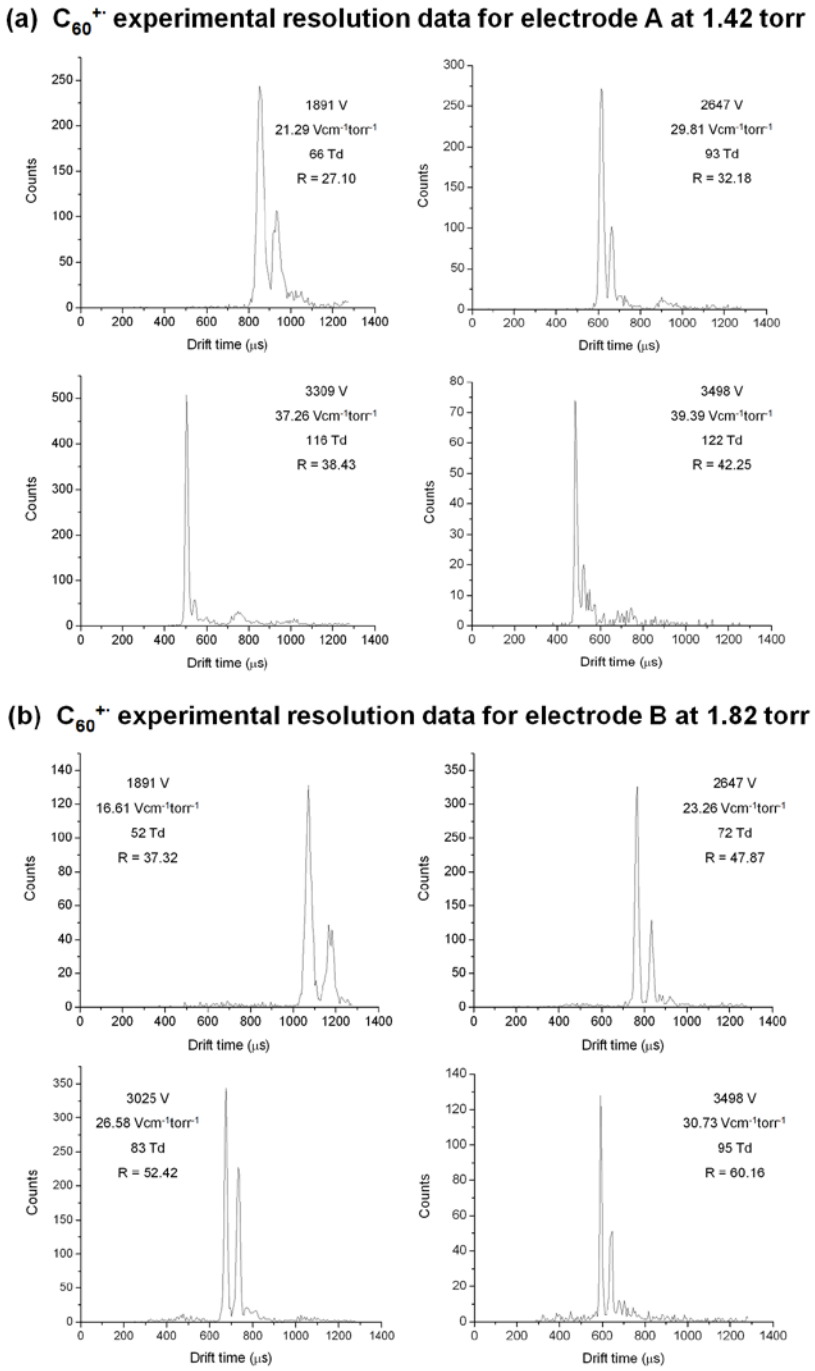

Figure 23. Experimental ion mobility spectra of $C_{60}^{+\cdot}$ and $C_{70}^{+\cdot}$ obtained from a 63 cm PDC IG equipped with 6.35 mm inner diameter electrodes (electrode configuration A) (a). Experimental ion mobility spectra of $C_{60}^{+\cdot}$ and $C_{70}^{+\cdot}$ obtained from the 63 cm PDC IG equipped with 8 mm inner diameter electrodes (electrode configuration B) (b). The applied voltage, *E/p* (*E/N*) values, and mobility resolution, R, are reported for $C_{60}^{+\cdot}$. The drift gas pressure for all spectra in (a) was 1.42 torr while all spectra in (b) was 1.82 torr.

The highest resolution for laser desorbed $C_{60}^{\bullet+}$ ions at 3500 V for configuration A at a pressure of 1.42 torr is 42.25 (Figure 23(a)). At a pressure of 1.82 torr, configuration B yields a resolution of 60.16 with 3500 V across the cell (Figure 23(b)). Notice that the simulated values (Figure 22(a)) are also in the range of these experimental values. The maximum resolution of configuration B represents a 42 percent increase over the maximum of configuration A. Experimentally, configuration B increases resolution by an average of 20-30 percent versus configuration A with only a slight decrease in ion transmission. It should be noted that an equivalent drift length was tested with uniform field electrodes and no appreciable signal was seen after 20 minutes of acquisition time, as suggested by the results of low percent transmission in SIMION simulations.

Two peptides were also studied, using configuration B for the drift cell electrodes, in the 63 cm length drift cell. The peptides were Val-4-Angiotensin I peptide, with amino acid sequence NRVVIHPFNL, and Glu-Fibrinopeptide B (Figure 24). The maximum resolution for each peptide approached 60, similar to the maximum resolution for $C_{60}^{\bullet+}$.

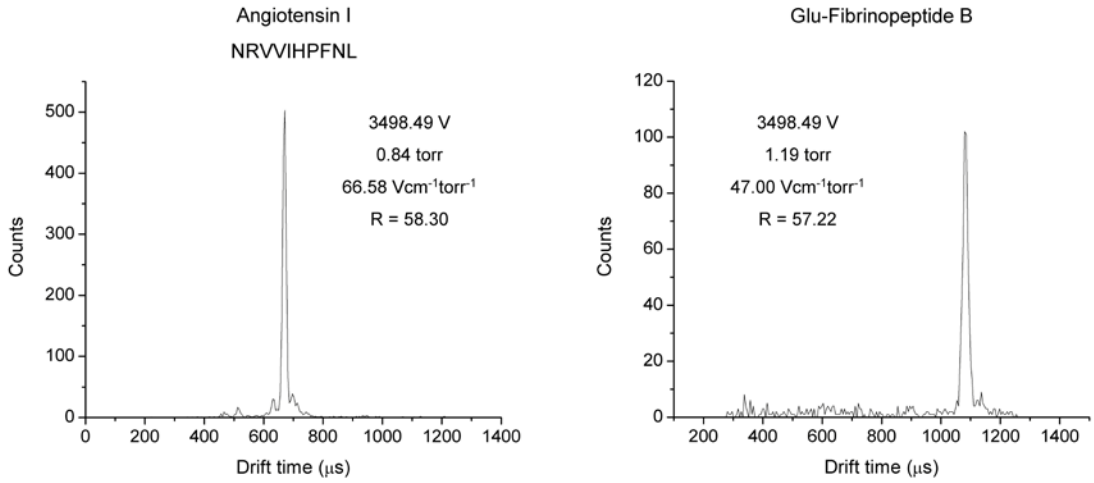

Figure 24. Ion mobility spectra displaying the highest mobility resolution achieved for peptide ions on the 63 cm PDC IG equipped with 8 mm inner diameter electrodes (electrode configuration B). The applied voltage, drift gas pressure, *E/p* (*E/N*) values, and mobility resolution, R, are displayed.

The pressure at which the maximum resolution was attained becomes important when considering low-field versus high-field mobility conditions. It is of utmost importance that in any mobility separation, especially for low mass ions, the contribution from the field energy to the overall ion energy and the resulting effective ion temperature, T_{eff}, be considered. The values of *E/p*, or *E/N*, become very important as applied voltage is increased or temperature is decreased. As *E/p* (*E/N*) is increased, the field energy, or energy gained by the ions due to the accelerating field, can raise the effective temperature of the ion to a point where ion mobility is no longer independent of the electric field [1]. There is intrinsic value in increasing field strength for separations as sensitivity is increased and separation times are reduced [145], but T_{eff} becomes critical especially if ion-neutral collision cross section data is desired [143, 146-147].

However, as ion mass increases larger *E/p* (*E/N*) values can be achieved while maintaining low effective ion temperatures. This can be demonstrated by comparing the deviations of the reduced mobility values with increasing *E/p* (*E/N*) values (Figure 25). The results for reduced ion mobility versus *E/p* (*E/N*) of the analytes studied agree well with previously published data where $C_{60}^{\bullet+}$ enters the high-field mobility limit at approximately 30-40 $Vcm^{-1}torr^{-1}$, evidenced by the deviation of the reduced ion mobility at this value of *E/p* [145]. The peptides show a slight deviation in reduced mobility between 60-70 $Vcm^{-1}torr^{-1}$. Therefore, as ion mass increases the field energy can be increased to higher values without a deviation in mobility.

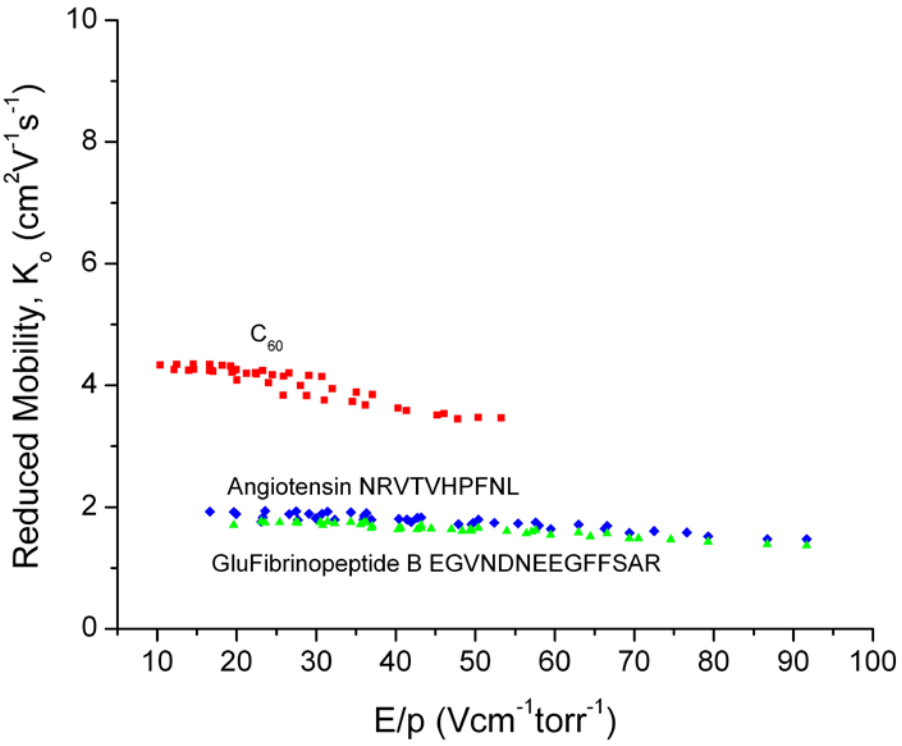

Figure 25. Plot of reduced ion mobility, K_0, versus *E/p* for the analytes investigated.

The ion mass discrepancy was taken into account by Wannier [1] as the calculation of the longitudinal coefficient factors in the mass of the ion, *m*, and the mass of the gas, *M*. Verbeck used a portion of Wannier's equation to calculate resolution for low-field and high-field ion mobility separation conditions [148].

$$R = 0.30\left(\frac{eLE}{k_b T + \mu_\omega E^2 K^2}\right)^{1/2} \tag{3.3-1}$$

In equation 3.3-1 *e* is ionic charge, *L* is drift length, *E* is electric field, k_b is the Boltzmann constant, *T* is drift gas temperature, *K* is ion mobility, and μ_ω is similar to a reduced mass term from Wannier's relation provided below.

$$\mu_\omega = \frac{M}{3}\frac{M + 3.72m}{M + 1908m} \tag{3.3-2}$$

A comparison is made between experimental resolution and the calculation of resolution of the analytes studied using equation 3 from classical theory and Verbeck's approximation using Wannier's equation. The results are presented in Table 3. The approximation provided by Verbeck for low-field and high-field determinations of resolution is only applicable to small ions, atomics, small organics, etc. This is due to the similarity of the mass of the ion and neutral drift gas. As the mass of the ion increases compared to the mass of the neutral drift gas (e.g. three orders of magnitude for the peptides studied) Wannier's relation becomes negligible and the calculated resolution is virtually unchanged from classical theory. Classical mobility theory and resolution calculations were developed for atomic ions, and as such large ions such as peptides and proteins behave much differently than small atomic ions. At high *E/p* values for example, ion mobility values of large ions are relatively unchanged yet the

resolution is much less than stated by classical theory. For this reason, the best approximation for resolution is established through SIMION simulations modeling ion mass, ion charge state, ion-neutral collisions, drift cell dimensions and drift gas pressure. This can be seen from the results in Table 3.

Table 3. A comparison of three theoretical calculations versus experimental mobility resolution for the three analytes tested on the 63 cm PDC IG drift cell equipped with electrode configuration B electrodes. Classical theory results are calculated from equation 17 in the introduction, Verbeck's approximation is taken from equation 19, and the simulated resolution is determined through SIMION simulations. The table shows that for analyte ions much larger than the drift gas ($\geq$ 3 orders of magnitude), Verbeck's approximation has a negligible effect on calculated resolution. For illustrative purposes, $Ar^{+\cdot}$ is shown to demonstrate the validity of Verbeck's approximation for ions of similar mass to that of the drift gas. This value was calculated from the $Ar^{+\cdot}$ in He gas reduced ion mobility value from the literature. [149]

Resolution Comparison

Analyte	m/z	Classical Theoretical R_d	Verbeck approximation	Simulated R	Experimental R
$C_{60}^{+\cdot}$	720.6	110.607	110.588	72.78	60.16
Angiotensin [N1,V4,N9]	1208.69	110.607	110.603	N/A	58.3
GluFibrinopeptide B	1570.68	110.607	110.63	N/A	57.22
$Ar^{+\cdot}$	39.95	110.607	45.36[a]	N/A	N/A

Another important point to note is that equation 3.1-1, the theoretical representation of diffusion limited resolving power, was derived for atomic ions separated with uniform field electrodes. As ion mass increases, experimental resolution never reaches the theoretical diffusion limited resolving power [150]. Factors leading to peak broadening are initial size and shape of the pulsed ion packet from a pulsed ionization source or gated continuous ion source [112, 137, 150-152], expansion of initial ion packet due to coulombic repulsion [150, 153], reactions with neutral

contaminants, and the presence of different ion conformations especially for peptide and protein ions [110, 132, 134, 146].

3.4 Conclusion

An investigation of the effective drift length, applied voltage and electrode geometry of a periodic-focusing DC ion guide ion mobility spectrometer on resolution and ion transmission is presented. Simulations and experiments were performed to determine resolution and ion transmission of different inner diameter electrode geometries. The analytical utility of PDC IG drift cells is apparent as ion transmission is increased with smaller inner diameter electrodes. The 8 mm inner diameter periodic electrodes are 28 times more sensitive than uniform field electrodes over a 63 cm drift length. The increase in ion transmission provided by the PDC IG does not have a large detrimental effect on resolution. This is evident by a mere 10 percent decrease in resolution for the optimum pressure performance region of 1-2 torr when compared to conventional uniform field designs and confirmed by the experimental resolution achieved for the 8 mm inner diameter PDC IG drift cell.

A 63 cm periodic drift cell composed of 8 mm inner diameter electrodes yielded a maximum resolution of 60 for the radical cation of C_{60} and two model peptides. On average, the 8mm i.d. periodic drift cell is capable of a resolution between 40 and 60. Future efforts will focus on the development of a high resolution PDC IG drift cell coupled with a time-of-flight mass analyzer.

4. ION MOBILITY IN A PERIODIC-FOCUSING DC ELECTRIC FIELD

4.1 Introduction

Our recent theoretical studies involving the periodic-focusing DC ion guide (PDC IG) focused on the radial ion focusing mechanism [125, 144], and an evaluation of the effect of the electrode geometry on ion transmission and resolution [154]. In this work, we develop first order ion mobility expressions based on the changing electric fields inside the PDC IG in order to calculate collision cross sections (Ω). In the past few decades, ion mobility spectrometry (IMS) has become an important platform for the elucidation of 3D structures and their changes in polyatomic frameworks including ion clusters [155-158], metal-ligand complexes [159], peptides [160-162] and proteins [133, 163-165]. Conventionally, the measurement is performed by "drift-time-based" IMS (DT IMS) whereby ions traverse a drift tube of length L filled with a neutral buffer gas under the influence of a uniform electric field (E) such that the mobility (K) is [1],

$$K = \frac{L}{t_d E} \tag{4.1-1}$$

where t_d is the drift time of the ion in the drift tube. Structural features may be deducted using the parameters K and the ion-neutral collision cross section Ω expressed in the relationship,

$$K = \left(\frac{3q}{16N}\right)\cdot\left(\frac{2\pi}{\mu K_B T_{eff}}\right)^{\frac{1}{2}}\cdot\left(\frac{1}{\Omega}\right) \tag{4.1-2}$$

where,

$$\mu = \frac{mM}{m+M} \tag{4.1-3}$$

The terms N, m, M, T_{eff} , and μ represent particle number density of the buffer gas, the mass of the ion, the mass of the buffer gas, the effective ion temperature, and the reduced mass, respectively. While K (or the reduced ion mobility coefficient, K_0 obtained by standardizing K to standard temperature and pressure [126]) offers information on relative variations between different structures, Ω provides additional detail on the average size and shape of the ions. Moreover, the accuracy of K measured by IMS for the subsequent calculation of Ω depends critically on the experimental and instrumental parameters employed. In addition, while t_d measured at the peak centroid (assuming a single conformation) is sufficient for obtaining K and σ, the resolution of the technique (R) becomes increasingly important when multiple analytes and/or structural conformations with similar mobilities are present. In DT IMS, the diffusion-limited resolution (R) is given by,

$$R = \frac{t_d}{\Delta t_d} = \frac{1}{4}\left(\frac{qLE}{K_B T \ln 2}\right)^{\frac{1}{2}} \tag{4.1-4}$$

where T is the temperature of the bath gas and Δt_d is the full width of the peak at half maximum height. In this work, we focus only on the impact of the instrumental parameters for the calculation of Ω with a brief discussion on R.

Our laboratory developed the electrostatic periodic-focusing DC ion guide (PDC IG) to improve ion transmission in dispersive IMS by modifying the DT IMS electrode geometry to achieve radial ion focusing during the IMS separation. Operation of the

PDC IG [141, 166], details on the radial focusing mechanism [125, 144], and geometric factors that affect ion transmission and resolution have been reported [154]. Briefly, the radial focusing in the PDC IG is attributed to both effective RF and effective potentials created by the changes in the radial electric field at the edges of the thick electrodes. While the effective RF tend to demonstrate a defocusing followed by a focusing effect inside one electrode unit, the net drift of an ion trajectory towards the central $r = 0$ position within the unit is attributed to the presence of effective potentials. The middle region of the electrode acts similar to a "collisional cooling cell" due to periodic maxima in collisional cooling initiated by the axial electric field ($E_z(z)$) oscillations. This collisional cooling assists the effective RF and effective potentials at the tailing edge of the electrode in periodically focusing ions toward the central drift axis. Compared to conventional DT IM-MS, the PDC IG-MS design allows for up to a substantial (up to 40-fold) increase in ion transmission accompanied by a modest (~10%) decrease in the IMS resolving power, depending on the experimental conditions and the drift tube design [154].

Although previous experimental data and ion optical simulations suggest that the mobility separation in the PDC IG is similar to DT IMS [154], an analytical description of the effect of field variations on Ω and R have not yet been provided. In the present work, we provide an analytical explanation for the agreement between the two IMS methods in terms of the aforementioned parameters. Theoretical results are compared with experimental data obtained from two PDC IG designs featuring different electrode geometries.

4.2 Experimental

4.2.1 Chemicals

A fullerene mixture, C_{60} and C_{70}, was purchased from Sigma-Aldrich (St. Louis, MO). The peptides were purchased from American Peptide Company, Inc. (Sunnyvale, CA) and used without further purification. A suspension of fullerene in benzene was deposited on the stainless steel MALDI probe target and allowed to dry prior to analysis. The peptides were dissolved in distilled water at a concentration of 1 mg ml^{-1} and mixed 1:1 (v:v) with 5 mg ml^{-1} alpha-cyano-4-hydroxycinnamic acid in 60% acetonitrile, 38% distilled water, 1% (10%) trifluoroacetic acid solution, 1% 1M ammonium phosphate. The mixture of peptide and matrix was then spotted on the MALDI target.

4.2.2 Instrumentation

Instrumentation used in this study has been described previously [154]. Briefly, Two PDC IG designs were constructed with different electrode geometries. The ratio between electrode spacing (*s*), electrode thickness (*t*) and the inner diameter of the electrode (*d*) was varied. Both PDC IG designs had $s = t = 6$ mm but different *d* values, specifically, 6 mm and 8 mm. The length, *L*, for both PDC IGs was 63 cm. The voltage drop, *V*, across both PDC IGs was about 3500 V. A third, higher resolution PDC IG design which retained the electrode geometry of $s = t = 6$ mm, $d = 8$ mm, but with $L =$ 125 cm and with a *V* about 4500 V was also employed in obtaining mobility data. Samples are spotted on a stainless steel insertion probe and inserted in to the drift cell between the first and second electrode. A nitrogen laser, $\lambda = 337$ nm (Stanford Research Systems; Sunnyvale, CA), was used to create ions with laser desorption ionization (for

fullerenes) and MALDI (for peptides). In this work, the buffer gas used is always He. The drift tube pressure was maintained between 1-3 torr. A linear voltage drop was established with a series of 1 MΩ resistors connecting adjacent electrodes. A 500 μm aperture was placed at the exit of the mobility cell to aid in differential pumping for ion detection with a Galileo Channeltron electron multiplier (CEM) detector (Burle Electro-Optics, Inc.; Lancaster, PA).

4.2.3 SIMION Simulations

The reported electric field profiles were calculated using SIMION 8.0 ion optics simulation program. Ion-neutral collisional dynamics were simulated for the two periodic-focusing electrostatic lens geometries using $C_{60}^{\bullet+}$ ions (*m/*z 720 Daltons, Ω = 124 $Å^2$) and helium buffer gas with a user program provided with SIMION 8.0 to include ion-neutral hard sphere elastic collisions at 300 K.

4.3 Results and Discussion

Figure 26 depicts two electrodes in a PDC IG along with the geometric variables and the cylindrical coordinate system referred to in this discussion. The periodic-focusing electric field contains harmonic axial (*z*) spatial oscillations of the axial electric field (E_z) along the drift tube at fixed radial (*r*) position, denoted as E_z(z), as well as radial variations in this axial profile, E_z(r). Both these variations ((E_z(z), E_z(r)), are dependent on the ratio of the geometric features in the PDC IG design, specifically, the electrode spacing (*s*), electrode thickness (*t*) and the inner diameter of the electrode (*d*).

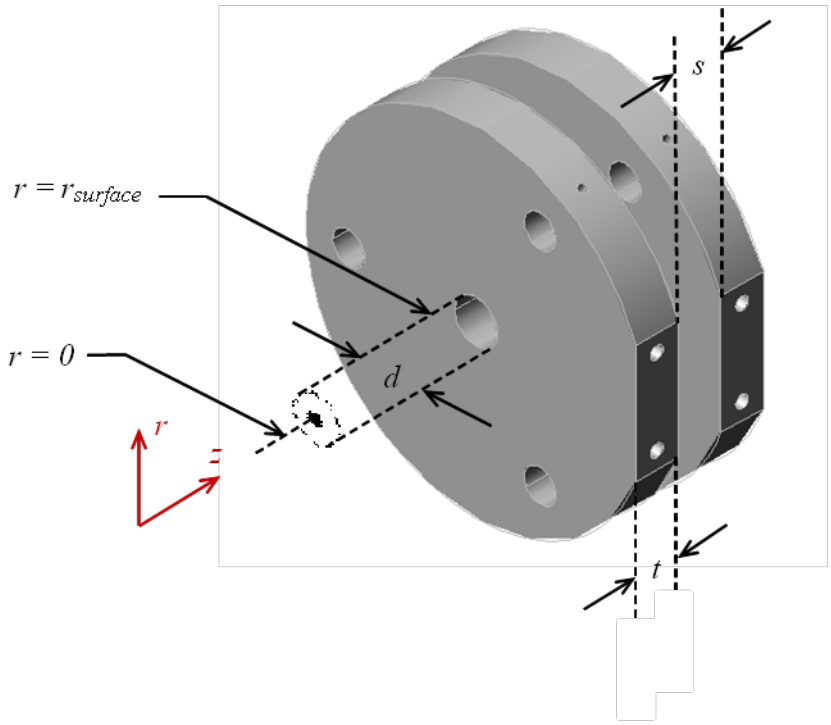

Figure 26. Two adjacent PDC IG electrodes. The radial (r) and axial (z) dimensions and the variables that define the aspect ratio (electrode inner diameter : thickness : spacing = $d : t : s$) are illustrated. The location of $r = r_{surface}$, where the boundary conditions for the electric field exist is also indicated. This figure can be found in reference [167].

Previous studies showed that an aspect ratio of 1:1:1 for s:t:d is optimal in terms of ion transmission [154]. Experimental data were obtained for two different PDC IG geometries with s and t values fixed at 6 mm but with different d values of 6 mm (aspect ratio 1:1:1) and 8 mm (aspect ratio of about 3:3:4). For simplicity, the two PDC IG designs will be referred to as PDC $IG_{1:1:1}$ and PDC $IG_{3:3:4}$ (referred to as electrode configuration A and B in Section 3), respectively. Figure 27(a) illustrates the axial electric field profile ($E_z(z)$) at $r = 0$ for the PDC $IG_{1:1:1}$ and the PDC $IG_{3:3:4}$. For both designs, at $r = 0$, $E_z(z)$ approximates a sine function where the electric field oscillates

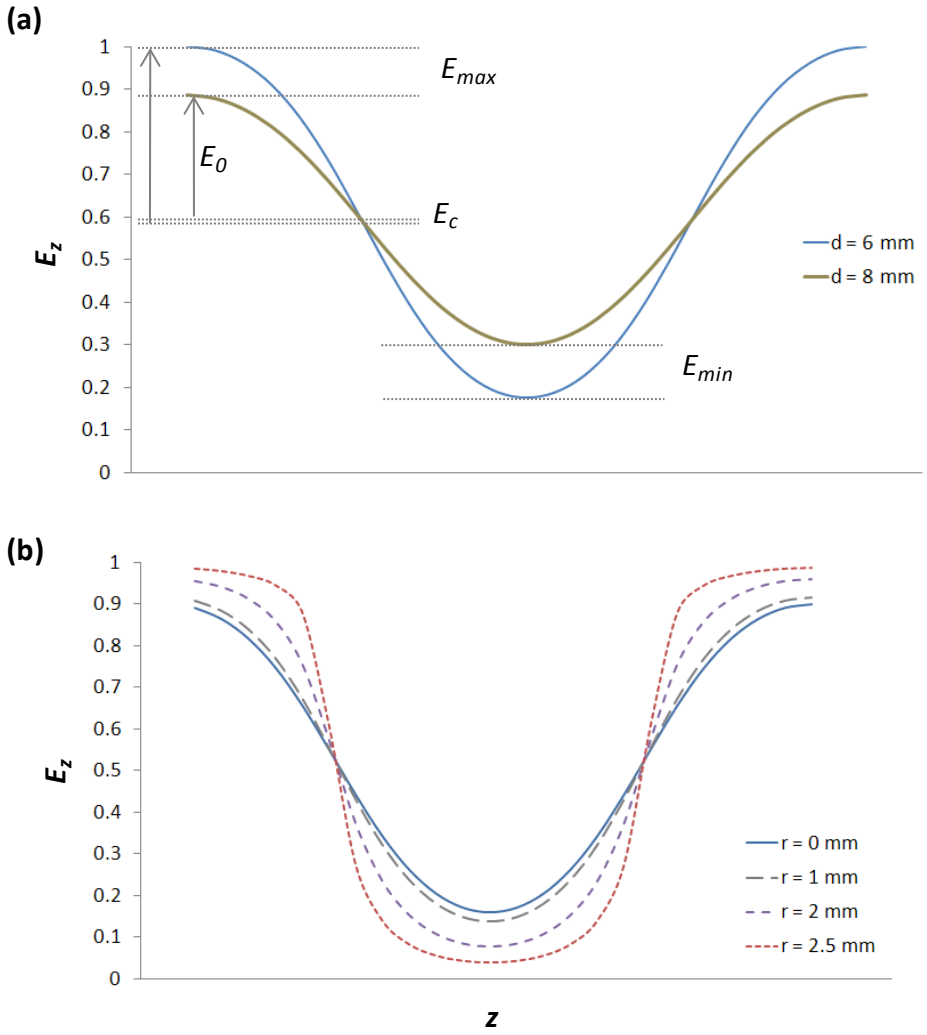

Figure 27. Axial electric field at r = 0 position for the 1:1:1 and 3:3:4 electrode configurations (a) and axial electric field at varied r position for the 1:1:1 electrode configuration (b). In both plots, the electric field is normalized to the maximum value shown. This figure can be found in reference [167].

about a central electric field, E_c. The amplitude of this sinusoidal function is denoted as E_0. Notice that E_0 for the PDC $IG_{3:3:4}$ is smaller compared to that of PDC $IG_{1:1:1}$, indicating less electric field variations when d is increased. The maximum electric field for $E_z(z)$ at $r = 0$ (E_{max}) is located in the middle of the gap between two electrodes and is equal to $E_c + E_0$. In the figure, the electric field values are normalized to the E_{max} of the PDC $IG_{3:3:4}$. The minimum electric field for the same waveform (E_{min}) is located in the middle of the electrode thickness (t) and is equal to $E_c - E_0$. Thus, the value of E_c can be obtained from,

$$E_c = \frac{E_{\max} + E_{\min}}{2} \tag{4.3-1}$$

However, when moving away from $r = 0$ position toward $r_{surface}$ (see Figure 26), as depicted in Figure 27(b) for the PDC $IG_{1:1:1}$, the shape of the axial electric field profile deviates slightly from a sinusoidal form while retaining the same spatial periodicity (wavelength) and phase. At $r_{surface}$, $E_z(z)$ may be approximated by a square wave, although some variations are observed near the edge of the electrode surface. The electric field in the gap between two electrodes is maximum in this case. In other words, at $r_{surface}$, E_{max} has moved to a value that yields the highest E_{max} that approximates the uniform electric field that exists between the walls of two adjacent electrodes at $r > r_{surface}$ (beyond the central orifice). For the approximated $E_z(z)$ square waveform at $r_{surface}$, E_{min}, the electric field on the inner electrode surface is always zero. Thus, the E_{max} and E_{min} values at $r_{surface}$ correspond to boundary conditions.

Figure 27(b) demonstrates that, as the r value is increased from $r = 0$, the movement of E_{min} towards zero boundary condition is rapid compared to the movement of E_{max} towards its boundary condition. Mathematically, this can be stated as,

$$\left|\frac{d(E_{\max})}{dr}\right| < \left|\frac{d(E_{\min})}{dr}\right| \tag{4.3-2}$$

which is a consequence of the fact that while the boundary condition for E_{max}, with a non-zero magnitude, is determined only by the voltage applied across the device and the distance s, the boundary condition for E_{min} is always fixed at zero. As a result of equation 4.3-2, E_c, decreases gradually from its value at $r = 0$ towards the value at $r = r_{surface}$. This is shown in the figure on page 96 for PDC $IG_{1:1:1}$ and PDC $IG_{3:3:4}$ electrode configurations. The drifting of E_c toward lower values with increasing r is an important consideration in diffusion-limited mobility calculations as will be discussed later.

In any ion mobility separation, as far as the required low- or intermediate-field conditions [1] are maintained, the changes in the electric field does not change the ion mobility coefficient, K, since the drift time in equation 4.1-1 decreases in proportion to E. Therefore, considering an ion traveling in the axial direction at a constant r position, even with the variations in the axial electric field profile, ion mobility equations 4.1-1 and 4.1-2 are valid if the changing electric field conditions are represented by one net electric field. In other words, for a fixed r position, the axial mobility separation can be described if the term E in equations 4.1-1 and 4.1-2 are replaced by an electric field ($\overline{E}$) obtained by integrating over the periodic axial electric field profile. First, let us use this

approach for ions traveling in the $r = 0$ position. The following derivation provides the net electric field for the sinusoidal axial electric field profile at $r = 0$.

Let us define the periodicity (wavelength) of the axial electric field to be $2\pi z_0$. This value is identical to the sum of the spacing between electrodes (s) and the electrode thickness (t).

$$s + t = 2\pi z_0 \tag{4.3-3}$$

The spatial variation of the axial electric field can be shown to be:

$$E_z(z) = E_0 \cos \omega_z z + E_c \tag{4.3-4}$$

where,

$$\omega_z = \frac{2\pi}{2\pi z_0} = \frac{1}{z_0} \tag{4.3-5}$$

We may define

$$\hat{z} = \frac{z}{z_0} \tag{4.3-6}$$

to yield

$$E_z(z) = E_0 \cos \hat{z} + E_c \tag{4.3-7}$$

Because of the periodicity of the $E_z(z)$ waveform, the net electric field resulting from the waveform at $r = 0$ can be obtained by integrating over one cycle of the waveform

$$\overline{E} = \int_0^{2\pi} (E_0 \cos \hat{z} + E_c) d\hat{z} \tag{4.3-8}$$

$$\overline{E} = E_c \tag{4.3-9}$$

In other words, for the ions travelling along the *z* axis at constant *r*-position of the PDC IG, the net electric field that contributes to the overall mobility separation is identical to a uniform electric field with the magnitude E_c. Therefore, in this case, the mobility coefficient *K* and the resolution *R* for PDC IG are explained by equations 4.1-1 and 4.1-4 and are identical to DT IMS with *E* in the expressions represented by E_c and are given by:

$$K = \frac{L}{t_D E_c} \tag{4.3-10}$$

$$R = \frac{t_D}{\Delta t_D} = \frac{1}{4}\left(\frac{LqE_c}{K_B T \ln 2}\right)^{\frac{1}{2}} \tag{4.3-11}.$$

At this point, it may be emphasized that, according to ion optics simulation results, (1) the ion migration to the radial regions with significant changes to the $E_z(z)$ sine waveform shape is minimal and (2) the intermediate $E_z(z)$ waveforms can also be approximated by smooth waveforms yielding a net electric field, $\overline{E} = E_c(r)$, (Figure 27(b)). Therefore, in a PDC IG, equations 4.3-10 and 4.3-11 accurately provide the mobility coefficient and the diffusion-limited resolution for ions that travel along the *z* dimension at a constant *r* position — for example for an ion travelling along the *z* axis at $r = 0$.

However, during the periodic-focusing mechanism, ions traverse at different radial positions and are being periodically refocused toward the $r = 0$ position. The simulations (not shown) indicate that after the first few periodic-focusing electrodes, the overall ion migration to *r* positions exceeding half the value of the radius ($r = d/4$) is

extremely rare. At these r values, the deviation of E_c from E_c(r = 0) is minimal, as demonstrated in Figure 3 (< 2 %). Therefore, it may be argued that equations 4.3-10 and 4.3-11 using $E_c = E_c(r = 0)$ can still provide an estimate of the overall theoretical K and R (diffusion-limited) values in the PDC IGs employed in this study. Note that, in essence, this translates into having K and R parameters in PDC IG described by expressions identical to those in DT IMS at a uniform electric field of $E_c(r = 0)$. This uniform electric field is calculated as the offset of the central $E_z(z)$ profile. However, E_c ($r = 0$) is slightly less than the applied field E for both electrode geometries, due to the fringing electric fields. It was also observed that with increasing d, $E_c(r = 0)$ value increases. The simulations show that this is also accompanied with a decrease of the amplitude of the E_c waveform (see Figure 27(a)), resulting in a more uniform-field-like behavior near the central z axis. Thus, with increasing d, an increase in E_c accompanied by decreased electric field variations increase the measurement resolution as observed in the experimental data discussed below. Finally, when further increasing d, the electric field near the z axis approaches a uniform electric field with the magnitude of the applied electric field, E, as in DT IMS. In other words, the amplitude term E_0 of the $E_c(r = 0)$ waveform approaches zero while E_c approaches E at large d values. The preceding discussion also implies that since the difference between E_c and E is small, ($E \approx E_c(r = 0)$) estimations of ion mobility coefficient and the resolution in PDC IG may be performed using the equations 4.1-1 and 4.1-4.

The K and R values obtained by the above expressions are rather closer to the best case scenario values assuming that the change in the net electric field caused by the

ion migration to different radial positions is minimal. To present a more accurate description, a modification can be introduced to the above equations using parameters that may only be calculated using other empirical approaches. This approach assumes that the net effect of the electric field variations the ions experience can be approximated by introducing a damping factor to the applied electric field *E*. The maximum net electric field the ions can experience is $E_c(r=0)$ and as shown in Figure 28, $E_c(r=0)$ decreases from $r = 0$ toward $r_{surface}$. Therefore, the net effect of the variable *r* position can be described as if an ion experiences a net field which is damped with respect to $E \approx E_c(r=0)$. Since some ions can still traverse at a constant $r = 0$ position along the drift tube experiencing a constant net electric field of $E \approx E_c(r=0)$ while other ions migrate to positions of $r \neq 0$, an ion mobility peak can be considered to have a contribution to its spread from different electric field conditions the ions experience, with a central average value. In other words, the average electric field experienced by a major fraction of the ion population may be described by multiplying the applied electric field, *E*, by an electric field damping coefficient, α.

$$K = \frac{L}{t_d \alpha E} \tag{4.3-12}$$

Equation 4.3-12 becomes 4.1-1 when α is considered to be one, assuming a minimal electric field damping.

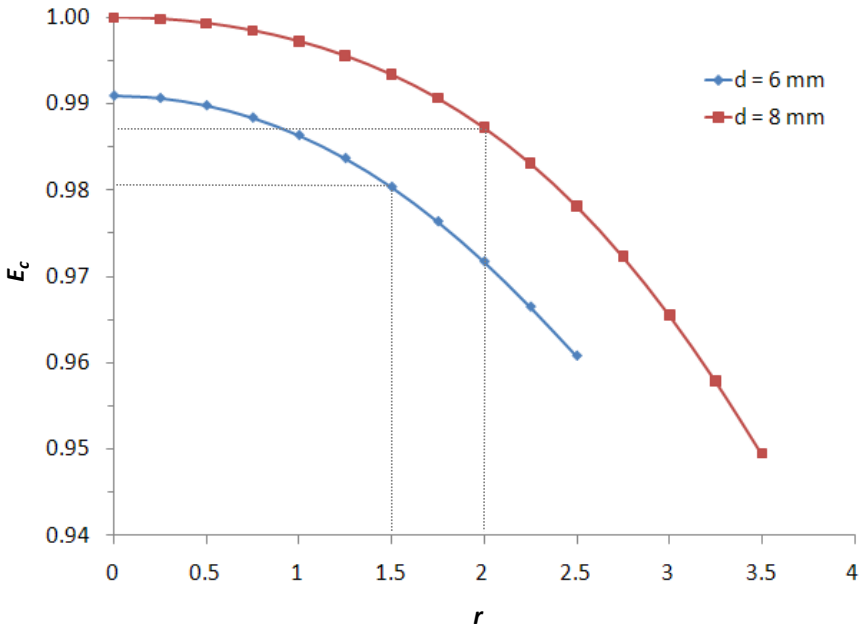

Figure 28. Percent of central electric field, E_c, normalized to E_c at r = 0 for PDC $IG_{3:3:4}$ as a function of radial position shown for both PDC $IG_{1:1:1}$ (s = t = d = 6 mm) (blue, squares) and PDC $IG_{3:3:4}$ (s = t = 6 mm, d = 8 mm) (red, diamonds). The vertical dashed lines indicate the r at half-radius (r = d/4) for both electrode configurations. Both half-radii values correspond to a similar decrease of < 2 % in E_c from E_c (r = 0) as indicated by the horizontal dashed lines. This figure can be found in reference [167].

The same α factor for mobility measurement may not be applicable for the resolution measurement. In the resolution measurement such a factor may be considered to be proportional to the spread of ion drift times caused by the different overall electric fields the ions are subjected to, with respect to the maximum $E \approx E_c(r = 0)$ experienced by the ions travelling at r = 0. The contributions for the decrease in resolution with respect to the theoretical best case scenario (all ions travel at r = 0) may also be thought of as a result of "damping" of the applied field E, however with a "damping factor" different from that of equation 4.3-3. When d is increased, the range of the different

overall electric fields become smaller, causing the overall effect to be closer to that at r = 0, and the resolution increases.

For accurate calculations of the collision cross sections, finding a value for α is more complicated since α depends on the drift tube design and the experimental conditions. However, since the ion mobility follows linear relationships with E and drift times similar to DT IMS according to equations 4.1-1 and 4.3-12, and since α may be considered to be a constant for a particular PDC IG design and a set of experimental conditions, calculations of collision cross sections can be performed with an accuracy similar to DT IMS using a simple calibration (*vide infra*). In the case of resolution, an upper limit for theoretical resolution of PDC IG can be obtained using equation 4.3-11.

It is important to note that in the preceding discussion, only the variations in the axial electric field in the axial direction (E_z(z)) and radial direction (E_z(r)) are considered since only E_z is important in the mobility separation along the drift tube. Conversely, the effective RF and effective potential concepts discussed in our previous work in terms of radial ion confinement mechanisms are mainly derived from the variations of the radial electric field (E_r) [144].

Ion mobility spectra obtained for the two different PDC IG geometries are shown in Figure 29. Experimental conditions and the measured quantities such as the drift times and the resolutions for the data are stated in the figure and the experimental section. The resolutions obtained for the PDC $IG_{3:3:4}$ is always higher than the PDC $IG_{1:1:1}$ under a constant set of other experimental conditions, in good agreement with the

Fullerenes

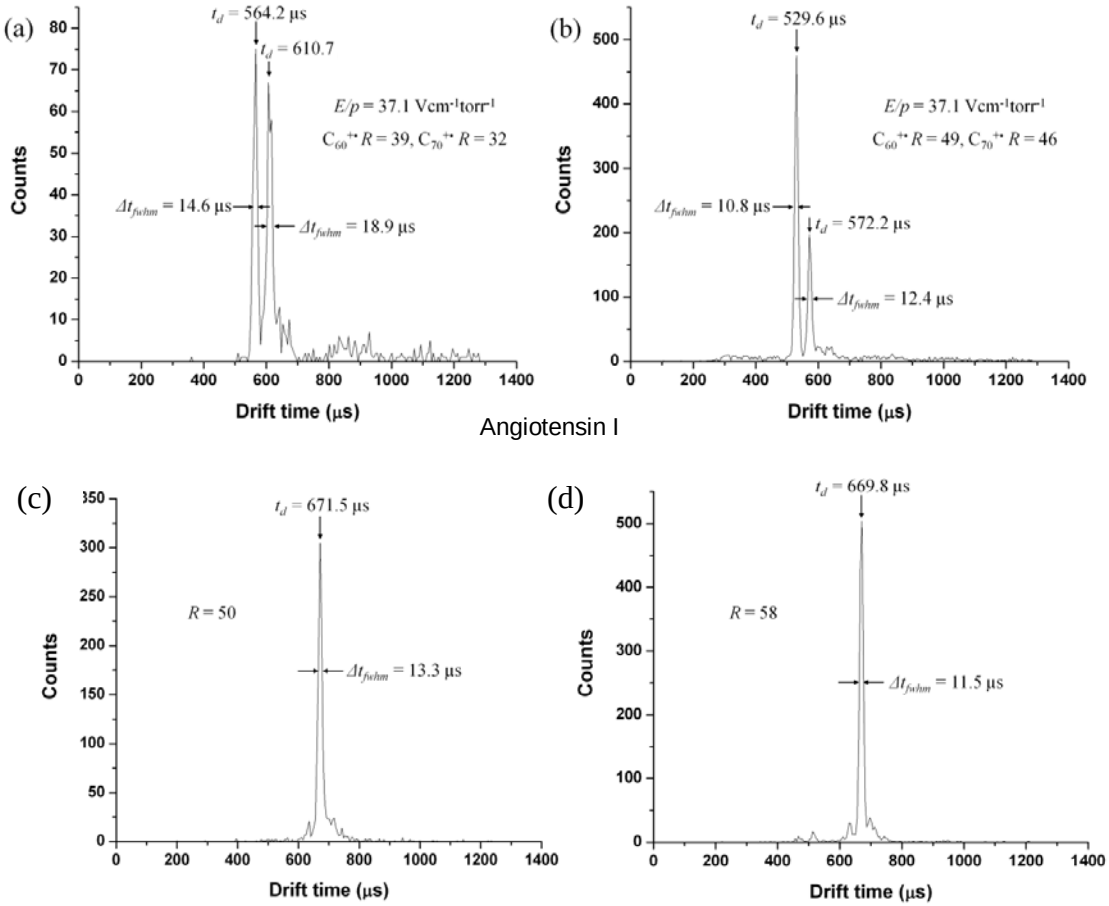

Figure 29. Drift time spectra for fullerenes ((a) and (b)) and protonated Val-4-Angiotensin I ((c) and (d)) on 63 cm PDC IG drift cells with two electrode configurations. The spectra at left, ((a) and (c)), are for PDC $IG_{1:1:1}$ (s = t = d = 6 mm) while the spectra at right, ((b) and (d)), are for PDC $IG_{3:3:4}$ (s = t = 6 mm, d = 8 mm). $C_{60}^{\bullet+}$ and $C_{70}^{\bullet+}$ spectra were obtained at 1.5 torr while the peptide spectra were obtained at 0.84 torr. This figure can be found in reference [167].

theoretical explanations provided above where a higher resolution is expected when *d* is increased.

Highest resolution obtained in these experiments is ~50 for the PDC $IG_{1:1:1}$ and ~60 for PDC $IG_{3:3:4}$. Calculations revealed that the upper limit of the resolution predicted by equation 4.3-11 is ~ 100 for both designs, with a maximum voltage drop of 3500 V across the drift tubes of length 63 cm (E = 56 V cm^{-1}) as employed to obtain data in Figures 4 and 5. Although the experimental resolutions reported here may be considered to be on the "high side" with respect to the resolutions routinely achieved in ion mobility methods, they are lower than the theoretical upper limit predicted by equation 4.3-11. This is because of other factors that affect the resolution including the initial kinetic energy and spatial spreads of the ions, drift gas pressure (or the E/N ratio), effect of different electric fields due to ion migration to different r positions.

In order to calculate collision cross sections, a calibration procedure can be employed since as already detailed, the overall mobility separation is similar to that of DT IMS, with a net electric field dampened with respect to the applied field. The collision cross section, Ω, may be approximated by the relationship in equation 4.1-2.

Thus for the same temperature, electric field and the PDC IG electrode design, the obtained drift time, t_d, may be approximated as directly proportional to the following terms, according to expressions 4.1-2 and 4.3-12 to yield:

$$t_d \propto N\Omega\sqrt{\mu} \tag{4.3-13}$$

Therefore, using the measured drift time t_{d1} for a compound of known collision cross section Ω_1 at a pressure p_1 and temperature T, an unknown collision cross section

Ω_2 of a compound of which the drift time is t_{d2} at a pressure p_2 and the same temperature can be readily obtained by:

$$\Omega_2 = \Omega_1 \frac{p_1}{p_2} \frac{t_{d2}}{t_{d1}} \frac{\sqrt{\mu_1}}{\sqrt{\mu_2}} \qquad (4.3\text{-}14)$$

In deriving 4.3-14, T_{eff} in 4.3-2 was assumed to be approximately the same for the two ions neglecting the effects from differing masses. However, a significant difference between DT IMS and PDC IG is the periodic changes in the effective ion temperature, initiated by the periodic variations in E_z(z), although the average T_{eff} remains similar to the values obtained for DT IMS, and thus can represent T_{eff} in 4.3-2. Potential impacts on the ion 3D structure due to the periodic annealing and cooling introduced by the variation of T_{eff} is also assumed to be negligible.

Following the above principles, collision cross sections were calculated for $C_{70}^{\bullet+}$ and several different protonated peptide ions using the known collision cross section of Ω_1 = 124 Å^2 for $C_{60}^{\bullet+}$. These data are presented in Figure 30. A maximum standard deviation of ± 5 Å^2 was associated with the measurements. Our previous measurements with another ion mobility spectrometer (Ionwerks, Inc.; Houston, TX) provided a collision cross section of 138 Å^2 for $C_{70}^{\bullet+}$, which is in agreement with the value calculated here (134 Å^2). Figure 30 also illustrates the different trend lines for fullerenes and peptides.

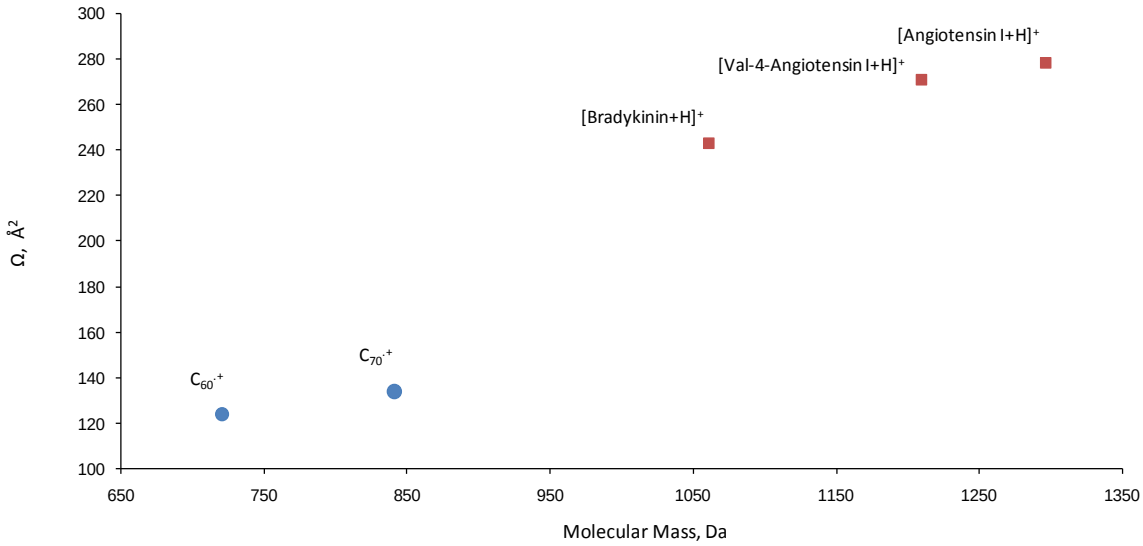

Figure 30. Calculated collision cross section data versus molecular mass. A maximum standard deviation of ± 5 Å^2 was associated with the measurements. The calculated value for $C_{70}^{\cdot+}$ is 134 Å^2. The calculated values for the protonated peptides are: bradykinin = 243 Å^2, Val-4-Angiotensin I = 263 Å^2 and Angiotensin I = 278 Å^2. This figure can be found in reference [167].

Traditionally, Ω has been accurately determined using DT IMS [78, 168-169] owing mostly to the fact that the electric field employed was constant and uniform. The obtained collision cross section value for bradykinin (243 ± 5 Å^2) is in excellent agreement with previously reported DT IMS-based collision cross section value (242 ± 5 Å^2) [169]. However, conventional DT IMS has several major drawbacks as it suffers from low instrument duty cycle (~1%) and poor ion transmission owing to the lack of an inherent ability to radially focus ions. The poor ion transmission is especially critical in the systems where IMS is coupled to mass spectrometry (MS). IM-MS systems yield mass-to-charge (*m*/*z*) characterization of the eluting mobility profile essential for confirming the identity (mass and charge) of structural conformers, isomers and isobaric

aions. To increase ion introduction and collection efficiency prior to MS, several research groups have coupled RF ion funnels to drift tubes [108, 121]. While RF ion funnels have successfully enhanced the sensitivity of IM-MS instrumentation, operation and theory is a field unto itself. In comparison, the PDC IG has the inherent capability of increasing the ion transmission using only low-power, DC voltages while yielding ion mobility data that can be processed using first principles.

Recently, the interest in Ω determination for macromolecules has been enhanced by the maturity of the commercially available traveling wave (TW) IMS-MS dispersive system (Synapt G2, Waters, Inc.). TW IMS offers high ion transmission *via* utilization of a series of pulsed ring electrodes with symmetric potential waves which propagate through the drift tube in the axial direction creating an electrodynamic field that behaves as an alternating RF with a pseudopotential for suppression of radial diffusion and coulombic expansion [170]. However, determination of Ω by TW IMS requires indirect calibration methods [20, 171-173] as the factors governing ion drift time depend heavily on the properties of the electrodynamic wave (*viz.* waveform, amplitude, and speed) which leads to mathematical derivations that deviates from first-order expressions. Other IMS instrument platforms such as differential mobility analysis (DMA) [174] and field asymmetric waveform IMS (FAIMS) [36, 175] produce continuous ion beams for select analyte targets such that measurement of K for the subsequent calculation of Ω involves complex methodology compared to DT IMS.

4.4 Conclusion

Ion mobility separation in PDC IG is shown to be the same as in DT IMS with a net uniform electric field slightly damped with respect to the applied field. While both TW IMS and the PDC IG produce high ion transmission, TW IMS does so at the expense of added operational complexity. The PDC IG has a single electrical variable, i.e., the net voltage drop across the drift tube whereas the TW IMS must be properly tuned with variables such as wave speed, wave height and wave-height ramping. PDC IG does show a modest decrease in resolution, due to electric field variations in the radial direction; however, the decrease in resolution can be overcome by simply increasing the drift length as predicted by equation 4.1-2. Note that ion transmission through the device is primarily governed by the size of the drift cell exit aperture. Also, ion dynamics in TW IMS deviate from first-order derivations for DT IMS whereas in PDC IG, calculations of collision cross sections can be performed using calibrants and the same principles as for DT IMS.

5. INCREASING THE DRIFT LENGTH OF A PERIODIC-FOCUSING DC ION GUIDE DRIFT CELL – EFFECTS ON MOBILITY RESOLUTION AND ION TRANSMISSION IN ION MOBILITY SPECTROMETRY*

5.1 Introduction

Ion mobility spectrometry (IMS) has significantly expanded our capabilities for mass spectrometry based studies for both small molecules [176-177] and macromolecules [178-179]. The orthogonal, two-dimensional separation of IM-MS offers increased peak capacity [135-136] as well as the ability to distinguish different chemical families [75, 77]. Mass spectrometry provides accurate measurement of mass-to-charge (*m/z*) ratios, whereas IMS separates gas-phase ions on the basis of ion-neutral collision cross section [1, 126]. The experimentally determined collision cross section can then be compared to collision cross sections determined by molecular dynamics (MD) simulations [180], and this information can be complementary to data obtained from tandem mass spectrometry and/or H/D exchange experiments for ion structure elucidation [75, 131].

Resolution is the most significant limitation of IMS for interrogation of complex biological mixtures whether for post-ionization separation, analytical applications, and/or structural characterization of ions which have similar ion-neutral collision cross sections [75, 181]. Diffusion limited resolution is defined by equation 5.1-1 [137, 182]

*Reprinted with permission from "Increased ion transmission in IMS: A high resolution, periodic-focusing DC ion guide ion mobility spectrometer" by R.C. Blase, J.A. Silveira, K.J. Gillig, C.M. Gamage, D.H. Russell, 2010. *International Journal of Mass Spectrometry*, doi:10.1016/j.ijms.2010.08.016, [2010] by Elsevier.

$$R_d = \left(\frac{ELez}{16 k_b T \ln 2} \right)^{1/2} \tag{5.1-1}$$

where E is the electric field, L is drift length, z and e are numbers of charges and elementary charge, k_b is the Boltzmann constant, and T is drift gas temperature. Several approaches designed for increasing resolution have been described, and each of these approaches are aimed at one of the fundamental resolution-determining elements given by equation 1, *viz.* drift cell length (L) [117, 132-134, 183-185], electric field strength (E) [127-129, 138, 140], and temperature of the drift gas (T) [139, 186-187]. The investigation of applied voltage, or electric field strength, on resolution has been limited owing to the use of drift cell lengths less than 30 cm. Increasing the drift cell length permits higher voltages to be applied prior to reaching electrical breakdown through the drift gas providing a better platform for investigating the effects of applied voltage, or electric field strength, on resolution.

The design of IMS drift cells is complicated because the cell geometries that lead to increased resolution also decrease ion transmission *viz.* increasing drift length and drift gas pressure results in increased ion losses due to diffusion. Furthermore, an increase in the electric field strength increases the effective temperature of the ions that could result in structural rearrangement and/or fragmentation of the ions [143]. We introduced the use of a PDC IG drift cell to provide increased ion transmission by means of correcting for the radial diffusion of ions [141, 166]. In addition, the periodic-focusing design offers mobility separations at lower pressures (1-3 torr) where uniform

field IMS suffers from low ion transmission owing to the lack of a radial-focusing mechanism. Operation of the drift cell at reduced pressure leads to faster mobility separation and allows for higher frequency ion introduction thereby increasing instrument duty cycle and sample throughput [188-190].

Here, we evaluate the performance of increased-length PDC IG drift cells in terms of ion transmission and resolution. Specifically, we present two different drift cell lengths to examine ion mobility resolution as a function of voltage. Also, two different periodic-focusing drift cell electrode geometries are simulated with SIMION and tested experimentally to compare focal properties of the electrodes and their effect on ion transmission and resolution. Finally, the electrode focal properties are examined as a function of drift gas pressure to determine an optimum pressure range for maximized ion transmission and resolution.

5.2 Experimental

5.2.1 Instrumentation

The instrument consists of a 125 centimeter periodic-focusing DC ion guide drift cell with drift electrodes of thickness, spacing, and inner diameter dimensions of 6.35 mm, 6.35 mm, and 8 mm (Figure 31(a)). The drift cell is comprised of 100 electrodes connected via high precision, 1 MΩ resistors (Mouser Electronics; Mansfield, TX) to provide the accelerating, non-uniform electric field. The voltage applied to the drift cell is supplied by a Spellman 15 kV high voltage power supply (Spellman High Voltage Electronics Corporation; Hauppauge, NY). Fullerene ions are created by laser-desorption ionization (LDI) using a nitrogen laser (λ=337 nm, 200 μJ, Stanford Research

a)

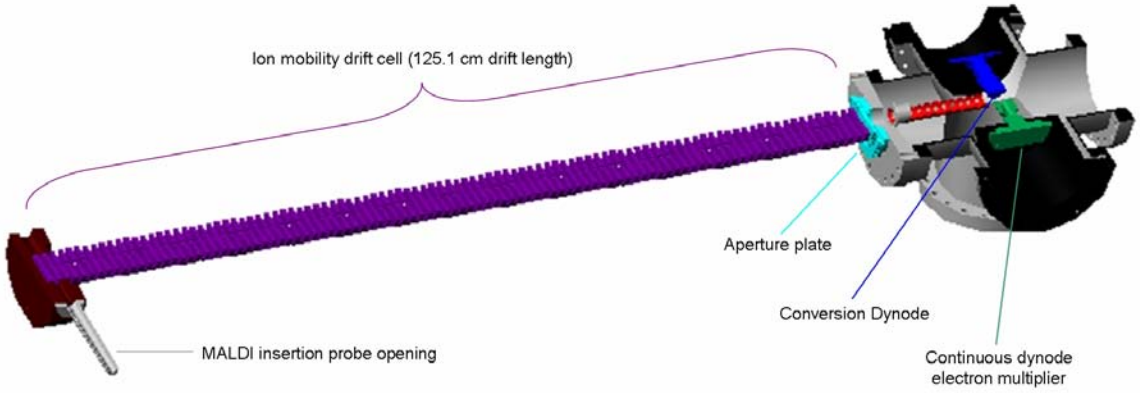

b)

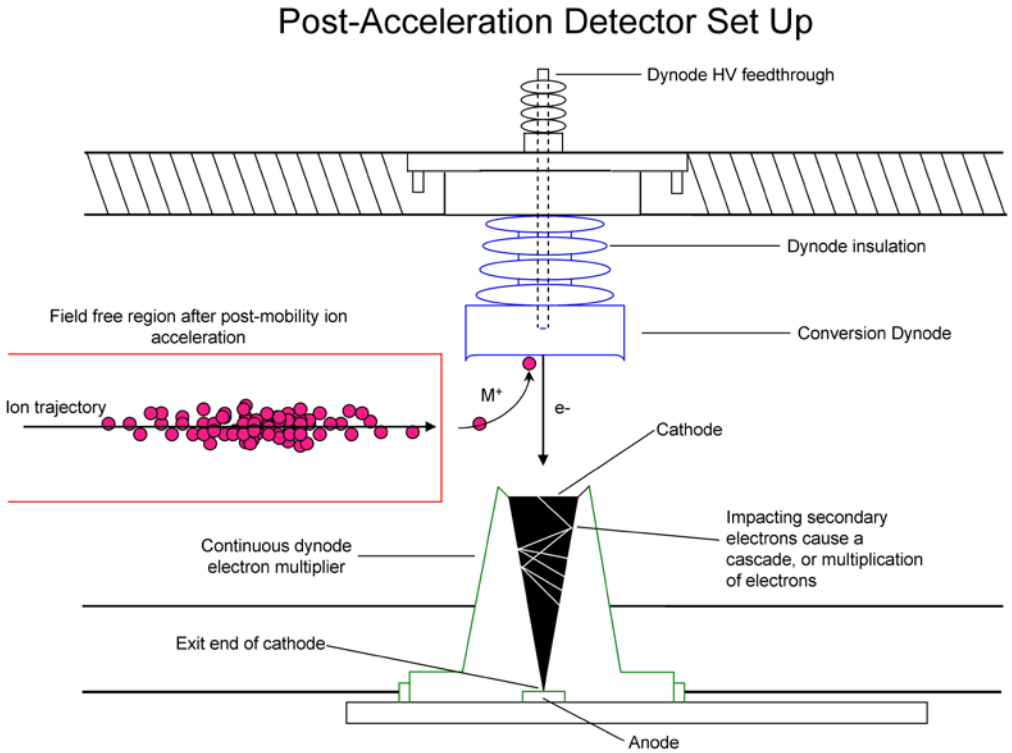

Figure 31. An AutoCAD drawing showing a cross sectional view of the 125 cm PDC IG drift cell (a). The source region is the same as the previous design described in Section 2. A post-acceleration detector was added to increase sensitivity. A schematic showing the basic operation of a post-acceleration detector (b).

Systems; Sunnyvale, CA). Ions are separated in ultrahigh purity Helium gas at pressures of 1-3 torr.

Ions exiting the drift cell pass through a 500 μm aperture that aids in differential pumping to achieve high vacuum pressures for ion detection. The aperture plate is connected to ground by a variable, trim-pot resistor (constructed in-house) capable of resistances from 0.5 to 5 MΩ. This allows for increased control of ion acceleration energies to the detector. After ions are accelerated from the mobility exit aperture, they traverse a field free region approximately 17 cm in length (through a small skimmer and tube lens defining the field free region). Upon exiting the tube lens, ions are detected by a post-acceleration detector (Figure 31(b)). Two aluminum flanges were designed in AutoCAD and constructed in the Texas A&M University Chemistry Machine Shop for mounting of the post-acceleration detector (Appendix C). The flanges were composed of three parts and welded together and mounted to an 8” Conflat 6-way cross vacuum chamber.

For ion detection ions are accelerated orthogonally to a 15 kV collision dynode operated at potentials from -10 kV to -15 kV. The impact of ions on the collision dynode causes a production of secondary electrons from the dynode surface. The secondary electrons are accelerated to the continuous dynode electron multiplier positioned across from the collision dynode. The continuous dynode electron multiplier is biased at a potential of -1.9 kV to -2 kV. As secondary electrons strike the cathode, electron multiplication occurs along the continuous dynode to the anode where the

current from the anode is sent to a 4-channel amplifier/discriminator (Ionwerks, Inc.; Houston, TX) and then to a time-to-digital converter (Ionwerks, Inc.; Houston, TX).

5.2.2 Chemicals

A mixture of fullerenes was purchased from Sigma-Aldrich (St. Louis, MO) and used without further purification. The fullerene mixture was suspended in benzene and spotted on a stainless steel probe inserted in the instrument between the first and second drift electrodes.

5.2.3 SIMION Simulations

SIMION version 8 (SIS; Ringoes, NJ) was used to simulate ion transmission and resolution for a variety of PDC IG electrode geometries and one specific PDC IG electrode geometry at varying drift lengths. Simulations were performed with the collision_hs1.lua user program with a collision cross section of 124 $Å^2$ for the radical cation of C_{60}, *m/z* value of 720 Daltons.

5.3 Results and Discussion

SIMION simulation results of resolution and percent ion transmission versus pressure for a 122 cm drift cell with 7000 V applied across the drift cell for a variety of PDC IG electrodes is presented in Figure 32. Much like the simulations presented in Section 3, mobility resolution is highest for a uniform field drift cell but ion transmission through a uniform field drift cell of length 122 cm is 1 percent or less for all pressures investigated. This corresponds to low throughput and requires increased acquisition time to achieve sufficient signal-to-noise ratios for experimental ion signals. By increasing ion transmission, acquisition time should decrease allowing for higher

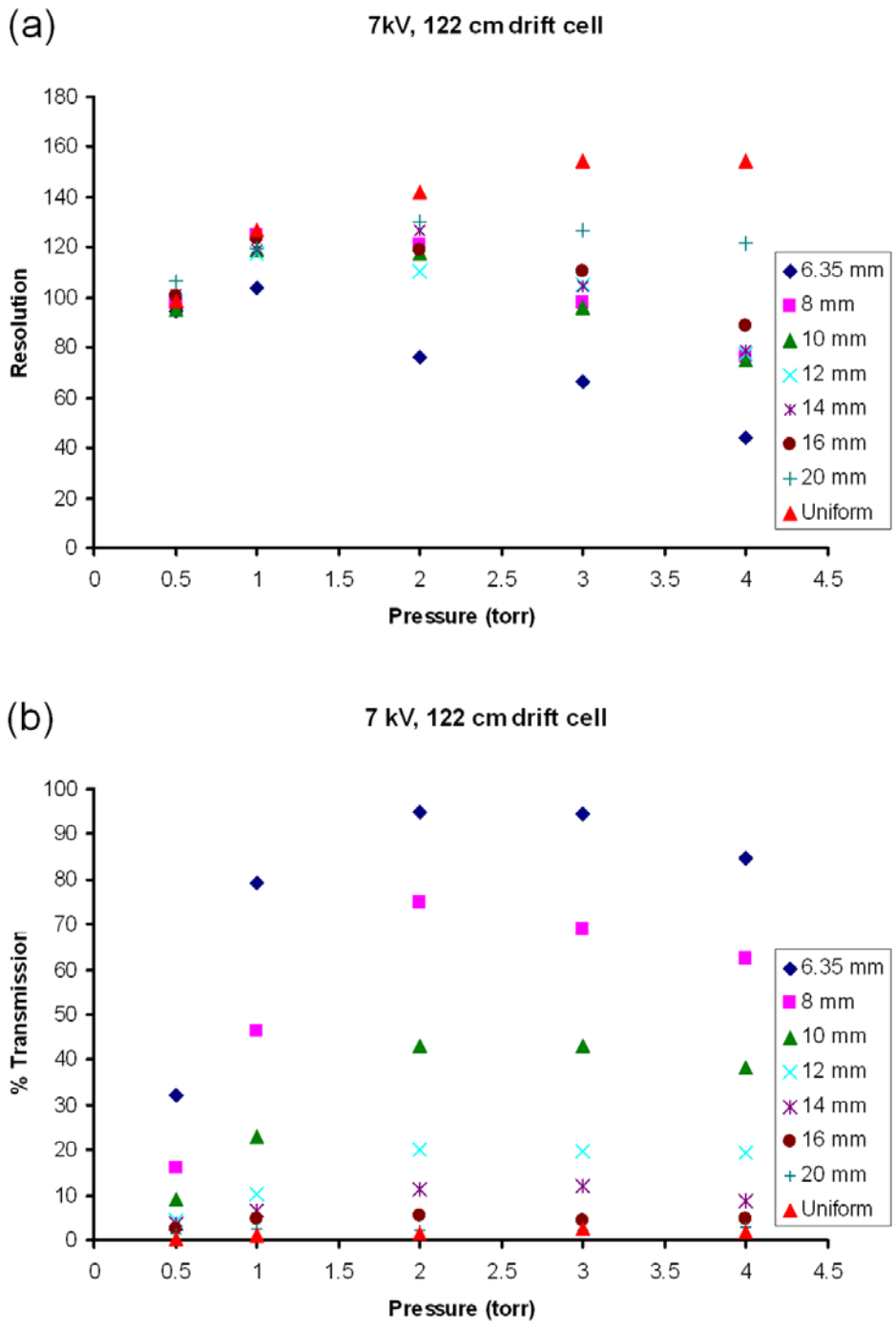

Figure 32. SIMION simulation results of resolution (a) and percent ion transmission (b) versus pressure for a variety of PDC IG electrode geometries on a 122 cm drift cell with 7000 volts applied across the drift cell.

throughput. It is also of note that for an 8 millimeter PDC IG the resolution increases by 45 percent according to simulations (Figure 32(a) versus Section 3-Figure 22(a) whereas theory says the increase should be 41 percent (equation 3.1-1).

Taking advantage of the radial focusing provided by PDC IG electrode geometries ion transmission can be increased without detrimental losses in mobility resolution. The trend that can be seen from Figure 32(a) is that as electrode inner diameter decreases, mobility resolution decreases. This trend can be attributed to greater penetration of the electric field into the electrode orifice that causes a greater variation in the axial electric field as a function of *z* position in the drift cell. The amplitude and direction of the radial electric field also varies as a function of ion position and serves to refocus ions at the back edge of the electrode. Finally, the decreased inner diameter leads to increased magnitude effective potentials at the electrode front and back edges (radial focusing described in detail in Section 2). The increase in variation of the axial electric field and magnitude of effective potentials results in increased radial focusing and thus greater ion transmission but lower mobility resolution. As ions diffuse radially from the central drift cell axis, ion trajectories are corrected by effective potentials at the back edge of each electrode. However, the drift length is increased by the off-axis, and subsequently corrected, trajectory compared to an ion traveling down the central drift axis. In addition, the axial electric field varies as a function of radial ion position and results in changes in ion axial velocity as a function of radial position. The product of these two effects lead to increased ion transmission but at the expense of increased broadening of the ion signal.

Ion transmission, on the other hand, increases as electrode inner diameter is decreased (as mentioned previously in Section 3). According to Figure 32(b), ion transmission increases from approximately 1 percent for a uniform field drift cell to greater than 80 percent for a 6.35 mm inner diameter PDC IG electrode in the pressure range of 1 to 4 torr. An 80-fold increase in ion transmission demonstrates the utility of PDC IG drift cells.

The optimum design of PDC IG electrodes must be considered for what type of mobility resolution and/or ion transmission capabilities are required for the experiment. For our purposes, an electrode design providing high ion transmission without a great decrease in mobility resolution compared to a uniform field drift cell design is most appealing. Consequently, the 8 mm inner diameter PDC IG electrode is ideal for both ion transmission and mobility resolution. In the pressure regime of 1 to 2 torr, the 8 mm inner diameter PDC IG electrode offers a 45- to 70-fold increase in ion transmission with only a 10 percent decrease in mobility resolution compared with a uniform field drift tube IMS design.

Further simulations were performed to investigate resolution and percent ion transmission for an 8 mm PDC IG drift cell at varying drift lengths. Two pressures were simulated, 1 and 2 torr, with the electric field over pressure value, *E/p*, held constant at 30 $Vcm^{-1}torr^{-1}$. A 1 mm aperture plate at the back of the drift cell was defined as the boundary for the end of the drift cell. The mobility resolution was calculated from the average of the recorded drift times in SIMION divided by the peak width of the drift time distributions at half maximum. The peak width at half maximum of the drift time

distributions is calculated from the product of the number 2.2 and the standard deviation of the recorded drift times. The percent ion transmission is calculated by counting the number of ions passing the aperture plate of the drift cell compared to the initial number of ions flown in the simulation. Three trials were performed for each drift length and pressure to determine an average value for resolution and percent ion transmission and the standard deviation of the three trials was used for error bars in the measurement.

According to theory (equation 5.1-1), increasing drift length should increase mobility resolution by the scale of $L^{1/2}$. The data for mobility resolution as a function of drift length is depicted in Figure 33(a). As expected, mobility resolution increases as drift length increases. The increase in mobility resolution at a pressure of 2 torr (red lines) compared to 1 torr (blue lines) can be explained by the fact that the electric field is doubled for these simulations in order to maintain an *E/p* value of 30 $Vcm^{-1}torr^{-1}$. The simulated results were plotted with the program Origin (OriginLab, Northampton, MA) and a fitting tool was used to fit the data to the equation

$$y = a(x)^b \tag{5.3-1}$$

In this equation, the independent variable, *x*, is the drift length, while the dependent variable *y* is mobility resolution. According to the best-fit equations for both sets of data, the value of *b* is nearly 0.5 (Figure 33(a)). This result affirms the theoretical expectation of mobility resolution increases proportional to the square root of the increase in drift length.

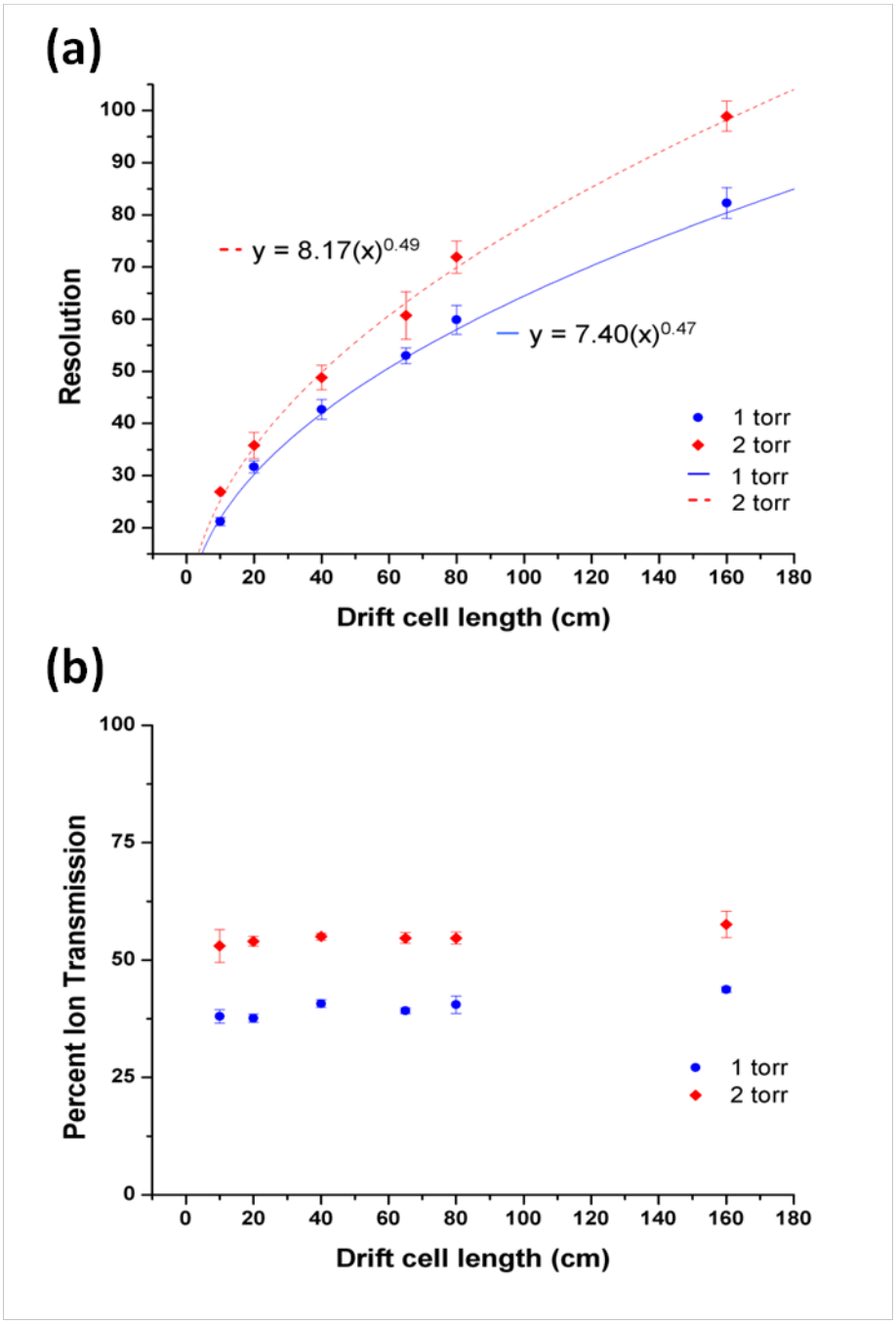

Figure 33. Plot of resolution (a) and percent ion transmission (b) versus drift cell length at pressures of 1 and 2 torr for a PDC IG with 8 mm inner diameter electrodes, configuration B. The error bars were calculated for three simulation trials. The lines shown in (a) are the best-fit lines that approach a square-root dependence of the resolution on drift cell length. The equations for the lines are shown in (a).

The simulated results for percent ion transmission are of utmost importance and need to be emphasized to explain the major analytical utility of the PDC IG. Figure 33(b) shows that percent ion transmission remains constant, approximately 40 percent at 1 torr and 55 percent at 2 torr, regardless of drift cell length. For a uniform field drift cell, ion transmission decreases exponentially with drift cell length. Herein lies the main advantage of periodic-focusing in that ion transmission is independent of drift cell length; rather, ion transmission is dependent on electrode geometry, the applied electric field, and aperture size used at the mobility exit. It can be estimated that ion transmission with the same parameters and a 500 μm aperture is approximately 10 to 15 percent in the pressure range of 1 and 2 torr. Ion transmission in a PDC IG would increase by increasing the aperture size or applied voltage.

Finally, the 125 cm PDC IG drift cell equipped with 8 millimeter inner diameter electrodes was tested experimentally to measure the increase in mobility resolution versus a 63 cm cell. Figure 34 shows two mobility spectra taken at different *E*/p (*E*/*N*) conditions with the mobility resolution calculated for $C_{60}^{\bullet+}$. The maximum mobility resolution for $C_{60}^{\bullet+}$ is ~82, corresponding to a 36 percent increase over the maximum resolution obtained for the 63 cm PDC IG drift cell (Section 3). The resolution increase is in good agreement with that predicted by theory, 41 percent, and the prediction provided by SIMION simulations, 45 percent.

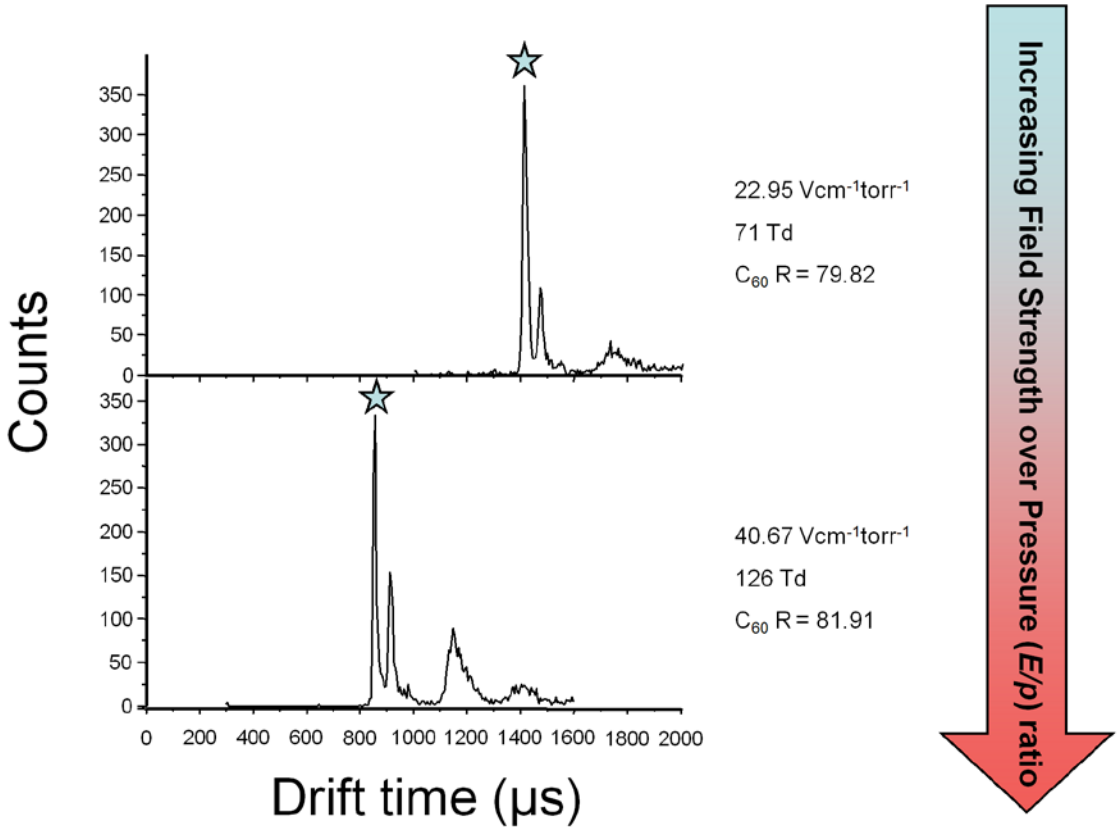

Figure 34. Drift time data from a fullerene mixture taken on the 125 cm PDC IG at two different *E/p* (*E/N*) values. The signal response for $C_{60}^{\bullet+}$ is denoted by the star while the mobility resolution is presented at right.

5.4 Conclusion

Increasing the length of a periodic-focusing DC ion guide drift cell provides analytical utility in that the mobility resolution increases according to the square root of the increase in drift length without decreasing ion transmission. In fact, the drift length of a PDC IG has no effect on ion transmission. The ion transmission is dependent on electrode geometry, the applied electric field, and the size of the aperture used at the mobility exit.

The drift length of the 8 mm inner diameter PDC IG was also increased to 125 cm (versus 63 cm in Section 3) and tested experimentally. The maximum resolution obtained for C_{60}^{+} was increased to ~82, a 36 percent increase compared to the 63 cm drift cell. Equation 5.1-1 reveals that *R* should scale as $L^{1/2}$, corresponding to a 41 percent increase in *R*, which is in good agreement with the observed increase.

Finally, it is interesting to project the practical significance of the manipulation of the variables contained from equation 1 in the limit of an ion population composed of a single conformer. For example, an increase in drift length (*L*) to 250 cm should provide an additional 41 percent increase in *R*, and increasing the field strength (*E*) of a 250 cm drift cell by a factor of 4 could potentially provide a 100 percent increase in resolution. In addition, operation of the drift cell at reduced temperature (*T*), *i.e.* 100 K rather than ambient (300 K), could provide an additional 70 percent increase in *R* [191]. Thus, optimization of the drift cell design and operational parameters in terms of *L*, *E*, and *T* could potentially increase mobility resolution to ~400 for a singly-charged ion!

6. INTERFACING THE PDC IG DRIFT CELL WITH ORTHOGONAL ACCELERATION TIME-OF-FLIGHT MASS SPECTROMETRY

6.1 Introduction

Ion mobility spectrometry separates gas-phase ions on the basis of their mobility in a certain drift gas. Ions with known mobilities in a drift gas are easily identifiable by IMS alone but ions of unknown mobilities, especially present in complex samples, are difficult to identify solely with IMS. For this reason, IMS has been coupled with MS to establish a two-dimensional separation that decreases ambiguity in identification owing to the mass characterization provided by MS for each ion signal. The two separations are extremely compatible as both are post-ionization gas-phase separations. Moreover, the information-rich two dimensional spectra is capable of separating different chemical families of molecules, *e.g.* peptides, carbohydrates, hydrocarbons, lipids. Briefly, the history of ion mobility coupled with a variety of mass analyzers will be examined.

The first IMS coupled to a mass analyzer was done by E.W. McDaniel at Georgia Tech University in 1962 [65]. The drift tube is coupled to a magnetic sector mass spectrometer for mass analysis of low-energy ion molecule reactions. The length of the drift cell and drift gas pressure can be varied to define the collision frequency of the ion with the drift gas and ultimately lead to accessing different reaction channels. Ion masses must be scanned through the magnetic sector by varying the accelerating potential of the ion gun (ion acceleration region of the magnetic sector mass analyzer). Soon after, a variety of ion mobility systems were coupled with quadrupole mass

spectrometers [66-67]. The first mass-selected atmospheric pressure ion mobility system was developed by Karasek *et al.* in 1971. This atmospheric pressure IMS-q-MS was developed into a commercial instrument [192]. Atmospheric pressure IMS coupled with quadrupole mass spectrometers was the instrumental platform of choice for most of the 1970s and 1980s. It was used to identify mobility-selected ions and even confirmed structurally different ions by mobility of the same mass [193-194].

More recently, the use of quadrupoles with IMS has been taken a step further utilizing linear and quadrupole ion trap (LIT and QIT) technology to isolate mobility selected ions for tandem mass spectrometry and MS^n analyses. Drift-time, also known as drift tube, IMS with a Bradbury-Nielsen gate at the mobility exit has been interfaced with a QIT to accumulate mobility selected ions to perform MS^n analyses [68-69]. In addition, QITs have been implemented prior to drift time IMS for accumulation and modification of isomeric ions. The bare isomeric ions could not be separated by IMS but modification of the ions with adducts allowed for sufficient separation [100]. Thermo Electron Corporation has released a commercial instrument with a form of differential mobility spectrometry (DMS) with a QIT or triple quadrupole mass spectrometer. Thermo has termed the DMS-MS as high-field asymmetric waveform ion mobility spectrometry, or FAIMS [195].

Ion mobility coupled with Fourier transform ion cyclotron resonance mass spectrometry is much less developed. One early experiment attempted to insert an ion mobility spectrometer in the ICR cavity [196]. The motivation was that the magnetic field from the ICR magnet could be used to confine drifting ions to the center of the drift

cell. This experiment proved to be very challenging and was not pursued after the original publication. More practically, dual gating of IMS coupled with FT-ICR mass spectrometers have been employed. The experimental design is similar to an IM-QIT design in that mobility-selected ions are introduced to the FT-ICR for mass analysis [197-199]. The main advantage of an FT-ICR is high mass resolution which becomes increasingly important with higher degrees of sample complexity, *e.g.* multiple protein proteolytic digests, petroleum crude oil samples, etc. However, the fact of the matter is for most samples an FT-ICR mass spectrometer is not required and the cost is therefore not justified.

Approximately the same time period as the introduction of IM-q-MS instruments, ion mobility time-of-flight instruments were introduced. The first instrument was produced in 1963[70] and several publications followed [71-72]. Ions traversed a drift tube IMS region and then were accelerated by an electric field to a set of parallel plates. The parallel plates were then pulsed to extract ions orthogonally into the time-of-flight mass analyzer [47]. To my knowledge, this is the earliest ion mobility orthogonal acceleration-time-of-flight mass spectrometer (IM-oa-TOFMS). The prevalence of IM-TOFMS was nearly non-existent until the improved capabilities in TOF provided by the reflectron and resurgence of orthogonal acceleration time-of-flight (oa-TOF) mass spectrometry.

Time-of-flight mass spectrometry made great strides with the dual stage extraction source and time-lag focusing provided by Wiley and McLaren [47]. The dual stage extraction source brought about more manipulation of the space focusing of ions in

the TOF while time-lag focusing aided in energy focusing of initial kinetic energy spreads of ions. In 1973, Mamyrin released the reflectron that provided another order of energy focusing in a time-of-flight mass analyzer [56]. This reflectron allowed for significant increases in mass resolving power and can be attributed as one of the main reasons time-of-flight mass spectrometry is a popular mass analyzer today. In 1989, Guilhaus *et al*. revisited the ideas of orthogonal acceleration time-of-flight mass spectrometry [73]. Its impact was quickly realized in a variety of experiments.

Orthogonal acceleration time-of-flight mass spectrometry became an important tool with continuous ionization sources such as electrospray ionization (ESI) [200]. The orthogonality allows for electrosprayed ions to be extracted orthogonally to the TOF whereas parallel, or inline, extraction would be much more complicated as additional gating techniques would need to be used to introduce ions to the TOF extraction source. In addition, parallel extraction suffered from low resolution owing to velocity distributions of ions from continuous gaseous ion sources such as electron impact ionization (EI) and chemical ionization (CI). In the orthogonal acceleration design, initial ion kinetic energy, or velocity distributions, and spatial distributions can be controlled by collimating lenses prior to the TOF extraction source and are therefore less detrimental to the mass resolution [74]. Orthogonal acceleration time-of-flight mass spectrometry has infiltrated a variety of commercial mass spectrometers and also has been interfaced with a variety of hybrid ion mobility-mass spectrometers.

Here, we present a simplistic design of an ion mobility orthogonal-acceleration time-of-flight mass spectrometer. Specifically, a 125 centimeter periodic-focusing DC

ion guide (PDC IG) drift cell is coupled to an orthogonal 22.8 centimeter linear time-of-flight mass analyzer. The two separation dimensions are used to construct two-dimensional mobility-mass contour plots providing more information as ion mobility signals are now correlated with mass spectrometry analyses to characterize ion mass. In this work, we will examine the mobility and mass resolution capabilities of this IM-oaTOF-MS design.

6.2 Experimental

6.2.1 Chemicals

A fullerene mixture was purchased from Sigma-Aldrich (St. Louis, MO) and dissolved in benzene prior for analysis of radical cations of C_{60} and C_{70} by LDI. Angiotensin I (MW = 1296 Daltons) was purchased from Sigma-Aldrich (St. Louis, Missouri) and used without further purification. A 0.1 mg/ml solution was mixed 1:1 (v:v) with a 5 mg ml^{-1} solution of alphacyano-4-hydroxycinnamic acid dissolved in 60 % ACN, 40 % distilled H_20, with 0.1% trifluoroacetic acid solution, and 10 mM dihydrogen ammonium phosphate.

6.2.2 Instrumentation

Ions are created by LDI or MALDI using a 355 nm N_2 laser (Stanford Research Systems; Sunnyvale, CA). The ion mobility drift cell is a 125 centimeter periodic-focusing DC ion guide (PDC IG) drift cell (described previously in Section 5). Briefly, the drift cell consists of 100 drift electrodes separated by precision ceramic spacers (~8 mm inner diameter, grade 25 high alumina nonporous ceramic spacers, McMaster-Carr, Robbinsville, NJ). The drift electrodes are connected by high-precision, 1 MΩ resistors

(Mouser Electronics, Mansfield, TX) to establish the electric field provided by a Spellman 15 kV high voltage power supply. Ions are separated in ultra-high purity Helium, operated at pressures of 1-3 torr.

Ions exiting the drift cell are transferred to the oa-TOF extraction source by a three-element einzel lens. The three elements of the einzel lens will be referred to as lens 1, lens 2, and lens 3. The dimensions of the einzel lens elements are as follows: lens 1 = 2.92" length, 0.925" inner diameter; lens 2 = 1.545" length, 0.925" inner diameter, lens 3 = 1.14", inner diameter 0.925" tapered down to 0.500" at 0.865" length. The ends of the lenses are welded to eV Parts® plates (Kimball Physics Inc., Wilton, NH) and the spacing between lenses is 0.075" and is established by precision eV Parts® ceramic spacers (Kimball Physics Inc.; Wilton, NH). The first element of the Einzel lens is operated at ground potential while the second element is at a negative potential and the third element is again at ground. The depth of the potential well, length of the lens elements, and ion velocity determines the focal point of the ions.

Ions are extracted in a pseudo-Wiley-McLaren TOF extraction source that actually consists of three electric field regions (a three-stage extraction source). The electric field can be varied in each of these stages to attempt to vary the space focus plane for optimum mass resolution at the detector. The first stage is referred to as the push region consisting of the push and static electrode of the extraction source while the second stage, the pull region, consists of the static and pull electrodes. The third stage consists of the pull electrode and the TOF entrance region. Ions are accelerated through the three stage extraction source, separated according to their mass-to-charge (*m/z*) in the

field free region, and detected by a MagneTOF® electron multiplier (Model DM291, SGE, Inc.; Australia). The two high voltage inputs of the electron multiplier are supplied by a Burle 10 kV floatable power supply (Type #PF1055, Serial #0204; Burle Electro-Optics; Lancaster, PA). The overall flight distance in the orthogonal, linear TOF is 22.8 centimeters.

6.3 Results and Discussion

A short linear, orthogonal TOF was chosen for mass characterization of ion mobility signals owing to its relative simplicity and facile operation. The dimensions of the TOF and its components must be considered, however, to achieve ion detection. Pertinent parameters for the experiment include physical positioning of the TOF extraction source and electron multiplier, time-of-flight distance, ion axial velocity exiting the mobility drift cell, and ion velocity in the time-of-flight region from orthogonal acceleration. These parameters are important as ions extracted from the TOF extraction source must be projected onto the surface of the electron multiplier detector. An AutoCAD drawing of the latter half of the instrument showing the einzel lens region, TOF extraction optics, TOF can, and TOF detector is given in Figure 35. The horizontal distance from the center of the TOF extraction region to the center of the electron multiplier is 3.8 centimeters. Considering the diameter of the TOF extraction plates (0.75”, 1.9 cm) and the diameter of the orifice in the TOF can (1”, 2.54 cm) prior to the electron multiplier, the distance from the outer edge of the TOF source to the opposite outer edge of the detection region is ~6 cm while the inner edge of the TOF source to the

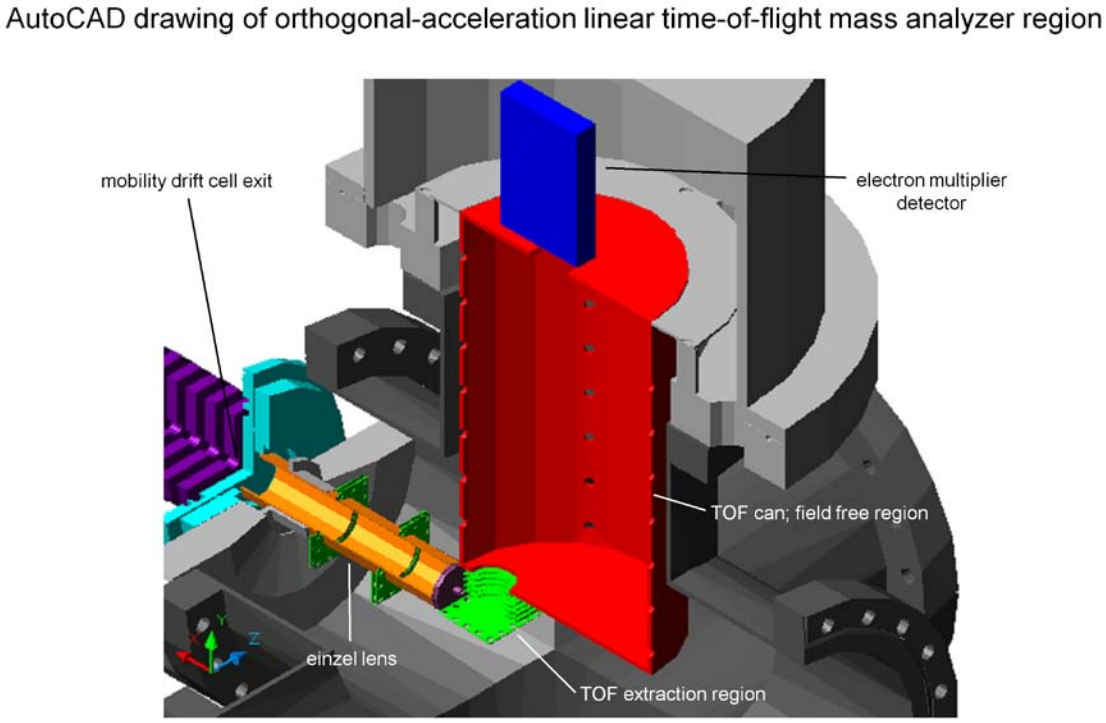

Figure 35. AutoCAD drawing of the orthogonal-acceleration linear time-of-flight mass spectrometer coupled to the PDC IG along with the einzel lens, TOF extraction source, and electron multiplier detector.

adjacent inner edge of the detection region is ~1.3 cm. The overall flight distance in the TOF is 22.8 cm. Therefore, in order to make sure extracted ions reach the detector, calculations should be performed to establish the ion velocity vector components in the axial direction, *z* (drift cell axis), and the orthogonal direction, *y*, (toward the time-of-flight detector).

Figure 36 shows a block diagram of the einzel lens and TOF region of the instrument with an example calculation provided for the radical cation of C_{60} and its displacement in the axial direction, *z*, from the TOF extraction source to the time-of-

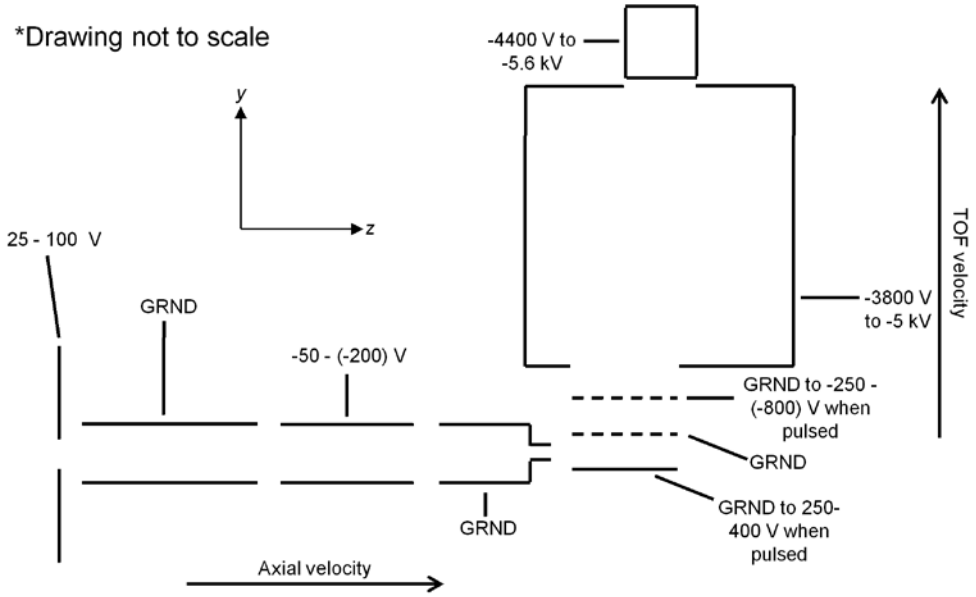

Acceleration energy in axial direction
Acceleration = 25 - 100 eV
$E_k = ½*m*v^2$
1 eV = $1.6x10^{-19}$ J
4.0×10^{-18} J= ½* (1.1956×10^{-24} kg) * v^2
1.6×10^{-17} J= ½* (1.1956×10^{-24} kg) * v^2
Axial velocity = 2587 - 5173 m/s

Acceleration energy in direction of TOF
Acceleration = ~4050 eV – 5400 eV
$E_k = ½*m*v^2$
1 eV = $1.6x10^{-19}$ J
6.5×10^{-16} J= ½* (1.1956×10^{-24} kg) * v^2
8.6×10^{-16} J= ½* (1.1956×10^{-24} kg) * v^2
TOF velocity = 32924 – 38017 m/s

Time-of-flight calculation
Flight distance = 0.228 m
$t = d / v$
t = 0.228 m / 32924 m/s
t = 0.228 m / 38017 m/s
TOF = 5.99 – 6.93 µs

Ion Displacement from Acceleration to Detection
$d = v * t$
d = 2587 m/s * 5.99 µs
d = 5173 m/s * 6.93 µs
d = 1.55 – 3.60 cm

Figure 36. Schematic diagram of einzel lens and TOF region and calculations to illustrate ion displacement in axial direction, *z*, from point of acceleration in the TOF extraction region to the detector. The ion used for the calculation is $C_{60}^{\bullet+}$, with an *m/z* value of 720 Daltons.

flight detector. From the physical location of the TOF extraction source, the electron multiplier detector, and the length of the TOF ions of *m/z* 720 must be accelerated with kinetic energies in the axial (orthogonal to TOF) and TOF directions as shown in Figure 36.

Another important instrumental aspect to consider in an IM-MS separation is the time of elution of an ion packet from the mobility cell in relation to the pulsing of the TOF extraction source. Consider that an ion packet is eluting the drift cell with an arrival time distribution of 480 μs and a baseline peak width of 40 μs. If a TOF extraction frequency of 25 kHz and pulse width of 2 μs is used to extract ions from the extraction source and the first TOF extraction occurs simultaneously with the initial laser pulse then the majority of the eluting ion packet profile will not be detected. According to the timing of ion extraction in the TOF source, only the leading and trailing edges of the eluting ion mobility packet would be analyzed from the aforementioned example (Figure 37(a)).

To ensure better sampling of the entire ion packet the TOF extraction frequency could be increased thereby decreasing the time interval between TOF extraction pulses. However, this strategy would be analyte dependent and the need for optimization of each analyte of interest would be time consuming. A more reasonable approach for varying the timing sequence of the TOF extraction is accomplished by a process called interleaving. Interleaving involves introducing a time delay, much like the operation of a delay generator, for a sequence of pulsed events. To illustrate, consider once again the

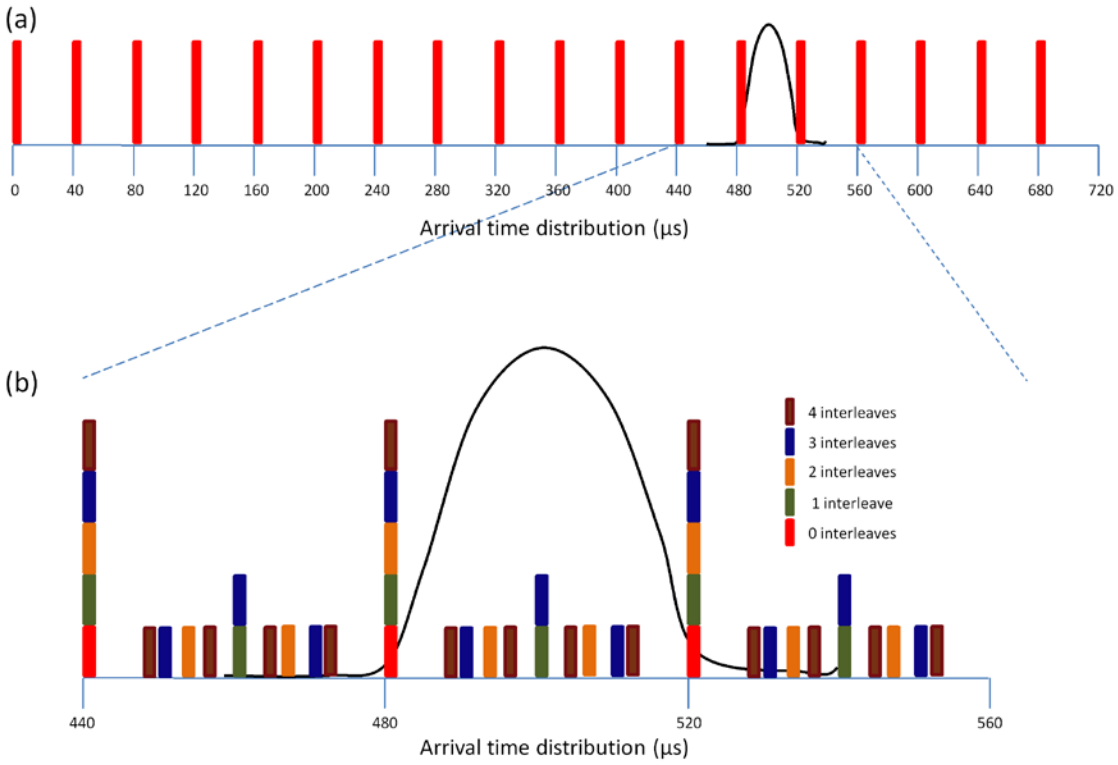

Figure 37. A representation of an arrival time distribution of an ion packet eluting the drift cell with a TOF extraction frequency of 25 kHz and pulse width of 2 µs (a). The same representation of the ion packet eluting the drift cell using interleaving in the TOF extraction timing (b).

example given above where a TOF extraction source is pulsed at a rate of 25 kHz with a pulse width of 2 µs. This corresponds to a pulse duration of 2 µs with a subsequent pulse occurring every 40 µs in the TOF extraction source. For the first ionization event (the first firing of the laser) all ions created would exit the mobility cell and be analyzed by the TOF with the timing sequence for extraction shown by the red bars in Figure 37(a). If one interleaving event is employed in the data acquisition software then upon the second ionization event ions created would exit the mobility cell but now extraction

of the ions in the TOF source would be shifted in time. Specifically, a 20 μs delay from the firing of the laser to the first TOF extraction would be implemented and each subsequent extraction would be 40 μs after the preceding pulse. Thus, the ion packet would now be extracted from the TOF source when the center of the ion cloud (peak centroid of the mobility signal) is passing through the TOF extraction source (denoted by olive green bar in Figure 37(b)). The number of interleaves can be increased to vary the time delay of each interleaving event resulting in extraction at different times of the eluting ion mobility profile (Figure 37(b)). The process of interleaving provides much better sampling across the entire profile of an eluting ion packet, increasing the sensitivity of the extracted and detected ion signal while also giving a more representative mobility profile in order to detect actual peak widths for calculating mobility resolution.

The PDC IG IM-oaTOF-MS instrument was tested experimentally with a fullerene mixture. A variety of instrument parameters were varied to test their effect on the performance of the instrument. Said parameters include electric field and pressure values for the IMS separation, acceleration voltage upon mobility exit, einzel lens voltages, TOF extraction voltages, and time-of-flight bias voltage. Example two-dimensional IM-MS spectra are shown in Figure 38**.** Changing the various parameters reflect minor changes in the sensitivity, mobility resolution, and mass resolution. Ion mobility resolution is consistently between 35 and 50 for the radical cations of C_{60} and C_{70} while the mass resolution of the ion signals is between 70 and 100 ($m/\Delta m_{fwhm}$). The

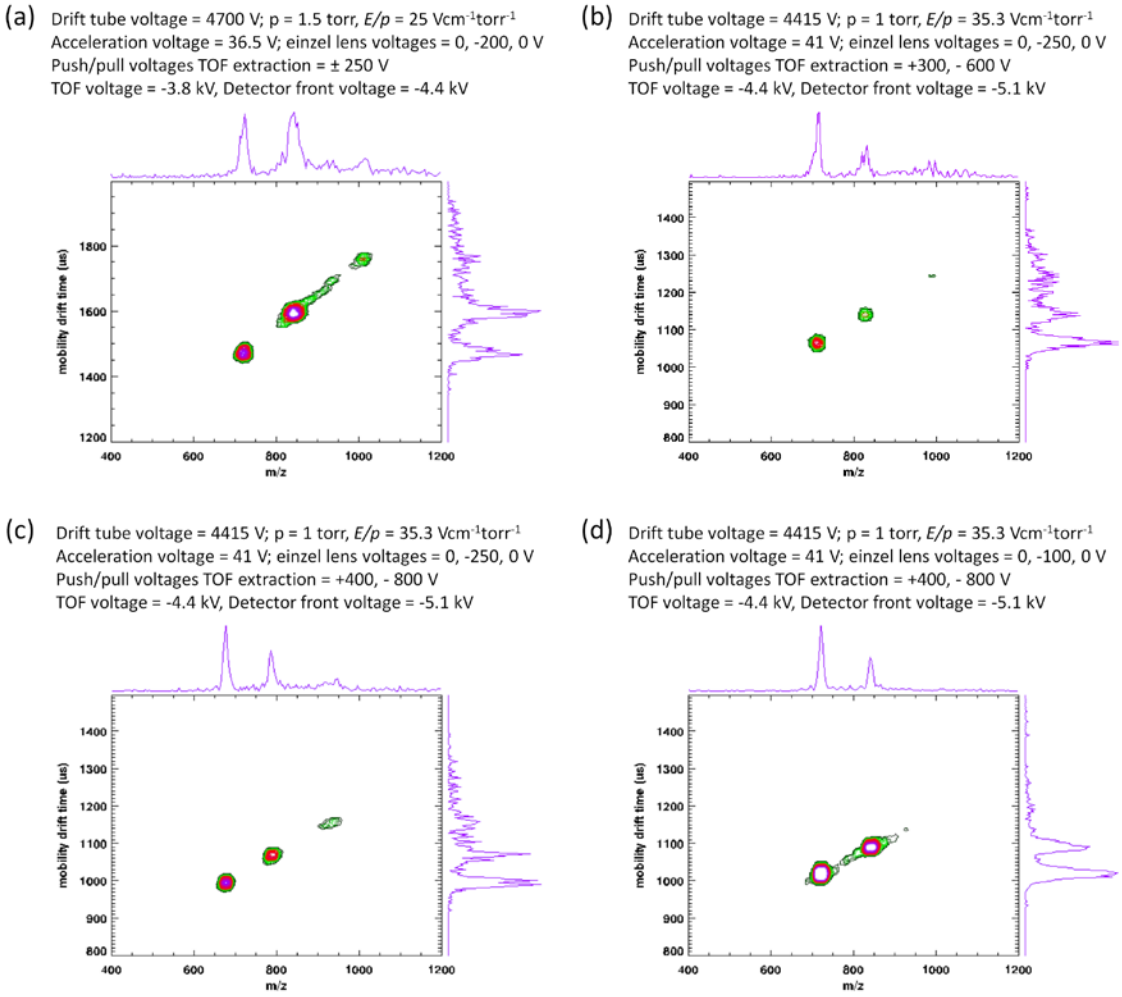

Figure 38. Two-dimensional ion mobility-mass spectra of a fullerene mixture showing different instrumental conditions of the PDC IG drift cell and TOF mass spectrometer.

larger mass ion signals are higher order carbon clusters, normally seen in LDI mass spectra of fullerene mixtures at higher laser intensities.

The mass resolution is sufficient for characterization of mobility separated ions. The mass resolution can be optimized by changing the voltage of the second einzel lens element in the three element einzel lens (Figure 39). A lower voltage on the second

einzel lens element decreases the number of ions transmitted through the einzel lens but focuses the ions into the TOF source better prior to extraction. On the other hand, increasing the voltage on the second einzel lens element focuses more ions to the TOF extraction source, increasing sensitivity.

Conversely, the mobility resolution is decreased when compared to results from Section 5. On the 125 centimeter PDC IG drift cell with a post-acceleration mobility detector, the resolution values for C_{60} and C_{70} were approximately 80, nearly double the resolution for the representative spectra in Figure 38.

Additional experiments on the PDC IG-IM-oa-TOF-MS were also performed on the model peptide, Angiotensin I. Similar mass resolution was provided by the TOF for the protonated molecule of Angiotensin I as for the fullerene radical cations. Once again, the mobility resolution for the protonated molecule of Angiotensin I is less than expected for a 125 cm length PDC IG drift cell. From Section 3 the mobility resolution of two peptides of similar *m/*z, a modified Angiotensin molecule, Val-4-Angiotensin I, and Glu-Fibrinopeptide B approached 60. Increasing the drift length by a factor of two should increase the mobility resolution by 41 percent, projecting a mobility resolution of ~85.

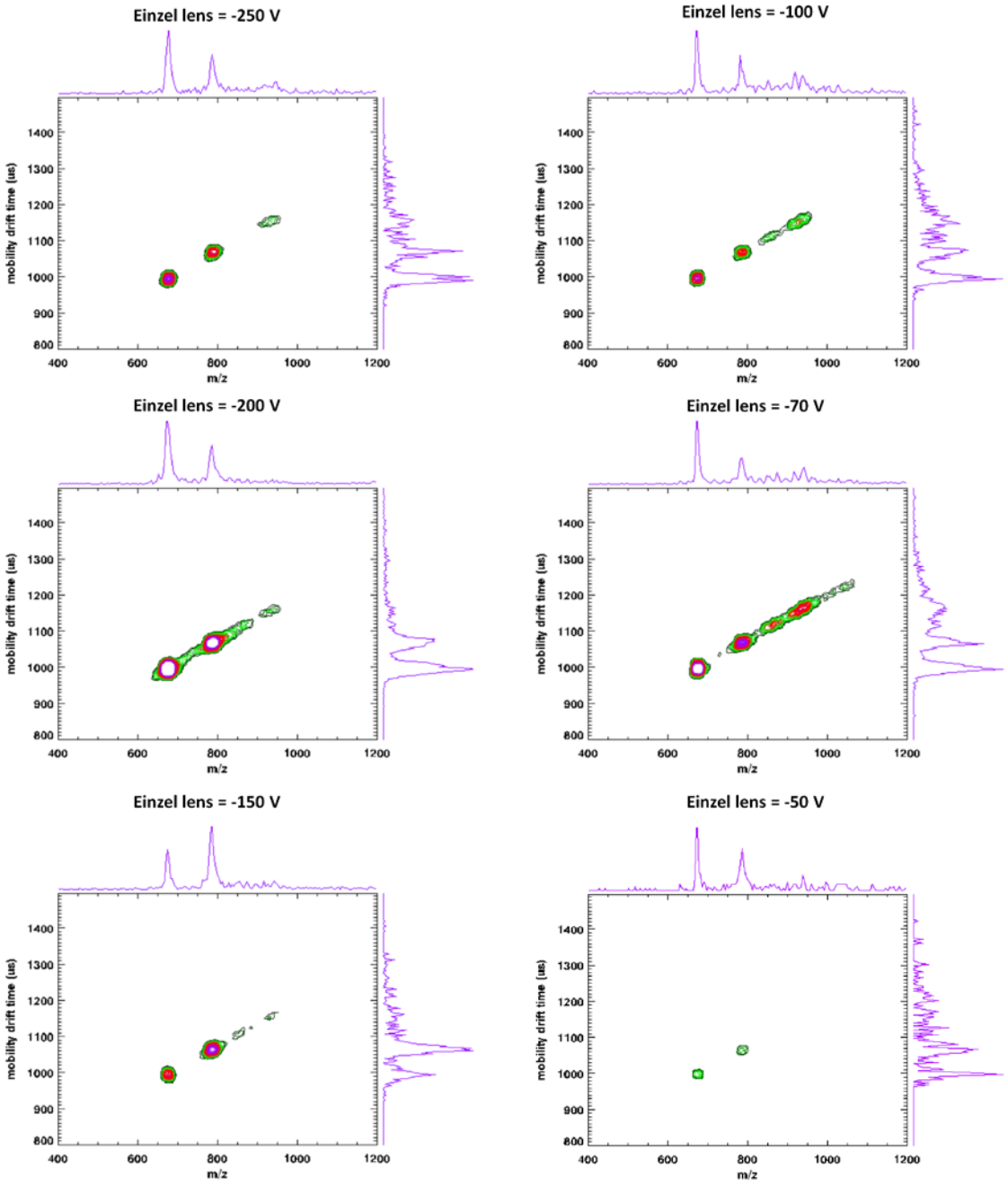

Figure 39. Two-dimensional ion mobility-mass spectra of $C_{60}^{\bullet+}$ and $C_{70}^{\bullet+}$ showing the effect of einzel lens voltage on the second einzel lens on the sensitivity and mass resolution of the orthogonal-acceleration linear time-of-flight mass spectrometer.

6.4 Conclusion

The 125 cm PDC IG drift cell was successfully coupled to a 22.8 cm orthogonal-acceleration linear time-of-flight mass analyzer. The mass resolution of the TOF ($m/\Delta m_{fwhm}$) is approximately 100 for the analytes investigated. Variation of the potential on the second einzel lens of the three-element einzel lens focusing optics can be used to optimize sensitivity or mass resolution in the TOF. Sensitivity can be increased by focusing more ions into the TOF extraction source while mass resolution can be increased by attenuating the ion beam entering the TOF extraction source.

The mobility resolution provided by the PDC IG is less than expected from previous experiments in Section 3 and projected resolution increases from increasing drift cell length in Section 4. Degradation of the mobility resolution is most likely occurring outside the drift cell. The fidelity of the eluting ion packet profile seems to be lost prior to TOF extraction. Further experiments must be done to improve ion transfer and ion focusing from the mobility cell exit aperture to the TOF extraction source.

7. IMPROVING THE ION OPTICS FOR ION FOCUSING AND ION TRANSFER IN THE INTERFACE OF AN ION MOBILITY ORTHOGONAL TIME-OF-FLIGHT MASS SPECTROMETER

7.1 Introduction

Ion mobility-mass spectrometry (IM-MS) has become a powerful post-ionization separation technique impacting nearly all areas of the 'omics' world [68, 102, 201-205]. The advent of MALDI [49-50] and ESI [80] enabled the analysis of large, intact biomolecules The fast separation times provided by ion mobility spectrometry (IMS) (microseconds to milliseconds) compared with that of liquid chromatography and capillary electrophoresis (minutes to hours) allow for higher throughput and increased instrumental duty cycle [188].

Moreover, the orthogonal mobility and mass separations afforded by IM-MS provides additional analyte information. The first dimension separates ions based on their mobilities, *K*, which are inversely proportional to their size, or ion-neutral collision cross section, Ω. The ion-neutral collision cross section provides structural information of the ion and has been used with molecular dynamics simulations to investigate probable, low energy ion structures [179, 206-207]. The second dimension separates ions according to their mass-to-charge ratio. The two-dimensional mobility-mass information provides additional, rich information pertaining to analyte molecular chemical family [75]. Put more simply, ions of different chemical families fall in different areas of conformation space, referred to as trendlines. These trendlines have

been used to separate peptide, carbohydrate, lipid, and hydrocarbon/fullerene ion signals [77]. Furthermore, studies are being done with covalently linked modifiers to act as shift reagents to shift ion signals away from specific trendlines. The idea of the separation of chemical families in conformation space can be improved with increased mobility resolution.

Mobility resolution can be affected by a number of experimental parameters including initial ion packet width (or gate width if an injected ion packet from a continuous ionization source), space charge effects (coulombic repulsion) from high ion concentrations, the presence of different conformations for a drifting ion, and diffusion. Ion diffusion is more often than not the main contributor to decreased resolution in mobility separations and its effect can be projected from equation 7.1-1

$$R_d = \left(\frac{ELez}{16 k_b T \ln 2} \right)^{1/2} \tag{7.1-1}$$

where E is electric field, L is drift length, e and z are elementary charge and numbers of charges, k_b is Boltzmann's constant, and T is drift gas temperature. Resolution, under the consideration of diffusion, can be increased by increasing E, L, or z or by decreasing T. This work will focus on increased mobility resolution through increased drift length.

One of the challenges of IM-MS is maintaining high ion transmission through the drift cell and efficiently transferring the ions through a differentially pumped region to the mass analyzer. Most IM-MS separations require a small sampling aperture at the mobility cell exit to serve as a conductance limit for gas flow into the mass analyzer region. This may aid in differential pumping but also diminishes ion transmission to the

mass analyzer. Compound this issue with increased drift lengths leading to more radially diffuse ions and decreases in ion transmission become substantial. In an effort to remedy this problem, two solutions have been proposed. The first is the use of an RF ion funnel (developed in the Smith laboratory) at the drift cell exit to correct for radially diffuse ion trajectories and increase the number of ions transmitted to the mass analyzer. The second proposal, created in our laboratory, employs a unique drift electrode geometry that takes advantage of non-linear electric fields to serve as a radial focusing mechanism for radially diffuse, drifting ions. The device has been termed a periodic-focusing DC ion guide (PDC IG) drift cell and preliminary data along with details of the focusing mechanism of the device have been published previously. The instrument presented herein utilizes a PDC IG for increased ion transmission through the drift cell.

Once ions exit the drift cell they must still be focused in a pneumatically divergent environment to the mass analyzer. Historically, skimmer cones have been used after the mobility exit to achieve a differential pumping region and eliminate gas molecules from entering the mass analyzer region. The skimmer cone, however, leads to further ion losses as some of the ions will be skimmed away with gas molecules resulting in lower ion transmission to the mass analyzer region. Herein, we propose a set of novel ion optics to transfer ions from the mobility exit to a mass analyzer in a region composed of a pressure gradient from mobility separation pressures to vacuum needed for time-of-flight analyses.

7.2 Experimental

7.2.1 Chemicals

All chemicals were purchased and used without further purification. A fullerene mixture composed of C_{60} and C_{70} was purchased from Sigma-Aldrich and used to characterize the ion optics used after the ion mobility exit. Three model peptides were used to demonstrate the capabilities of the PDC IG drift cell and ion optics to transmit ions up to 2500 *m/z*. The peptides used were Bradykinin (MW = 1060.5 Da), Angiotensin I (MW = 1296 Da), and ACTH clip 18-39 (MW = 2465.2 Da). The peptides were purchased from American Peptide Company and used without further purification.

7.2.2 Instrumentation

7.2.2.1 Drift Cell

Ions are formed by MALDI in the drift cell using a Nd:YAG laser, $\lambda = 355$ nm (Teem Photonics; Meylan, France). The PDC IG drift cell portion of the instrument has been described previously. Briefly, the drift cell is composed of 100 individual electrodes resulting in a 125 cm drift length. The drift electrode dimensions of inner diameter, thickness, and spacing are 8 mm, 6.35 mm, and 6.35 mm, respectively. The electrodes are connected by 1 MΩ, high precision resistors (Mouser Electronics; Mansfield, TX) to establish a voltage drop across the drift cell. All mobility experiments were performed with ultra-high purity He drift gas at pressures of 1-3 torr. The mobility exit is defined by a 500 μm aperture which provides a pressure differential for the mass

analyzer region. The aperture plate is connected to ground via a 0.5 – 5 MΩ variable resistor to control the acceleration energy of ions exiting the drift cell.

7.2.2.2 Ion Optics System

Ions eluting the drift cell are transferred to the extraction region of an orthogonal, linear time-of-flight mass analyzer by a set of ion optical lenses. The first lens setup is a typical three element einzel lens, described also in Section 4, which is used to focus ions exiting the mobility cell to the TOF extraction source. The dimensions of the einzel lens elements are as follows: lens 1 = 2.92" length, 0.925" inner diameter; lens 2 = 1.545" length, 0.925" inner diameter, lens 3 = 1.14", inner diameter 0.925" tapered down to 0.500" at 0.865" length (lens 3 is the same lens used for both ion optical systems). The spacing between adjacent lenses was 0.075". The voltages to einzel lens 1 and 2 are supplied using 2 channels of a CAEN 4-channel high voltage power supply (Model N472, CAEN Technologies, Inc., Staten Island, NY). The voltage for einzel lens 3 is supplied by a Bertan 5 kV DC supply (Model 325, Bertan; Hicksville, NY). The voltage for einzel lens 3 is also the bias voltage applied to the push, static, and pull plates of the time-of-flight extraction source.

The second optical lens system utilizes a novel combination of exact replicas of the drift electrodes used in the PDC IG drift cell along with a three element einzel lens (Appendix E). The dimensions of the drift electrodes are mentioned above. There are three PDC IG electrodes directly following the exit aperture of the mobility drift cell and we will refer to these as transfer lenses throughout this manuscript. The electrodes are connected via 1 MΩ, high precision resistors (Mouser Electronics; Mansfield, TX) to

ground. The voltage supplied to these electrodes comes from one of the channels of the CAEN 4-channel high voltage DC supply (Model N472, CAEN Technologies, Inc.; Staten Island, NY). The nonlinear electric field produced by the electrode geometry serves to focus radially diffuse ions back to the electrode central axis. This is accomplished by the differences in the radial component of the electric field as a function of radial ion position. The transfer lenses also focus ions well at higher pressures owing to ion-neutral collisions leading to lower ion velocities and thus a greater extent of ion focusing. As ions traverse this region, off-axis trajectory ions from diffusion and collisional scattering will be refocused to the central electrode axis and transmit a high percentage of ions to the three element einzel lens prior to the TOF extraction source.

The second set of lenses is a typical three-element einzel lens to focus ions to a point in the TOF extraction region. The dimensions of the einzel lens element are as follows: lens 1 = 1 inch length, 0.625” inner diameter; lens 2 = 1” length, 0.625” diameter, and lens 3 = 1.14” length, 0.925” inner diameter tapered down to 0.500” at 0.865” length of the lens. The exit to lens 3 has a 3 mm axial slit to define the ion packet spread entering the TOF extraction source. Each lens is spaced 0.1” from the next adjacent lens using precision ceramic spacers (Kimball Physics, Inc.; Wilton, NH). The voltages for the lenses are supplied by the same power supplies listed previously.

The ion focusing of the two lens systems was modeled by SIMION and also tested experimentally.

7.2.2.3 TOF extraction source

The TOF extraction source used in this study is a Wiley-McLaren type utilizing a dual field extraction region. The dual field extraction region is established by three, stainless steel plates which will be referred to as the push, static, and pull plates. The plates are eV parts® purchased from Kimball Physics, Inc. (Wilton, NH). The plates are 0.025" thick, 1.4" length and width. The static and pull plates have an inner diameter orifice of 0.75" with 70 lines-per-inch Nickel grid stretched over the surface to create a defined electric field between the plates. The spacing between the push and static plate is 0.100" while the spacing between the static plate and pull plate is 0.075". The spacing between the plates in the source and the voltage drop between plates from the pulse amplitude defines the dual electric field extraction region. The extraction source is pulsed through an RF circuit shown in Figure 40(a).

The push, static, and pull plates of the extraction source are held at the same negative potential until they are pulsed to extract ions. The source is held at -175 volts by a Bertan Model 325 dual polarity 0 to 5 kilovolt DC power supply (Hicksville, NY). In order to pulse the push and pull plates (depicted in Figure 40(b)), two ± 6,000 V pulse generators (DEI model PVX-4130, Directed Energy, Inc.; Fort Collins, CO) were used in conjunction with two Glassman high voltage power supplies (Model # PS/EH01.5R65L11, Glassman High Voltage, Inc., High Bridge, NJ). The DEI pulse generators have two inputs and one output channel: a –HV input, a +HV input, and a pulse output channel. The push plate uses the positive DEI pulser to achieve a positive polarity pulse. In this setup, the –HV input of the pulser is grounded while the +HV

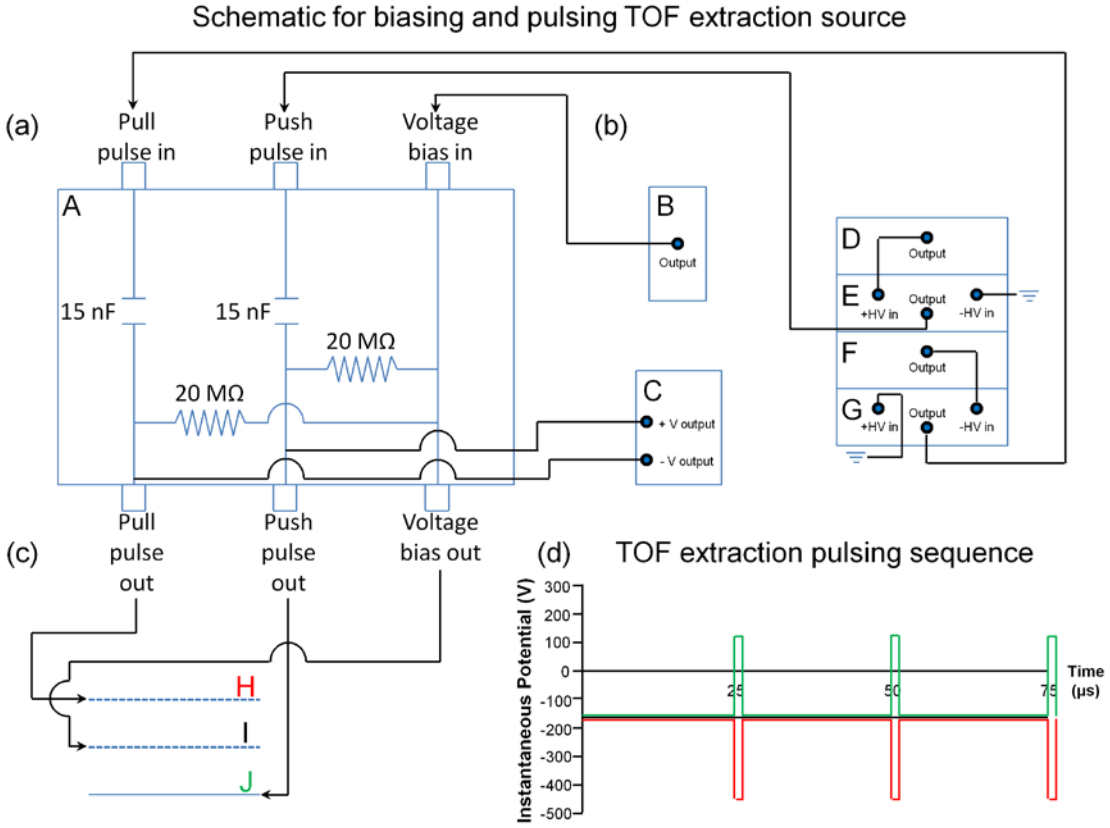

Figure 40. A schematic diagram of the biasing and pulsing of the TOF extraction source. The capacitively coupled box (A) used for pulsing the TOF extraction source is shown in (a). This box has three inputs for the push, pull, and static plates of the source. The pulse generators and power supplies used for the TOF extraction source are shown in (b). The power supplies and pulse generators are as follows: TOF source bias supply (B), baseline shift correction power supply (C), negative (pull pulse) polarity power supply (D), negative pulse generator (E), positive (push pulse) polarity power supply (F), positive pulse generator (G). The TOF extraction source showing the pull (H), static (I), and push (J) plates of the Wiley-McLaren type source are shown in (c). The resulting TOF extraction pulsing sequence is shown in (d).

input receives a positive polarity voltage from the Glassman high voltage power supply. The DEI pulser output stays at ground potential until it receives a trigger to output a pulse to the push plate with an amplitude defined by the Glassman high voltage power supply. Likewise, the pull plate uses a negative pulse from the DEI pulser where the +HV input is grounded while the –HV supply receives a negative potential from the Glassman high voltage power supply. The output from the DEI is ground potential until the trigger induces a negative pulse with an amplitude defined by the Glassman supply. The output channels of the DEI pulsers go to the push pulse in and pull pulse in inputs of the RC circuit shown in Figure 40(a). Even though the DEI pulsers output a ground potential until pulsed, the RC circuit provides the voltage bias from the Bertan supply to the push, static, and pull plates of the TOF extraction source. The pulsing of the plates through the RF circuit causes a baseline shift of the output pulse. The baseline shift can be easily calculated from the equation given below:

$$Baseline\ shift = \frac{Extraction\ pulse\ width}{Time\ between\ extraction\ pulses} \times (100) \times Pulse\ Amplitude \quad (7.2\text{-}1)$$

where the extraction pulse width divided by the time between consecutive extraction pulses can be referred to as the duty cycle of the TOF extraction source (Table 4). The shift in the baseline of the output pulse can be corrected by adding a DC bias voltage to the push and pull pulse outputs (Figure 40(b)). The correction voltage is supplied by a DC power supply (Model TP340A Triple Output DC power supply, Power Designs, Inc.; Westbury, NY) with 100 KΩ resistors in the circuit to shield the power supply from the pulse voltage from the DEI pulser. The push pulse has a negative polarity shift and thus a positive correction voltage is applied while a negative correction voltage must be

applied for the positive polarity shift for the pull pulse. After voltage correction, the output pulses go into the instrument to the push, static, and pull plates as depicted in Figure 40(c). A more comprehensive study of baseline shift correction voltage tests and its effect on mass resolution of the time-of-flight mass spectrometer is shown in the Appendix section (Appendix D).

The TOF extraction source plates are held at -175 V until the push and pull plates receive a pulse from the DEI pulse generators. The pulse generators output a pulse amplitude of ± 300 V. The pulse frequency for the TOF is 40 kHz with a pulse width of 2 µs. This corresponds to a duty cycle of 8 percent. Thus, the baseline shift of the pulse output is ±24 V. This baseline shift is accounted for by a correction voltage of the same amplitude but opposite polarity. The summary of the pulsing sequence with instantaneous potential versus time is shown in Figure 40(d).

Table 4. Table for determining the baseline shift through an RC circuit with parameters of TOF frequency, TOF pulse width, duty cycle, and TOF pulse amplitude to calculate a baseline shift correction voltage. The parameters used for the TOF extraction in this experiment are shown in bold.

Baseline Shift pulsing through RC circuit					
TOF frequency (kHz)	TOF pulse time frequency (µs)	TOF pulse width (µs)	Duty Cycle	Pulse amplitude (V)	Baseline shift (V)
10	100	1	0.01	300	3.00
10	100	2	0.02	300	6.00
10	100	5	0.05	300	15.00
20	50	1	0.02	300	6.00
20	50	2	0.04	300	12.00
20	50	5	0.10	300	30.00
30	33.3	1	0.03	300	9.01
30	33.3	2	0.06	300	18.02
30	33.3	5	0.15	300	45.05
40	25	1	0.04	300	12.00
40	**25**	**2**	**0.08**	**300**	**24.00**
40	25	5	0.20	300	60.00
50	20	1	0.05	300	15.00
50	20	2	0.10	300	30.00
50	20	5	0.25	300	75.00
60	16.7	1	0.06	300	17.96
60	16.7	2	0.12	300	35.93
60	16.7	5	0.30	300	89.82

7.2.2.4 Time-of-Flight Mass Analyzer

Ions focused into the TOF extraction source are accelerated orthogonally into a 22.8 cm linear time of flight mass analyzer. The TOF lining is held at a bias of -5.6 kV. Thus, ions are accelerated with approximately -6.2 keV of kinetic energy towards the TOF detector. The TOF detector is a dual microchannel plate setup with the front MCP held at -6 kV and the back MCP at -3.9 kV. A block diagram of the entire instrument is shown in Figure 41.

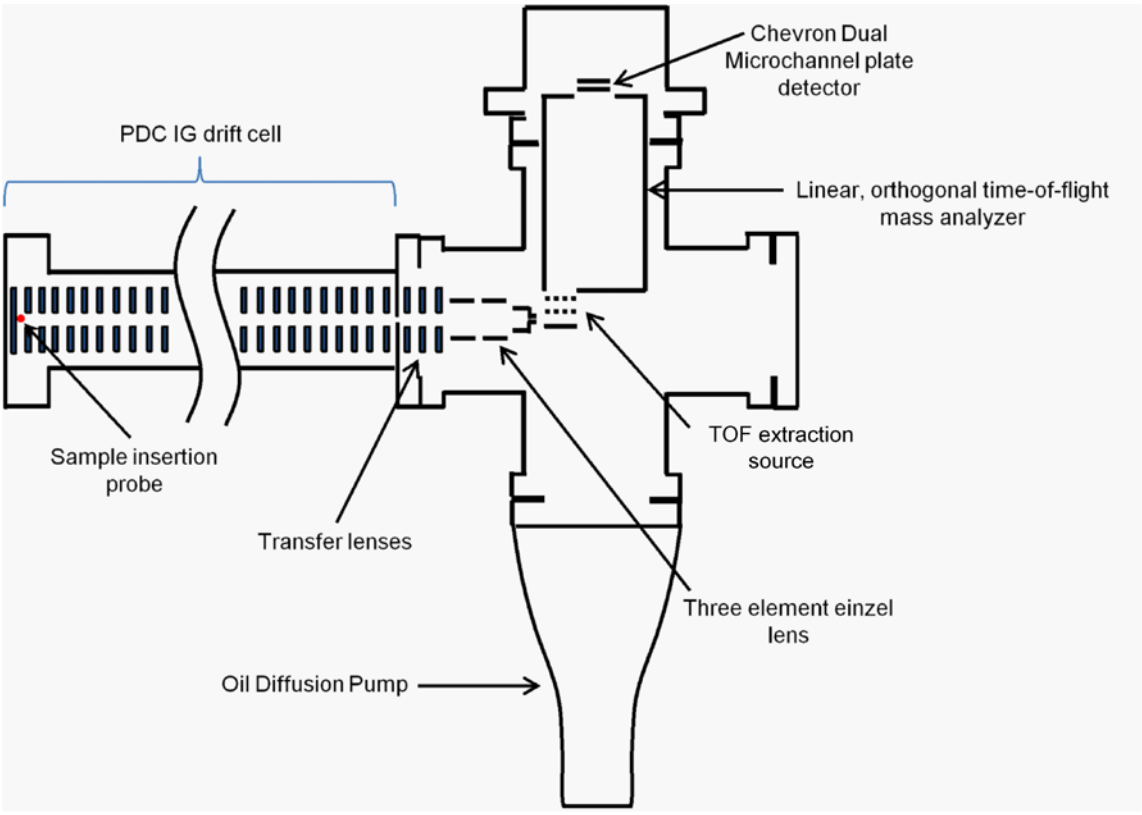

Figure 41. Schematic diagram of the 1.25 meter periodic-focusing DC ion guide ion mobility-orthogonal time-of-flight (PDC IG-IM-oaTOF) mass spectrometer.

7.2.3 SIMION simulations

SIMION version 8.0 (SIS; Ringoes, NJ) simulations were conducted to test the ion focusing and ion transfer capabilities of the two ion optical systems. The collision_hs1.lua user program was slightly modified to incorporate a boundary defined static pressure region followed by a boundary defined linear pressure gradient. After the linear pressure gradient, another boundary defined static pressure region is incorporated to the simulation. The ion used for all simulations is $C_{60}^{\cdot+}$ with an ion-neutral collision cross section of 124 $Å^2$.

7.3 Results and Discussion

SIMION version 8.0 simulations were conducted to compare the ion focusing and ion transfer capabilities of the ion optics systems from the mobility exit to the TOF extraction source. The simulation for the single, three element einzel lens is given in Figure 42. The simulation shows the last 4 drift electrodes of the PDC IG drift cell followed by the mobility exit aperture. The next electrode is a portion of the flange which is at ground potential followed by the three element einzel lens prior to the TOF extraction source. The first pressure boundary is from the first drift electrode shown in the simulation to the mobility exit aperture. The pressure of helium gas in this boundary is 1 torr. The second pressure boundary is from the mobility exit aperture to the end of the first lens. The pressure in this region is simulated as a linear pressure gradient from 1 to 1 x 10^{-4} torr. This pressure was estimated from the conductance limit of the aperture along with the conductance limit provided by the first einzel lens (the einzel lens is

positioned closely to the backside of the aperture plate). In the third boundary region the pressure is considered to be 1×10^{-4} torr.

The simulation in Figure 42(a) reveals that ions do not have sufficient kinetic energy to overcome the potential barriers created by the fringing fields at the edges of the einzel tube lenses. The kinetic energy is critical owing to the ion-neutral collisions that decrease ion velocity in the field free region of the einzel tube lenses. This is especially apparent from the ion trajectories in the first einzel lens. As ions experience collisions with the neutral drift gas molecules in this high-pressure region ion velocities decrease and collisional scattering and ion diffusion begin to dominate the ion motion. Ions can still be accelerated by the decrease in potential (potential well depth) and refocused into the second einzel lens by the fringing electric fields but will be decelerated by the last einzel lens element. The decrease in initial velocity from ion-neutral collisions in the first einzel lens requires an increase in post-mobility acceleration to result in higher ion transmission.

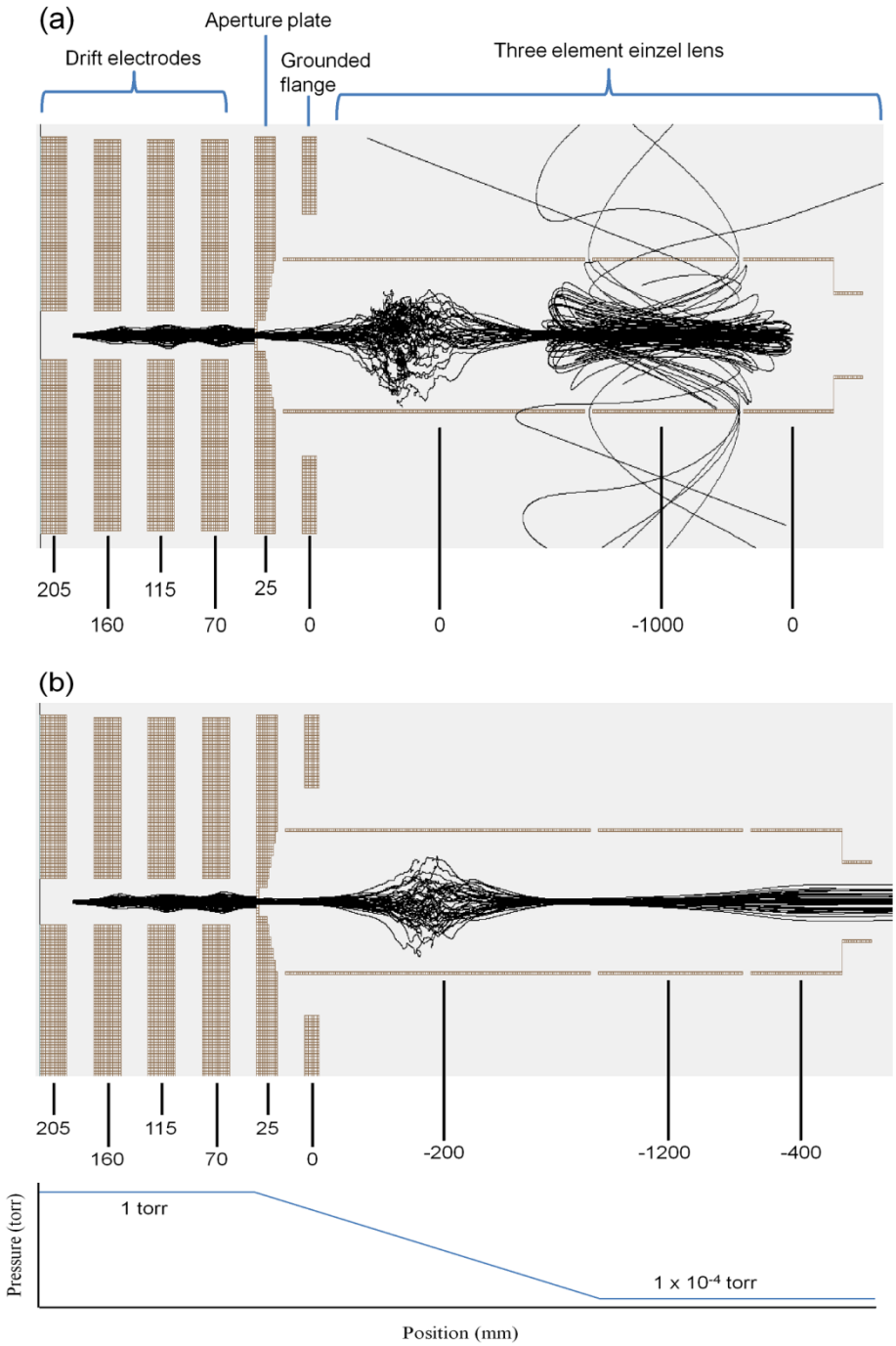

Figure 42. SIMION simulation depicting ion transmission through a typical, three element einzel lens after exiting the mobility drift cell and prior to TOF extraction. The electrodes and potentials applied to said electrodes are depicted in (a) and (b).

The post-mobility acceleration is increased by 400 eV in Figure 42(b). Initially ions are accelerated with 225 eV of kinetic energy from the potential drop from the aperture plate to the entrance to the first einzel lens. This is an increase of 200 eV compared to the simulation in Figure 42(a). The increased initial kinetic energy (and ion velocity) leads to less ion diffusion in einzel lens 1; however, diffusion is still prevalent in the ion trajectories shown in Figure 42(b). An increase in the potential well depth of einzel lens 2 (from -200 V in (a) to -1200 V in (b)) refocuses diffuse ions owing to the fringing electric fields penetrating into einzel lens 1 and also serves to reaccelerate low velocity ions toward einzel lens 3. Einzel lens 3 defines the final 200 eV of acceleration from the mobility cell to the TOF extraction region. This acceleration energy is sufficient to transfer ions to the TOF; however, broadening of the ion packet in both simulations owing to diffusion in einzel lens 1 degrades the mobility resolution.

Experimental data reveals that the spatial spreading of the ion packet in the einzel lens degrades mobility resolution regardless of the potentials applied to the einzel lens and the overall laboratory frame acceleration energy from the mobility cell exit to the TOF extraction region. The mobility resolution is consistently between 30-50 for the radical cation signals of C_{60} and C_{70} (data not shown). Moreover, when the entire einzel lens setup is kept at ground, the mobility resolution is relatively unchanged. This suggests that the lens system does a very poor job of focusing ions into the TOF extraction region and that a pneumatic focusing effect from the pressure differential from the mobility cell exit to the TOF extraction region is more responsible for transferring ions than the einzel lens system itself.

The second optical lens design utilizes transfer lenses, exact replicas of the PDC IG drift electrodes, in conjunction with a three-element einzel lens of shorter length than the previous design. The same pressure boundaries were used in the simulation with the drift cell at a pressure of 1 torr. After the mobility exit aperture, a pressure boundary is defined until the first einzel lens element. The pressure in this region is defined as a linear gradient from 1 torr to 1 x 10^{-6} torr. This pressure gradient is estimated from the conductance limit of the mobility aperture and the space between lenses providing access for the diffusion pump to evacuate gas molecules exiting the drift cell. After this boundary, the pressure is considered to remain at 1 x 10^{-6} torr.

The transfer lenses serve to refocus radially diffuse ions in the high pressure region (similarly to the focusing provided in the drift cell). The thickness of the lens and the velocity of the ions play a key role in ion focusing. In the previous design, the first tube lens is very thick (2.92”) and has a significant field free region in the center of the lens. The thinner PDC IG replica electrodes have a much smaller field free region before the next electrode and thus the decrease in ion velocity is less pronounced. Furthermore, the PDC IG replica electrodes utilize fringing electric fields that create effective potentials at the electrode entrance and exit that focus collisionally scattered (radially divergent) ions back to the central axis of the lens system.

After this higher pressure region, a set of einzel lenses of shorter lengths are used to focus ions into the TOF extraction source (Figure 43). The pressure in this region is considered to be 1 x 10^{-6} torr, a more optimum pressure for the vacuum focusing of an einzel lens system. At high vacuum, ions travelling through the einzel lens do not experience a high collision frequency with gas molecules as in the previous design. This results in less collisional scattering and higher velocity ions through the lens system. Thus, less overall kinetic energy is required to transfer ions through the einzel lens system. Furthermore, higher velocity ions and a shallower potential well in the second einzel lens decreases the magnitude of effective potentials felt at the entrance and exit of each einzel tube lens and ion trajectories become less divergent. The major advantage of this optical design is that ions do not experience collisional scattering and diffusion in the high pressure region immediately following the mobility exit aperture. This leads to less overall diffusional broadening of the ion packet in the transfer region between the mobility drift cell and the TOF extraction region and maintains the fidelity of the eluting ion packet profile quite well.

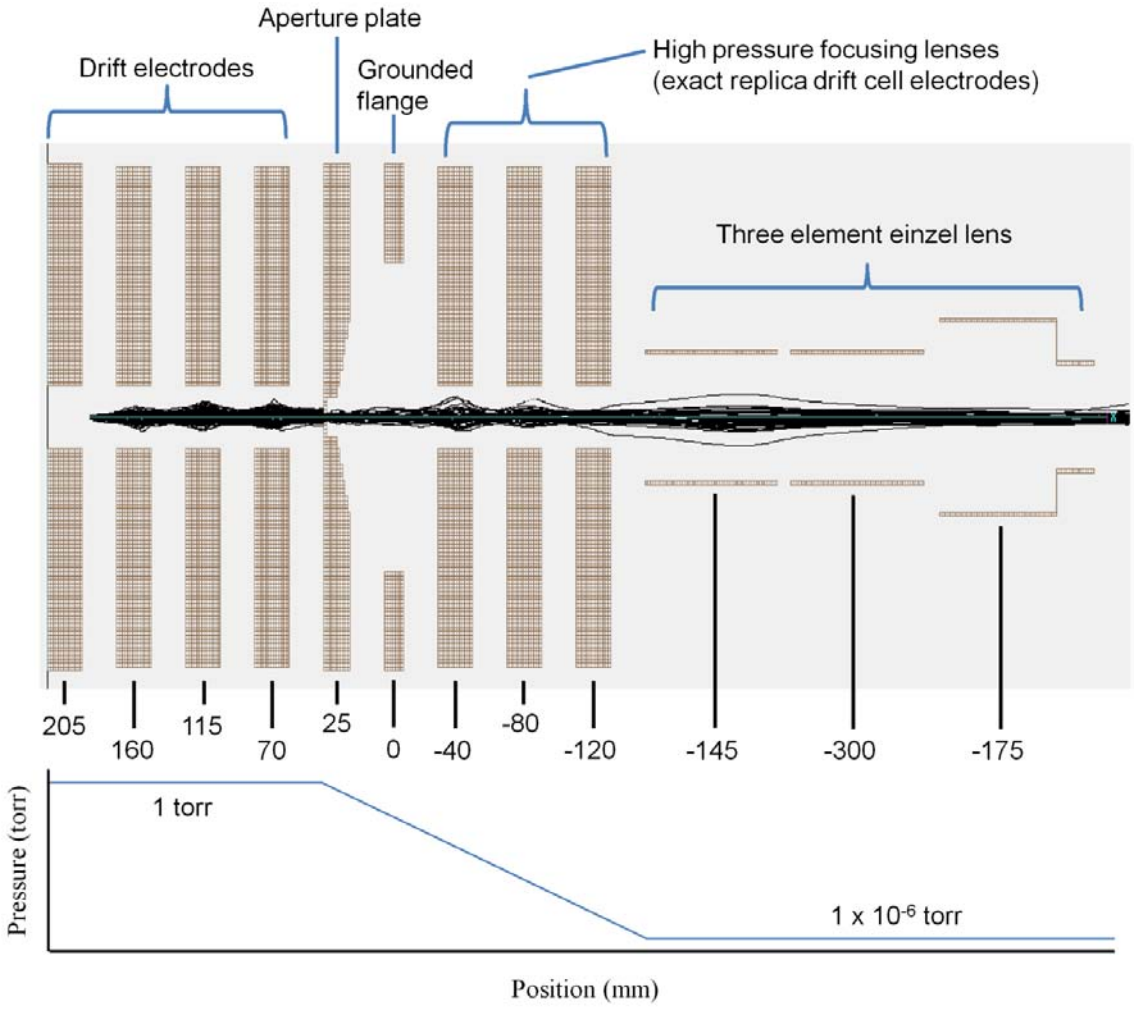

Figure 43. SIMION simulation depicting ion transmission through a novel combination of transfer lenses (PDC IG electrodes) and a three element einzel lens. The pressure profile with respect to position is also provided.

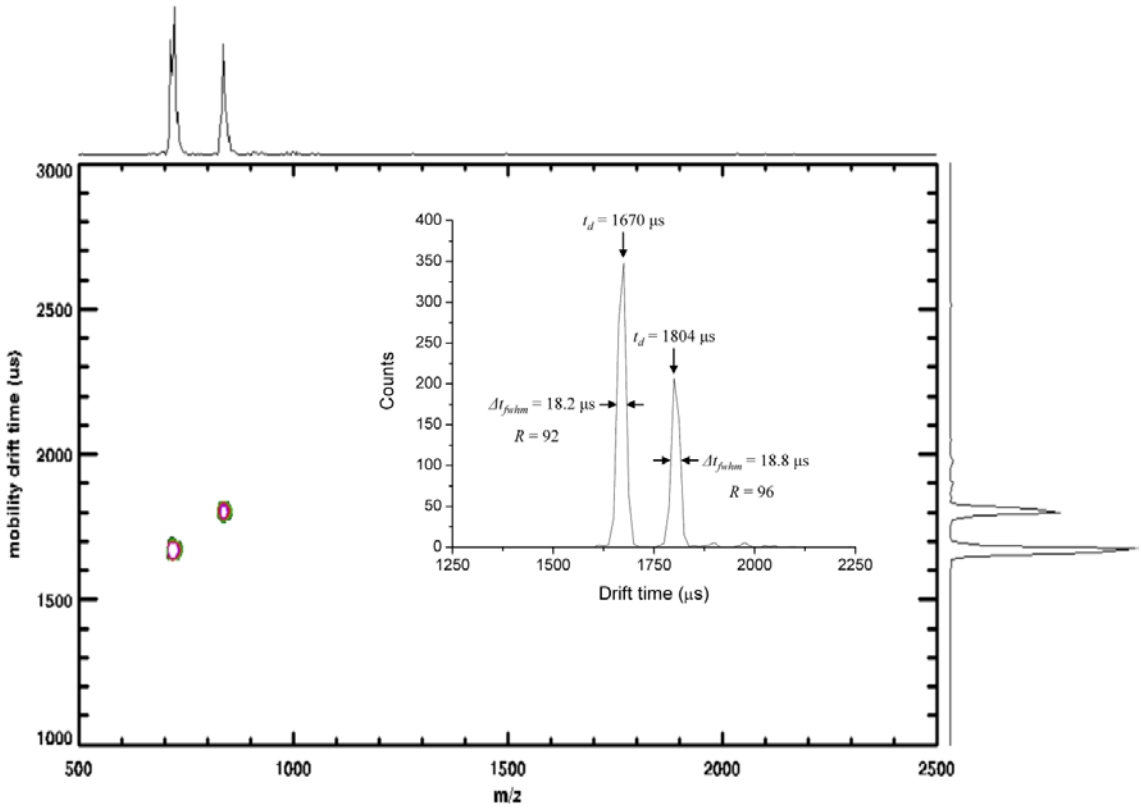

Figure 44. Two-dimensional mobility-mass plot of a fullerene mixture with mobility drift time on the y-axis and *m/z* on the x-axis. The ion signals are completely baseline separated by mobility and their identification is confirmed by mass in the time-of-flight mass analyzer. The figure inset shows the single dimension ion mobility spectrum. The inset shows the drift time and peak width at half maximum of the ion signals for $C_{60}^{\bullet+}$ and $C_{70}^{\bullet+}$, corresponding to a mobility resolution of 92 and 96.

The experimental result for the second optical lens design is shown in Figure 44. The figure depicts the two dimensional mobility-mass spectra showing the ion signals for $C_{60}^{\bullet+}$ and $C_{70}^{\bullet+}$ and a figure inset showing the one-dimensional mobility spectrum. The experimental parameters for the mobility separation are as follows: applied drift voltage of 4600 V, He drift gas pressure of 1.87 torr (slightly higher than 1 torr used in the simulation in Figure 43), resulting in an *E/p* of 19.7 $Vcm^{-1}torr^{-1}$. Ions are accelerated

with 25 eV of laboratory frame energy upon exiting the PDC IG drift cell. Ions then traverse the differential pressure region where focusing occurs from the novel combination of ion optics. The voltages applied to the lens elements are as follows: -41 V on transfer lens 1, -82 V on transfer lens 2, -123 V on transfer lens 3, -142 V on einzel lens 1, -300 V on einzel lens 2, and -175 V on einzel lens 3. The potentials applied for the experimental data are nearly the same as the potentials used for the simulation in Figure 43. The experimental result in Figure 5 confirms the focusing capabilities of the novel combination of ion optics. The ion signals for $C_{60}^{\bullet+}$ and $C_{70}^{\bullet+}$ in Figure 44 are completely baseline separated and the experimental mobility resolution calculated from the drift time divided by the time width at half maximum corresponds to 92 and 96, respectively. It appears that there is minimal degradation of the ion packet profile and hence the mobility resolution in the ion transfer region between the mobility cell exit and the orthogonal TOF extraction source.

To further demonstrate the high resolution capabilities of the PDC IG and efficient ion transfer to the TOF extraction region a mixture of two model peptides, Bradykinin and Angiotensin I, is presented in Figure 45. The experimental parameters for the mobility separation are as follows: applied drift voltage of 4500 V, He drift gas pressure of 1.48 torr, resulting in an *E/p* of 24.3 $Vcm^{-1}torr^{-1}$. The decrease in drift gas pressure is associated with the slight increase in ion mass resulting in increased collision frequency. To achieve similar focusing capabilities of the PDC IG (mobility resolution and ion transmission) the drift gas pressure must be lowered to increase the ion axial

velocity through the PDC IG. The radial focusing capabilities of the PDC IG and the effects of ion mass and ion axial velocity are presented in a previous publication.

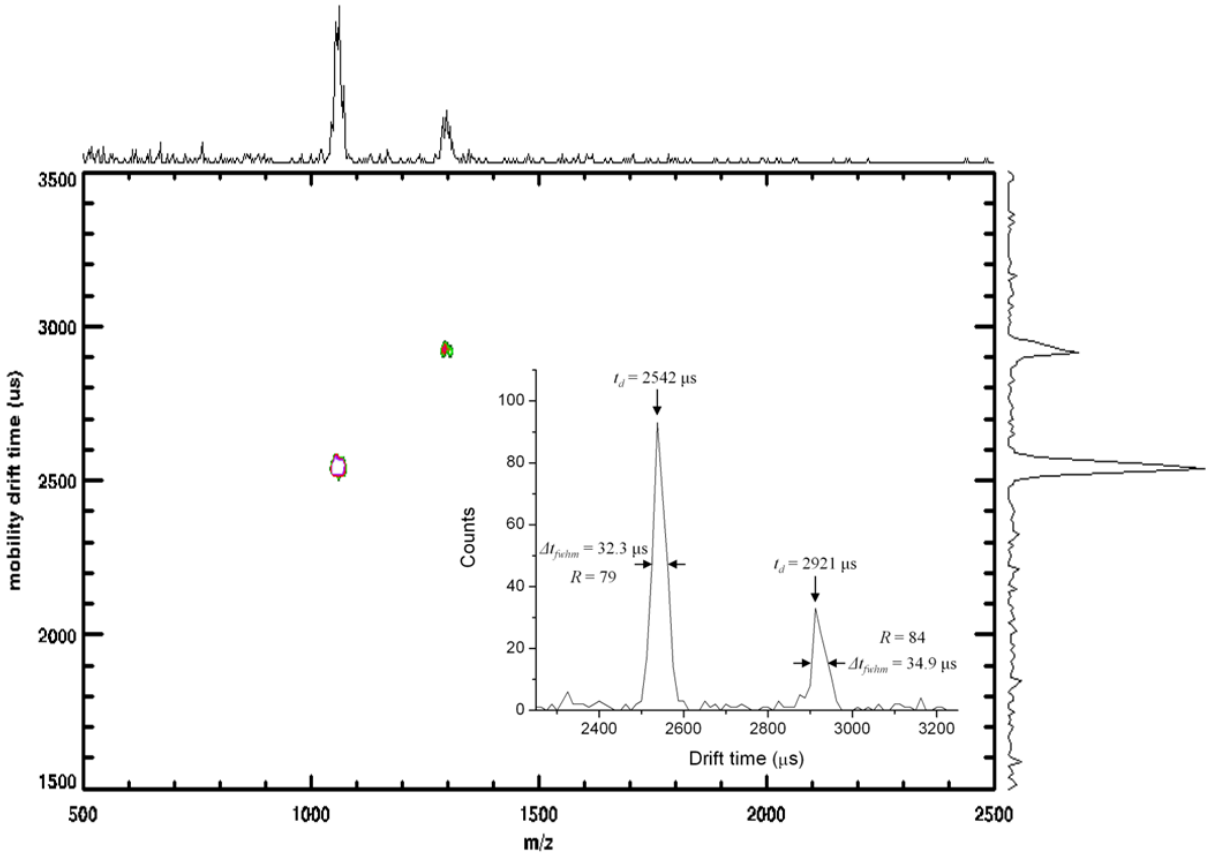

Figure 45. Two-dimensional mobility-mass plot of a peptide mixture of Bradykinin and Angiotensin I. The figure inset shows the single dimension ion mobility spectrum. The drift time and peak width at full width half maximum for Bradykinin and Angiotensin I correspond to a mobility resolution of 79 and 84, respectively.

Ions are again accelerated with 25 eV of laboratory frame energy when exiting the PDC IG drift cell. The potentials applied to the lens elements are the same as those stated above for the separation of the fullerene radical cations. The experimental result from the inset of Figure 45 reveals a mobility resolution of 79 and 84 for Bradykinin and

Angiotensin I, respectively. The slightly lower resolution for these peptide ions may be a result of interconverting ion conformers in the drift cell.

Finally, a higher mass peptide ion in ACTH clip 18-39 is presented in Figure 46. The experimental parameters for the mobility separation are as follows: applied drift voltage of 4780 V, He drift gas pressure of 1.22 torr, resulting in an *E/p* of 33.7 $Vcm^{-1}torr^{-1}$. Ions are accelerated from the mobility exit with the same energy as the previous experimental data, however, the increase in mass requires a change in potentials applied to the novel focusing optics employed. The applied potentials are as follows: -48 V on transfer lens 1, -96 V on transfer lens 2, -144 V on transfer lens 3, -300 V on einzel lens 1, -700 V on einzel lens 2, and -175 V on einzel lens 3. Specifically, the potentials on the transfer lenses are increased increase ion axial velocity in this region for better ion focusing as well as increasing the potential well depth of einzel lens 2 for better point focusing of ions to the TOF extraction source. The mobility resolution calculated for the ion mobility signal in the inset of Figure 46 is 121. According to equation 1 using the experimental parameters for this experiment, the diffusion limited resolution is calculated to be 129. This is a prime example of the high resolution capabilities of the PDC IG drift cell.

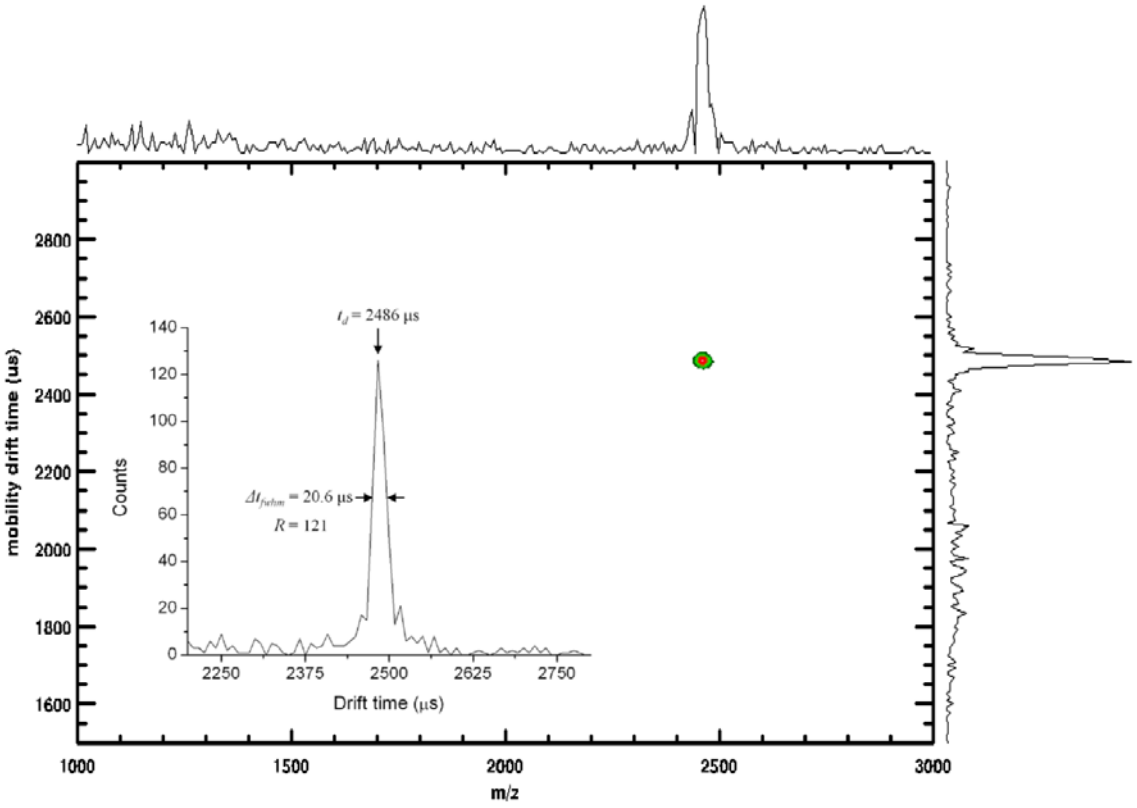

Figure 46. A two-dimensional mobility-mass plot of the peptide ACTH 18-39. The figure inset shows the signal for the single-dimension ion mobility spectrum. The drift time and peak width at full width half maximum of the ion signal of ACTH 18-39 correspond to a mobility resolution of 121.

Another important point to note is the increase in mobility resolution with increasing ion mass (evidenced by the high resolution value for ACTH clip 18-39). This observation confirms what is predicted by the theoretical spreading of an ion cloud through a drift cell. The spreading of an ion cloud is defined by the equation

$$\frac{|\bar{x}|}{L} = \left(\frac{4D}{\pi v_d L} \right)^{1/2} \tag{7.3-1}$$

where L is drift length, D is the diffusion coefficient, v_d is drift velocity, and x is the distance of spread from the center of the ion cloud (in one direction). The drift velocity term in equation 7.3-1 can be eliminated by substitution from the following equation.

$$v_d = \frac{L}{t_d} \tag{7.3-2}$$

After substitution and rearrangement equation 7.3-1 becomes

$$\frac{|\bar{x}|}{L} = \left(\frac{4Dt_d}{\pi L^2} \right)^{1/2} \tag{7.3-3}$$

and now multiplying both sides by L eliminates L from the equation. The term $(4/\pi)^{1/2}$ can be denoted as a constant, which will be referred to as A. Thus, the equation becomes

$$|\bar{x}| = A(Dt_d)^{1/2} \tag{7.3-4}$$

where it can be seen that the spreading of the ion cloud is dependent on the diffusion coefficient of the ion in the drift gas and the drift time of the ion. For increasing ion mass within the same chemical family, drift time increases while the diffusion coefficient decreases. The decreasing diffusion coefficient coupled with the square root relationship of the product of the diffusion coefficient and drift time lead to higher resolution for high mass ions. For example, even if the diffusion coefficient remained constant for a high mass versus low mass ion and the drift time was doubled the mobility resolution would still increase by the square root of two.

There are instrumental limits, however, to mobility resolution in relation to ion mass. As ion mass increases the electric field must be increased or drift gas pressure decreased to maintain proper ion axial velocity to achieve the radial focusing properties

of the PDC IG. This is evident from the two-dimensional mobility-mass plot of a mixture of ACTH clip 18-39 and Insulin (Figure 47). The mobility resolution of the insulin ion signal is low owing to mitigated radial focusing properties of high mass ions.

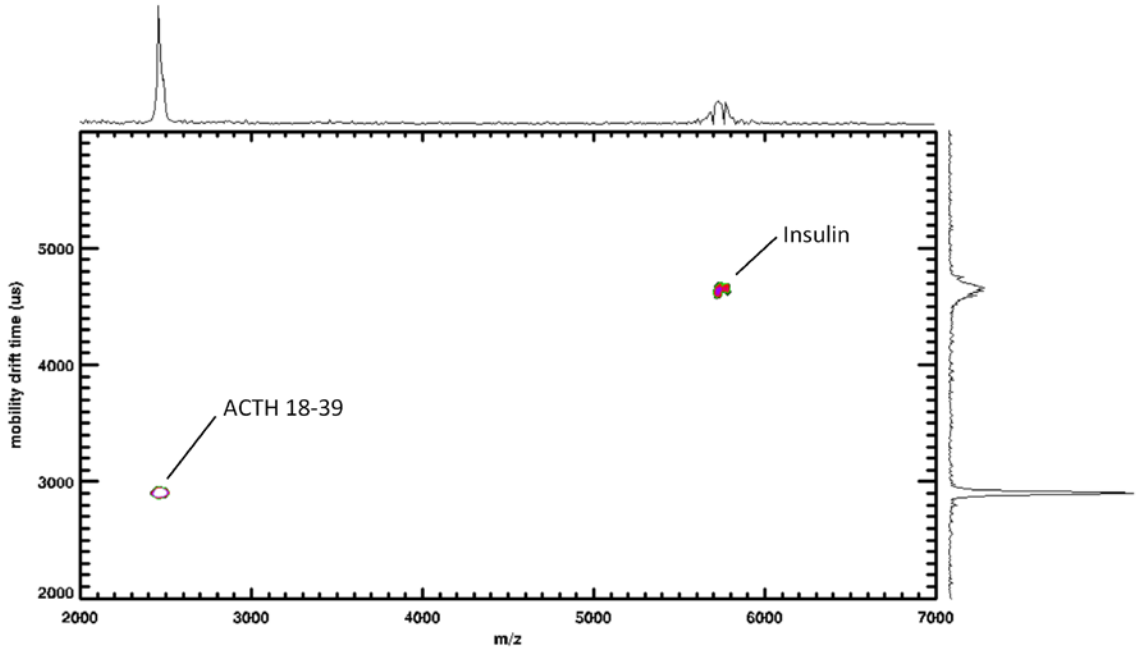

Figure 47. A two-dimensional mobility-mass plot of ACTH clip 18-39 and Insulin.

7.4 Conclusion

A novel combination of ion optics for ion transfer from the mobility cell exit aperture to a TOF extraction source is presented. Employing PDC IG electrode geometries over the high pressure region of the differential pressure region maintains the fidelity of the mobility peak profile and transfers ions to a set of three short einzel lenses for ion focusing into the TOF extraction source.

The optical interface region was tested with SIMION simulations as well as experimentally. SIMION simulations reveal much more efficient ion transfer to the TOF extraction region with the novel design over a simple three-element einzel lens. This is owing to the large field free region in the center of a long lens where the fidelity of the mobility peak profile is lost from diffusion of the ion cloud and collisional scattering of ions off the neutral drift gas. The novel ion optics design continues to radially focus ions, much like in the PDC IG drift cell, until a sufficient pressure is reached to employ an einzel lens system.

Experimentally, the efficiency of the novel ion optical design is confirmed from the high mobility resolution for a number of analytes. In fact, the mobility resolution is increased for fullerene radical cations in the IM-MS design presented here compared to the previous IMS design presented in Section 3. The mobility resolution of the radical cations of C_{60} and C_{70} is 92 and 96, respectively, compared to ~80 in the previous IMS design in Section 3. This is most likely attributed to the long field free region inside the tube lens employed in the previous IMS design. High mobility resolution was also attained for the protonated molecules Bradykinin and Angiotensin I, 79 and 84. A higher mass peptide, ACTH clip 18-39 yielded a mobility resolution of 121, near the theoretical diffusion-limit of 129.

8. A NOVEL, MODULAR ION MOBILITY DRIFT CELL

8.1 Introduction

Tandem mass spectrometry utilizes two stages of mass analysis: 1) a mass selection stage followed by ion activation and dissociation and 2) a mass analysis stage of the fragment ions produced by ion activation and dissociation of the mass selected precursor [208]. Tandem MS has been performed with a variety of mass analyzers including hybrid sector instruments [209-210], sector/quadrupole instruments [211], triple quadrupole instruments [212], FT-ICR instruments, and TOF/TOF instruments. Ion activation and dissociation is also possible through a variety of methods including collision-induced dissociation (CID) [213-217], surface-induced dissociation (SID) [218-219], photodissociation (PD) [220], electron capture dissociation (ECD) [221] and electron transfer dissociation (ETD) [222].

Tandem MS has been advantageous in ion structural elucidation from characteristic fragment ions from a precursor ion. The advent of ESI and MALDI opened a new avenue for tandem MS as a tool for biomolecule analyses-especially in the field of proteomics through amino acid sequencing of peptides and proteins [223]. Peptide fragment ion nomenclature has been established by Biemann according to the position of bond dissociation along the peptide backbone or amino acid side chains [224].

Ion mobility spectrometry coupled with tandem MS provides increased information in structural elucidation through ion-neutral collision cross section

information and fragment ion spectra. However, the availability of IM-MS/MS instrumentation is limited. In-house built instrument designs have been employed to incorporate IM-MS/MS technology. Previously, our laboratory incorporated surface-induced dissociation (SID) after ion mobility separations for ion activation and dissociation of mobility separated ions [188, 225-226]. The mass analyzed fragment ions all have the same mobility drift time, drastically simplifying data interpretation. Similarly, modifications in an interface region between the mobility cell exit and TOF extraction region of a commercial MALDI-IM-oaTOF-MS were made to incorporate collision-induced dissociation (CID) of mobility separated ions prior to TOF MS analyses [227-228]. Elsewhere, post-mobility CID has also been performed with a quadrupole-octapole collision cell where the quadrupole serves to transmit all ions exiting the mobility cell to the octapole where ions are activated and dissociated prior to mass analysis by an orthogonal-acceleration reflectron TOF-MS [229-230].

The Clemmer Laboratory at the University of Indiana has built tandem IMS-MS instruments where mobility selected ions separated in the first IMS stage can be activated and dissociated in an RF ion funnel and the fragment ions can be injected into the second IMS stage for mobility separation followed by TOF MS analyses[122]. Fragment ion structures can now be analyzed in the second IMS stage and subsequently confirmed by mass in the orthogonal-acceleration TOF mass spectrometer. Identification of cyclical versus non-cyclical fragment ions has been achieved with this instrument [231].

The structural information provided by IMS can be a powerful tool when combined with molecular dynamics simulations, hydrogen-deuterium exchange experiments, and tandem mass spectrometry. All of these techniques are complementary in that they provide a different angle, or viewing perspective, of the structural integrity of the ion of interest. However, the capabilities of these techniques in one instrumental platform is quite limited. In fact, the Waters Synapt G2 and original Waters Synapt HDMS are perhaps the only commercially available products with the availability of IMS separations with tandem mass spectrometry.

In this section a modular, PDC IG drift cell is coupled to the ABI Sciex QSTAR Pulsar, a commercial quadrupole-time-of-flight (qTOF) mass spectrometer. The instrumental capabilities of the triple quadrupole plus the high mass resolution orthogonal-acceleration reflectron TOF increase the experimental capacity after the dispersive IMS separation. Capabilities include ion activation and dissociation along with ion trapping for ion-ion reaction experiments of mobility separated ions.

8.2 Experimental

8.2.1 Chemicals

Two model peptides were used in the study of the modular, PDC IG drift cell. The peptide, ALILTLVS (MW = 828.5 Daltons) was provided by ABI Sciex and is a common calibration peptide for the QSTAR instrument. The peptide was dissolved in 49.5 % water, 49.5 % methanol, and 1% acetic acid solution (1 M) at a concentration of 1×10^{-5} M. The model peptide Bradykinin (MW = 1295.7 Da) was purchased from American Peptide Company, Inc. (Sunnyvale, CA) and used without further purification.

The peptide was dissolved in the same solution conditions as ALILTLVS at a concentration of 7.7 x 10^{-5} M.

8.2.2 Instrument

The instrument consists of an ABI Sciex Q-star Pulsar commercial q-TOF mass spectrometer (Figure 48) and a home-built electrospray ion-funnel source and modular, periodic-focusing DC ion guide drift cell. One of the motivations for such a design is the versatility of a triple quadrupole time-of-flight instrument. The overall goal for this instrument is to be able to mobility-select an ion of interest and perform further experiments with the advantages provided by the qTOF commercial mass spectrometer.

The potential experiments that can be performed on the proposed instrument include, but are not limited to, ion activation and dissociation via collision induced dissociation (CID) of mobility-selected ions, ion-neutral and ion-ion chemistry, and electron transfer dissociation (ETD) performed in the Q_2 quadrupole. The CID experiment of mobility-selected ions can be performed without any instrument modifications. To perform ion-neutral and ion-ion chemistry along with ECD in the Q_2 quadrupole, modifications may be required for the end caps of the Q_2 Pulsar quadrupole. Moreover, a second ion source and polarity switching of the power supplies is required to introduce ions of opposite polarity into the instrument to be trapped simultaneously with the analyte ion in Q_2. This has been demonstrated by McLuckey and coworkers in a number of publications on a variety of triple-quadrupole mass spectrometers [232-236], including the ABI Sciex QSTAR XL [237-239]. A second ion source could be added at the entrance to

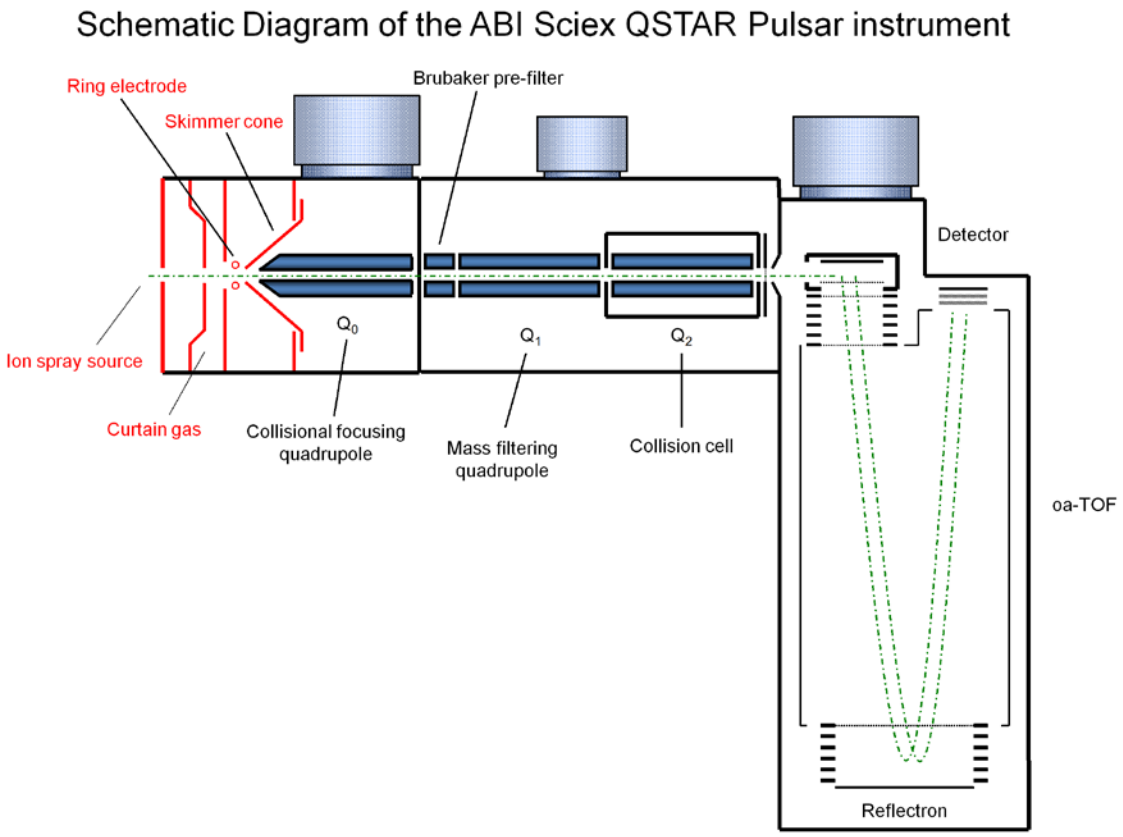

Figure 48. A schematic diagram of the ABI Sciex QSTAR pulsar q-TOF instrument with the important components of the instrument labeled. The text and instrument portions highlighted in red are electrodes and regions requiring modification for mounting the electrospray ion funnel source and modular, PDC IG drift cell to the commercial instrument.

the heated capillary for experiments requiring dual polarity ion trapping for ion-ion reactions.

The commercial Ionspray® source was removed from the instrument as well as the ring electrode and skimmer cone in front of Q_0, the focusing quadrupole that serves to collisionally cool and focus ions after the electrospray source and into the Q_1 quadrupole. An adapting flange similar to the flange for the Ionspray® source was

designed and machined to couple the modular ion mobility drift cell to the vacuum chamber, housing the quadrupoles, near Q_0 (Figure 49).

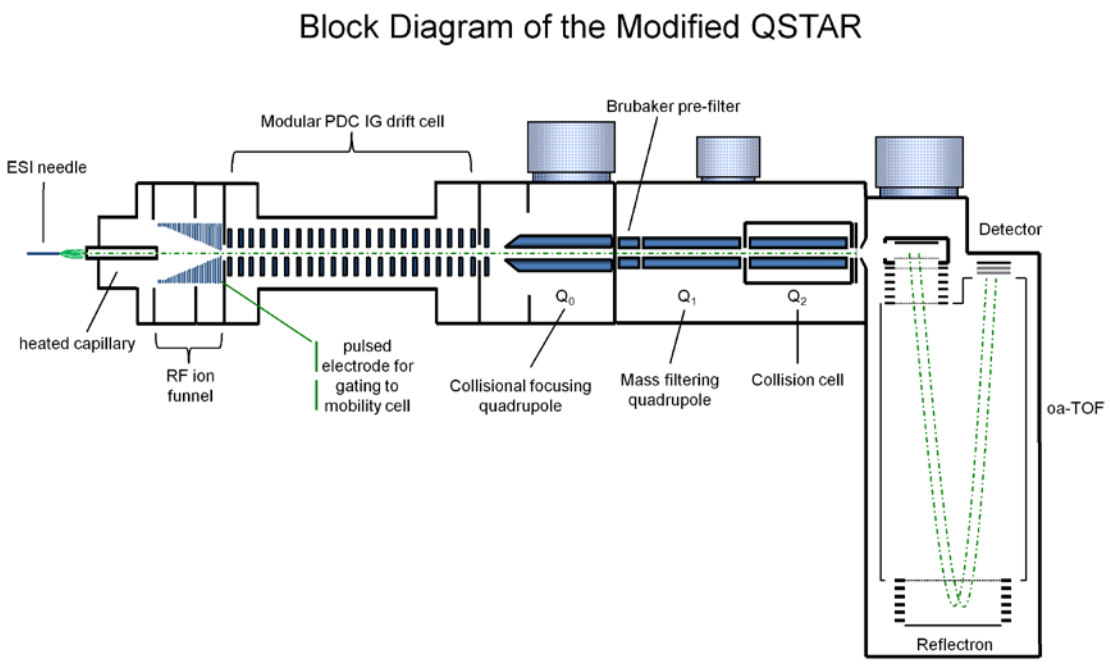

Figure 49. A schematic diagram of the modified QSTAR showing the electrospray ion funnel source and modular PDC IG drift cell coupled to the commercial instrument.

8.2.3 Electrospray Source

A 70 micrometer pulled capillary (Polymicro Technologies, Phoenix, AZ) was used for the electrospray source. The capillary tip was pulled by a method utilizing a blow torch to heat the capillary while under tension from a weight suspended from the bottom of the capillary. As the capillary is heated, it begins to weaken and pull apart. The break in the capillary serves as a pulled tip for the electrospray process. The pulled

capillary is placed in a vice made from Macor® mounted on an x, y ,z – translational stage to control the physical orientation of the electrospray needle. Ions are sprayed from atmosphere into a heated capillary (Finnigan P/N 70005-P803F, Thermo Scientific) for ion transfer to the RF ion funnel and desolvation of ions. The heated capillary is 4.50” (11.4 cm) in length with a 0.40 mm inner diameter. Operating temperature of the capillary is 75 degrees Celsius for all experiments presented. The end of the heated capillary is positioned at the first electrode of the RF ion funnel.

8.2.4 RF Ion Funnel

The RF ion funnel is constructed from 39 stainless steel electrode eV Parts® plates (Kimball Physics, Inc., Wilton, New Hampshire). The electrodes are 0.025” (0.64 mm) in thickness with varying inner diameters. The spacing between electrodes in the funnel is also 0.025” (0.64 mm), resulting in an overall length of 1.90” (48 mm). The first 15 electrodes of the ion funnel have the largest inner diameter of 1” (25.4 mm) while the last electrode of the funnel with the smallest inner diameter is 0.085” (2.15 mm). The inner diameters of the electrodes are tapered down in a manner that the overall angle of the ion funnel is 33 degrees.

The ion funnel must receive both DC and RF voltages. The DC voltage provided by a CAEN 4-channel high voltage power supply (CAEN Technologies Inc., Staten Island, New York) is needed for a voltage gradient to provide an electric field to accelerate ions through the funnel. The RF voltage (Ardara 2 channel RF power supply, Ardara Technologies, Ardara, Pennsylvania) focuses ions through the funnel to increase ion transmission. The RF frequency of the supply is set to 880 kHz. The electrodes of

the ion funnel are connected via 11 MΩ resistors (±5 %, acquired from Texas A&M University Physics Electronics Shop) establishing a DC voltage gradient across the ion funnel, and 1000 pF (±5 %, 1 kV rating, Mouser Electronics, Mansfield, Texas) capacitors for the RF voltage. The RF voltage applied to adjacent electrodes is 180 degrees out of phase; electrode 1 and 3 would be at the same phase while electrodes 2 and 4 would be out of 180 degrees out of phase.

An electrically isolated electrode, termed the orifice plate (0.025" (0.64 mm) thickness, 2.15 mm inner diameter), directly follows the RF ion funnel. The orifice plate can function much like a Tyndall gate. The plate can be pulsed to gate ions into the mobility drift cell to determine mobility arrival time distribution information. The pulse voltage for the gate is supplied by a DEI PVX-4150 high-voltage pulse generator (Directed Energy Inc., Fort Collins, Colorado) with the +HV input voltage provided by one channel from a CAEN 4-channel high voltage power supply and the –HV input voltage provided by a Glassman high voltage DC power supply (Model EH1.5R65L, Glassman High Voltage, Inc., High Bridge, New Jersey).

8.2.5 Modular, PDC IG Drift Cell

One of the priorities was to fabricate a modular drift cell that could couple individual modules, or sections, for easy variation of drift length while also having the capability to incorporate the drift modules to a variety of commercial ionization sources or mass spectrometers. The modular, PDC IG drift cell is constructed from two Delrin® flanges designed in house. The AutoCAD drawing of the Delrin® flange is shown in the appendix (Appendix F). The exterior side of the flange (pre- and post-mobility) has a 6"

Con-flat knife edge for mating to a variety of commercial ion sources and mass spectrometers. The Delrin® flange has two ¼”-NPT pipe thread fitting tapped holes for pumping and pressure monitoring ports. The flange is also equipped with a hole to mount hermetically sealed MHV feedthroughs (Surplus Sales of Nebraska; Omaha, NE). The hermetically sealed MHV feedthrough center conductors are soldered to nickel plated copper wire. The copper wire is then used to create electrical contact with the first and last electrode of the drift cell electrode stack.

The drift electrodes have the following dimensions: 6.35 mm (0.25”) thickness, 6.35 mm spacing from adjacent electrode, and 8 mm inner diameter. The 6.35 mm spacing between electrodes is established from 8 mm diameter precision ceramic balls (grade 25, high alumina nonporous ceramic, McMaster-Carr; Robbinsville, NJ). The electrodes are connected by 1 MΩ resistors (Mouser Electronics; Mansfield, TX) to establish the electric field across the drift cell. The first and last electrodes of the electrode stack for each module is a top-hat design that snaps into the orifice hole of the Delrin® flange to aid in compression of the electrode stack. The first modular drift cell design is composed of 28 electrodes with an overall drift length of 35 centimeters.

The improved modular, PDC IG drift cell is composed of 17 electrodes with dimensions: 6.35 mm (0.25”) thickness, 6.35 mm electrode spacing, and 8 mm inner diameter. The electrodes are separated with ~8 mm diameter precision ceramic balls (grade 25, high alumina nonporous ceramic, McMaster-Carr, Robbinsville, NJ) with an overall drift length of 21 centimeters. An electric field is established by applying a

voltage across the electrode stack connected via 1 MΩ, high precision resistors (Mouser Electronics, Mansfield, TX).

8.3 Results and Discussion

The first experiments performed on the modified instrument involved a peptide of sequence ALILTLVS (MW = 828.5 Daltons), normally used for calibration of the ABI Sciex QSTAR Pulsar. The concentration of the peptide solution was 1 x 10^{-5} M. The experiment looked at the effects of injection energy, or laboratory frame acceleration energy from the mobility cell exit into the Q_0 quadrupole. The experimental parameters used for the experiment are shown in Table 5 along with a schematic depicting pertinent electrodes and regions of the instrument listed in the table.

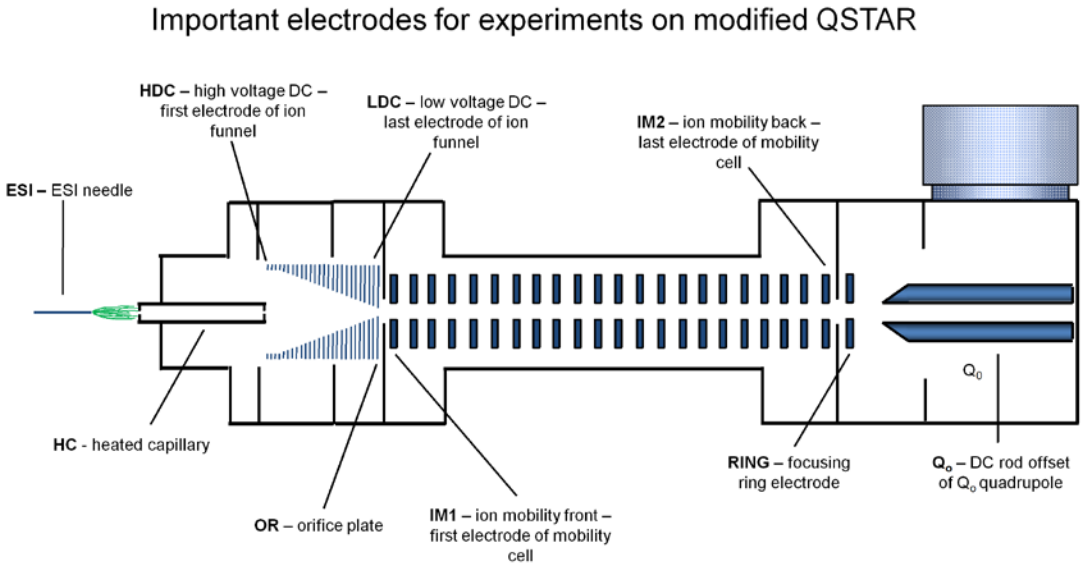

Figure 50. Important electrodes for experiments performed on modified QSTAR. Important pressure regions are pressure in the ion funnel and pressure in the Q_0 quadrupole region.

Table 5. Table showing the applied voltages to electrodes in the ALILTLVS injection energy experiments. The defined injection energy (in volts) is calculated from the voltage drop between the ion mobility exit, IM2, and the Q_0 quadrupole DC rod bias. Another important parameter for the injection energy experiments are the pressures in the ion funnel and Q_0 regions.

Important Voltages and Pressures in QSTAR ALILTLVS experiments						
2 V injection energy experiment				22 V injection energy experiment		
Electrode	Voltage (V)	Pressure (torr)		Electrode	Voltage (V)	Pressure (torr)
ESI	4500			ESI	4500	
HC	1050			HC	1050	
HDC	1075			HDC	1075	
LDC	1025			LDC	1025	
OR	1010			OR	1010	
IM1	1000			IM1	1000	
IM2	20			IM2	40	
RING	10			RING	20	
Q_0	18			Q_0	18	
IF pressure		1.46		IF pressure		1.46
Q_0 pressure		0.005		Q_0 pressure		0.005

The first injection energy experiment injects ions into the Q_0 quadrupole with a laboratory frame acceleration energy of 2 volts. The resulting mass spectrum is shown in Figure 50(a). The spectrum shows the protonated molecule, $[M+H]^+$, of ALILTLVS along with the sodium adducted and potassium adducted peptide ion signals. The spectrum also shows the b_7 and b_6 fragment ions from the precursor ion, the protonated molecule. The relative abundance, or numbers of counts, for all of these ion signals is very low, indicative of low ion transmission through the modified instrument. The injection energy was increased to 22 V of laboratory frame energy and the mass spectrum is shown in Figure 50(b). The relative abundance (number of counts) of all ion signals increases with the increase in injection energy to the Q_0 quadrupole, however, the number of fragment ion signals and their relative abundance also increase. This can be detrimental to the experiment as a precursor ion eluting the drift cell can be activated

and dissociated via CID and deplete the relative abundance of the precursor ion detected in the TOF mass spectrometer. The depletion in relative abundance leads to issues of analytical figures of merit such as sensitivity, and possibly limit of detection, if low concentration analytes are to be detected. On the other hand, post-mobility ion activation and dissociation via CID can be advantageous to the experiment as MS^3 experiments could be performed without any instrument modifications. To illustrate, an ion eluting the drift cell could fragment and the resultant fragment ions would be transferred to the Q_0 quadrupole where they would be collisionally cooled and focused in to Q_1. A fragment ion of interest could then be selected in Q_1 and sent to the Q_2 collision cell to undergo CID for MS^3 information thereby increasing the structural information obtained from the ion mobility separation and tandem mass spectrometry.

Low relative abundance ion signals in Figure 51(a) and (b) are a result of electrical breakdown problems and low ion transmission through the instrument. The voltage applied across the drift cell is ~980 volts. This was the maximum voltage that could be put across the drift cell owing to electrical breakdown in the funnel region from the voltages applied to the heated capillary and ion funnel electrodes (breakdown would sometimes occur while acquiring data at this voltage setting). At this drift length, the electric field over pressure, *E/p*, ratio is approximately 19 $Vcm^{-1}torr^{-1}$. Increasing the *E/p* ratio should result in increased ion transmission and increase the relative abundance of the ion signals detected in the TOF. The optimum operating pressure of Q_0 for collisional cooling and ion focusing is 10 millitorr, but to obtain this pressure the pressure of the ion funnel and drift cell region must be increased accordingly.

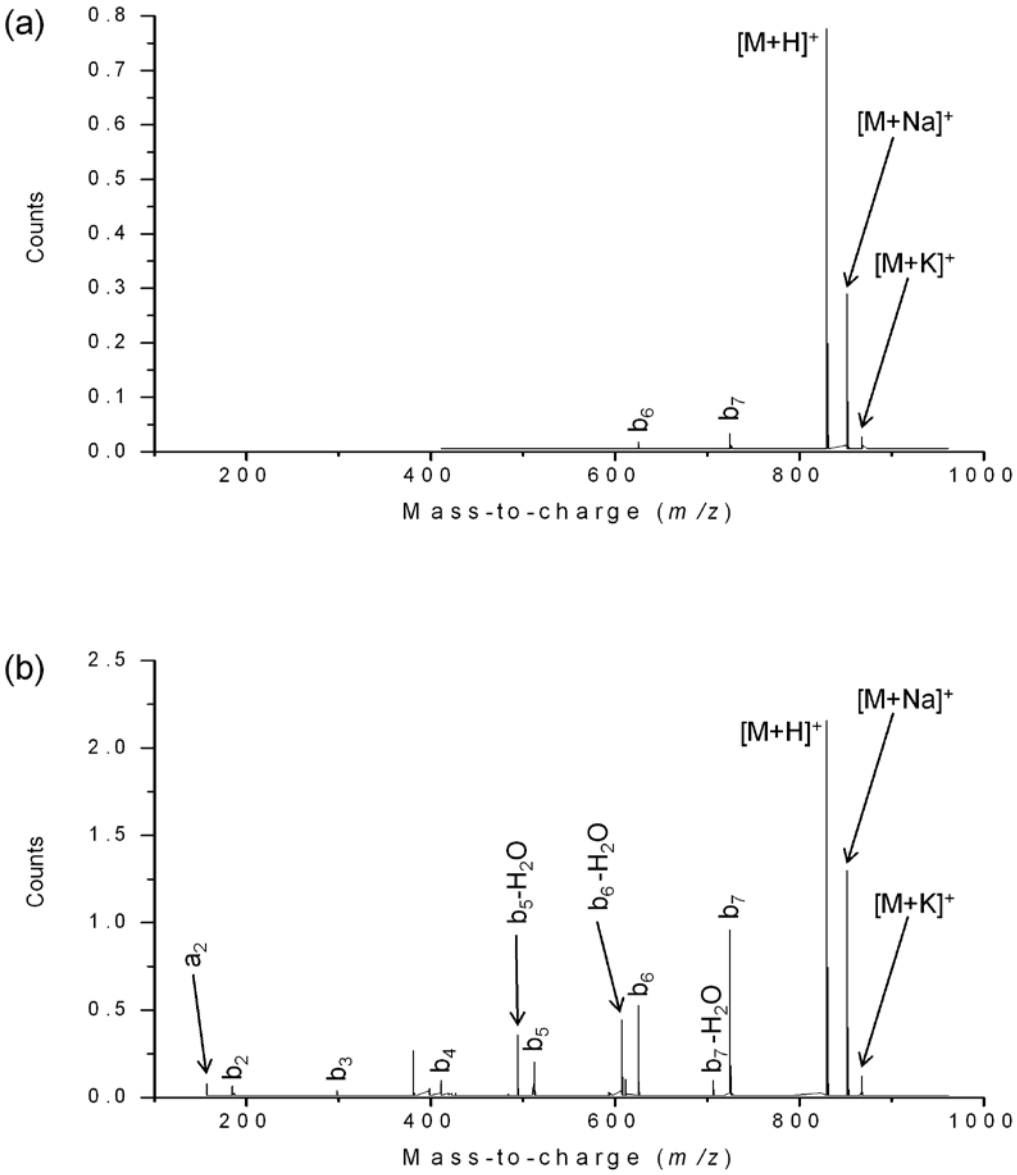

Figure 51. Mass spectra of ALILTLVS injected from the 35 centimeter, modular PDC IG drift cell into the Q_0 quadrupole at two different laboratory frame acceleration energies. The top spectrum (a) is taken with a 2 V laboratory frame acceleration energy while the bottom spectrum (b) is taken with a 22 V laboratory frame acceleration energy.

A modification was made by decreasing the drift length of the modular drift cell to 19 centimeters, allowing similar *E/p* ratios to be applied across the drift cell with much lower voltage amplitudes applied to the heated capillary and funnel electrodes, thus eliminating problems with electrical breakdown in the ion funnel region. The 22 volt injection energy experiment was performed on the modified 19 cm drift cell at a pressure of 1.7 torr, resulting in a similar *E/p* ratio of 19 $Vcm^{-1}torr^{-1}$, and a Q_0 pressure of 7 millitorr. The increase in the pressure of Q_0 seems to dramatically increase ion transmission through the quadrupole and thereby increase the relative abundance of ions detected in the TOF (Figure 52).

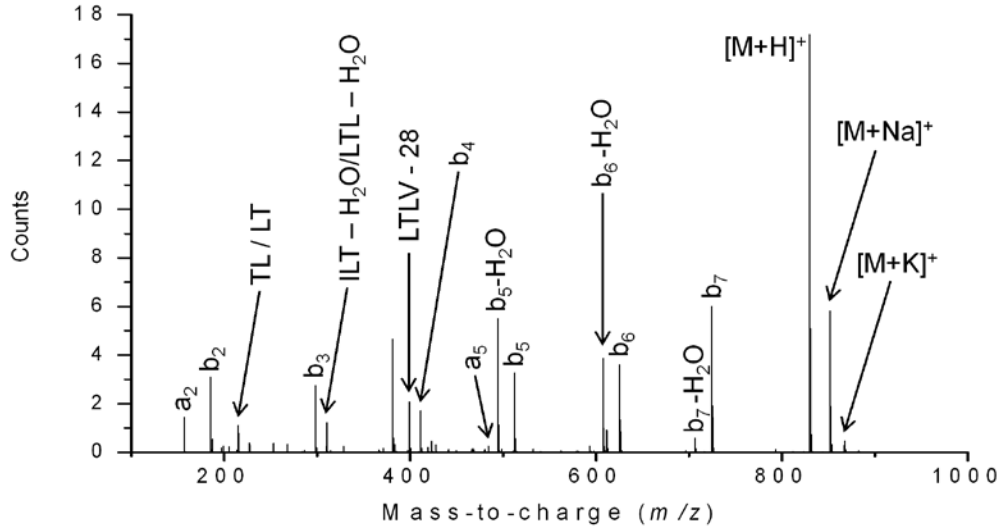

Figure 52. Mass spectrum of ALILTLVS injected from the 19 centimeter, PDC IG drift cell into the Q_0 quadrupole with 22 volts laboratory frame acceleration energy.

The pressure increase in the Q_0 region was further investigated with the standard peptide Angiotensin I (amino acid sequence: DRVYIHPFHL). The concentration of the Angiotensin I solution was 7 x 10^{-5} M in 50/50 (v:v) water:methanol with 0.1% acetic acid. The operating conditions for the following experiment are listed in Table 6. The pressure of the ion funnel region is increased to 3.46 torr while the Q_0 region is increased to the optimum operating pressure of 10 millitorr. The *E/p* ratio in the modular, PDC IG drift cell varies from 10 to 11 $Vcm^{-1}torr^{-1}$ depending on the potential applied to the last electrode of the drift cell that partially defines the injection energy into Q_0. The mass spectra for the injection energy experiments are shown in Figure 53.

Table 6. Injection energy conditions for standard peptide Angiotensin I (sequence = DRVYIHPFHL). The potentials defining the injection energy into the Q_0 quadrupole are depicted in red text.

Important Voltages and Pressures for Angiotensin I (DRVYIHPFHL) injection energy experiments								
Injection energy (V)	-18	-8	-2	6	14			
Electrode	Voltage (V)	Voltage (V)	Voltage (V)	Voltage (V)	Voltage (V)		Region	Pressure (torr)
ESI	3500	3500	3500	3500	3500		IF	3.46
HC	750	750	750	750	750		Q_0	0.01
HDC	725	725	725	725	725			
LDC	675	675	675	675	675			
OR	665	665	665	665	665			
IM1	655	655	655	655	655			
IM2	0	10	16	24	32			
RING	20	20	20	20	20			
Q_0	18	18	18	18	18			

The mass spectra in Figure 53 reveal that the Angiotensin I molecule is doubly and triply protonated owing to the three basic residues in the amino acid sequence along with the N-terminal amine. Figure 53(a) shows that decelerating ions with 18 V laboratory frame energy (36 V and 54 V deceleration for the +2 and +3 charge state,

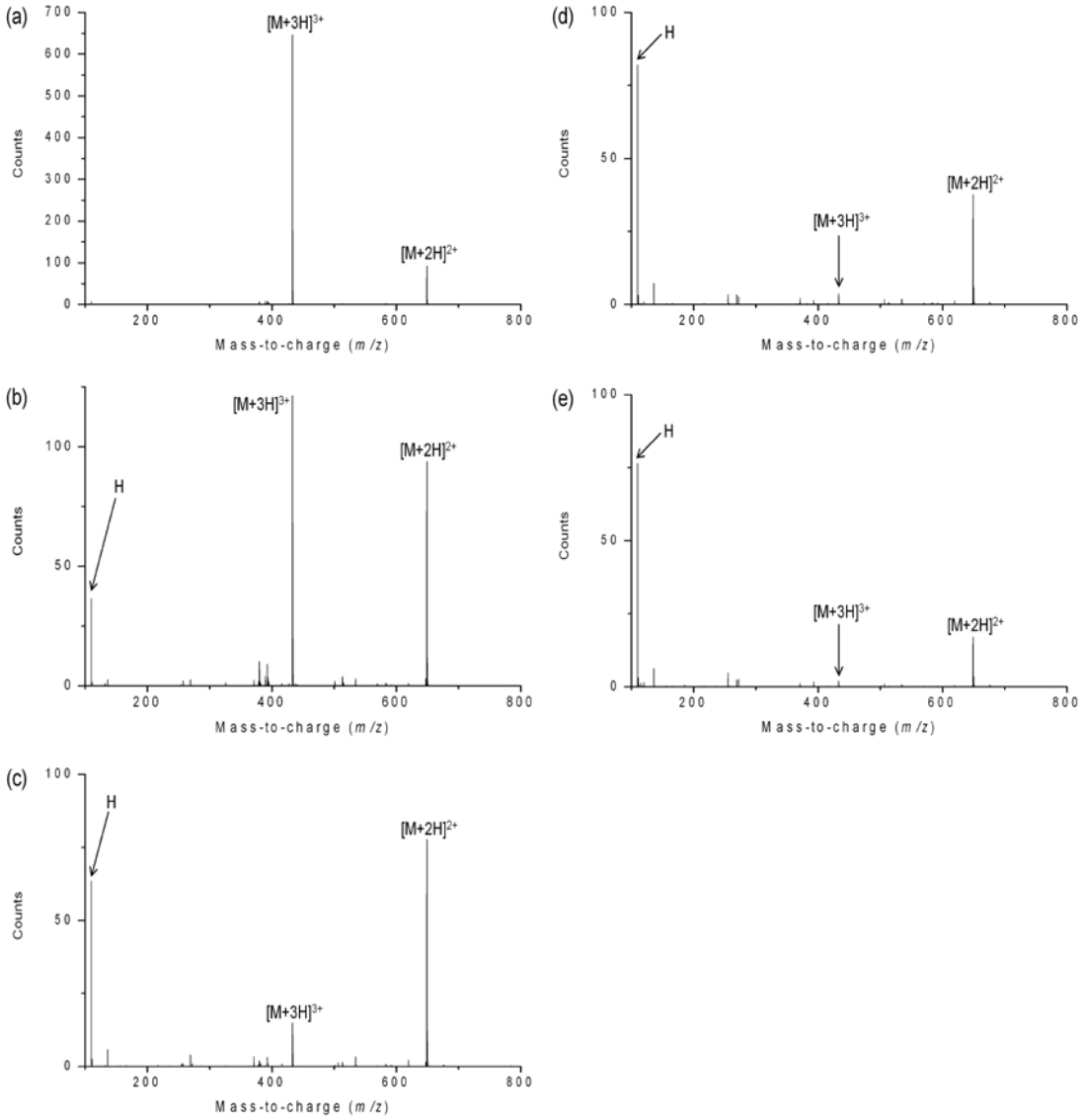

Figure 53. Mass spectra of different injection energies into Q_0 for the doubly and triply protonated Angiotensin I molecule. The injection energies are (a) -18 V (b) -8 V (c) -2 V (d) +6 V and (e) +14 V.

respectively) prior to injecting them into the Q_0 quadrupole results in transmission of the precursor ions, $[M+2H]^{2+}$ and $[M+3H]^{3+}$ ions of Angiotensin I. As the injection energy is increased to -8V (16V and 24 V deceleration), the threshold for activation and dissociation of the $[M+3H]^{3+}$ ion is achieved as there is a significant decrease in the relative abundance of the ion and the presence of fragment ions in the spectrum (Figure 53(b)). The activation and dissociation threshold of the $[M+2H]^{2+}$ ion has not been met as the relative abundance is the same as that of the ion signal in Figure 53(a). The threshold for activation and dissociation of the $[M+2H]^{2+}$ is reached when the injection energy is increased to -2V (4 V and 6 V deceleration). This is apparent from the relative abundance decrease in Figure 53(c) compared to that of (a) and (b). Figure 53(d) and (e) show the continued trend in the decrease of relative abundance of the $[M+2H]^{2+}$ and $[M+3H]^{3+}$ ion signals. In Figure 53(e) the $[M+3H]^{3+}$ ion signal is near complete depletion meaning that the fragmentation efficiency of the $[M+3H]^{3+}$ is almost 100 percent and the $[M+2H]^{2+}$ ion signal is at about 20 percent of its original abundance suggesting an 80 percent fragmentation efficiency.

One interesting observation is that many of the fragment ions in Figure 53(b) (better shown in Figure 54) decrease in relative abundance or disappear entirely from the mass spectra when the injection energy is increased (Figure 53(c)-(e)). This seems to be the result of the increase in relative abundance of the histidine immonium ion as the injection energy is increased. Energetically speaking, it can be hypothesized that as the internal energy of the ion is increased while the lifetime of the ion remains relatively similar, as fragment ions from activation and dissociation of the precursor ion are

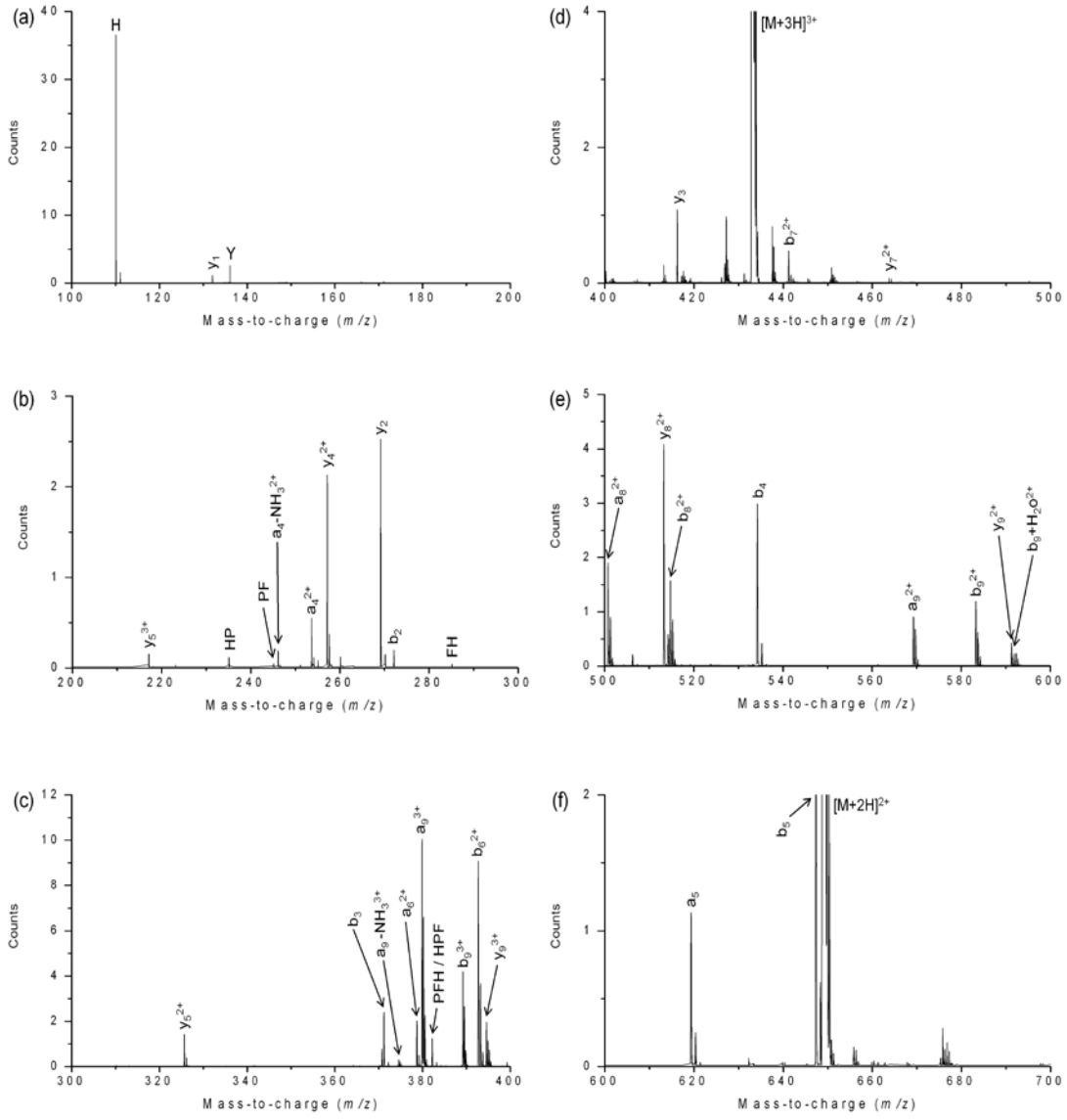

Figure 54. Fragment ion mass spectra for the -8 V injection energy experiment of Angiotensin I. The fragment ion spectra are broken down into 100 Dalton *m/z* windows, (a)-(f), and the number of counts of each spectra is adjusted to the most abundant fragment ion (fragment ion base peak) to observe all pertinent fragment ions.

quenched quickly in Q_0, the favorable reaction channel will change. In this specific case, it seems that at higher ion internal energies the favored reaction channel is to form the histidine immonium ion.

It is also important to note that the ion activation and dissociation occurring at very low energies (actually ions are decelerated after the mobility cell) is most likely owing to multiply charged analytes requiring less energy for ion activation and the pressure differential between the mobility cell exit and Q_0. The gas flow from the mobility exit into Q_0 contributes to the axial velocity of the ion resulting in more efficient ion activation. Couple the gas flow and pressure differential region with multiply charged analytes and ion activation and dissociation occurs at much lower ion internal energies.

According to the ion injection energy experiments of ALILTLVS and Angiotensin I (DRVYIHPFHL) the interface region of the modular, PDC IG drift cell exit and the Q_0 quadrupole is efficient for ion activation and dissociation via CID. The activation and dissociation in this region would allow for MS^3 experiments to be carried out on the instrument. Additional information of ion structure could then be obtained when comparing ion mobilities, or ion-neutral collision cross sections, with MS^2 and MS^3 tandem mass spectrometry.

Attempts were made to collect two-dimensional mobility-mass spectra with a separate four channel TDC (Ionwerks TDC x 4, Ionwerks, Inc.; Houston, TX) and personal computer with Ionwerks 2D Acquisition software (Ionwerks, Inc.; Houston, TX). The personal computer contains a National Instruments PCI-6602 timing card

(National Instruments, Austin, TX) along with an Ionwerks Fishcamp card (Ionwerks, Inc.; Houston, TX) to control all of the timing issues for the experiment. The timing issues for the experiment are the time start for the mobility spectra which is established by pulsing the orifice electrode prior to the mobility cell for gating ions into the mobility cell. The pulse is provided from the Ionwerks data acquisition software and serves as the start clock for the mobility spectrum. The next timing issue in the experiment is the pulsing of the TOF extraction region for acquiring time-of-flight mass spectra. The TOF is normally pulsed through the QSTAR 4 channel TDC (Ionwerks TDC x 4), however, the in 1 and in 2 channels on the pulser module (1005960) of the QSTAR are now pulsed with the TOF extraction frequency settings provided by the Ionwerks data acquisition software on the separate computer. Finally, the signal from one of the anodes from the multi-anode detector is sent to an amplifier/discriminator and then to the four-channel TDC for detection on the Ionwerks acquisition software.

A variety of gate frequencies and pulse widths were tested and the resulting two-dimensional spectra were collected. The spectra for ALILTLVS at a gate frequency of 400 Hz and gate width of 100 μs, corresponding to a duty cycle of four percent, is shown in Figure 55(a). From the two-dimensional spectra, it is evident that the mobility signal for each ion occurs at every point across the arrival time distribution time window. This means that the initial ion packet introduced into the mobility cell is broadened as the ions traverse the quadrupoles. To investigate if mobility broadening could be defeated to achieve discernable mobility signal, the gate frequency was decreased to 10 Hz and the gate width was narrowed to 5 μs (Figure 55(b)). This two-dimensional spectra was

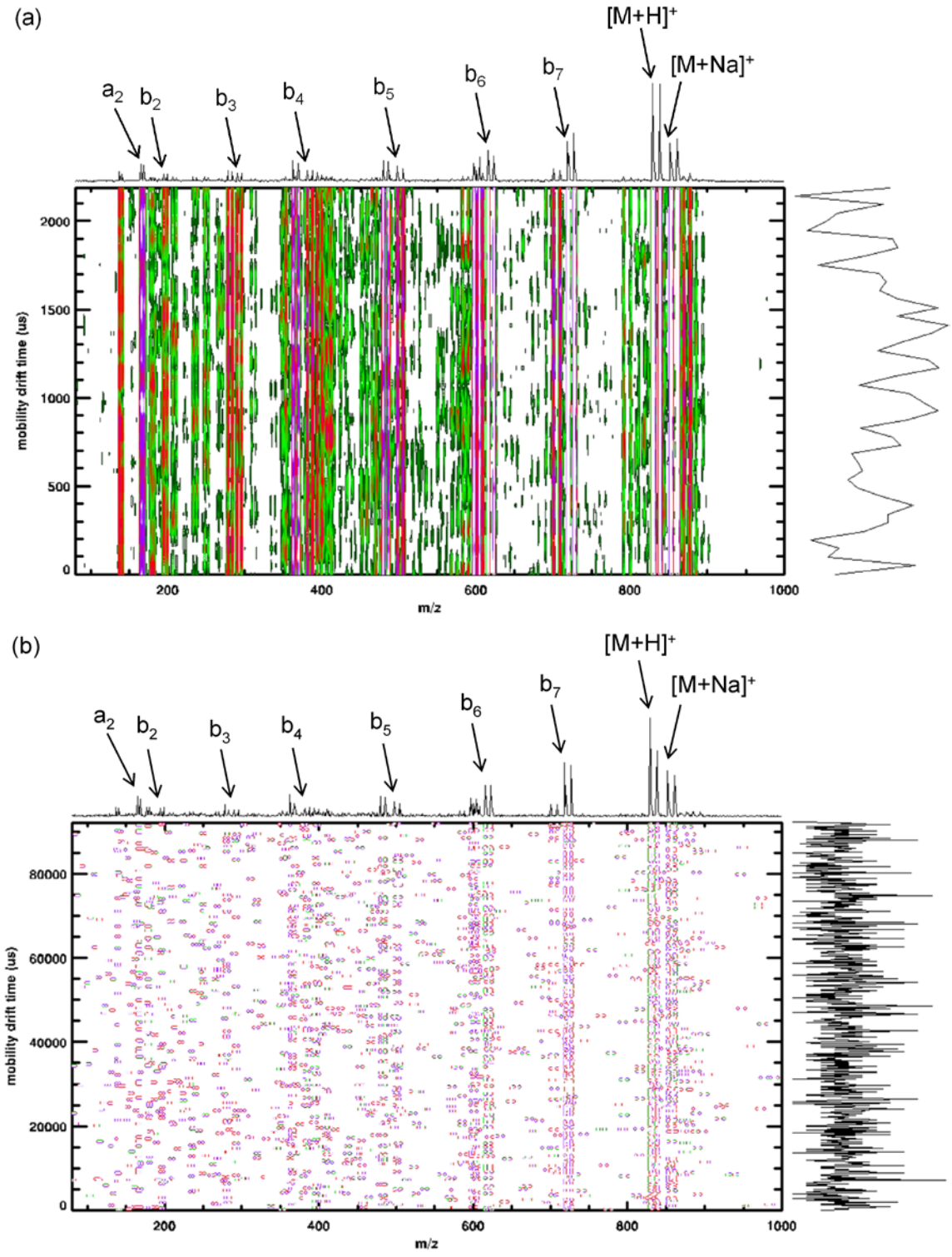

Figure 55. Arrival time distribution spectra for ALILTLVS at different gate frequencies and widths. The gate frequency and width are (a) 400 Hz, 100 µs and (b) 10 Hz, 5 µs.

acquired for 30 minutes due to low ion concentrations being admitted into the drift cell for each individual gating event. The relative abundance of all ion signals in Figure 55(b) is decreased compared to that of Figure 55(a), however the broadening of the mobility signal is still apparent. Note also that there is mobility signal from time zero to the last time being monitored in the mobility spectrum. It should not be expected to have signal at time zero of a mobility spectrum unless there are ions that have not yet reached the TOF detector prior to the next gating event.

The mobility broadening observed in the QSTAR was explained by a 2001 publication by Chernushevich, Loboda, and Thomson in which AP MALDI was performed [240]. In the publication it is stated, "…The pulsed MALDI ion beam spreads in time as it passes through the collisional ion guide. In MALDI, ions are typically generated by a few nanosecond wide laser pulse. As the ions leave the collisional ion guide, the width of their temporal distribution increases up to tens of milliseconds [241]. This represents a time spread of over six orders of magnitude." For this reason, mobility signals cannot be obtained with the current instrumental setup.

One solution to ion broadening in the Q_0 quadrupole was proposed by Tang *et al* by adding in a differentially pumped region prior to Q_0 [108]. In this region a short, 24 mm quadrupole, referred to as Q00, is added to focus ions from this higher pressure region into Q_0. The region is evacuated with a 12.8 L s^{-1} mechanical pump to establish a pressure of 0.3 torr. A 2.5 mm conductance limiting lens is placed after Q00 to define the gas flow into the Q_0 quadrupole. This design allowed IMS arrival time distribution spectra to be obtained, however the focusing properties of the Q_0 quadrupole change

dramatically at much higher pressures (calculated to be approximately 4.3 x 10^{-4} torr with the conductance limiting aperture of 2.5 mm and a pumping speed of 700 L s^{-1} in the Q_0 region) decreasing the ion transmission through Q_0. Increasing the amplitude of the RF and DC voltages (*V* and *U*) on the Q_0 quadrupole should provide a stronger radial effective potential to overcome the loss of radial ion focusing through collisional damping at higher pressures.

A second solution to the problem is an orthogonal mobility detector could be inserted after the mobility cell exit (Figure 56). Ions exiting the mobility cell would be deflected by a two-dimensional quadrupole bender to a differentially pumped chamber housing an electron multiplier or microchannel plate detector for mobility detection. An exit gate to the mobility cell is required for selection of a single ion mobility signal for further analysis. After selecting a single mobility signal and recording the arrival time distribution at the orthogonal mobility detector, the two-dimensional quadrupole bender would now allow ions to pass through to Q_0 for further experiments such as tandem MS, ion-ion reactions, etc. The proposed instrument would be a powerful tool for proteomics as ion conformers could be mobility selected and analyzed by tandem MS. The resulting fragment ion spectrum could then be compared to candidate ion structures provided by molecular dynamics simulations to aid in structural determination of ions.

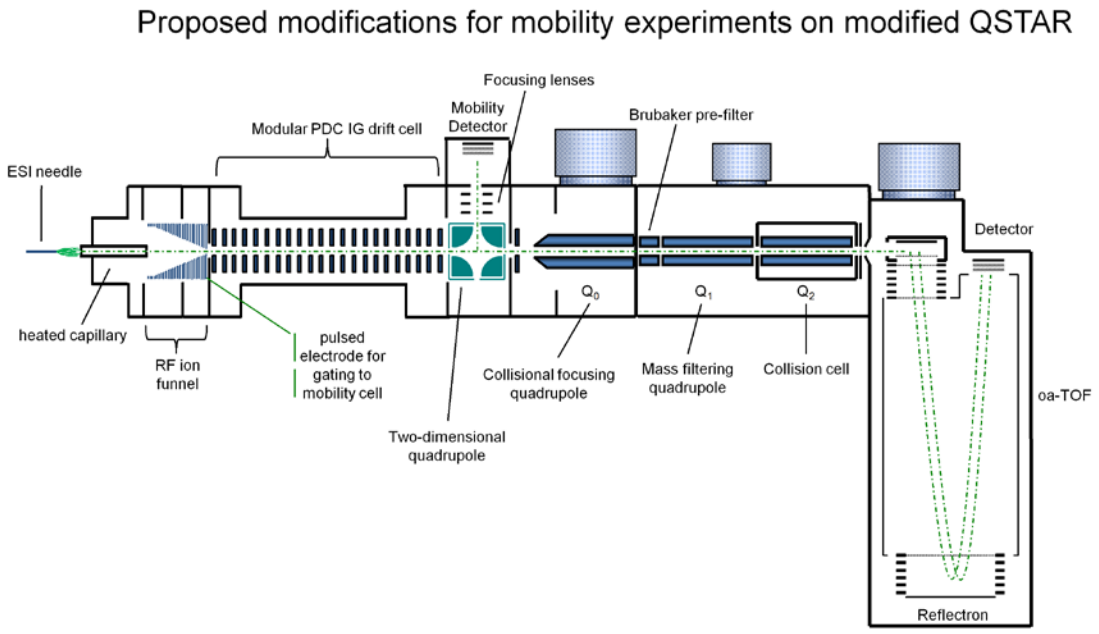

Figure 56. Schematic diagram of proposed modifications to allow for ion mobility experiments to be performed on the modular, PDC IG drift cell coupled to the QSTAR.

8.4 Conclusion

The electrospray-RF-ion funnel modular, PDC IG drift cell works and is effective at transmitting a high number of ions. When the Q_0 quadrupole was operated at an optimum pressure, the total ion current and ion relative abundance in the mass spectrum was quite high. The high ion transmission through the modular drift cell is encouraging as it could potentially be used with a variety of commercial instruments.

The interface between the modular, PDC IG drift cell and Q_0 is also very efficient for ion activation and dissociation by collision induced dissociation. Two ion activation and dissociation regions are now available, providing the instrument with MS^3 capabilities.

One major deleterious effect to the mobility experiment is the temporal spreading of ions exiting the Q_0 collisional-focusing quadrupole. Defined ion packets exiting the mobility cell are spread in time so that discernible arrival time distributions of mobility separated ions are not plausible in the current instrument design. Adding a mobility detector orthogonal to the mobility exit would allow for ion mobility detection as well as the aforementioned capabilities of the commercial qTOF mass spectrometer.

9. CONCLUSION

9.1 Conclusion

The periodic-focusing DC ion guide (PDC IG) has great potential as an ion mobility spectrometer. It has great analytical utility in that the ion transmission through the device is increased compared to conventional uniform field drift cells. Ion transmission is increased by the radial focusing properties provided by the radial electric field, the effective RF, and effective potentials. The confining effective potential, that can be seen as the slow drift in ion motion toward the drift cell central axis, is very similar to the effective potentials produced by the superimposed RF voltage on a traveling wave IMS. Actually, the parallels between the PDC IG and traveling wave IMS are strikingly similar, however the PDC IG utilizes an effective RF rather than a superimposed RF in the device.

The geometry of the electrode, specifically the relatively small inner diameter and larger electrode thickness, produce variations in the radial electric field that lead to an effective RF (position varying waveform) experienced by ions as they traverse the drift cell. The variations in the radial electric field in conjunction with the effective RF produce effective potentials originating from the front and back edges of each electrode. The radial ion confinement, or magnitude of displacement, is more pronounced at the back edge of an electrode owing to the radial electric field force being in the direction of the center of the drift axis along with an increased magnitude effective potential. The increase in the effective potential magnitude is a direct result of the variation in the axial

electric field as a function of axial position which results in an oscillating ion axial velocity. At the back edge of the electrode the ion axial velocity is low resulting in an increase in the effective potential magnitude and thereby increasing radial ion focusing.

Variation of electrode geometry changes the ion transmission and mobility resolution obtained on the PDC IG. The inner diameter of the PDC IG can be varied to optimize ion transmission or resolution. As a rule of thumb, smaller electrode inner diameters decrease mobility resolution but increase ion transmission. This observation was first made through SIMION simulations and confirmed experimentally on a 63 cm PDC IG drift cell. Ion transmission increases for smaller inner diameter PDC IG electrodes can be explained by larger variations in the axial and radial electric field from more pronounced fringing fields as well as increased magnitude effective potentials. As electrode inner diameter is increased, the drift cell operates similarly to the conventional uniform field design owing to a decrease in the non-uniform, fringing fields of larger inner diameter electrodes. Moreover, without variations in the axial and radial electric field a radial focusing mechanism does not exist thereby decreasing ion transmission.

An 8 mm inner diameter PDC IG electrode provided a 40-70 fold increase in ion transmission over conventional uniform field electrodes with only a 10 percent decrease in mobility resolution in the pressure regime of 1 to 2 torr. This electrode geometry (*d, t,* and *s*) was chosen for construction of an experimental PDC IG. A 63 cm PDC IG provided a mobility resolution of ~60 for $C_{60}^{\cdot+}$ and a few model peptide ions. Increasing the drift length by a factor of two increased mobility resolution by 36 percent, in good agreement with the 41 percent increase predicted by theory.

The PDC IG drift cell can be easily coupled with orthogonal-acceleration time-of-flight mass spectrometry. Preliminary experiments utilizing a three-element einzel lens (consisting of long length lenses) revealed that ions are not transmitted efficiently through the lenses. In fact, the ion-neutral collision frequency is too high and ion velocity is dampened leading to ion motion dominated by collisional scattering and diffusion. Mobility resolution is degraded in the high pressure region following the mobility cell exit aperture. However, introduction of transfer lenses (exact PDC IG replica electrodes) continues to radially focus ions, much like in the PDC IG drift cell, in the high pressure region prior to shorter length einzel lenses. Ion transfer and ion focusing is improved considerably. In fact, mobility resolution provided on the improved PDCIG-IM-oaTOF-MS instrument exceeded resolution of the PDC IG with a post-acceleration mobility detector alone. This result can most likely be explained by the long, field-free region inside a tube lens prior to the post-acceleration detector used in the previous IMS studies.

Finally, a modular, PDC IG was successfully coupled to the ABI Sciex QSTAR Pulsar with good ion transmission through the PDC IG. The acceleration energy from the mobility cell exit to the Q_0 quadrupole could be varied to reach the threshold for activation and dissociation of ions, increasing the experimental possibilities of the instrument by providing MS^3 capabilities. Although the initial arrival time distribution IMS experiments were unsuccessful on the QSTAR, the problem is in the instrumental operation of the Q_0 quadrupole of the commercial mass spectrometer. Modifications could be made to the QSTAR to achieve mobility detection.

9.2 Future Directions

9.2.1 A Multi-Pass PDC IG Drift Cell

The idea of a multiple pass drift cell was first developed by Johnsen *et al.* at the University of Pittsburgh 40 years ago [242-244]. It was termed a reversible field apparatus in that prior to ions exiting the drift tube, the electric field applied to the drift tube is reversed. As the field is reversed, ions turn around and drift back toward the ion source. Ions would then be reversed again prior to reaching the ion source region and drift to the detector region.

The number of passes that can be done for a packet of ions depends on the initial concentration of ions, the diffusion coefficient of the ion in the drift gas, and the overall effective drift length. At some point, diffusion of the ions in the drift gas will lead to insufficient ion current to detect an appreciable signal at the detector. On the other hand, employing a radial ion focusing mechanism to the drift cell would increase ion transmission. This is because radially diffuse ions normally striking drift electrodes or simply not reaching the detector will be refocused to the center of the drift cell increasing ion flux at the detector.

One year ago, Professor David Clemmer's laboratory introduced a high-resolution ion cyclotron mobility spectrometer utilizing a multiple pass approach for high resolution IMS [184]. The cyclotron drift tube is composed of four 90 degree sections of drift electrodes. A short drift cell section is used to transmit ions into the four-section drift cell and another small section can be used to transmit ions to a time-of-flight mass analyzer. Once ions are introduced to the cyclotron drift tube, each section is

pulsed to establish an electric field to accelerate ions through the drift gas. At the end of each section, an RF ion funnel serves as a radial focusing mechanism to correct radially diffuse ion trajectories and transmit a greater number of ions to the next drift section. As the ion cloud exits the first drift section and funnel region, the second section of the cyclotron drift tube is pulsed. This process is repeated for all sections of the cyclotron drift tube. One pass through the cyclotron drift tube corresponds to traversing eight drift cell sections.

While this design is very intuitive and creative, there are some problems in relation to ion motion, ion mobility resolution, and analytical utility. The first in relation to ion motion is that the ion swarm will actually feel a race track effect as a function of radial position in the drift cell. Ions closest to the inner electrode wall (inside lane of the race track) will experience a larger magnitude electric field and also a shorter drift distance to the next drift cell section. On the other hand, ions at the outer electrode wall (outside lane) will experience a smaller magnitude electric field and a longer drift distance. This results in increased spatial and therefore temporal broadening of the ion packet.

The second problem, which is more related to ion mobility resolution and analytical utility, is the pulsing of the electric field within each drift cell section. The pulsing of the sections corrects for the temporal broadening from the race track effect but distorts the mobility resolution and also transmits only one ion of interest at a time, limiting the analytical utility of the device. For example, an ion packet with a given mobility must be selected to pass through one drift section and be accelerated at the right

time into the next drift section. Slight changes in the pulsing frequency of the sections would select a different portion of the ion swarm profile, such as the leading or trailing edges or the central density of the ion swarm. As a result, the temporal broadening from the race track effect is removed from this signal chopping. However, ion mobility resolution is not governed by diffusion, but rather the pulsing frequency. This is evident from the data given in the publication. Two charge states of the peptide Substance P were separated in the cyclotron drift cell. As the number of passes increase, the resolution also increases as is expected. The unusual result is that the +2 charge state of Substance P exhibits a higher mobility resolution than the +3 charge state. This result does not correlate well with diffusion limited mobility resolution theory that states that as ion charge state increases mobility resolution increases, owing to the fact that resolution is governed by the pulsing frequency which leads to chopping of the ion packet.

The idea of the reversible field drift apparatus has resurfaced in Professor David Clemmer's research laboratory. They have termed their instrument the PING-PONG ion mobility spectrometer [245]. The device utilizes a uniform field drift cell with two RF ion funnel regions at each end. The RF ion funnel is gated to only allow ions of a certain mobility in the funnel region while other ions are deflected and lost in the separation. PING-PONG mobility can only be used to transmit an ion with a mobility that is in resonance with the frequency of the RF ion funnel trap, limiting its analytical utility.

A pulsed PDC IG drift cell could used to evaluate mobility resolution through multiple passes in a fixed drift length. The multiple passes are established by reversing

the electric field during ion drift through the drift cell. This allows for variation in drift length while maintaining a bench top size instrument. One advantage of a pulsed PDC IG drift cell is that the pulsing frequency could be set where one ion would elute from the drift cell while another ion would be turned around from the reversal of the electric field thereby enhancing the separation of two components. Another advantage of doing a multi-pass experiment in the PDC IG is the radial focusing properties of the device (Section 2). Drifting ions should stay near the central axis of the drift cell regardless of the length of time in the drift cell or the number of turn-around events experienced.

It should be mentioned that the multi-pass PDC IG could only be used as a separations device. Calculation of the ion-neutral collision cross sections should be avoided because of unknown drift lengths in the multi-pass device. This has been detailed by Johnsen in previous work in what he describes as an inability to eliminate end effects in drift velocity measurements that can be eliminated in a fixed drift length design. To illustrate this point imagine that ions are created in the source region, *S*, and then drift from the source region to the detector, *D*. The distance *S*-*D* is a fixed parameter and can therefore be used to estimate a theoretical eluting peak profile of the ion swarm. However, if the electric field is reversed before ions reach the detector, *D*, the ion swarm will turn around at point *A*. The ions would then be allowed to drift back toward the source region before the field would be reversed a second time, referred to as point *B*, where ions will now be traveling in the original direction toward the detector, *D*. The distances of *S*-*A*, *A*-*B*, and *B*-*D* are actually unknown. The overall drift distance can be inferred from the overall drift velocity, or drift time, of the ion swarm and the

timing of the application of the electric field in the forward, reverse, and again in the forward drift direction until detection [243].

9.2.2 Variation of Drift Length with PDC IG Drift Cell Modules

Early experiments involving variation of drift length in drift tube IMS utilized translational ion sources. Ion source position could be altered within the drift tube while the drift tube exit aperture remained stationary. One example of such an instrument was the low pressure drift tube-mass spectrometer constructed at the Georgia Institute of Technology. The instrument consisted of an electron impact ion source, a drift tube, and a quadrupole mass spectrometer after the drift tube exit. The electron impact ion source is mounted on a stainless-steel bellows whose length can be varied outside the instrument. The ion source can be moved with an accuracy of a few thousandths of an inch varying the drift length from 1 to 44 centimeters [246].

In a similar design, Iinuma *et al.* constructed a drift tube mass spectrometer used for flight distance scanning. The drift tube was made from a cylindrical tube made of high-purity aluminous porcelain and this surface was coated with an inorganic thick-film resistor.[247] An axial electric field can be applied by applying a potential gradient across the cylinder. In the flight distance method of operation, the ion source is moved slowly down the drift tube while the delay time for ion gating to the mass spectrometer is kept constant.[248] The spatial distribution of the ions is mapped versus the distance of flight (or perhaps a better term would be distance of drift).

Simpler variation of drift length can be accomplished with isolated drift cell modules that can be easily mated. The modular drift cell was introduced in Section 8

and could be used to construct long length drift cells (greater than the 125 cm PDC IG) with little difficulty and relatively low cost. An AutoCAD drawing of a first prototype MALDI source with one modular drift cell section is shown in Figure 57. Increasing the PDC IG drift length to 3 meters should increase the ion mobility resolution for $C_{60}^{\bullet+}$ to 135 according to extrapolation of the equation provided in Figure 33(a). In addition, the radial focusing properties of the PDC IG allow for infinite drift lengths without a decrease in ion transmission (Figure 33(b)), however, there are limits to voltage amplitudes applied across the drift cell and issues of electrical breakdown.

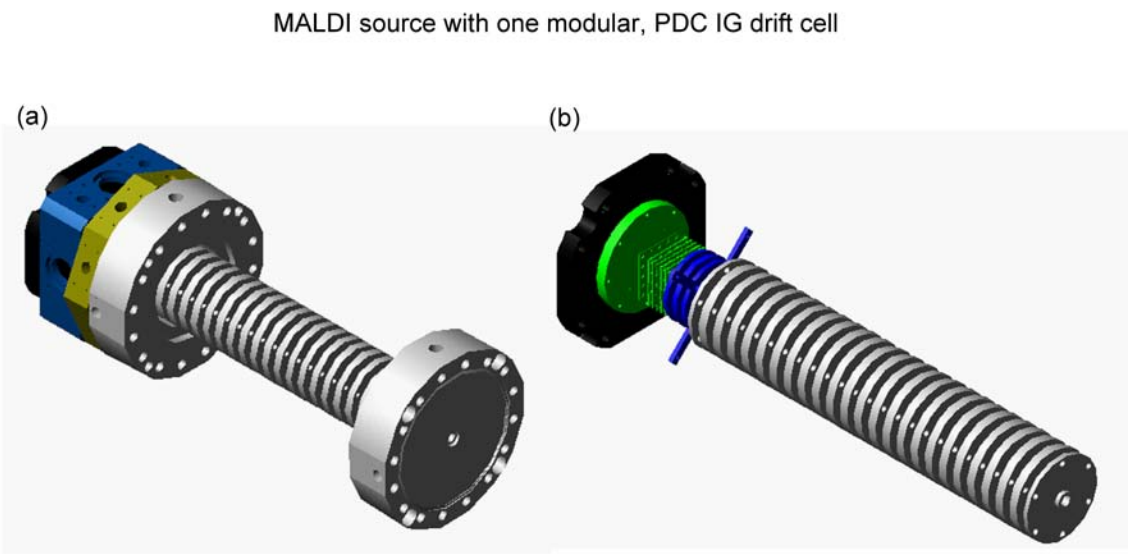

Figure 57. Schematic diagram of a prototype MALDI source with one modular drift cell shown with vacuum flange components (a) and without vacuum flange components (b).

REFERENCES

[1] E.A. Mason, E.W. McDaniel, Transport Properties of Ions in Gases, John Wiley & Sons, 1988.

[2] J.J. Thomson, E. Rutherford, Phil. Mag., November, (1896).

[3] J. Zeleny, V. The velocity of the ions produced in gases by rontgen rays, Phil. Trans. Roy. Soc. A, 195 (1900) 193-234.

[4] G.R. Asbury, H.H. Hill, Jr., Using different drift gases to change separation factors (α) in ion mobility spectrometry, Anal. Chem., 72 (2000) 580-584.

[5] M.J. Cohen, F.W. Karasek, Plasma chromatography™ - A new dimension for gas chromatography and mass spectrometry, J. Chromatogr. Sci., 8 (1970) 330-337.

[6] J.A. Hornbeck, Microsecond transient currents in the pulsed townsend discharge, Phys. Rev., 83 (1951) 374-379.

[7] J.A. Hornbeck, The drift velocities of molecular and atomic ions in helium, neon, and argon, Phys. Rev., 84 (1951) 615-620.

[8] H.W. Ellis, R.Y. Pai, E.W. McDaniel, E.A. Mason, L.A. Viehland, Transport properties of gaseous ions over a wide energy range, Atomic Data and Nuclear Data Tables, 17 (1976) 177-210.

[9] H.W. Ellis, E.W. McDaniel, D.L. Albritton, L.A. Viehland, S.L. Lin, E.A. Mason, Transport properties of gaseous ions over a wide energy range. Part II, Atomic Data and Nuclear Data Tables, 22 (1978) 179-217.

[10] J.H. Whealton, E.A. Mason, Transport coefficients of gaseous ions in an electric field, Annals of Physics, 84 (1974) 8-38.

[11] J.H. Mitchell, K.E.W. Ridler, The speed of positive ions in nitrogen, Proc. R. Soc. Lond. A, 146 (1934) 911-921.

[12] A.M. Tyndall, A.F. Pearce, The variation of the mobility of gaseous ions with temperature. I. Positive ions in their own gas, Proc. R. Soc. Lond. A, 149 (1935) 426-434.

[13] A.F. Pearce, The variation of the mobility of gaseous ions with temperature. II. Caesium and sodium ions in helium, Proc. R. Soc. Lond. A, 155 (1936) 490-498.

[14] L.B. Loeb, Basic processes of gaseous electronics, University of California Press, Berkeley and Los Angeles, California, (1955).

[15] S.D. Pringle, K. Giles, J.L. Wildgoose, J.P. Williams, S.E. Slade, T. Konstantinos, R.H. Bateman, M.T. Bowers, J.H. Scrivens, An investigation of the mobility separation of some peptide and protein ions using a new hybrid quadrupole/travelling wave IMS/oa-TOF instrument, Int. J. Mass Spectrom., 261 (2007) 1-12.

[16] K. Giles, S.D. Pringle, K.R. Worthington, D. Little, J.L. Wildgoose, R.H. Bateman, Applications of a travelling wave-based radio-frequency-only stacked ring ion guide, Rapid Comm. Mass Spectrom., 18 (2004) 2401-2414.

[17] D. Gerlich, In State-Selected and State-to-State Ion-Molecule Reaction Dynamics, Part 1: Experiment, vol. LXXXIII, Ng CY, Baer M (eds). John Wiley, (1992) 1-176.

[18] A.V. Tolmachev, T. Kim, H.R. Udseth, R.D. Smith, T.H. Bailey, J.H. Futrell, Simulation-based optimization of the electrodynamic ion funnel for high sensitivity electrospray ionization mass spectrometry, Int. J. Mass Spectrom., 203 (2000) 31-47.

[19] B.T. Ruotolo, K. Giles, I. Campuzano, A.M. Sandercock, R.H. Bateman, C.V. Robinson, Evidence for macromolecular protein rings in the absence of bulk water, Science, 310 (2005) 1658-1661.

[20] B.T. Ruotolo, S.-J. Hyung, P.M. Robinson, K. Giles, R.H. Bateman, C.V. Robinson, Ion mobility-mass spectrometry reveals long-lived, unfolded intermediates in the dissociation of protein complexes, Angew. Chem. Int. Ed., 46 (2007) 8001-8004.

[21] B.T. Ruotolo, J.L.P. Benesch, A.M. Sandercock, S.-J. Hyung, C.V. Robinson, Ion mobility-mass spectrometry analysis of large protein complexes, Nat. Protoc., 3 (2008) 1139-1152.

[22] E.O. Knutson, K.T. Whitby, Aerosol classification by electric mobility: Apparatus, theory, and applications, J. Aerosol Sci., 6 (1975) 443-452.

[23] E.O. Knutson, K.T. Whitby, Accurate measurement of aerosol electric mobility moments, J. Aerosol Sci., 6 (1975) 453-460.

[24] S.L. Kaufman, Analysis of biomolecules using electrospray and nanoparticle methods: The gas-phase electrophoretic mobility molecular analyzer (GEMMA), J. Aerosol Sci., 29 (1998) 537-552.

[25] F. Zarrin, S.L. Kaufman, F. Dorman, Method and apparatus for determining concentration of macromolecules and colloids in a liquid sample, U.S. Patent No. 5,076,097, (1991).

[26] S.L. Kaufman, A.R. Kuchumov, M. Kazakevich, S.N. Vinogradov, Analysis of a 3.6-MDa hexagonal bilayer hemoglobin from *Lumbricus terrestris* using a gas-phase electrophoretic mobility molecular analyzer, Anal. Biochemistry, 259 (1998) 195-202.

[27] S.L. Kaufman, J.W. Skogen, F.D. Dorman, F. Zarrin, Macromolecule analysis based on electrophoretic mobility in air: Globular proteins, Anal. Chem., 68 (1996) 1895-1904.

[28] J. Agarwal, G. Sem, Continuous flow, single-particle-counting condensation nucleus counter, J. Aerosol Sci., 11 (1980) 343-357.

[29] J.A. Koropchak, S. Sadain, X. Yang, L.-E. Magnusson, M. Heybroek, M. Anisimov, S.L. Kaufman, Nanoparticle detection technology, Anal. Chem., (1999) 386A-394A.

[30] J. Fernandez de la Mora, L. de Juan, T. Eichler, J. Rosell, Differential mobility analysis of molecular ions and nanometer particles, Trends in Analytical Chemistry, 17 (1998) 328-339.

[31] G. Bacher, W.W. Szymanski, S.L. Kaufman, P. Zollner, D. Blaas, G. Allmaier, Charge-reduced nano electrospray ionization combined with differential mobility analysis of peptides, proteins, glycoproteins, noncovalent protein complexes and viruses, J. Mass Spectrom., 36 (2001) 1038.

[32] C.J.J. Hogan, J. Fernandez de la Mora, Tandem ion mobility-mass spectrometry (IMS-MS) study of ion evaporation from ionic liquid-acetonitrile nanodrops, Phys. Chem. Chem. Phys., 11 (2009) 8079-8090.

[33] C. Hogan, J. Fernandez de la Mora, Mobility measurement non-denatured protein and protein cluster ions by DMA-MS, 58th American Society for Mass Spectrometry Conference on Mass Spectrometry and Allied Topics, ThOC am session, Recent Developments in Ion Mobility MS (2010).

[34] I.A. Buryakov, E.V. Krylov, E.G. Nazarov, U.K. Rasulev, A new method of separation of multi-atomic ions by mobility at atmospheric pressure using a high-frequency amplitude-asymmetric strong electric field, Int. J. Mass Spectrom. Ion Processes, 128 (1993) 143-148.

[35] A.A. Shvartsburg, Differential ion mobility spectrometry: Nonlinear ion transport and fundamentals of FAIMS, CRC Press, Taylor and Francis Group, LLC; Boca Raton, FL, (2009).

[36] R.W. Purves, R. Guevremont, S. Day, C.W. Pipich, M.S. Matyjaszczyk, Mass spectrometric characterization of a high-field asymmetric waveform ion mobility spectrometer, Rev. Sci. Instrum., 69 (1998) 4094-4105.

[37] C.G. Herbert, R.A.W. Johnstone, Mass Spectrometry Basics, CRC Press, 2003.

[38] A.J. Dempster, Proc. Am. phil. Soc., 75 (1935) 755.

[39] K.T. Bainbridge, E.B. Jordan, Mass spectrum analysis: 1. The mass spectrograph. 2. The existence of isobars of adjacent elements, Phys. Rev., 50 (1936) 282-296.

[40] A.O. Nier, N.R. Roberts, Phys. Rev., 81 (1951) 508.

[41] E.G. Johnson, A.O. Nier, Angular abberations in sector shaped electromagnetic lenses for focusing beams of charged particles, Phys. Rev., 91 (1953) 10-17.

[42] J. Mattauch, R.F.K. Herzog, Z. Phys., 89 (1934) 786.

[43] W.E. Stephens, A pulsed mass spectrometer with time dispersion, Phys. Rev. (Proceedings of the American Physical Society), 69 (1946) 691.

[44] A.E. Cameron, D.F. Eggers, An ion "velocitron", Rev. Sci. Instrum., 19 (1948) 605-607.

[45] R. Keller, Helv. Phys. Acta, 22 (1949) 386.

[46] M.M. Wolff, W.E. Stephens, A pulsed mass spectrometer with time dispersion, Rev. Sci. Instrum., 24 (1953) 616-617.

[47] I.H. McLaren, W.C. Wiley, Time-of-flight mass spectrometer with improved resolution, Rev. Sci. Instrum., 26 (1955) 1150-1157.

[48] H.S. Katzenstein, S.S. Friedland, New time-of-flight mass spectrometer, Rev. Sci. Instrum., 26 (1955) 324-327.

[49] M. Karas, F. Hillenkamp, Laser desorption ionization of proteins with molecular masses exceeding 10,000 daltons, Anal. Chem., 60 (1988) 2299-2301.

[50] K. Tanaka, H. Waki, Y. Ido, S. Akita, Y. Yoshida, T. Yohida, Protein and polymer analyses up to *m/z* 100,000 by laser ionization time-of-flight mass spectrometry, Rapid Comm. Mass Spectrom., 2 (1988) 151-153.

[51] R.S. Brown, J.J. Lennon, Mass resolution improvement by incorporation of pulsed ion extraction in a matrix-assisted laser desorption/ionization linear time-of-flight mass spectrometer, Anal. Chem., 67 (1995) 1998-2003.

[52] S.M. Colby, T.B. King, J.P. Reilly, Improving the resolution of matrix-assisted laser desorption/ionization time-of-flight mass spectrometry by exploiting the correlation between ion position and velocity, Rapid Comm. Mass Spectrom., 8 (1994) 865-868.

[53] U. Bahr, J. Stahl-Zeng, E. Gleitsmann, M. Karas, Delayed extraction time-of-flight MALDI mass spectrometry of proteins above 25000 Da, J. Mass Spectrom., 32 (1997) 1111-1116.

[54] D.C. Barbacci, R.D. Edmonson, D.H. Russell, Evaluation of the variables that affect resolution in delayed extraction MALDI-TOF, Int. J. Mass Spectrom. Ion Processes, 165/166 (1997) 221-235.

[55] M.L. Vestal, P. Juhasz, S.A. Martin, Delayed extraction matrix-assisted laser desorption time-of-flight mass spectrometry, Rapid Comm. Mass Spectrom., 9 (1995) 1044-1050.

[56] B.A. Mamyrin, V.I. Karataev, D.V. Shmikk, V.A. Zagulin, The mass-reflectron, a new nonmagnetic time-of-flight mass spectrometer with high resolution, Sov. Phys. *JETP*, 37 (1973) 45-48.

[57] K.G. Standing, R. Beavis, G. Bollbach, W. Ens, F. LaFortune, D. Main, B. Schueler, X. Tang, J.B. Westmore, Secondary ion time-of-flight mass spectrometers and data systems, Analytical Instrumentation, 16 (1987) 173-189.

[58] X. Tang, R. Beavis, W. Ens, F. Lafortune, B. Schueler, K.G. Standing, A secondary ion time-of-flight mass spectrometer with an ion mirror, Int. J. Mass Spectrom. Ion Processes, 85 (1988) 43-67.

[59] W. Paul, H.P. Reinhard, U. von Zahn, Z. Naturforsch A, 8 (1953) 448.

[60] R.E. March, J.F.J. Todd, Quadrupole Ion Trap Mass Spectrometry, Second Edition, John Wiley and Sons, Inc., (2005).

[61] W. Paul, M. Raether, Z. Phys., 140 (1955) 262-273.

[62] W. Paul, H.P. Reinhard, U. von Zahn, Z. Phys., 152 (1958) 143-182.

[63] J.A. Hipple, H. Sommer, H.A. Thomas, A precise method of determining the faraday by magnetic resonance, Phys. Rev., 76 (1949) 1877-1878.

[64] A.G. Marshall, C.L. Hendrickson, G.S. Jackson, Fourier transform ion cyclotron resonance mass spectrometry: A primer, Mass Spectrom. Rev., 17 (1998) 1-35.

[65] E.W. McDaniel, D.W. Martin, W.S. Barnes, Drift-tube mass spectrometer for studies of low-energy ion-molecule reactions, Rev. Sci. Instrum., 33 (1962) 2-7.

[66] D.L. Albritton, T.M. Miller, D.W. Martin, E.W. McDaniel, Mobilities of mass-identified ions in hydrogen, Phys. Rev., 171 (1968).

[67] E.W. McDaniel, Possible sources of large error in determinations of ion-molecule reaction rates with drift tube-mass spectrometers, J. Chem. Phys., 53 (1970).

[68] B.H. Clowers, H.H. Hill, Jr., Mass analysis of mobility-selected ion populations using dual gate, ion mobility, quadrupole ion trap mass spectrometry, Anal. Chem., 77 (2005) 5877-5885.

[69] B.H. Clowers, H.H. Hill, Jr., Influence of cation adduction on the separation characteristics of flavonoid diglycoside isomers using dual gate-ion mobility-quadrupole ion trap mass spectrometry, J. Mass Spectrom., 41 (2006).

[70] K.B. McAfee, Jr., D. Edelson, Identification and mobility of ions in a townsend discharge by time-resolved mass spectrometry, Proc. Phys. Soc., 81 (1963).

[71] K.B. McAfee, Jr., D.P. Sipler, D. Edelson, Mobilities and reactions of ions in argon, Phys. Rev., 160 (1967).

[72] L.G. McKnight, K.B. McAfee, Jr., D.P. Sipler, Low-field drift velocities and reactions of nitrogen ions in nitrogen, Phys. Rev., 164 (1967).

[73] J.H.J. Dawson, M. Guilhaus, Orthogonal-acceleration time-of-flight mass spectrometer, Rapid Comm. Mass Spectrom., 3 (1989) 155-159.

[74] M. Guilhaus, D. Selby, V. Mlynski, Orthogonal acceleration time-of-flight mass spectrometry, Mass Spectrom. Rev., 19 (2000) 65-107.

[75] J.A. McLean, B.T. Ruotolo, K.J. Gillig, D.H. Russell, Ion mobility-mass spectrometry: a new paradigm for proteomics, Int. J. Mass Spectrom., 240 (2005) 301-315.

[76] P.B. Fellgett, The multiplex advantage., Thesis, University of Cambridge, UK, (1951).

[77] A. Woods, M. Ugarov, T. Egan, J. Koomen, K.J. Gillig, K. Fuhrer, M. Gonin, J.A. Schultz, Lipid/Peptide/Nucleotide Separation with MALDI-Ion Mobility-TOF MS, Anal. Chem., 76 (2004) 2187-2195.

[78] S.J. Valentine, A.E. Counterman, D.E. Clemmer, A database of 660 peptide ion cross sections: use of intrinsic size parameters for bona fide predictions of cross sections, J. Am. Soc. Mass Spectrom., 10 (1999) 1188-1211.

[79] L. Tao, J.R. McLean, J.A. McLean, D.H. Russell, A collision cross-section database of singly-charged peptide ions, J. Am. Soc. Mass Spectrom., 18 (2007) 1232-1238.

[80] J.B. Fenn, M. Mann, C.K. Meng, S.F. Wong, C.M. Whitehouse, Electrospray ionization for mass spectrometry of large biomolecules, Science, 246 (1989) 64-71.

[81] G. Wang, R.B. Cole, Disparity between solution-phase equilibria and charge state distributions in positive-ion electrospray mass spectrometry, Org. Mass Spectrom., 29 (1994) 419-427.

[82] J.C.Y. Le Blanc, J. Wang, R. Guevremont, K.W.M. Siu, Electrospray mass spectra of protein cations formed in basic solutions, Org. Mass Spectrom., 29 (1994) 587-593.

[83] R.B. Cole, A. Kamel Harrata, Solvent effect on analyte charge state, signal intensity, and stability in negative ion electrospray mass spectrometry; Implications for the mechanism of negative ion formation, J. Am. Soc. Mass Spectrom., 4 (1993) 546-556.

[84] A.T. Iavarone, E.R. Williams, Supercharging in electrospray ionization: effects on signal and charge, Int. J. Mass Spectrom., 219 (2002) 63-72.

[85] A.T. Iavarone, J.C. Jurchen, E.R. Williams, Supercharged protein and peptide ions formed by electrospray ionization, Anal. Chem., 73 (2001) 1455-1460.

[86] A.T. Iavarone, E.R. Williams, Mechanism of charging and supercharging molecules in electrospray ionization, J. Am. Chem. Soc., 125 (2003) 2319-2327.

[87] H.J. Sterling, E.R. Williams, Origin of supercharging in electrospray ionization of noncovalent complexes from aqueous solution, J. Am. Soc. Mass Spectrom., 20 (2009) 1933-1943.

[88] N.E. Bradbury, R.A. Nielsen, Absolute values of the electron mobility in hydrogen, Phys. Rev., 49 (1936) 388-393.

[89] W. Paul, H. Steinwedel, Apparatus for separating charged particles of different specific charges, U.S. Patent 2,939,952, (1960).

[90] J.C. Schwartz, M.W. Senko, J.E.P. Syka, Ion trap mass spectrometer system and method, U.S. Patent No. 5,420,425, (1995).

[91] J.C. Schwartz, M.W. Senko, J.E.P. Syka, A two-dimensional quadrupole ion trap mass spectrometer, J. Am. Soc. Mass Spectrom., 13 (2002) 659-669.

[92] J.W. Hager, Axial ejection in a multipole mass spectrometer, U.S. Patent No. 6,177,668, (2001).

[93] J.W. Hager, A new linear ion trap mass spectrometer, Rapid Comm. Mass Spectrom., 16 (2002) 512-526.

[94] S.A. Shaffer, D.C. Prior, G.A. Anderson, H.R. Udseth, R.D. Smith, An ion funnel interface for improved ion focusing and sensitivity using electrospray ionization mass spectrometry, Anal. Chem., 70 (1998) 4111-4119.

[95] S.A. Shaffer, K. Tang, G.A. Anderson, D.C. Prior, H.R. Udseth, R.D. Smith, A novel ion funnel for focusing ions at elevated pressure using electrospray ionization mass spectrometry, Rapid Comm. Mass Spectrom., 11 (1997) 1813-1817.

[96] S.A. Shaffer, A.V. Tolmachev, D.C. Prior, G.A. Anderson, H.R. Udseth, R.D. Smith, Characterization of an improved electrodynamic ion funnel interface for electrospray ionization mass spectrometry, Anal. Chem., 71 (1999) 2957-2964.

[97] B.H. Clowers, W.F. Siems, H.H. Hill, Jr., S.M. Massick, Hadamard transform ion mobility spectrometry, Anal. Chem., 78 (2006) 44-51.

[98] A.W. Szumlas, S.J. Ray, G.M. Hieftje, Hadamard transform ion mobility spectrometry, Anal. Chem., 78 (2006) 4474-4481.

[99] M. Harwit, N.J.A. Sloane, Hadamard Transform Optics, Academic Press Inc., (1979).

[100] C.S. Creaser, M. Benyezzar, J.R. Griffiths, J.W. Stygall, A tandem ion trap / ion mobility spectrometer Anal. Chem., 72 (2000).

[101] S.C. Henderson, S.J. Valentine, A.E. Counterman, D.E. Clemmer, ESI/ion trap/ion mobility/time-of-flight mass spectrometry for rapid and sensitive analysis of biomolecular mixtures, Anal. Chem., 71 (1999) 291-301.

[102] C.S. Hoaglund, S.J. Valentine, D.E. Clemmer, An ion trap interface for ESI-ion mobility experiments, Anal. Chem., 69 (1997) 4156-4161.

[103] C.S. Hoaglund-Hyzer, D.E. Clemmer, Ion trap/ion mobility/quadrupole/time-of-flight mass spectrometry for peptide mixture analysis, Anal. Chem., 73 (2001) 177-184.

[104] S. Myung, Y.J. Lee, M.H. Moon, J. Taraszka, R. Sowell, S.L. Koeniger, A.E. Hilderbrand, S.J. Valentine, L. Cherbas, P. Cherbas, T.C. Kaufman, D.F. Miller, Y. Mechref, M.V. Novotny, M.A. Ewing, C.R. Sporleder, D.E. Clemmer, Development of high-sensitivity ion trap ion mobility spectrometry time-of-flight techniques: A high-throughput nano-LC-IMS-TOF separation of peptides arising from a *Drosophila* protein extract, Anal. Chem., 75 (2003) 5137-5145.

[105] S.J. Valentine, S.L. Koeniger, D.E. Clemmer, A split-field drift tube for separation and efficient fragmentation of biomolecular ions, Anal. Chem., 75 (2003) 6202-6208.

[106] S.J. Valentine, X. Liu, M. Plasencia, A.E. Hilderbrand, R.T. Kurulugama, S.L. Koeniger, D.E. Clemmer, Developing liquid chromatography ion mobility mass spectrometry techniques, Expert Rev. Proteomics, 2 (2005) 553-565.

[107] E.S. Baker, B.H. Clowers, F. Li, K. Tang, A.V. Tolmachev, D.C. Prior, M.E. Belov, R.D. Smith, Ion mobility spectrometry-mass spectrometry performance using electrodynamic ion funnels and elevated drift gas pressures, J. Am. Soc. Mass Spectrom., 18 (2007) 1176-1187.

[108] K. Tang, A.A. Shvartsburg, H.-N. Lee, D.C. Prior, M.A. Buschbach, F. Li, A.V. Tolmachev, G.A. Anderson, R.D. Smith, High-sensitivity ion mobility spectrometry/mass spectrometry using electrodynamic ion funnel interfaces, Anal. Chem., 77 (2005) 3330-3339.

[109] B.H. Clowers, Y.M. Ibrahim, D.C. Prior, W.F.I. Danielson, M.E. Belov, R.D. Smith, Enhanced ion utilization efficiency using an electrodynamic ion funnel trap as an injection mechanism for ion mobility spectrometry, Anal. Chem., 80 (2008) 612-623.

[110] S.L. Koeniger, S.I. Merenbloom, D.E. Clemmer, Evidence for many resolvable structures within conformation types of electrosprayed ubiquitin ions, J. Phys. Chem. B, 110 (2006) 7017-7021.

[111] F. Paschen, Annalen der Physik, 273 (1889) 69-75.

[112] G.R. Asbury, J. Herbert H. Hill, Evaluation of ultrahigh resolution ion mobility spectrometry as an analytical separation device in chromatographic terms, J. Microclumn Separations, 12 (2000) 172-178.

[113] K. Dreisewerd, Chem. Rev., 103 (2003) 395-426.

[114] G. Javahery, B.A. Thomson, A segmented radiofrequency-only quadrupole collision cell for measurements of ion collision cross section on a triple quadrupole mass spectrometer, J. Am. Soc. Mass Spectrom., 8 (1997) 697-702.

[115] K. Thalassinos, S.E. Slade, K.R. Jennings, J.H. Scrivens, K. Giles, J.L. Wildgoose, J. Hoyes, R.H. Bateman, M.T. Bowers, Ion mobility mass spectrometry of proteins in a modified commercial mass spectrometer, Int. J. Mass Spectrom., 236 (2004) 55-63.

[116] T. Wyttenbach, P.R. Kemper, M.T. Bowers, Design of a new electrospray ion mobility mass spectrometer Int. J. Mass Spectrom., 212 (2001) 13-23.

[117] P.R. Kemper, N.F. Dupuis, M.T. Bowers, A new, higher resolution, ion mobility mass spectrometer, Int. J. Mass Spectrom., 287 (2009) 46-57.

[118] Q. Zhao, G.M. Schieffer, M.W. Soyk, T.J. Anderson, R.S. Houk, E.R. Badman, Effects of ion/ion proton transfer reactions on conformation of gas-phase cytochrome *c* ions, J. Am. Soc. Mass Spectrom., 21 (2010) 1208-1217.

[119] Q. Zhao, M.W. Soyk, G.M. Schieffer, K. Fuhrer, M.M. Gonin, R.S. Houk, E.R. Badman, An ion trap-ion mobility-time of flight mass spectrometer with three ion sources for ion/ion reactions, J. Am. Soc. Mass Spectrom., 20 (2009) 1549-1561.

[120] S.L. Koeniger, D.E. Clemmer, Resolution and structural transitions of elongated states of ubiquitin, J. Am. Soc. Mass Spectrom., 18 (2007) 322-331.

[121] S.L. Koeniger, S.I. Merenbloom, S.J. Valentine, M.F. Jarrold, H.R. Udseth, R.D. Smith, D.E. Clemmer, An IMS-IMS analogue of MS-MS, Anal. Chem., 78 (2006) 4161-4174.

[122] S.I. Merenbloom, S.L. Koeniger, S.J. Valentine, M. Plasencia, D.E. Clemmer, IMS-IMS and IMS-IMS-IMS/MS for separating peptide and protein fragment ions, Anal. Chem., 78 (2006) 2802-2809.

[123] S.I. Merenbloom, B.C. Bohrer, S.L. Koeniger, D.E. Clemmer, Assessing the peak capacity of IMS-IMS separations of tryptic peptide ions in He at 300 K, Anal. Chem., 79 (2007) 515-522.

[124] S. Guan, A.G. Marshall, Stacked-ring electrostatic ion guide, J. Am. Soc. Mass Spectrom., 7 (1996) 101-106.

[125] J.A. Silveira, C.M. Gamage, R.C. Blase, D.H. Russell, Gas-phase ion dynamics in a periodic-focusing DC ion guide (Part 2), submitted to Int. J. Mass Spectrom., (2010).

[126] G.A. Eiceman, Z. Karpas, Ion Mobility Spectrometry, CRC Press, Boca Raton, 1994.

[127] M. Zhu, B. Bendiak, B. Clowers, J. Herbert H. Hill, Ion mobility-mass spectrometry analysis of isomeric carbohydrate precursor ions, Anal. Bioanal Chem., 394 (2009) 1853-1867.

[128] J.G. Slaton, H.A. Sawyer, D.H. Russell, Low-pressure ion mobility-time-of-flight mass spectrometry for metalated peptide ion structural characterization: tyrosine-containing tripeptides and homologous septapeptides, Int. J. Ion Mobility Spectrom., 8 (2005) 13-18.

[129] C. Wu, W.F. Siems, J. Klasmeier, J. Hill, H.H., Separation of isomeric peptides using electrospray ionization/high-resolution ion mobility spectrometry, Anal. Chem., 72 (2000) 391-395.

[130] B.T. Ruotolo, C.C. Tate, D.H. Russell, Ion mobility-mass spectrometry applied to cyclic peptide analysis: conformational preferences of gramicidin S and linear analogs in the gas phase, J. Am. Soc. Mass Spectrom., 15 (2004) 870-878.

[131] H.A. Sawyer, J.T. Marini, E.G. Stone, B.T. Ruotolo, K.J. Gillig, D.H. Russell, The Structure of Gas-Phase Bradykinin Fragment 1-5 (RPPGF) Ions: An Ion Mobility Spectrometry and H/D Exchange Ion-Molecule Reaction Chemistry Study, J. Am. Soc. Mass Spectrom., 16 (2005) 893-905.

[132] P. Dugourd, R.R. Hudgins, D.E. Clemmer, M.F. Jarrold, High-resolution ion mobility measurements, Rev. Sci. Instrum., 68 (1997) 1122-1129.

[133] R.R. Hudgins, J. Woenckhaus, M.F. Jarrold, High resolution ion mobility measurements for gas phase proteins: correlation between solution phase and gas phase conformations, Int. J. Mass Spectrom. and Ion Processes, 165/166 (1997) 497-507.

[134] A.A. Shvartsburg, R.R. Hudgins, P. Dugourd, M.F. Jarrold, Structural Elucidation of Fullerene Dimers by High-Resolution Ion Mobility Measurements and Trajectory Calculation Simulations, J. Phys. Chem. A, 101 (1997) 1684-1688.

[135] B.T. Ruotolo, K.J. Gillig, E.G. Stone, D.H. Russell, Peak capacity of ion mobility mass spectrometry: Separation of peptides in helium buffer gas, J. Chromatogr. B, 782 (2002) 385-392.

[136] B.T. Ruotolo, J.A. McLean, K.J. Gillig, D.H. Russell, Peak capacity of ion mobility mass spectrometry: the utility of varying drift gas polarizability for the separation of tryptic peptides, J. Mass Spectrom., 39 (2004) 361-367.

[137] S. Rokushika, H. Hiroyuki, M.A. Baim, J. Herbert H. Hill, Resolution measurement for ion mobility spectrometry, Anal. Chem., 57 (1985) 1902-1907.

[138] C.A. Srebalus, J. Li, W.S. Marshall, D.E. Clemmer, Gas-phase separations of electrosprayed peptide libraries, Anal. Chem., 71 (1999) 3918-3927.

[139] M. Tabrizchi, Temperature effects on resolution in ion mobility spectrometry, Talanta, 62 (2004) 65-70.

[140] C. Wu, W.F. Siems, G.R. Asbury, J. Herbert H. Hill, Electrospray ionization high-resolution ion mobility spectrometry-mass spectrometry, Anal. Chem., 70 (1998) 4929-4938.

[141] K.J. Gillig, B.T. Ruotolo, E.G. Stone, D.H. Russell, An electrostatic focusing ion guide for ion mobility-mass spectrometry, Int. J. Mass Spectrom., 239 (2004) 43-49.

[142] O. Soppart, J.I. Baumbach, Meas. Sci. Technol., (2000) 1473-1479.

[143] F.A. Fernandez-Lima, H. Wei, Y.Q. Gao, D.H. Russell, On the Structure Elucidation Using Ion Mobility Spectrometry and Molecular Dynamics, J. Phys. Chem. A, 113 (2009) 8221-8234.

[144] J.A. Silveira, C.M. Gamage, R.C. Blase, J.C. May, D.H. Russell, Gas-phase ion dynamics in a periodic-focusing DC ion guide, Int. J. Mass Spectrom., 296 (2010) 36-42.

[145] B.T. Ruotolo, J.A. McLean, K.J. Gillig, D.H. Russell, The influence and utility of varying field strength for the separation of tryptic peptides by ion mobility-mass spectrometry, J. Am. Soc. Mass Spectrom., 16 (2005) 158-165.

[146] P.R. Kemper, M.T. Bowers, Electronic-state chromatography: application to first-row transition-metal ions, J. Phys. Chem., 95 (1991) 5134-5146.

[147] L.A. Viehland, E.A. Mason, Gaseous Ion mobility in electric fields of arbitrary strength, Ann. Phys., 91 (1975) 499-533.

[148] G.F. Verbeck, B.T. Ruotolo, K.J. Gillig, D.H. Russell, Resolution equations for high-field ion mobility, J. Am. Soc. Mass Spectrom., 15 (2004) 1320-1324.

[149] H.W. Ellis, R.Y. Pai, E.W. McDaniel, E.A. Mason, L.A. Viehland, At. Data Nucl. Data Tables, 17 (1976) 177-210.

[150] P. Watts, A. Wilders, On the resolution obtainable in practical ion mobility systems, Int. J. Mass Spectrom. Ion Processes, 112 (1992) 179-190.

[151] A.B. Kanu, M.M. Gribb, J. Hill, H.H., Predicting Optimal Resolving Power for Ambient Pressure Ion Mobility Spectrometry, Anal. Chem., 80 (2008) 6610-6619.

[152] W.F. Siems, C. Wu, E.E. Traver, J. Herbert H. Hill, Measuring the Resolving Power of Ion Mobility Spectrometers, Anal. Chem., 66 (1994) 4195-4201.

[153] J. Xu, W.B. Whitten, J.M. Ramsey, Space Charge Effects on Resolution in a Miniature Ion Mobility Spectrometer, Anal. Chem., 72 (2000) 5787-5791.

[154] R.C. Blase, J.A. Silveira, K.J. Gillig, C.M. Gamage, D.H. Russell, Increased ion transmission in IMS: A high resolution, periodic-focusing DC ion guide ion mobility spectrometer, Int. J. Mass Spectrom., doi:10.1016/j.ijms.2010.08.016 (2010).

[155] D.E. Clemmer, M.F. Jarrold, Metal-containing carbon clusters: Structures, isomerization, and formation of NbCn+ clusters, J. Am. Chem. Soc., 117 (1995) 8841-8850.

[156] P. Dugourd, R.R. Hudgins, J.M. Tenenbaum, M.F. Jarrold, Observation of new ring isomers for carbon cluster anions, Phys. Rev. Letters, 80 (1998) 4197-4200.

[157] M.F. Jarrold, V.A. Constant, Silicon cluster ions: Evidence for a structural transition, Phys. Rev. Letters, 67 (1991) 2994-2997.

[158] G. von Helden, P.R. Kemper, N.G. Gotts, M.T. Bowers, Isomers of small carbon cluster anions: Linear chains with up to 20 atoms, Science, 259 (1993) 1300-1302.

[159] P. Weis, P.R. Kemper, M.T. Bowers, Structures and energetics of $V_n(C_6H_6)_m^+$ clusters: Evidence for a quintuple-decker sandwich, J. Phys. Chem. A, 101 (1997) 8207-8213.

[160] G.A. Breaux, M.F. Jarrold, Probing helix formation in unsolvated peptides, J. Am. Chem. Soc., 125 (2003) 10740-10747.

[161] R.R. Hudgins, M.F. Jarrold, Helix formation in unsolvated alanine-based peptides: Helical monomers and helical dimers, J. Am. Chem. Soc., 121 (1999) 3494-3501.

[162] R.R. Hudgins, M.F. Jarrold, Conformations of unsolvated glycine-based peptides, J. Phys. Chem. B, 104 (2000) 2154-2158.

[163] D.E. Clemmer, R.R. Hudgins, M.F. Jarrold, Naked protein conformations: cytochrome c in the gas phase, J. Am. Chem. Soc., 117 (1995) 10141-10142.

[164] K.B. Shelimov, D.E. Clemmer, R.R. Hudgins, M.F. Jarrold, Protein structure *in vacuo*: Gas-phase conformations of BPTI and cytochrome c, J. Am. Chem. Soc., 119 (1997) 2240-2248.

[165] K.B. Shelimov, M.F. Jarrold, Conformations, unfolding, and refolding of apomyoglobin in vacuum: An activation barrier for gas-phase protein folding, J. Am. Chem. Soc., 119 (1997) 2987-2994.

[166] K.J. Gillig, D.H. Russell, Periodic field focusing ion mobility spectrometer, US Patent 6,639,213, (2003).

[167] C.M. Gamage, R.C. Blase, J.A. Silveira, D.H. Russell, Ion mobility in a periodic-focusing DC electric field, manuscript in preparation, (2010).

[168] T. Wyttenbach, M.T. Bowers, Gas-phase conformations: The ion mobility/ion chromatography method, Top. Curr. Chem., 225 (2003) 207-232.

[169] T. Wyttenbach, G. von Helden, M.T. Bowers, Gas-phase conformation of biological molecules: Bradykinin, J. Am. Chem. Soc., 118 (1996) 8355-8364.

[170] A.A. Shvartsburg, R.D. Smith, Fundamentals of traveling wave ion mobility spectrometry, Anal. Chem., 80 (2008) 9689-9699.

[171] J.L. Wildgoose, K. Giles, S.D. Pringle, S.L. Koeniger, S.J. Valentine, R.H. Bateman, D.E. Clemmer, Proceedings of the 54th Conference of the American Society for Mass Spectrometry, ThP 05 (2006).

[172] J.P. Williams, J.H. Scrivens, Coupling desorption electrospray ionisation and neutral desorption/extractive electrospray ionisation with a travelling-wave based ion mobility mass spectrometer for the analysis of drugs, Rapid Comm. Mass Spectrom., 22 (2008) 187-196.

[173] J.P. Williams, T. Bugarcic, A. Habtemariam, K. Giles, I. Campuzano, P.M. Rodger, P.J. Sadler, Isomer separation and gas-phase configurations of organoruthenium anticancer complexes: Ion mobility mass spectrometry and modeling, J. Am. Soc. Mass Spectrom., 20 (2009) 1119-1122.

[174] R.C. Flagan, History of electrical aerosol measurements, Aerosol Science and Technology, 28 (1998) 301-380.

[175] R.W. Purves, R. Guevremont, Electrospray ionization high-field asymmetric waveform ion mobility spectrometry-mass spectrometry, Anal. Chem., 71 (1999) 2346-2357.

[176] C. Becker, K. Qian, D.H. Russell, Molecular Weight Distributions of Asphaltenes and Deasphaltened Oils Studied by Laser Desorption Ionization and Ion Mobility Mass Spectrometry, Anal. Chem., 80 (2008) 8592-8597.

[177] F.A. Fernandez-Lima, C. Becker, A.M. McKenna, R.P. Rodgers, A.G. Marshall, D.H. Russell, Petroleum Crude Oil Characterization by IMS-MS and FTICR MS, Anal. Chem., 81 (2009) 9941-9947.

[178] B.C. Bohrer, S.I. Merenbloom, S.L. Koeniger, A.E. Hilderbrand, D.E. Clemmer, Biomolecule analysis by ion mobility spectrometry, Annu. Rev. Anal. Chem., 1 (2008).

[179] F.A. Fernandez-Lima, R.C. Blase, D.H. Russell, A study of ion-neutral collision cross-section values for low charge states of peptides, proteins, and peptide/protein complexes, Int. J. Mass Spectrom., 298 (2010) 111-118.

[180] L. Tao, J.R. McLean, J.A. McLean, D.H. Russell, J. Am. Soc. Mass Spectrom., 18 (2007) 1232-1238.

[181] J.A. McLean, The Mass-Mobility Correlation Redux: The Conformational Landscape of Anhydrous Biomolecules, J. Am. Soc. Mass Spectrom., 20 (2009) 1775-1781.

[182] H.E. Revercomb, E.A. Mason, Theory of plasma chromatography/gaseous electrophoresis - A Review, Anal. Chem., 47 (1975) 970-983.

[183] R. Kurulugama, F.M. Nachtigall, S. Lee, S.J. Valentine, D.E. Clemmer, Overtone Mobility Spectrometry: Part 1. Experimental Observations, J. Am. Soc. Mass Spectrom., 20 (2009) 729-737.

[184] S.I. Merenbloom, R.S. Glaskin, Z.B. Henson, D.E. Clemmer, High-Resolution Ion Cyclotron Mobility Spectrometry, Anal. Chem., 81 (2009) 1482-1487.

[185] S.J. Valentine, S.T. Stokes, R. Kurulugama, F.M. Nachtigall, D.E. Clemmer, Overtone Mobility Spectrometry: Part 2. Theoretical Considerations of Resolving Power, J. Am. Soc. Mass Spectrom., 20 (2009) 738-750.

[186] J.C. May, in: Development of a Cryogenic Drift Cell Spetrometer and Methods for Improving the Analytical Figures of Merit for Ion Mobility-Mass Spectrometry Analysis, Ph.D. Dissertation, Department of Chemistry, Texas A&M University, (2009).

[187] G.F. Verbeck, K.J. Gillig, D.H. Russell, Variable-temperature ion mobility time-of-flight mass spectrometry studies of electronic isomers of Kr^{2+} and $CH_3OH^{+\cdot}$ radical cations, Eur. J. Mass Spectrom., 9 (2003) 579-587.

[188] W. Sun, J.C. May, K.J. Gillig, D.H. Russell, A dual time-of-flight apparatus for an ion mobility-surface-induced-dissociation-mass spectrometer for high-throughput peptide sequencing, Int. J. Mass Spectrom., 287 (2009) 39-45.

[189] J.A. McLean, W.K. Russell, D.H. Russell, A High Repetition Rate (1 kHz) Microcrystal Laser for High Throughput Atmospheric Pressure MALDI-Quadrupole-Time-of-Flight Mass Spectrometry, Anal. Chem., 75 (2003) 648-654.

[190] J.A. McLean, D.H. Russell, Data Acquisition Based on Analyte Dispersion in Two Dimensions: More Signal More of the Time, Int. J. Ion Mobility Spectrom., 8 (2005) 66-71.

[191] J.C. May, in: Development of a cryogenic drift cell spectrometer and methods for improving the analytical figures of merit for ion mobility-mass spectrometry analysis, Ph.D. Dissertation, Department of Chemistry, Texas A&M University, (2009).

[192] F.W. Karasek, M.J. Cohen, D.I. Carroll, Trace studies of alcohols in the plasma chromatography-mass spectrometer, Journal of Chromatographic Science, 9 (1971).

[193] F.W. Karasek, S.H. Kim, H.H. Hill, Jr., Mass identified mobility spectra of p-nitrophenol and reactant ions in plasma chromatography, Anal. Chem., 48 (1976).

[194] S.H. Kim, G.E. Spangler, Ion mobility spectrometry / mass spectrometry (IMS/MS) of two structurally different ions having identical ion mass, Anal. Chem., 57 (1985).

[195] J. Kapron, D.A. Barnett, Selectivity improvement for drug urinalysis using FAIMS and H-SRM on the Finnigan TSQ Quantum Ultra, Thermo Electron Corporation: San Jose, CA, USA., Application Note: 362 (2006).

[196] B.K. Blum, K.J. Gillig, D.H. Russell, Development of a Fourier-transform ion cyclotron resonance mass spectrometer-ion mobility spectrometer, Rev. Sci. Instrum., 71 (2000).

[197] X. Tang, J.E. Bruce, H.H. Hill, Jr., Design and performance of an atmospheric pressure ion mobility Fourier transform ion cyclotron resonance mass spectrometer, Rapid Commun. Mass Spectrom., 21 (2006).

[198] E.W. Robinson, E.R. Williams, Multidimensional separations of ubiquitin conformers in the gas phase: relating ion cross sections to H/D exchange measurements, J. Am. Soc. Mass Spectrom., 16 (2005).

[199] E.W. Robinson, D.E. Garcia, R.D. Leib, E.R. Williams, Enhanced mixture analysis of ploy(ethylene glycol) using high-field assymetric waveform ion mobility spectrometry combined with fourier transform ion cyclotron resonance mass spectrometry, Anal. Chem., 78 (2006).

[200] O.A. Mirgorodskaya, A. Shevchenko, I.V. Chernushevich, A.F. Dodonov, A.I. Miroshnikov, Electrospray ionization time-of-flight mass spectrometry in protein chemistry, Anal. Chem., 66 (1994) 99-107.

[201] P. Dwivedi, P. Wu, S.J. Klopsch, G.J. Puzon, L. Xun, H.H. Hill, Jr., Metabolic profiling by ion mobility mass spectrometry (IMMS), Metabolomics, 4 (2008) 63-80.

[202] S.J. Valentine, M. Plasencia, X. Liu, M. Krishnan, S. Naylor, H.R. Udseth, R.D. Smith, D.E. Clemmer, Toward plasma proteome profiling with ion mobility-mass spectrometry, J. Proteome Res., 5 (2006) 2977-2984.

[203] J. Zaia, Mass spectrometry and the emerging field of glycomics, Chem. Biol., 15 (2008) 881-892.

[204] B.H. Clowers, P. Dwivedi, W.E. Steiner, H.H. Hill, Jr., B. Bendiak, Separation of sodiated isobaric disaccharides and trisaccharides using electrospray ionization-atmospheric pressure ion mobility-time of flight mass spectrometry, J. Am. Soc. Mass Spectrom., 16 (2005) 660-669.

[205] T.O. Metz, J.S. Page, E.S. Baker, K. Tang, J. Ding, Y. Shen, R.D. Smith, High-resolution separations and improved ion production and transmission in metabolomics, Trends in Analytical Chemistry, 27 (2008) 205-214.

[206] J.R. McLean, J.A. McLean, Z. Wu, C. Becker, L.M. Perez, C.N. Pace, J.M. Scholtz, D.H. Russell, Factors that influence helical preferences for singly charged gas-phase peptide ions: The effects of multiple potential charge-carrying sites, J. Phys. Chem. B, 114 (2010) 809-816.

[207] L. Tao, D.B. Dahl, L.M. Perez, D.H. Russell, The contributions of molecular framework to IMS collision cross-sections of gas-phase peptide ions, J. Am. Soc. Mass Spectrom., 20 (2009) 1593-1602.

[208] E. de Hoffmann, Tandem mass spectrometry: a primer, J. Mass Spectrom., 31 (1996) 129-137.

[209] F.W. McLafferty, P.J. Todd, D.C. McGilvery, M.A. Baldwin, High-resolution tandem mass spectrometer (MS/MS) of increased sensitivity and mass range, J. Am. Chem. Soc., 102 (1980) 3360-3363.

[210] T.L. Kruger, J.F. Litton, R.W. Kondrat, R.G. Cooks, Mixture analysis by mass-analyzed ion kinetic energy spectrometry, Anal. Chem., 48 (1976) 2113-2119.

[211] S.A. McLuckey, G.L. Glish, R.G. Cooks, Kinetic energy effects in mass spectrometry/mass spectrometry using a sector/quadrupole tandem instrument, Int. J. Mass Spectrom. Ion Physics, 39 (1981) 219-230.

[212] R.A. Yost, C.G. Enke, Selected ion fragmentation with a tandem quadrupole mass spectrometer, J. Am. Chem. Soc., 100 (1978) 2274-2275.

[213] K.R. Jennings, Collision-induced decompositions of aromatic molecular ions, Int. J. Mass Spectrom. Ion Physics, 1 (1968) 227-235.

[214] W.F. Haddon, F.W. McLafferty, Metastable ion characteristics. VII. Collision-induced metastables, J. Am. Chem. Soc., 90 (1968) 4745-4746.

[215] N.J. Jensen, M.L. Gross, Mass spectrometry methods for structural determination and analysis of fatty acids, Mass Spectrom. Rev., 6 (1987) 497-536.

[216] F.W. McLafferty, Tandem mass spectrometry (MS/MS): A promising new analytical technique for specific component determination in complex mixtures, Acc. Chem. Res., 13 (1980) 33-39.

[217] J.M. Wells, S.A. McLuckey, Collision-induced dissociation (CID) of peptides and proteins, Methods in Enzymology, 402 (2005) 148-185.

[218] R.G. Cooks, D.T. Terwilliger, T. Ast, J.H. Beynon, T. Keough, Surface modified mass spectrometry, J. Am. Chem. Soc., 97 (1974) 1583-1585.

[219] A.R. Dongre, A. Somogyi, V.H. Wysocki, Surface-induced dissociation: An effective tool to probe structure, energetics, and fragmentation mechanisms of protonated peptides, J. Mass Spectrom., 31 (1996) 339-350.

[220] W.D. Bowers, S.S. Delbert, R.L. Hunter, R.T.J. McIver, Fragmentation of oligopeptide ions using ultraviolet laser radiation and Fourier transform mass spectrometry, J. Am. Chem. Soc., 106 (1984) 7288-7289.

[221] R.A. Zubarev, N.L. Kelleher, F.W. McLafferty, Electron capture dissociation of multiply charged protein cations. A nonergodic process, J. Am. Chem. Soc., 120 (1998) 3265-3266.

[222] J.E.P. Syka, J.J. Coon, M.J. Schroeder, J. Shabanowitz, D.F. Hunt, Peptide and protein sequence analysis by electron transfer dissociation mass spectrometry, Proc. Natl. Acad. Sci. USA, 101 (2004) 9528-9533.

[223] N.L. Kelleher, H.Y. Lin, G.A. Valaskovic, D.J. Aaserud, E.K. Fridriksson, F.W. McLafferty, Top down versus bottom up protein characterization by tandem high-resolution mass spectrometry, J. Am. Chem. Soc., 121 (1999) 806-812.

[224] K. Biemann, Appendix 5. Nomenclature for peptide fragment ions (positive ions), Methods in Enzymology, 193 (1990) 886-887.

[225] E.G. Stone, K.J. Gillig, B.T. Ruotolo, D.H. Russell, Optimization of a matrix-assisted laser desorption ionization-ion mobility-surface-induced dissociation-orthogonal-time-of-flight mass spectrometer: simultaneous acquisition of multiple correlated MS^1 and MS^2 spectra, Int. J. Mass Spectrom., 212 (2001) 519-533.

[226] W. Sun, J.C. May, D.H. Russell, A novel surface-induced dissociation instrument for ion mobility-time-of-flight mass spectrometry, Int. J. Mass Spectrom., 259 (2007) 79-86.

[227] C. Becker, F.A. Fernandez-Lima, K.J. Gillig, W.K. Russell, S.M. Cologna, D.H. Russell, A novel approach to collision-induced dissociation (CID) for ion mobility-mass spectrometry experiments, J. Am. Soc. Mass Spectrom., 20 (2009) 907-914.

[228] F.A. Fernandez-Lima, C. Becker, K.J. Gillig, W.K. Russell, S.E. Tichy, D.H. Russell, Ion mobility-mass spectrometer interface for collisional activation of mobility separated ions, Anal. Chem., 81 (2009) 618-624.

[229] Y.J. Lee, C.S. Hoaglund-Hyzer, C.A. Srebalus Barnes, A.E. Hilderbrand, S.J. Valentine, D.E. Clemmer, Development of high-throughput liquid chromatography injected ion mobility quadrupole time-of-flight techniques for analysis of complex peptide mixtures, J. Chromatogr. B, 782 (2002) 343-351.

[230] M.H. Moon, S. Myung, M. Plasencia, A.E. Hilderbrand, D.E. Clemmer, Nanoflow LC/ion mobility/CID/TOF for proteomics: Analysis of a human urinary proteome, Journal of Proteome Research, 2 (2003) 589-597.

[231] N.C. Polfer, B.C. Bohrer, M. Plasencia, B. Paizs, D.E. Clemmer, On the dynamics of fragment isomerization in collision-induced dissociation of peptides, J. Phys. Chem. A, 112 (2008) 1286-1293.

[232] S.A. McLuckey, T.-Y. Huang, Ion/ion reactions: New chemistry for analytical MS, Anal. Chem., 81 (2009) 8669-8676.

[233] Y. Xia, S.A. McLuckey, Evolution of instrumentation for the study of gas-phase ion/ion chemistry via mass spectrometry, J. Am. Soc. Mass Spectrom., 19 (2008) 173-189.

[234] G.E. Reid, J.M. Wells, E.R. Badman, S.A. McLuckey, Performance of a quadrupole ion trap mass spectrometer adapted for ion/ion reaction studies, Int. J. Mass Spectrom., 222 (2003) 243-258.

[235] S.J. Pitteri, P.A. Chrisman, J.M. Hogan, S.A. McLuckey, Electron transfer ion/ion reactions in a three-dimensional quadrupole ion trap: Reactions of doubly and triply protonated peptides with SO_2^-, Anal. Chem., 77 (2005) 1831-1839.

[236] Y. Xia, J. Wu, F.A. Londry, J.W. Hager, S.A. McLuckey, Mutual storage mode ion/ion reactions in hybrid linear ion trap, J. Am. Soc. Mass Spectrom., 16 (2005) 71-81.

[237] J. Liu, T.-Y. Huang, S.A. McLuckey, Simultaneous transmission mode collision-induced dissociation and ion/ion reactions for top-down protein identification/characterization using a quadrupole/time-of-flight tandem mass spectrometer, Anal. Chem., 81 (2009) 2159-2167.

[238] Y. Xia, H. Han, S.A. McLuckey, Activation of intact electron-transfer products of polypeptides and proteins in cation transmission mode ion/ion reactions, Anal. Chem., 80 (2008) 1111-1117.

[239] Y. Xia, P.A. Chrisman, D.E. Erickson, J. Liu, X. Liang, F.A. Londry, M.J. Yang, S.A. McLuckey, Implementation of ion/ion reactions in a quadrupole/time-of-flight tandem mass spectrometer, Anal. Chem., 78 (2006) 4146-4154.

[240] I.V. Chernushevich, A.V. Loboda, B.A. Thomson, An introduction to quadrupole-time-of-flight mass spectrometry, J. Mass Spectrom., 36 (2001) 849-865.

[241] A.N. Krutchinsky, A.V. Loboda, V.L. Spicer, W.E. Dworschak, K.G. Standing, Orthogonal injection of matrix-assisted laser desorption/ionization ions into a time-of-flight spectrometer through a collisional damping interface, Rapid Commun. Mass Spectrom., 12 (1998) 508-518.

[242] J.M. Heimerl, R. Johnsen, M.A. Biondi, Ion-molecule reactions, $He^+ + O_2$ and $He^+ + N_2$, at thermal energies and above, J. Chem. Phys., 51 (1969) 5041-5048.

[243] R. Johnsen, H.L. Brown, M.A. Biondi, Ion-molecule reactions involving N_2^+, N^+, O_2^+, and O^+ ions from 300K to about 1 eV, J. Chem. Phys., 52 (1970) 5080-5084.

[244] R. Johnsen, M.A. Biondi, Measurements of the $O^+ + N_2$ and $O^+ + O_2$ reaction rates from 300K to 2 eV, J. Chem. Phys., (1973) 3504-3509.

[245] S. Lee, S.J. Valentine, D.E. Clemmer, Development of a "ping-pong" drift tube: Theoretical considerations of resolving power, Poster Presentation at the 58th ASMS Conference on Mass Spectrometry and Allied Topics, WP 639, (2010).

[246] E.W. McDaniel, Possible sources of large error in determinations of ion-molecule reaction rates with drift tube mass spectrometers, J. Chem. Phys., 52 (1970) 3931-3935.

[247] K. Iinuma, M. Takebe, Y. Satoh, K. Seto, Design of a continuous guard ring and its application to swarm experiments., Rev. Sci. Instrum., 53 (1982) 845-850.

[248] K. Iinuma, M. Takebe, Y. Satoh, K. Seto, Measurements of mobilities and longitudinal diffusion coefficients by a flight-distance scanning method: Comparison with the flight-time scanning method, J. Chem. Phys., 79 (1983) 3906-3910.

APPENDIX A

A-1

DRIFT TIME SPECTRA OF RADICAL CATIONS OF C_{60} AND C_{70} ON A 62.5 CM PDC IG DRIFT CELL EQUIPPED WITH ELECTRODE CONFIGURATION A ELECTRODES

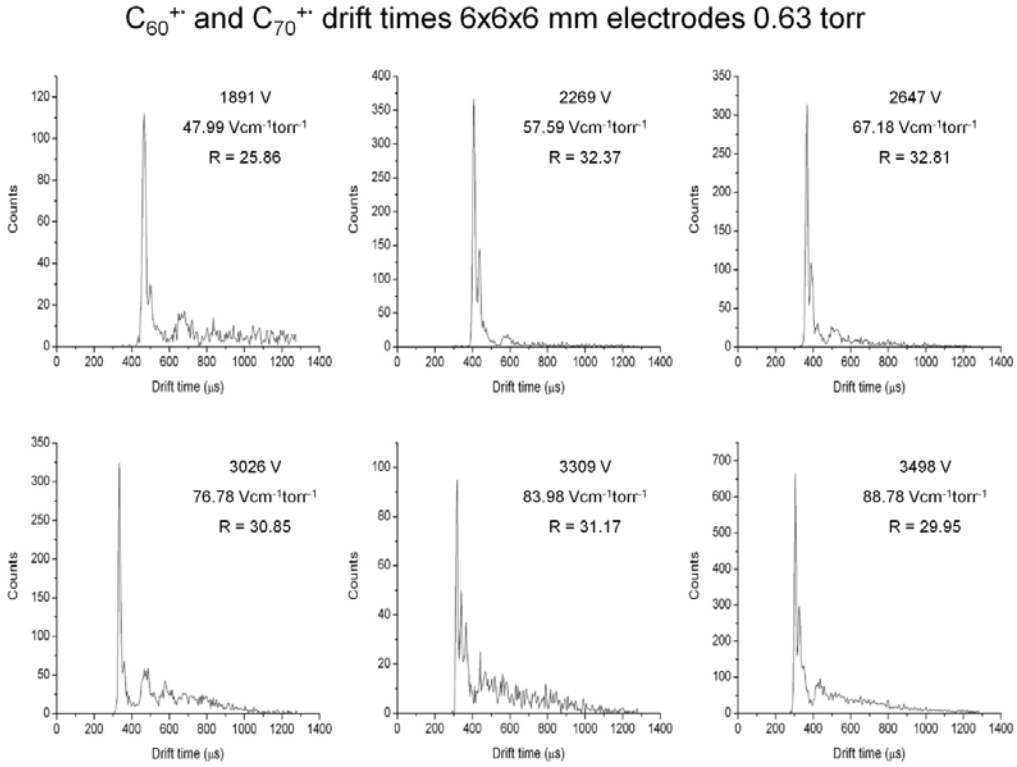

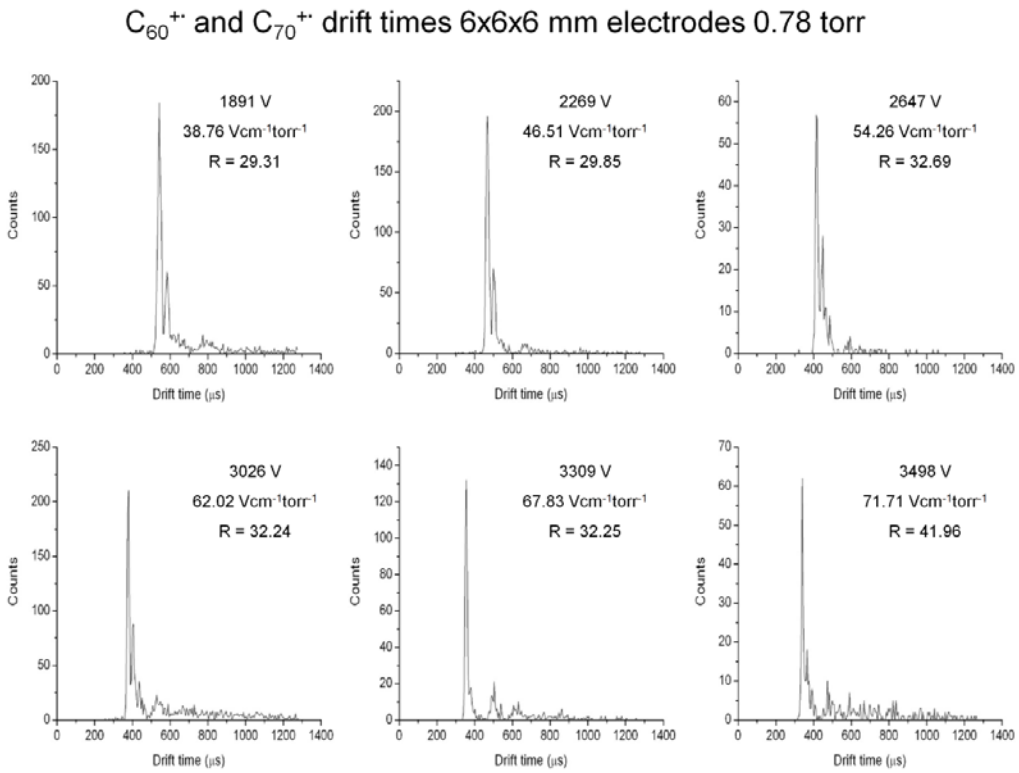
$C_{60}^{+\cdot}$ and $C_{70}^{+\cdot}$ drift times 6x6x6 mm electrodes 0.78 torr
1891 V
38.76 Vcm⁻¹torr⁻¹
R = 29.31
2269 V
46.51 Vcm⁻¹torr⁻¹
R = 29.85
2647 V
54.26 Vcm⁻¹torr⁻¹
R = 32.69
3026 V
62.02 Vcm⁻¹torr⁻¹
R = 32.24
3309 V
67.83 Vcm⁻¹torr⁻¹
R = 32.25
3498 V
71.71 Vcm⁻¹torr⁻¹
R = 41.96
Counts
Drift time (μs)

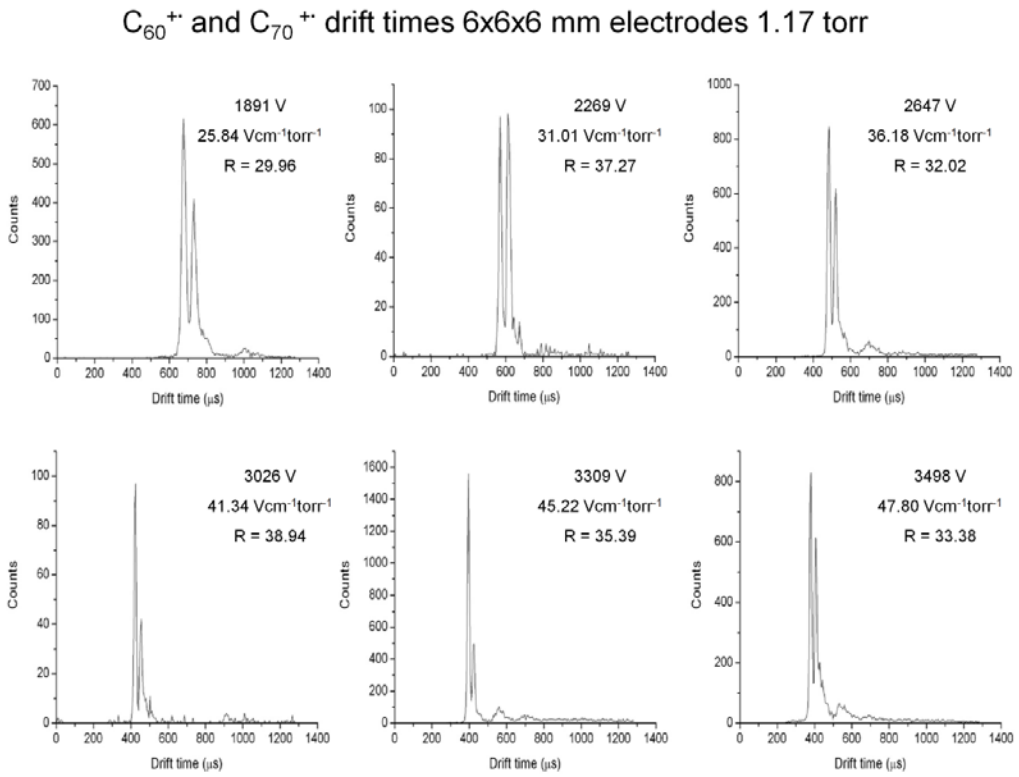
$C_{60}^{+\cdot}$ and $C_{70}^{+\cdot}$ drift times 6x6x6 mm electrodes 1.17 torr
1891 V
25.84 Vcm⁻¹torr⁻¹
R = 29.96
2269 V
31.01 Vcm⁻¹torr⁻¹
R = 37.27
2647 V
36.18 Vcm⁻¹torr⁻¹
R = 32.02
3026 V
41.34 Vcm⁻¹torr⁻¹
R = 38.94
3309 V
45.22 Vcm⁻¹torr⁻¹
R = 35.39
3498 V
47.80 Vcm⁻¹torr⁻¹
R = 33.38
Counts
Drift time (μs)

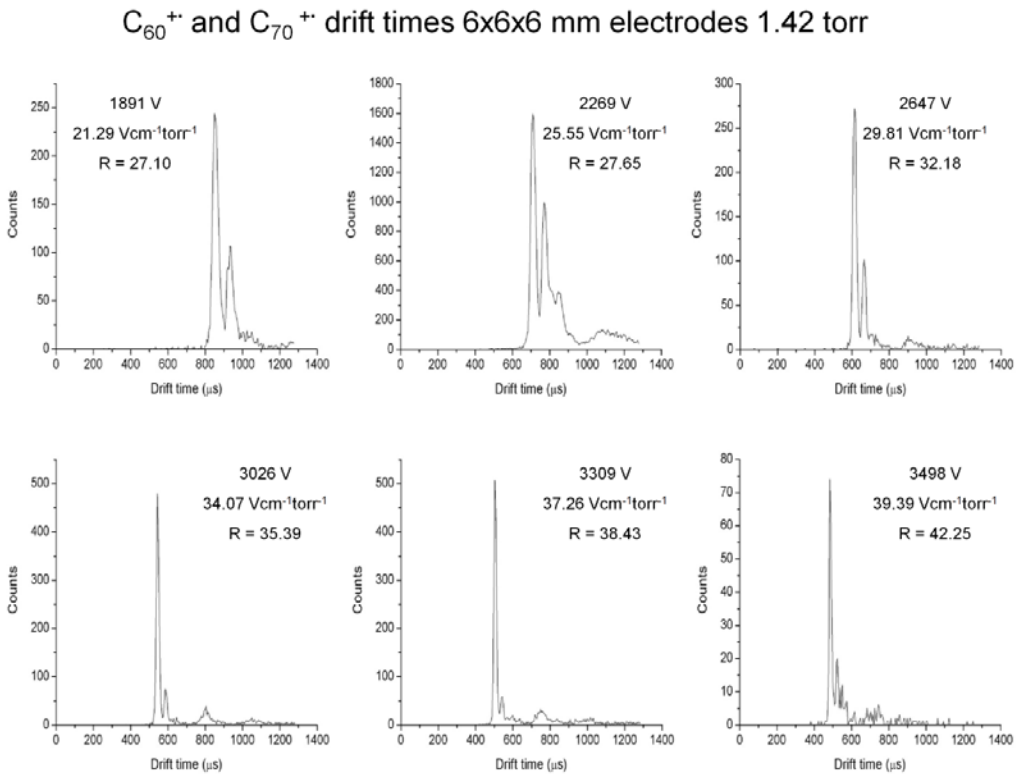
$C_{60}^{+\cdot}$ and $C_{70}^{+\cdot}$ drift times 6x6x6 mm electrodes 1.42 torr
1891 V
21.29 Vcm⁻¹torr⁻¹
R = 27.10
2269 V
25.55 Vcm⁻¹torr⁻¹
R = 27.65
2647 V
29.81 Vcm⁻¹torr⁻¹
R = 32.18
3026 V
34.07 Vcm⁻¹torr⁻¹
R = 35.39
3309 V
37.26 Vcm⁻¹torr⁻¹
R = 38.43
3498 V
39.39 Vcm⁻¹torr⁻¹
R = 42.25
Counts
Drift time (μs)

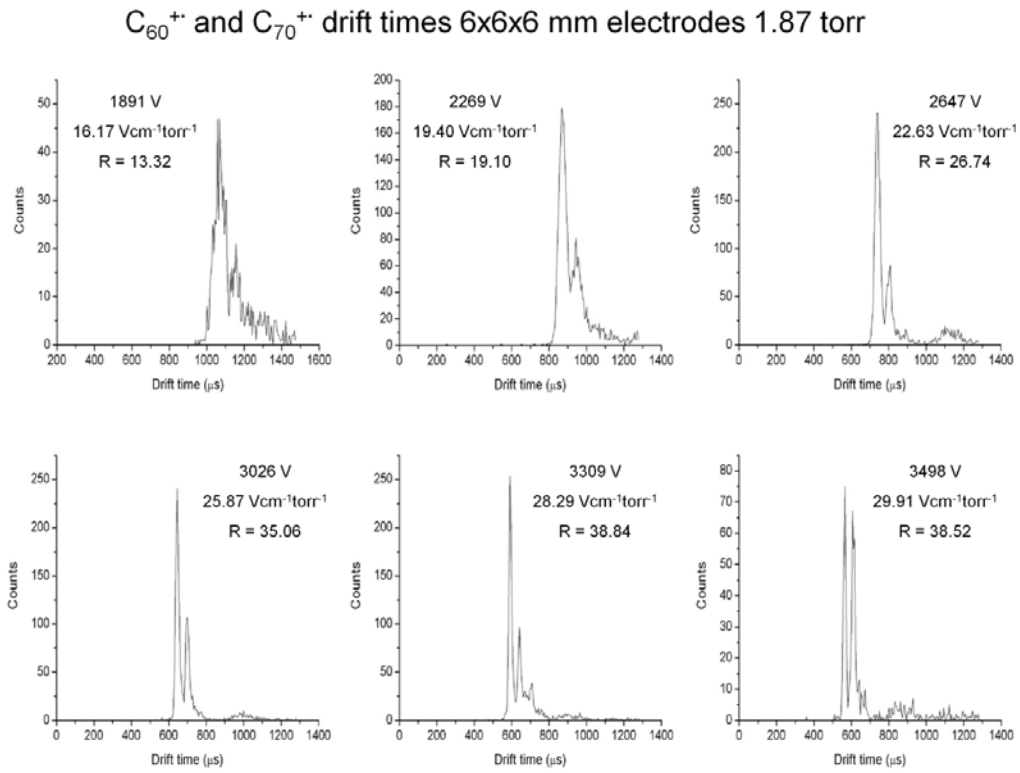
$C_{60}^{+\cdot}$ and $C_{70}^{+\cdot}$ drift times 6x6x6 mm electrodes 1.87 torr
1891 V
16.17 Vcm⁻¹torr⁻¹
R = 13.32
2269 V
19.40 Vcm⁻¹torr⁻¹
R = 19.10
2647 V
22.63 Vcm⁻¹torr⁻¹
R = 26.74
3026 V
25.87 Vcm⁻¹torr⁻¹
R = 35.06
3309 V
28.29 Vcm⁻¹torr⁻¹
R = 38.84
3498 V
29.91 Vcm⁻¹torr⁻¹
R = 38.52
Counts
Drift time (μs)

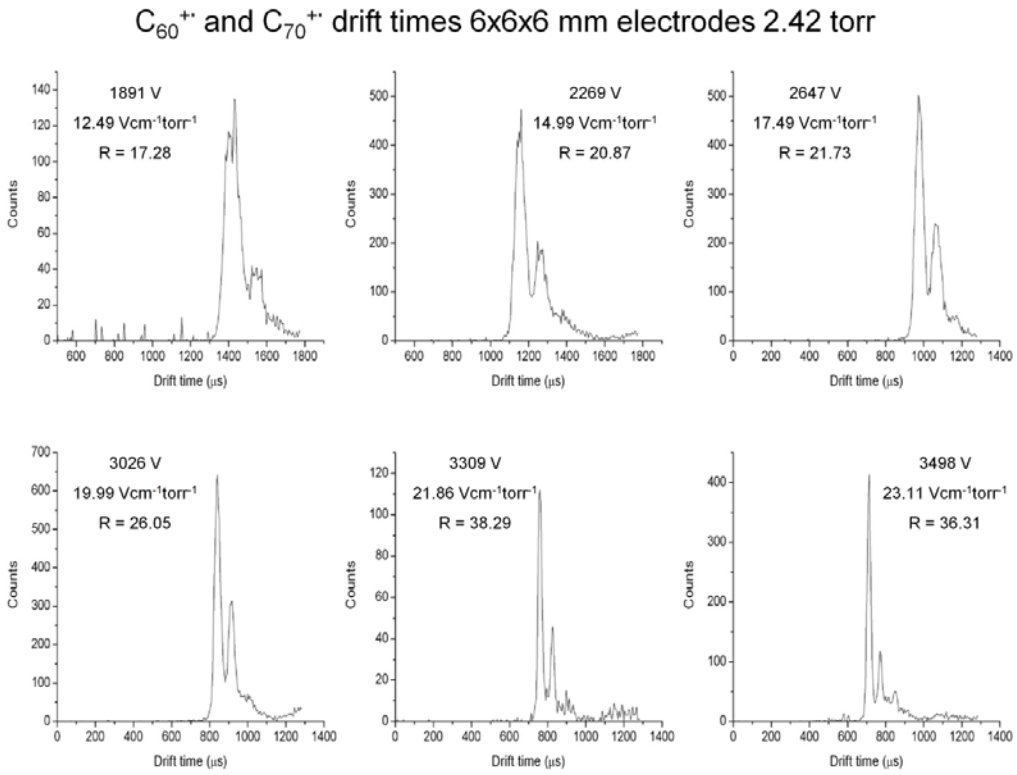
$C_{60}^{+\cdot}$ and $C_{70}^{+\cdot}$ drift times 6x6x6 mm electrodes 2.42 torr
1891 V
12.49 Vcm⁻¹torr⁻¹
R = 17.28
2269 V
14.99 Vcm⁻¹torr⁻¹
R = 20.87
2647 V
17.49 Vcm⁻¹torr⁻¹
R = 21.73
3026 V
19.99 Vcm⁻¹torr⁻¹
R = 26.05
3309 V
21.86 Vcm⁻¹torr⁻¹
R = 38.29
3498 V
23.11 Vcm⁻¹torr⁻¹
R = 36.31
Counts
Drift time (μs)

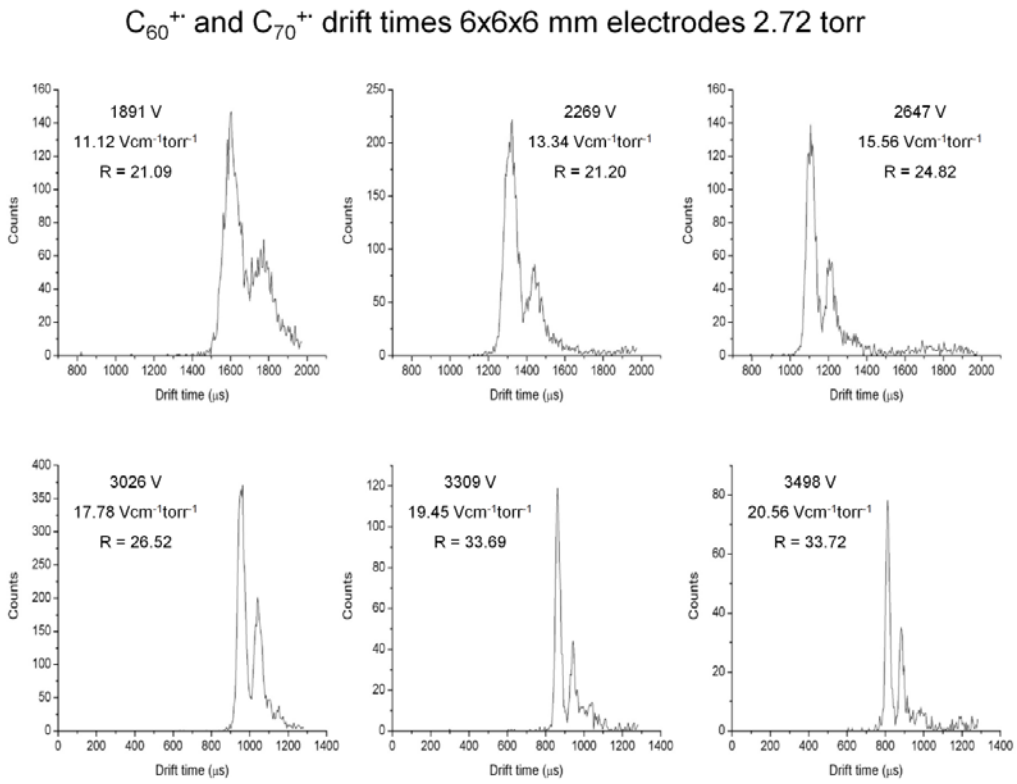
$C_{60}^{+\cdot}$ and $C_{70}^{+\cdot}$ drift times 6x6x6 mm electrodes 2.72 torr
1891 V
11.12 Vcm⁻¹torr⁻¹
R = 21.09
2269 V
13.34 Vcm⁻¹torr⁻¹
R = 21.20
2647 V
15.56 Vcm⁻¹torr⁻¹
R = 24.82
3026 V
17.78 Vcm⁻¹torr⁻¹
R = 26.52
3309 V
19.45 Vcm⁻¹torr⁻¹
R = 33.69
3498 V
20.56 Vcm⁻¹torr⁻¹
R = 33.72
Counts
Drift time (μs)

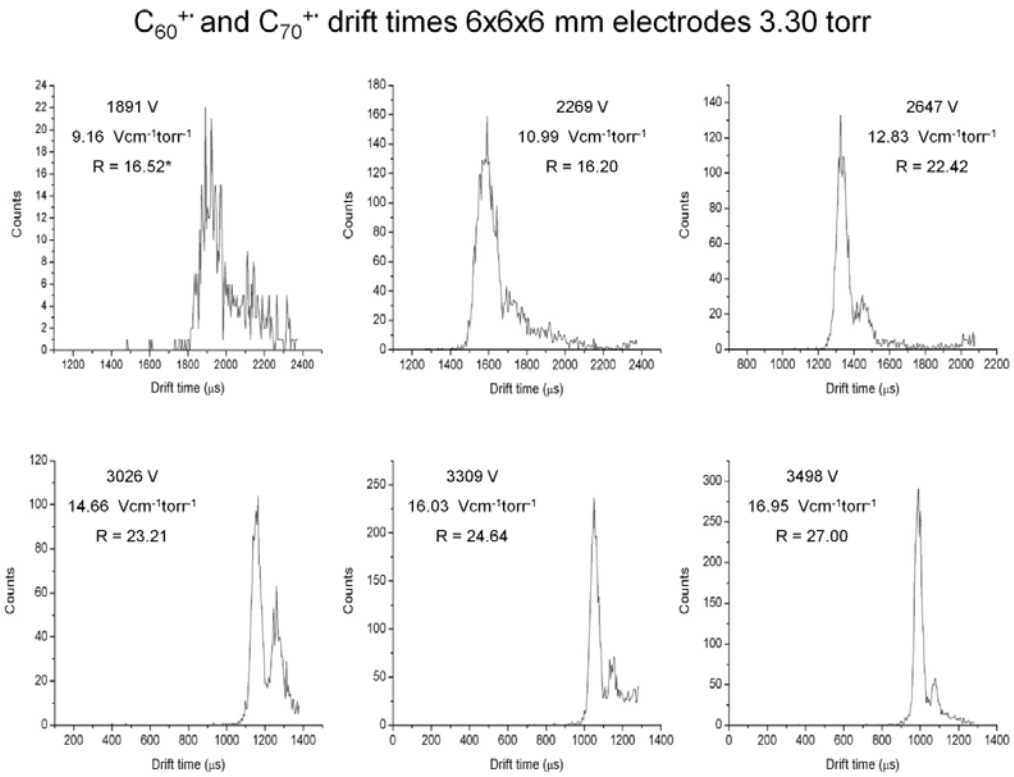
$C_{60}^{+\cdot}$ and $C_{70}^{+\cdot}$ drift times 6x6x6 mm electrodes 3.30 torr
1891 V
9.16 Vcm⁻¹torr⁻¹
R = 16.52*
2269 V
10.99 Vcm⁻¹torr⁻¹
R = 16.20
2647 V
12.83 Vcm⁻¹torr⁻¹
R = 22.42
3026 V
14.66 Vcm⁻¹torr⁻¹
R = 23.21
3309 V
16.03 Vcm⁻¹torr⁻¹
R = 24.64
3498 V
16.95 Vcm⁻¹torr⁻¹
R = 27.00
Counts
Drift time (μs)

A-2

DRIFT TIME SPECTRA OF PROTONATED VAL-4-ANGIOTENSIN I ON A 62.5 CM PDC IG DRIFT CELL EQUIPPED WITH ELECTRODE CONFIGURATION A ELECTRODES

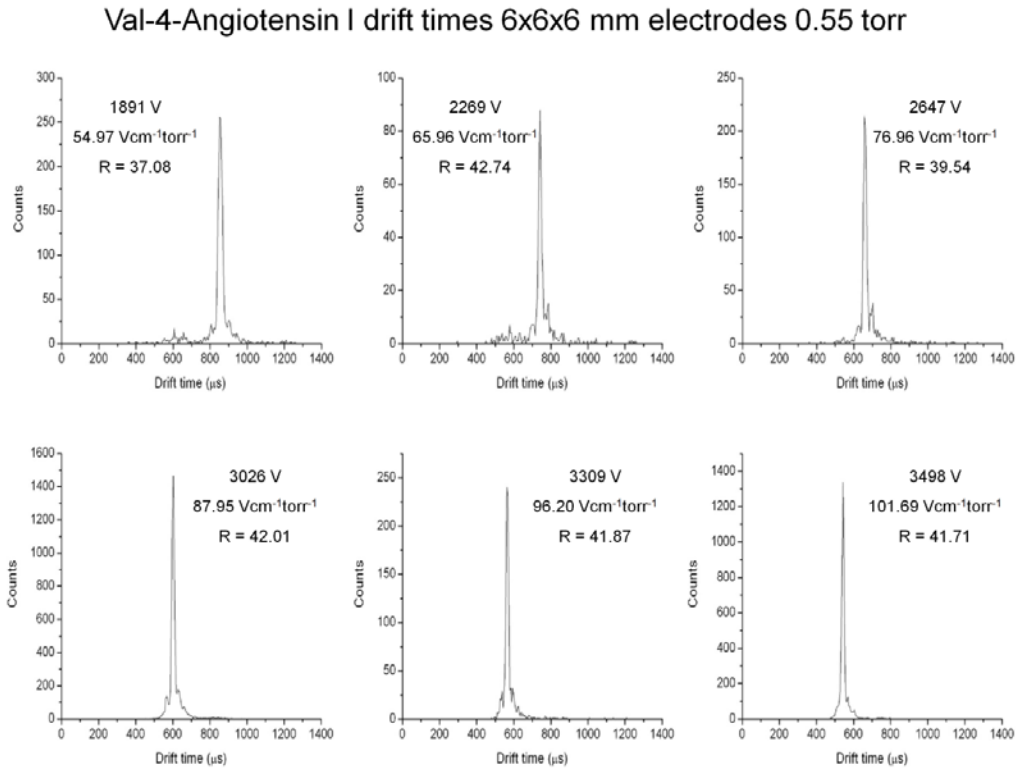

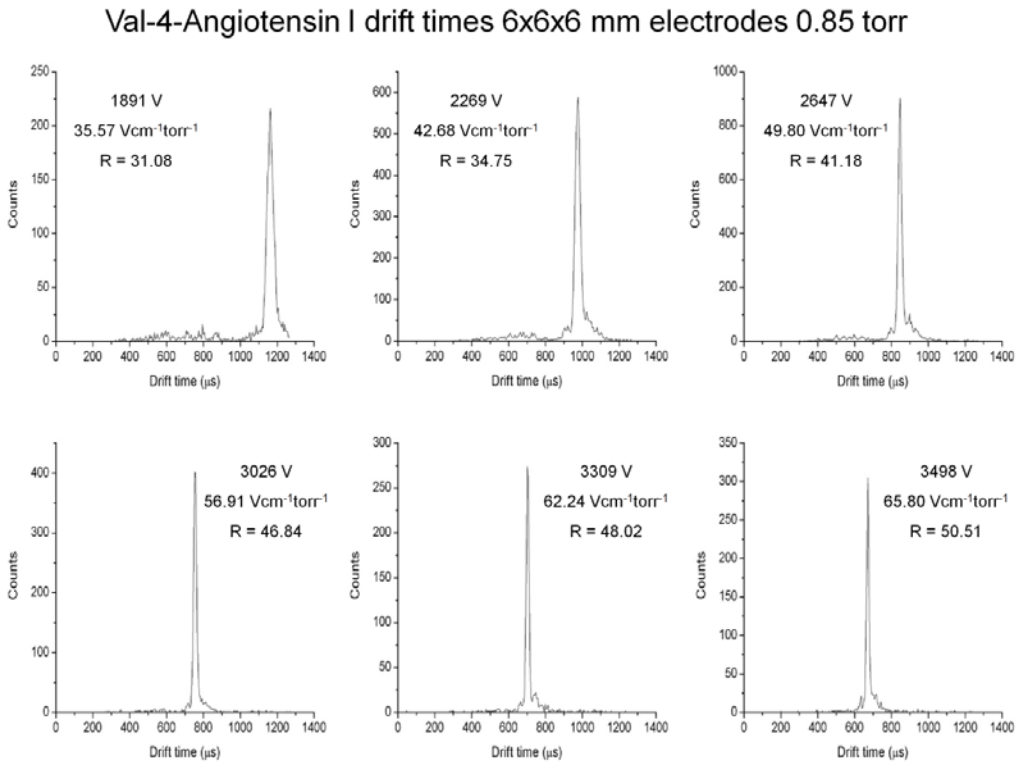
Val-4-Angiotensin I drift times 6x6x6 mm electrodes 0.85 torr
1891 V
35.57 Vcm-1torr-1
R = 31.08
2269 V
42.68 Vcm-1torr-1
R = 34.75
2647 V
49.80 Vcm-1torr-1
R = 41.18
3026 V
56.91 Vcm-1torr-1
R = 46.84
3309 V
62.24 Vcm-1torr-1
R = 48.02
3498 V
65.80 Vcm-1torr-1
R = 50.51
Counts
Drift time (μs)

Val-4-Angiotensin I drift times 6x6x6 mm electrodes 1.24 torr

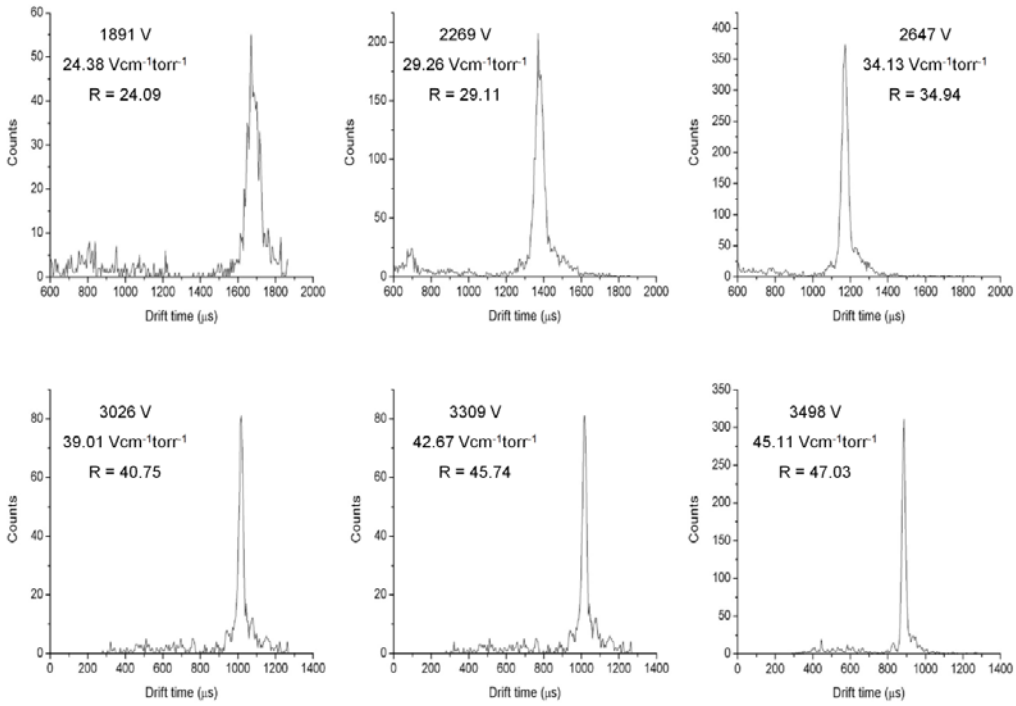

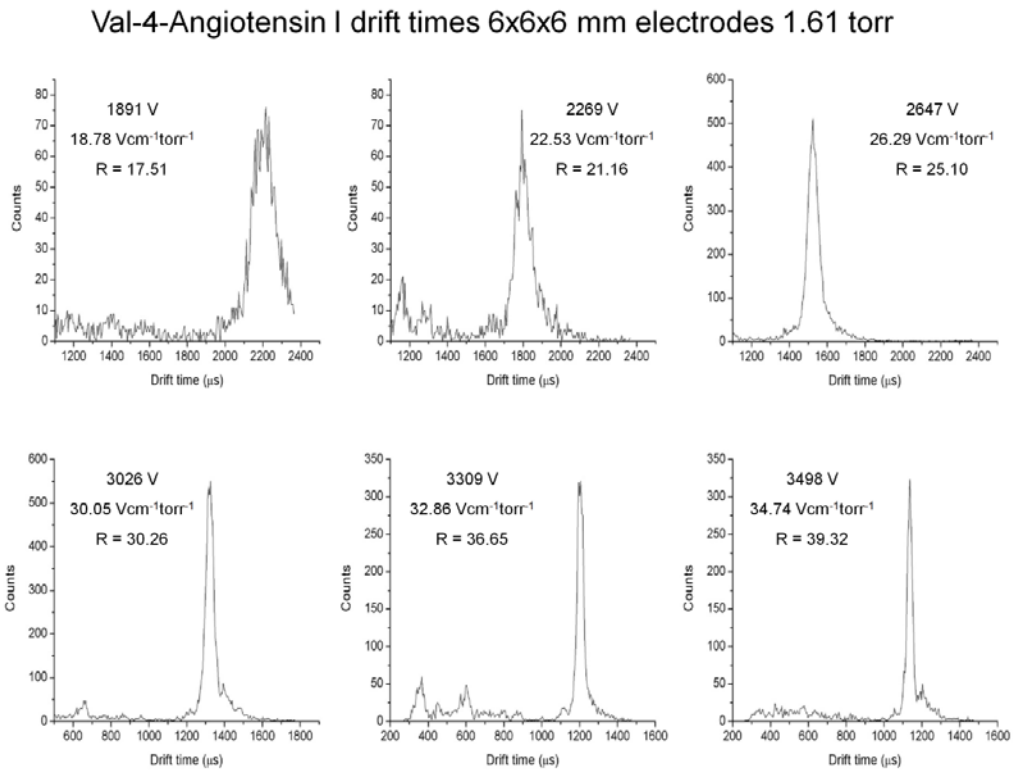
Val-4-Angiotensin I drift times 6x6x6 mm electrodes 1.61 torr
1891 V
18.78 Vcm-1torr-1
R = 17.51
2269 V
22.53 Vcm-1torr-1
R = 21.16
2647 V
26.29 Vcm-1torr-1
R = 25.10
3026 V
30.05 Vcm-1torr-1
R = 30.26
3309 V
32.86 Vcm-1torr-1
R = 36.65
3498 V
34.74 Vcm-1torr-1
R = 39.32
Counts
Drift time (µs)

Val-4-Angiotensin I drift times 6x6x6 mm electrodes 1.97 torr

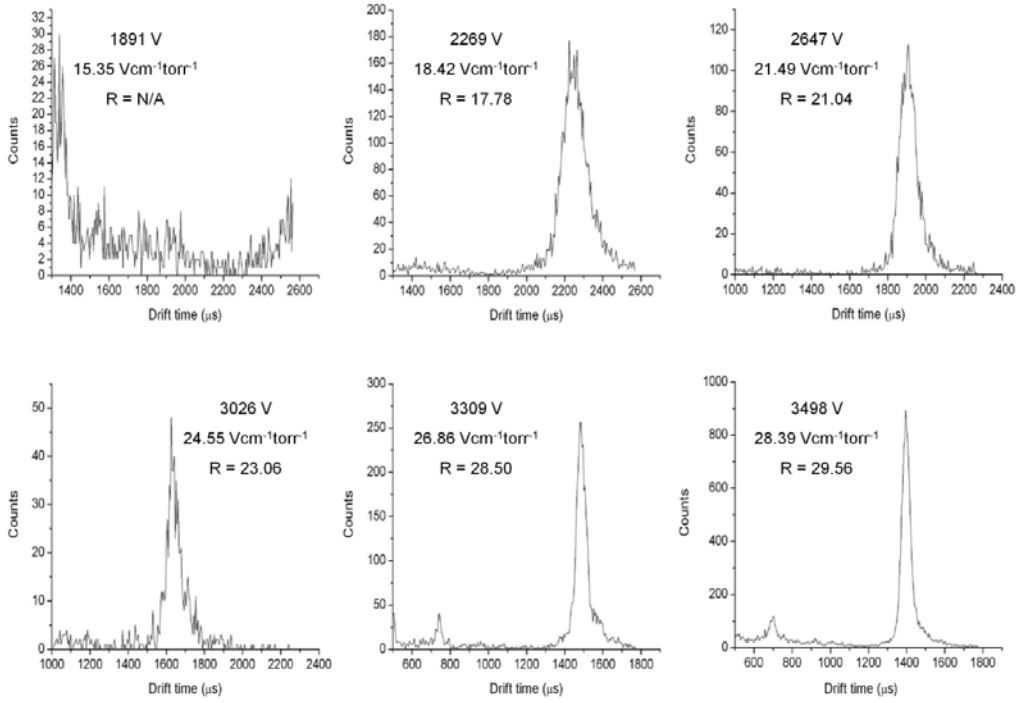

A-3

DRIFT TIME SPECTRA OF PROTONATED GLU-FIBRINOPEPTIDE B ON A 62.5 CM PDC IG DRIFT CELL EQUIPPED WITH ELECTRODE CONFIGURATION A ELECTRODES

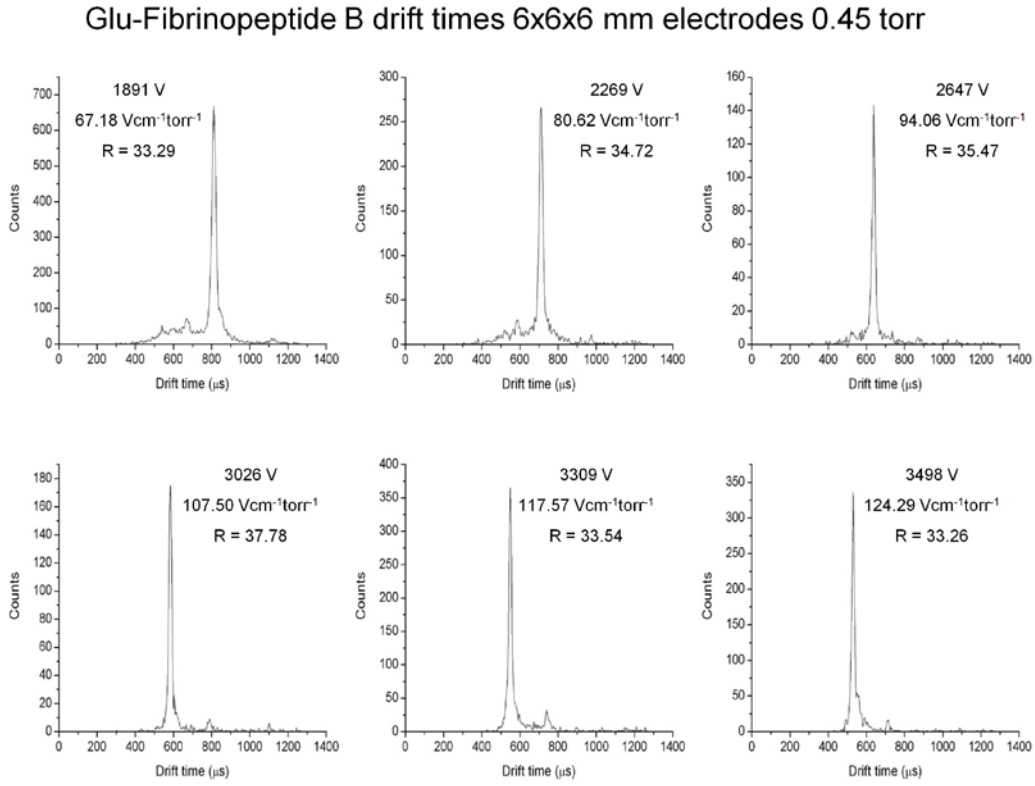

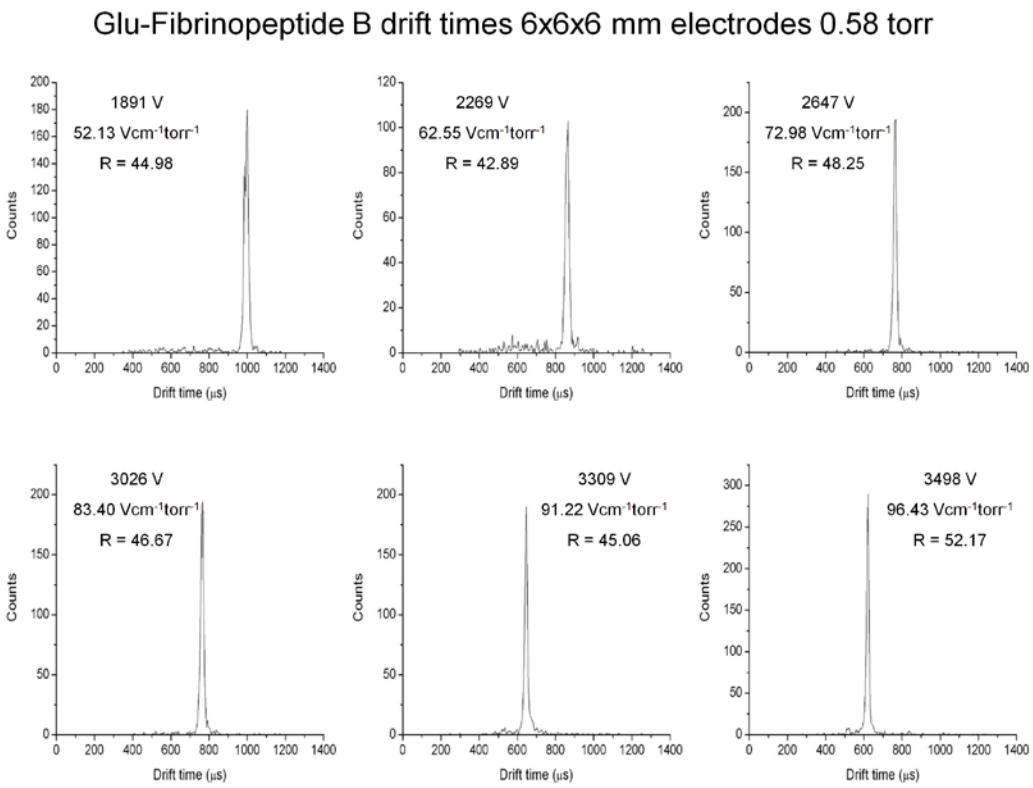
Glu-Fibrinopeptide B drift times 6x6x6 mm electrodes 0.58 torr
1891 V
52.13 Vcm-1torr-1
R = 44.98
2269 V
62.55 Vcm-1torr-1
R = 42.89
2647 V
72.98 Vcm-1torr-1
R = 48.25
3026 V
83.40 Vcm-1torr-1
R = 46.67
3309 V
91.22 Vcm-1torr-1
R = 45.06
3498 V
96.43 Vcm-1torr-1
R = 52.17
Counts
Drift time (µs)

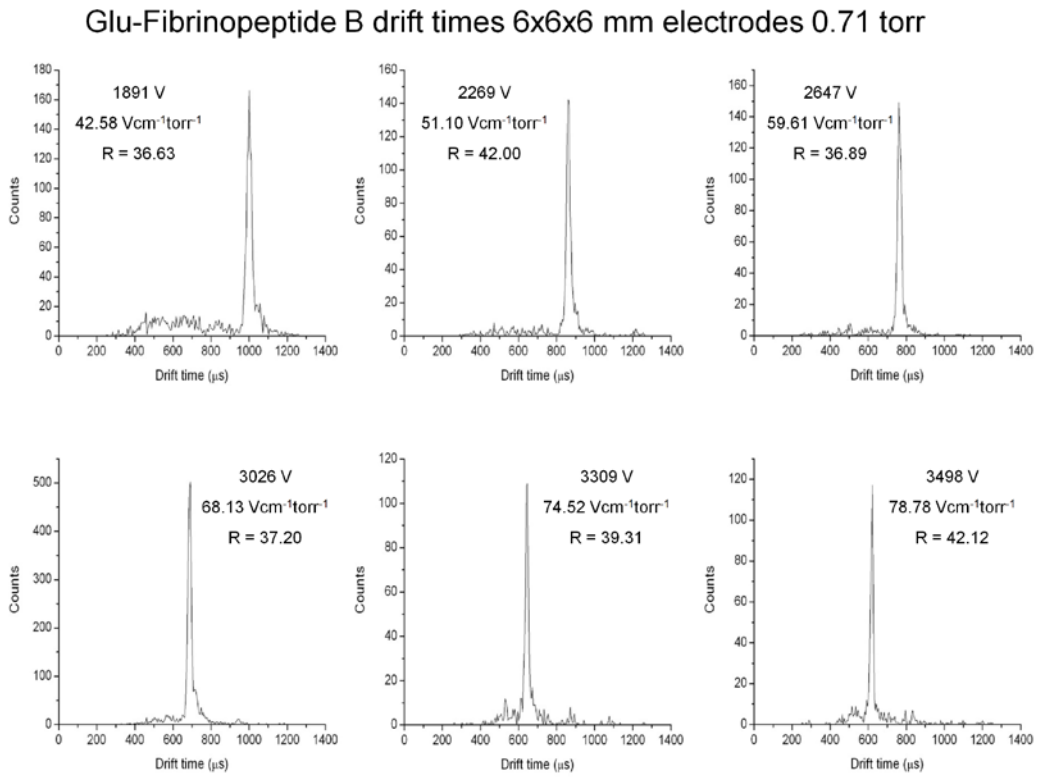
Glu-Fibrinopeptide B drift times 6x6x6 mm electrodes 0.71 torr
1891 V
42.58 Vcm-1torr-1
R = 36.63
2269 V
51.10 Vcm-1torr-1
R = 42.00
2647 V
59.61 Vcm-1torr-1
R = 36.89
3026 V
68.13 Vcm-1torr-1
R = 37.20
3309 V
74.52 Vcm-1torr-1
R = 39.31
3498 V
78.78 Vcm-1torr-1
R = 42.12
Counts
Drift time (µs)

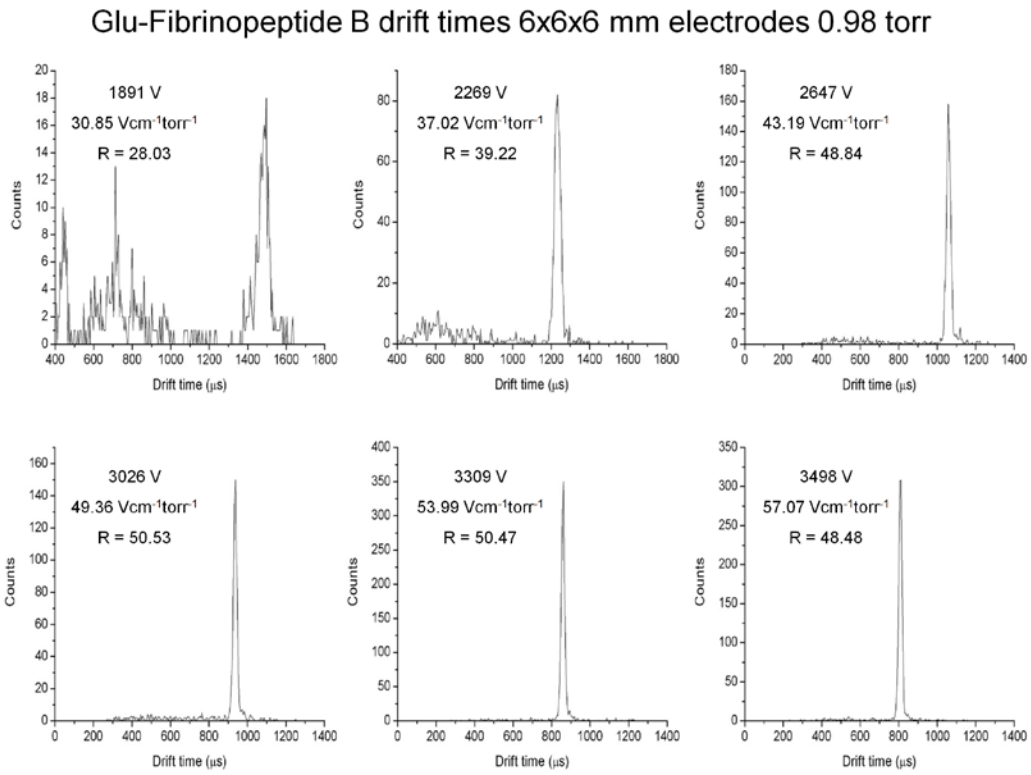
Glu-Fibrinopeptide B drift times 6x6x6 mm electrodes 0.98 torr
1891 V
30.85 Vcm-1torr-1
R = 28.03
2269 V
37.02 Vcm-1torr-1
R = 39.22
2647 V
43.19 Vcm-1torr-1
R = 48.84
3026 V
49.36 Vcm-1torr-1
R = 50.53
3309 V
53.99 Vcm-1torr-1
R = 50.47
3498 V
57.07 Vcm-1torr-1
R = 48.48
Counts
Drift time (μs)

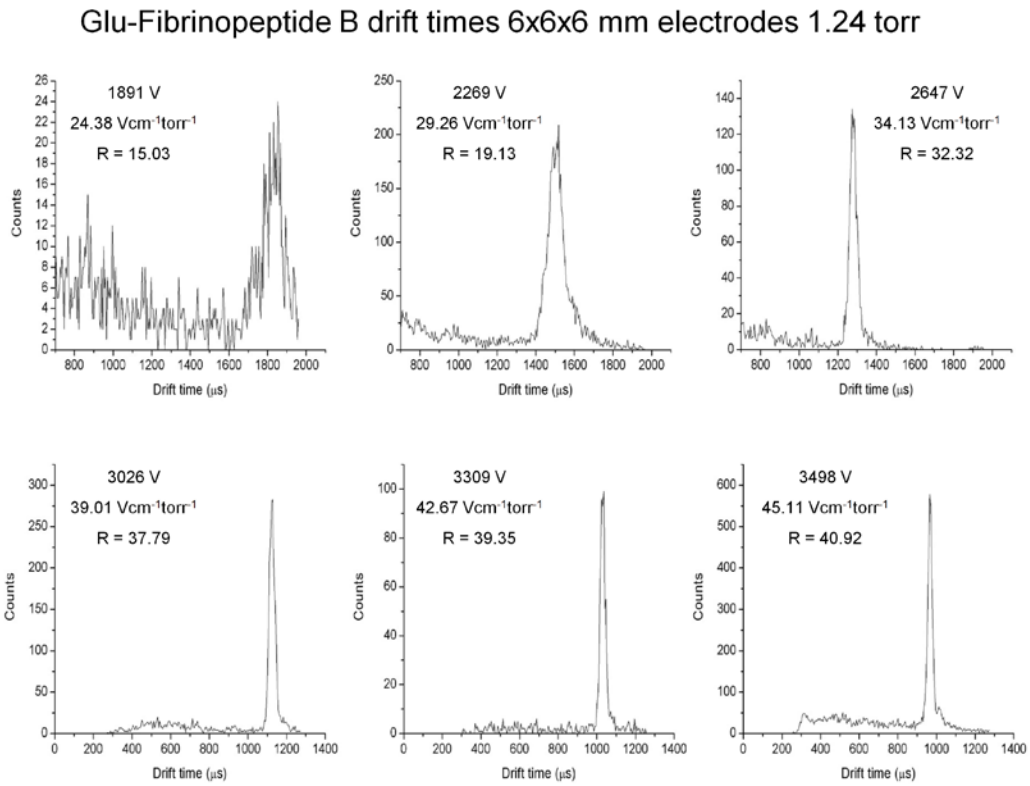
Glu-Fibrinopeptide B drift times 6x6x6 mm electrodes 1.24 torr
1891 V
24.38 Vcm-1torr-1
R = 15.03
2269 V
29.26 Vcm-1torr-1
R = 19.13
2647 V
34.13 Vcm-1torr-1
R = 32.32
3026 V
39.01 Vcm-1torr-1
R = 37.79
3309 V
42.67 Vcm-1torr-1
R = 39.35
3498 V
45.11 Vcm-1torr-1
R = 40.92
Counts
Drift time (μs)

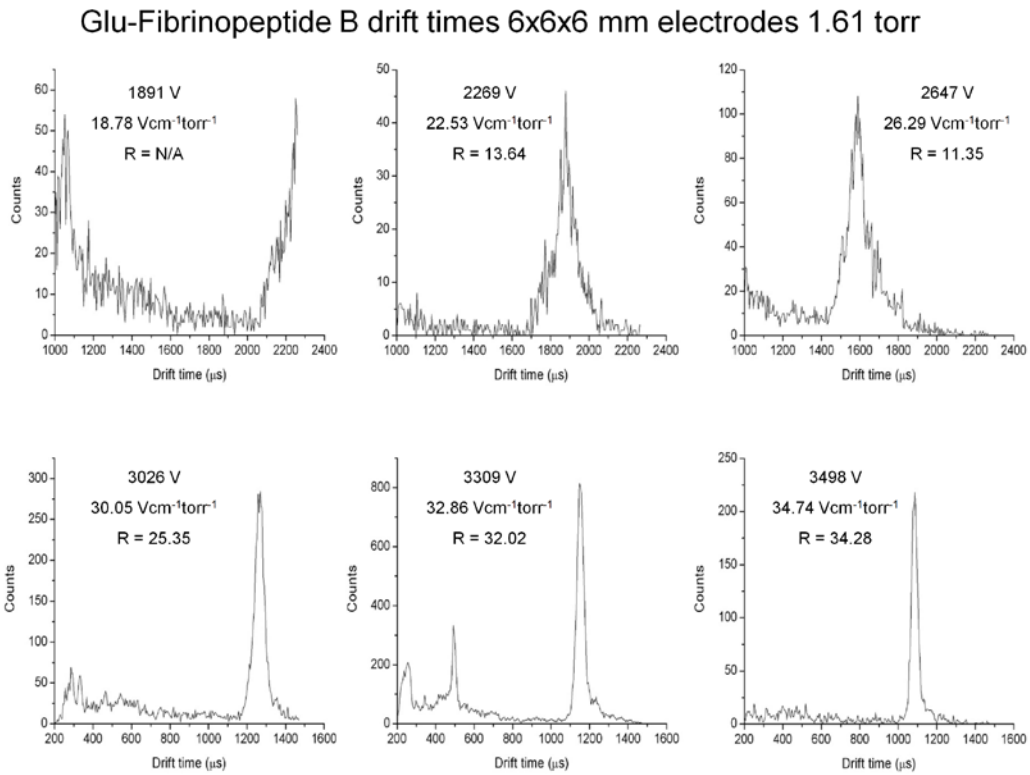
Glu-Fibrinopeptide B drift times 6x6x6 mm electrodes 1.61 torr
1891 V
18.78 Vcm-1torr-1
R = N/A
2269 V
22.53 Vcm-1torr-1
R = 13.64
2647 V
26.29 Vcm-1torr-1
R = 11.35
3026 V
30.05 Vcm-1torr-1
R = 25.35
3309 V
32.86 Vcm-1torr-1
R = 32.02
3498 V
34.74 Vcm-1torr-1
R = 34.28
Counts
Drift time (μs)

A-4

DRIFT TIME SPECTRA OF RADICAL CATIONS OF C_{60} AND C_{70} ON A 62.5 CM PDC IG DRIFT CELL EQUIPPED WITH ELECTRODE CONFIGURATION B ELECTRODES

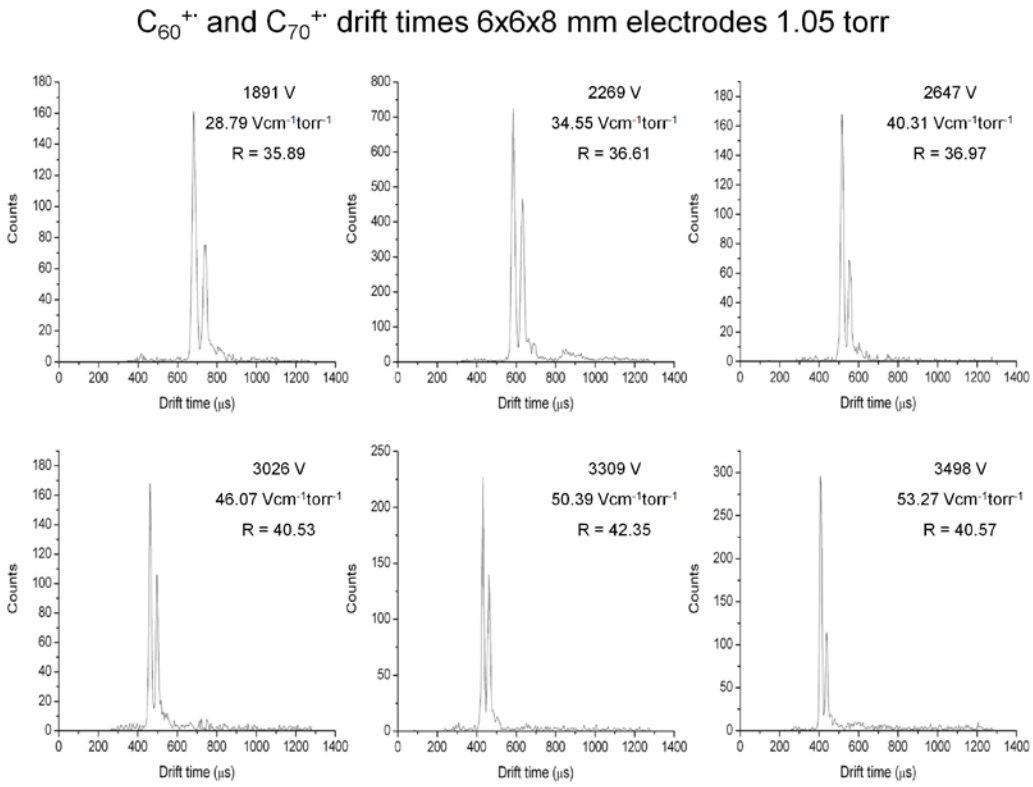

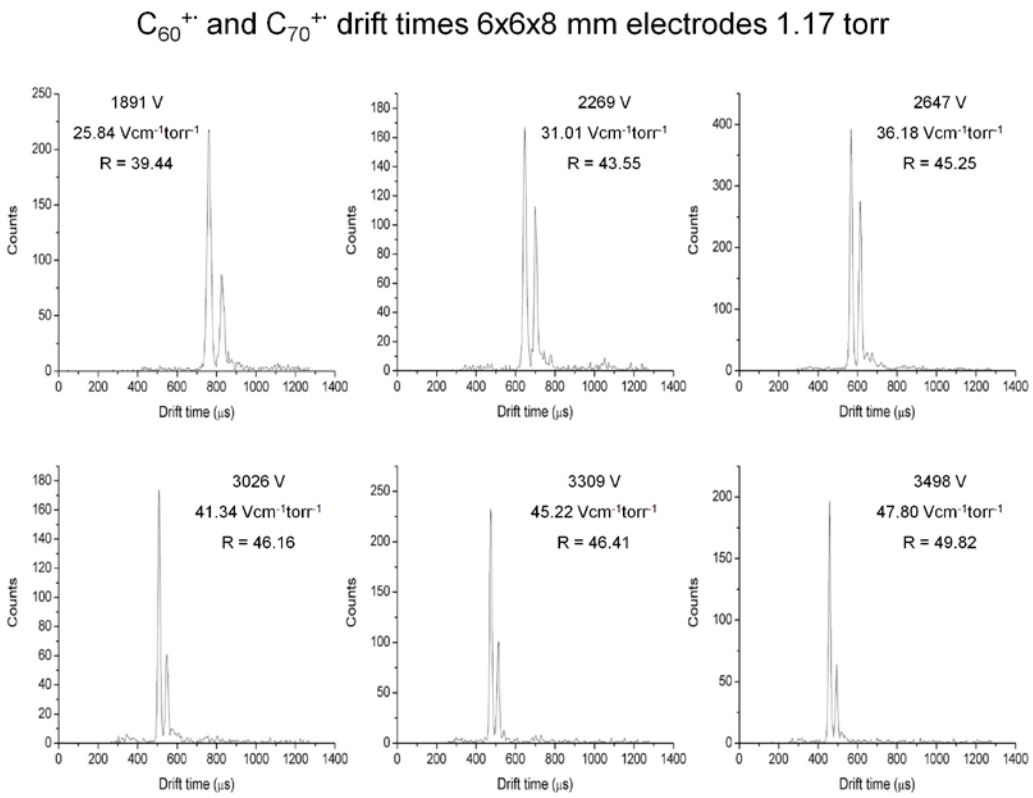
C60+· and C70+· drift times 6x6x8 mm electrodes 1.17 torr
1891 V
25.84 Vcm-1torr-1
R = 39.44
2269 V
31.01 Vcm-1torr-1
R = 43.55
2647 V
36.18 Vcm-1torr-1
R = 45.25
3026 V
41.34 Vcm-1torr-1
R = 46.16
3309 V
45.22 Vcm-1torr-1
R = 46.41
3498 V
47.80 Vcm-1torr-1
R = 49.82
Counts
Drift time (μs)

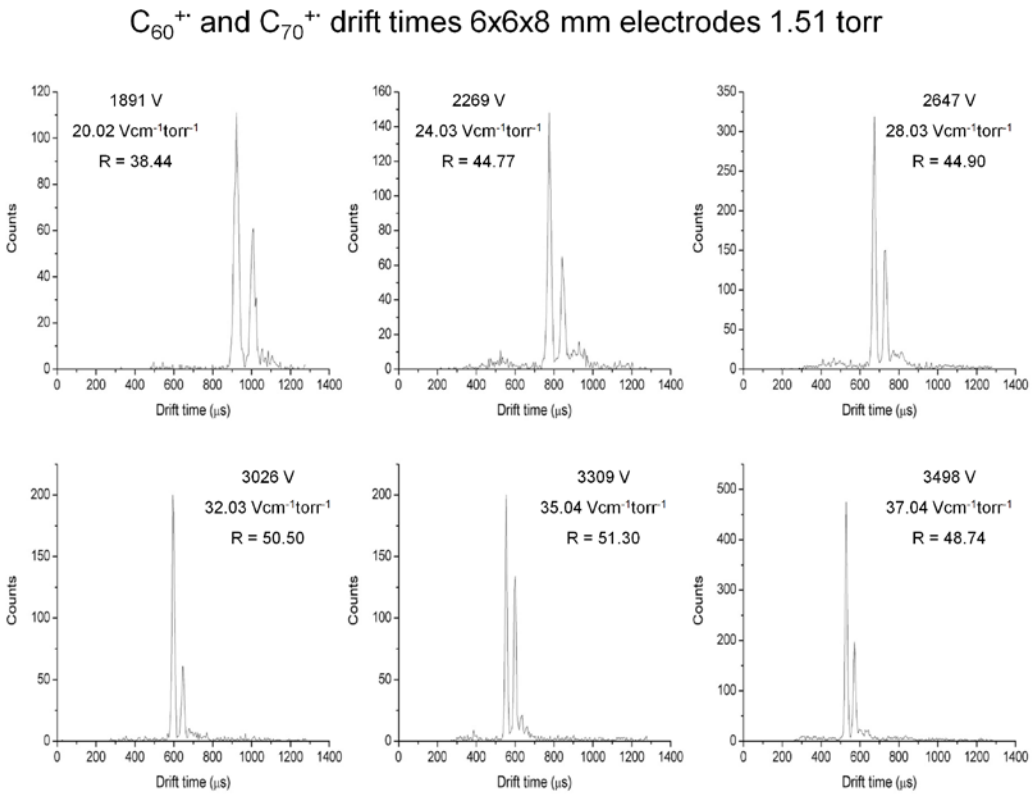
$C_{60}^{+\cdot}$ and $C_{70}^{+\cdot}$ drift times 6x6x8 mm electrodes 1.51 torr
1891 V
20.02 Vcm⁻¹torr⁻¹
R = 38.44
2269 V
24.03 Vcm⁻¹torr⁻¹
R = 44.77
2647 V
28.03 Vcm⁻¹torr⁻¹
R = 44.90
3026 V
32.03 Vcm⁻¹torr⁻¹
R = 50.50
3309 V
35.04 Vcm⁻¹torr⁻¹
R = 51.30
3498 V
37.04 Vcm⁻¹torr⁻¹
R = 48.74
Counts
Drift time (μs)

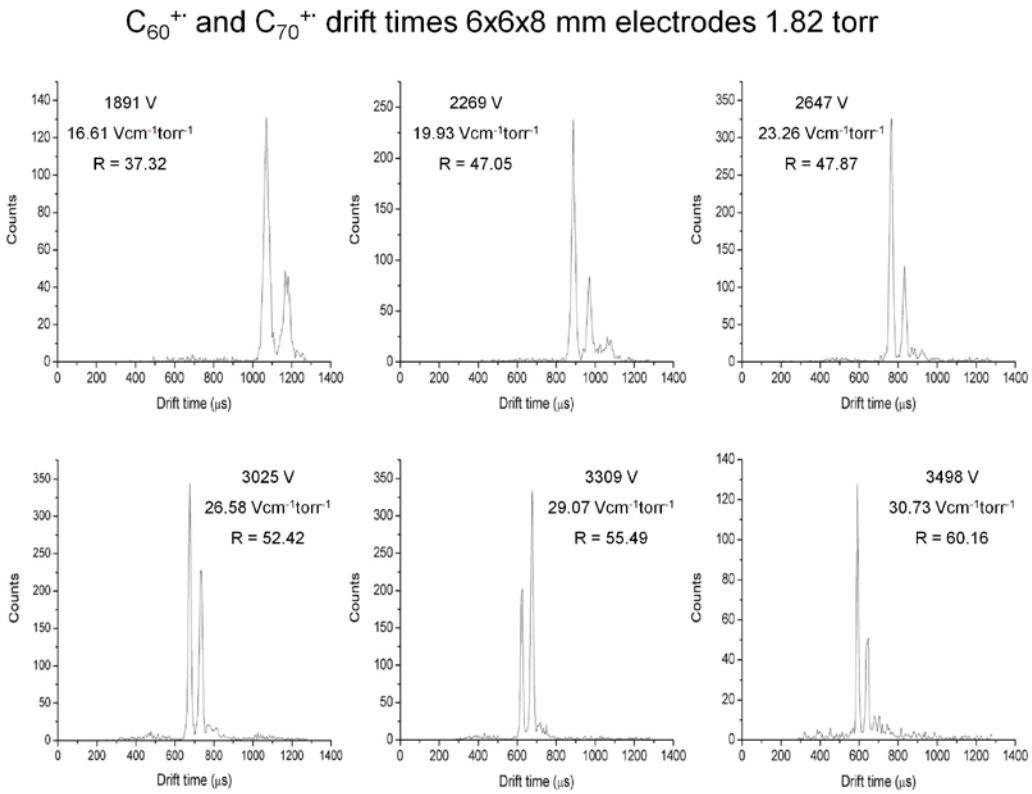
$C_{60}^{+\cdot}$ and $C_{70}^{+\cdot}$ drift times 6x6x8 mm electrodes 1.82 torr
1891 V
16.61 Vcm⁻¹torr⁻¹
R = 37.32
2269 V
19.93 Vcm⁻¹torr⁻¹
R = 47.05
2647 V
23.26 Vcm⁻¹torr⁻¹
R = 47.87
3025 V
26.58 Vcm⁻¹torr⁻¹
R = 52.42
3309 V
29.07 Vcm⁻¹torr⁻¹
R = 55.49
3498 V
30.73 Vcm⁻¹torr⁻¹
R = 60.16
Counts
Drift time (μs)

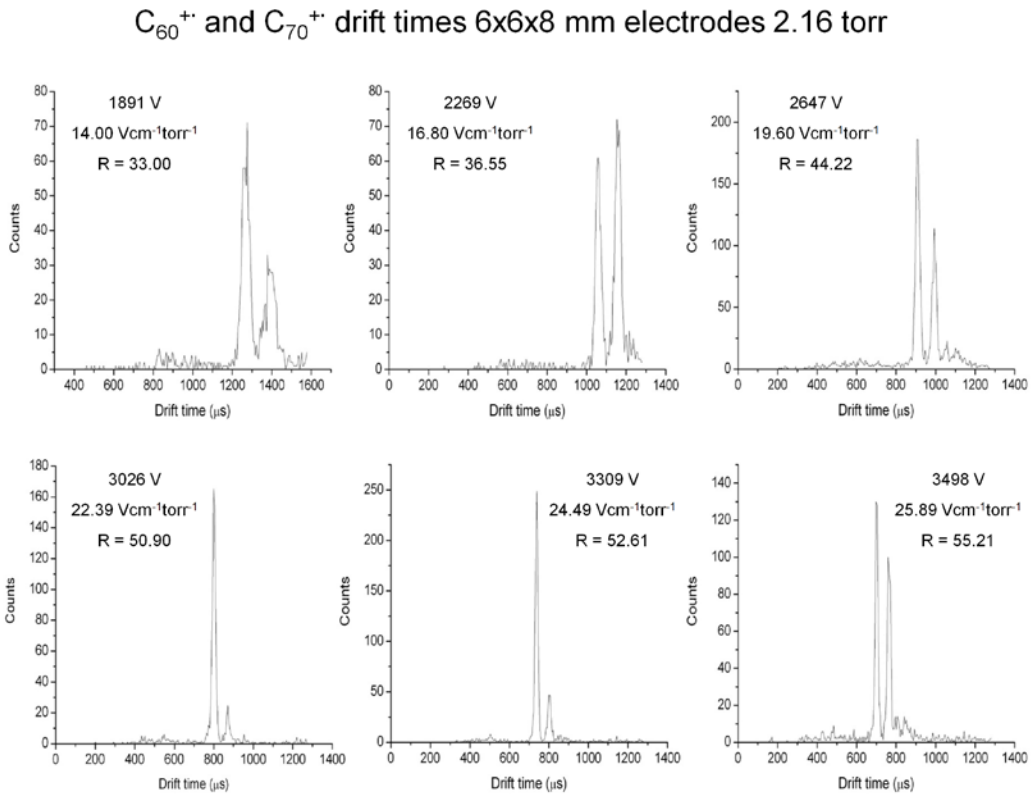
$C_{60}^{+\cdot}$ and $C_{70}^{+\cdot}$ drift times 6x6x8 mm electrodes 2.16 torr
1891 V
14.00 Vcm-1torr-1
R = 33.00
2269 V
16.80 Vcm-1torr-1
R = 36.55
2647 V
19.60 Vcm-1torr-1
R = 44.22
3026 V
22.39 Vcm-1torr-1
R = 50.90
3309 V
24.49 Vcm-1torr-1
R = 52.61
3498 V
25.89 Vcm-1torr-1
R = 55.21
Counts
Drift time (μs)

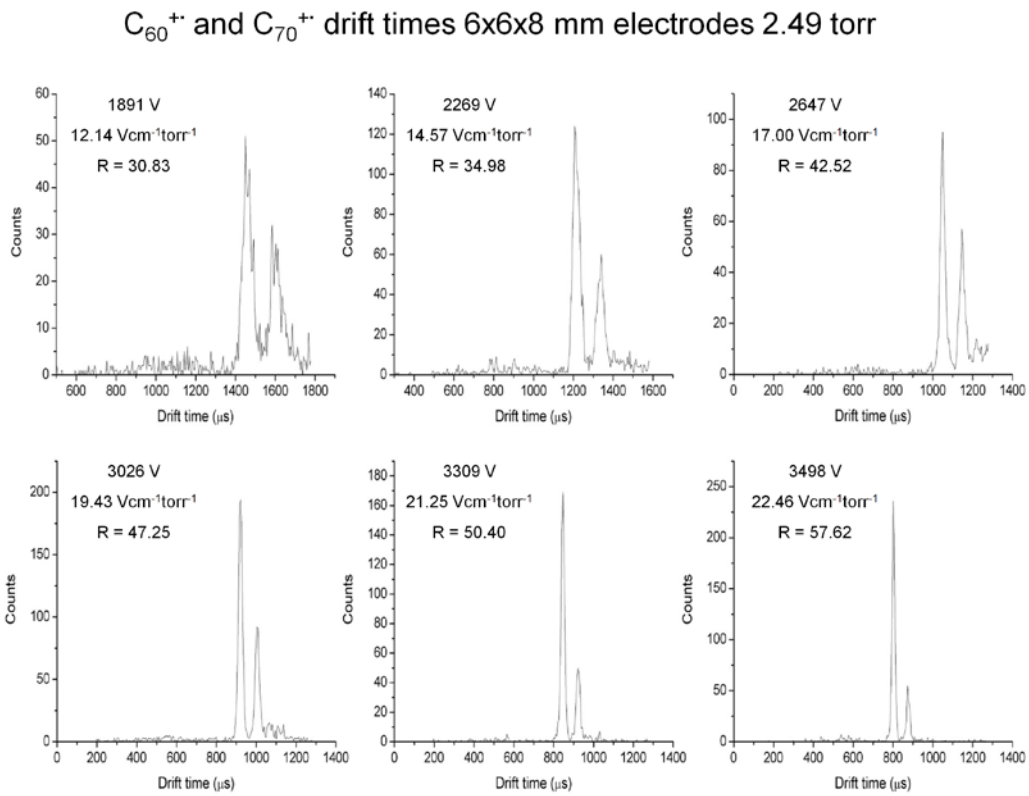
$C_{60}^{+\cdot}$ and $C_{70}^{+\cdot}$ drift times 6x6x8 mm electrodes 2.49 torr
1891 V
12.14 Vcm⁻¹torr⁻¹
R = 30.83
2269 V
14.57 Vcm⁻¹torr⁻¹
R = 34.98
2647 V
17.00 Vcm⁻¹torr⁻¹
R = 42.52
3026 V
19.43 Vcm⁻¹torr⁻¹
R = 47.25
3309 V
21.25 Vcm⁻¹torr⁻¹
R = 50.40
3498 V
22.46 Vcm⁻¹torr⁻¹
R = 57.62
Counts
Drift time (μs)

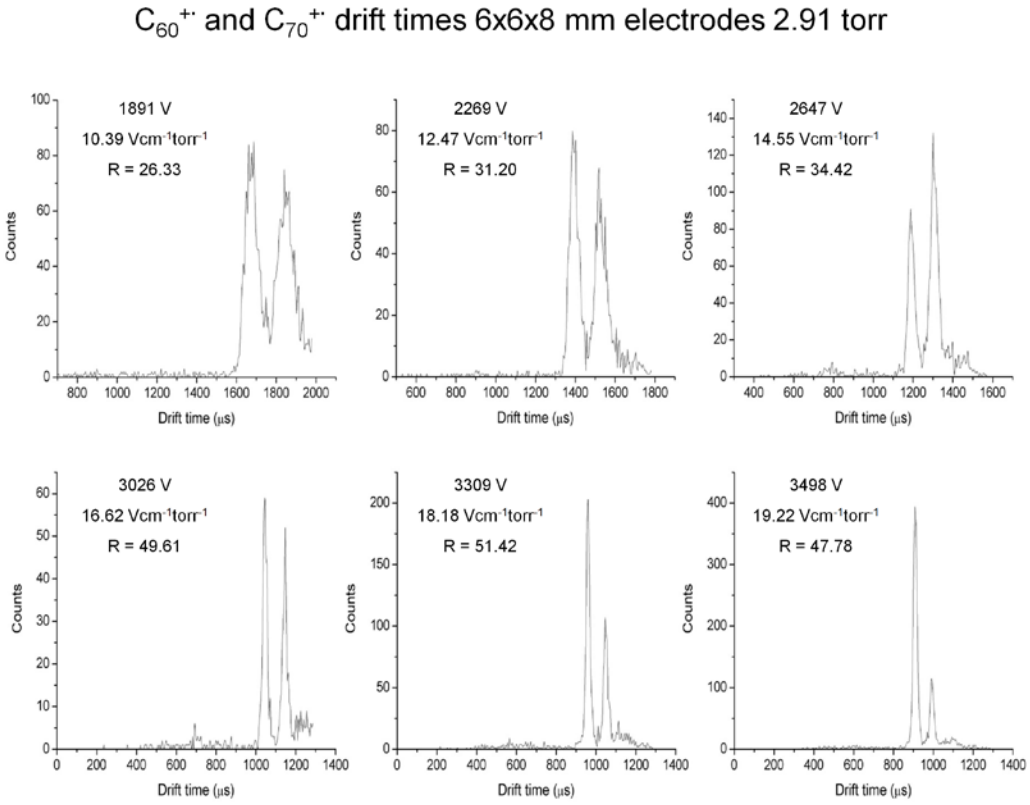
C60+· and C70+· drift times 6x6x8 mm electrodes 2.91 torr
1891 V
10.39 Vcm-1torr-1
R = 26.33
2269 V
12.47 Vcm-1torr-1
R = 31.20
2647 V
14.55 Vcm-1torr-1
R = 34.42
3026 V
16.62 Vcm-1torr-1
R = 49.61
3309 V
18.18 Vcm-1torr-1
R = 51.42
3498 V
19.22 Vcm-1torr-1
R = 47.78
Counts
Drift time (µs)

A-5

DRIFT TIME SPECTRA OF PROTONATED VAL-4-ANGIOTENSIN I ON A 62.5 CM PDC IG DRIFT CELL EQUIPPED WITH ELECTRODE CONFIGURATION B ELECTRODES

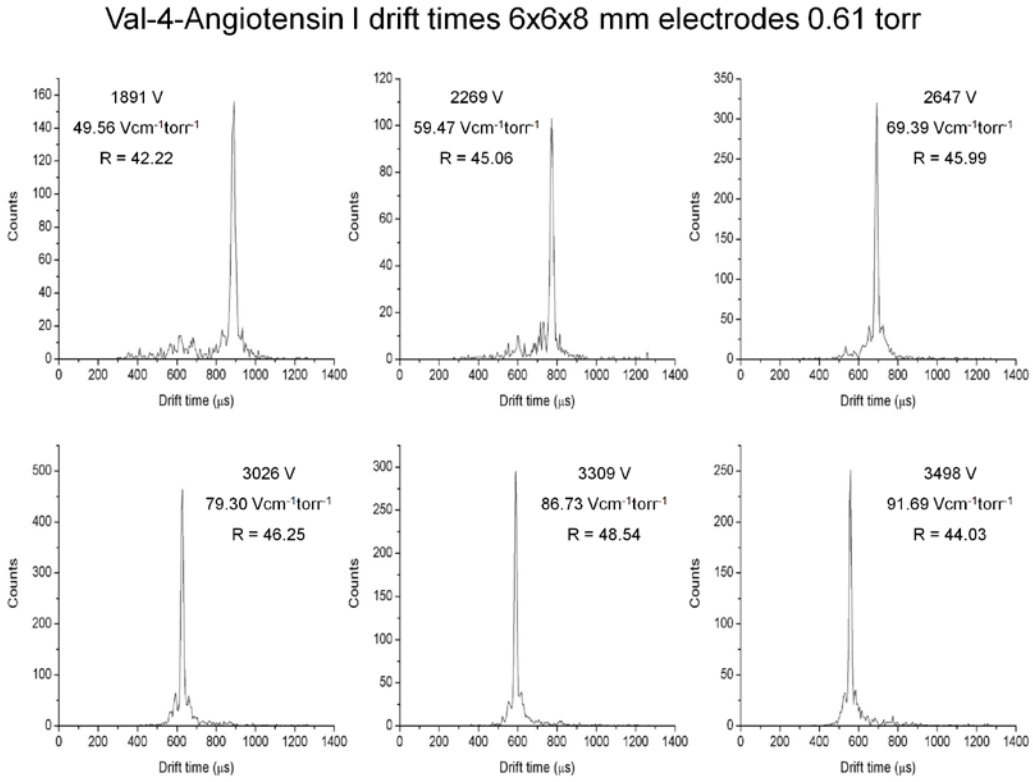

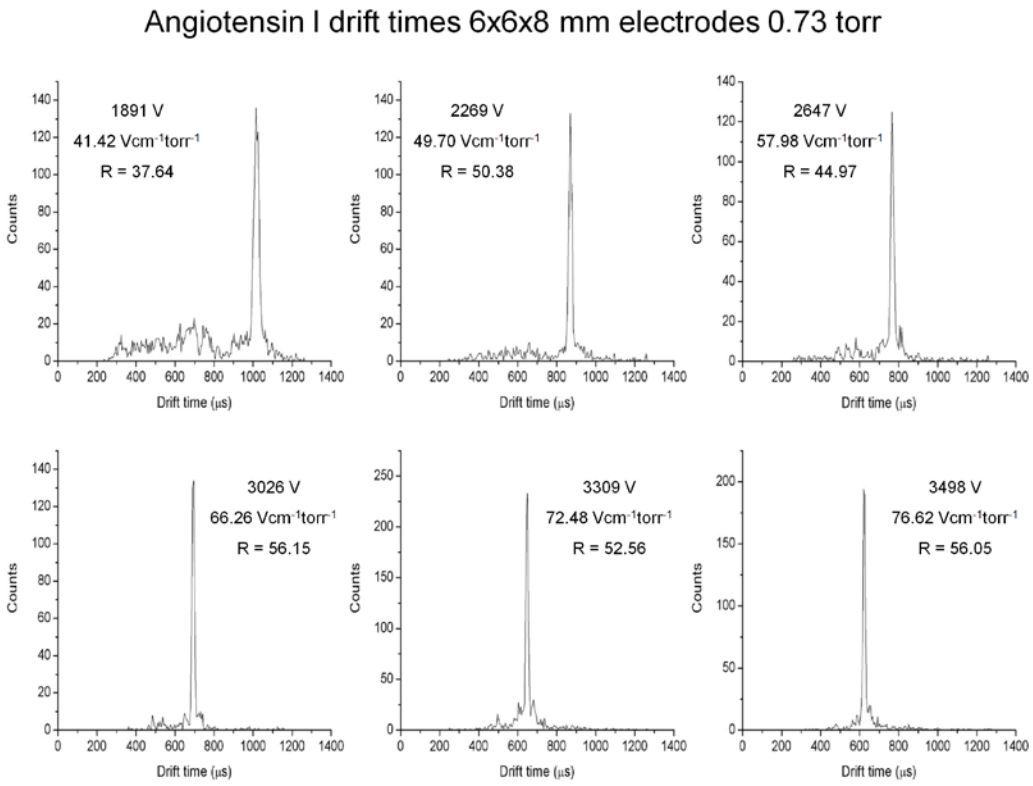
Angiotensin I drift times 6x6x8 mm electrodes 0.73 torr
1891 V
41.42 Vcm-1torr-1
R = 37.64
2269 V
49.70 Vcm-1torr-1
R = 50.38
2647 V
57.98 Vcm-1torr-1
R = 44.97
3026 V
66.26 Vcm-1torr-1
R = 56.15
3309 V
72.48 Vcm-1torr-1
R = 52.56
3498 V
76.62 Vcm-1torr-1
R = 56.05
Counts
Drift time (μs)

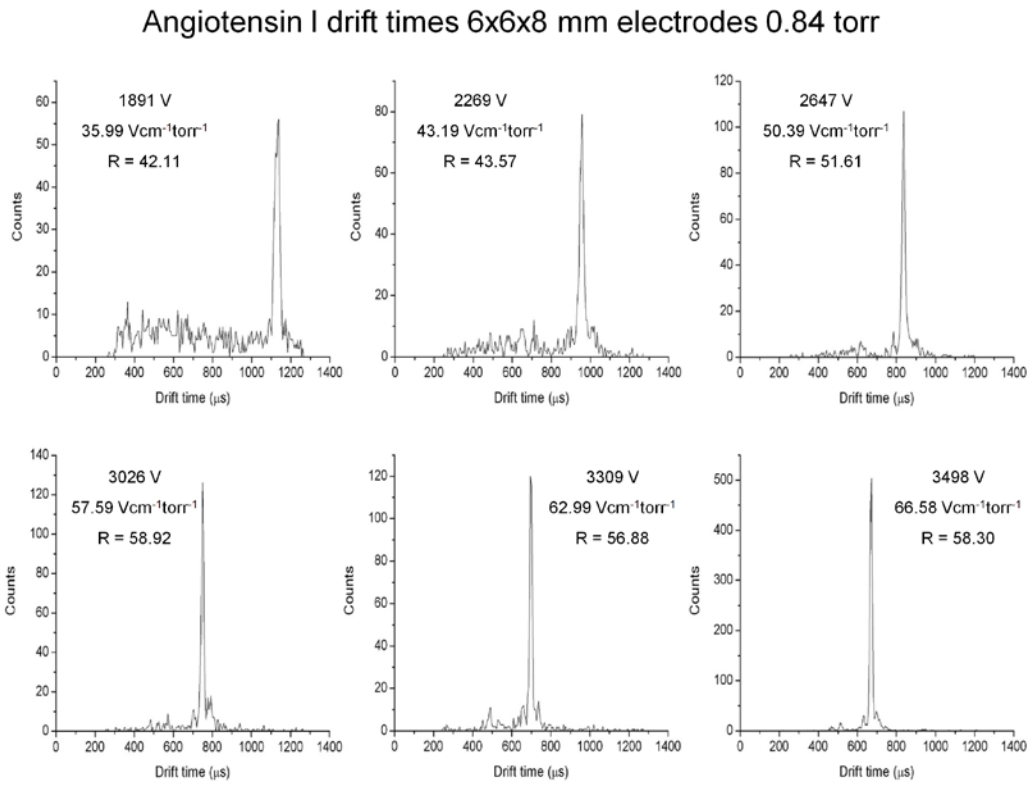
Angiotensin I drift times 6x6x8 mm electrodes 0.84 torr
1891 V
35.99 Vcm-1torr-1
R = 42.11
2269 V
43.19 Vcm-1torr-1
R = 43.57
2647 V
50.39 Vcm-1torr-1
R = 51.61
3026 V
57.59 Vcm-1torr-1
R = 58.92
3309 V
62.99 Vcm-1torr-1
R = 56.88
3498 V
66.58 Vcm-1torr-1
R = 58.30
Counts
Drift time (μs)

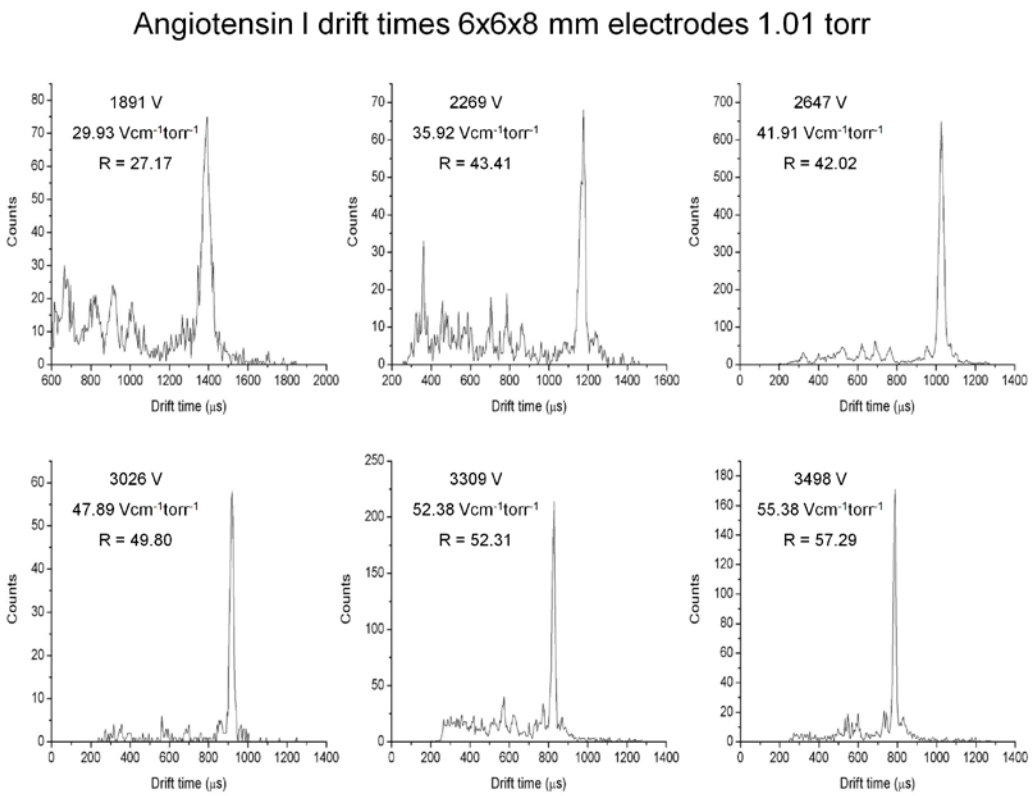
Angiotensin I drift times 6x6x8 mm electrodes 1.01 torr
1891 V
29.93 Vcm-1torr-1
R = 27.17
2269 V
35.92 Vcm-1torr-1
R = 43.41
2647 V
41.91 Vcm-1torr-1
R = 42.02
3026 V
47.89 Vcm-1torr-1
R = 49.80
3309 V
52.38 Vcm-1torr-1
R = 52.31
3498 V
55.38 Vcm-1torr-1
R = 57.29
Counts
Drift time (µs)

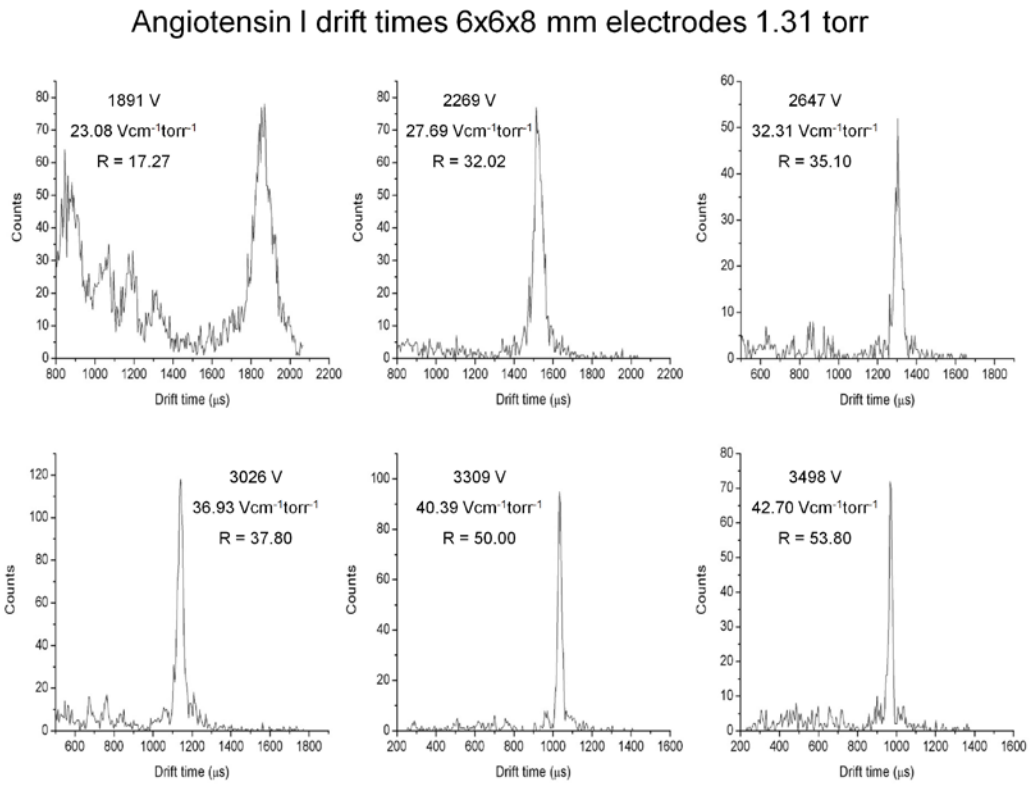
Angiotensin I drift times 6x6x8 mm electrodes 1.31 torr
1891 V
23.08 Vcm-1torr-1
R = 17.27
2269 V
27.69 Vcm-1torr-1
R = 32.02
2647 V
32.31 Vcm-1torr-1
R = 35.10
3026 V
36.93 Vcm-1torr-1
R = 37.80
3309 V
40.39 Vcm-1torr-1
R = 50.00
3498 V
42.70 Vcm-1torr-1
R = 53.80
Counts
Drift time (µs)

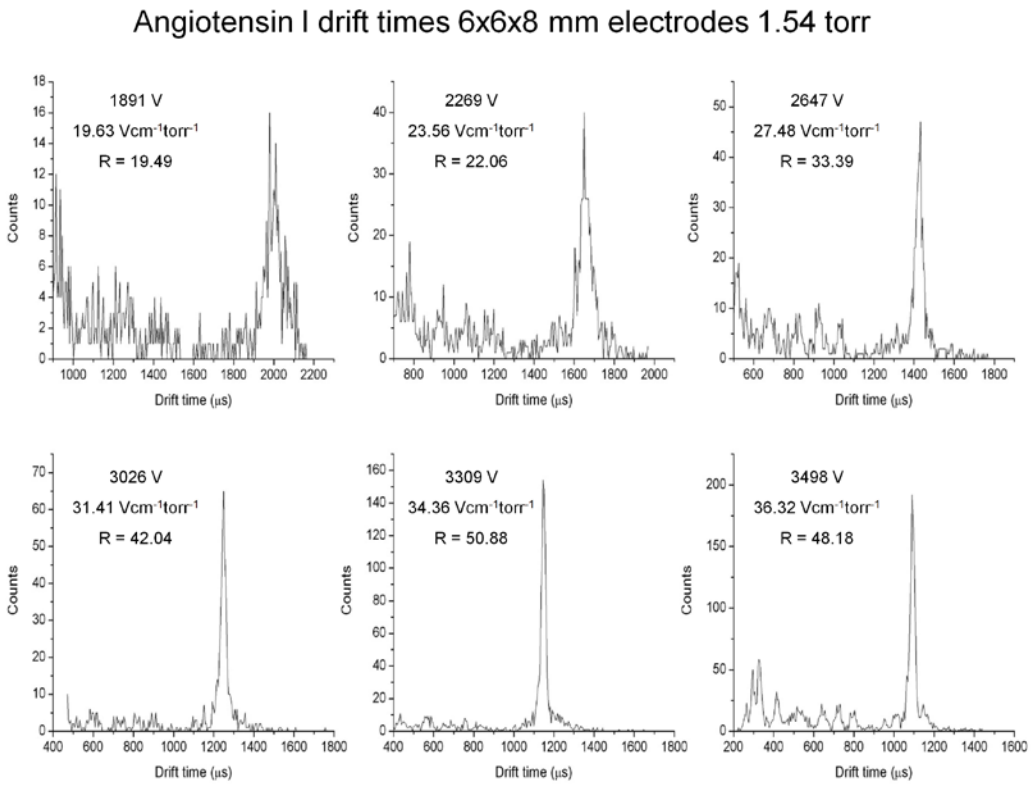
Angiotensin I drift times 6x6x8 mm electrodes 1.54 torr
1891 V
19.63 Vcm-1torr-1
R = 19.49
2269 V
23.56 Vcm-1torr-1
R = 22.06
2647 V
27.48 Vcm-1torr-1
R = 33.39
3026 V
31.41 Vcm-1torr-1
R = 42.04
3309 V
34.36 Vcm-1torr-1
R = 50.88
3498 V
36.32 Vcm-1torr-1
R = 48.18
Counts
Drift time (μs)

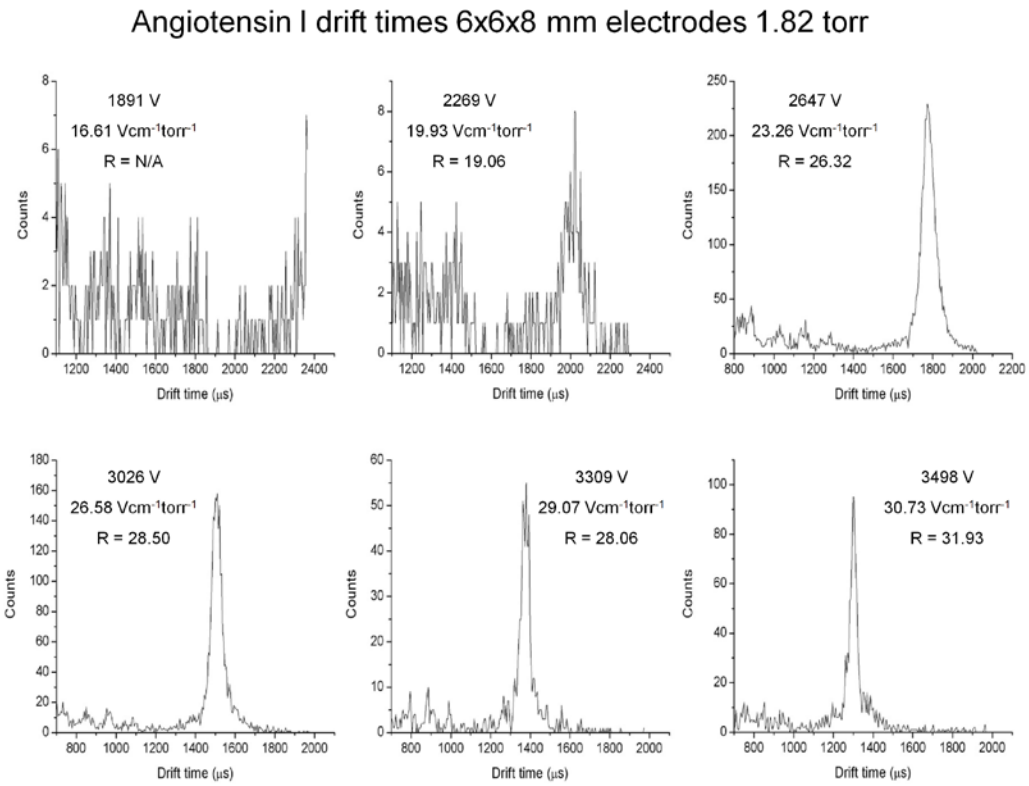
Angiotensin I drift times 6x6x8 mm electrodes 1.82 torr
1891 V
16.61 Vcm-1torr-1
R = N/A
2269 V
19.93 Vcm-1torr-1
R = 19.06
2647 V
23.26 Vcm-1torr-1
R = 26.32
3026 V
26.58 Vcm-1torr-1
R = 28.50
3309 V
29.07 Vcm-1torr-1
R = 28.06
3498 V
30.73 Vcm-1torr-1
R = 31.93
Counts
Drift time (µs)

A-6

DRIFT TIME SPECTRA OF PROTONATED GLU-FIBRINOPEPTIDE B ON A 62.5 CM PDC IG DRIFT CELL EQUIPPED WITH ELECTRODE CONFIGURATION B ELECTRODES

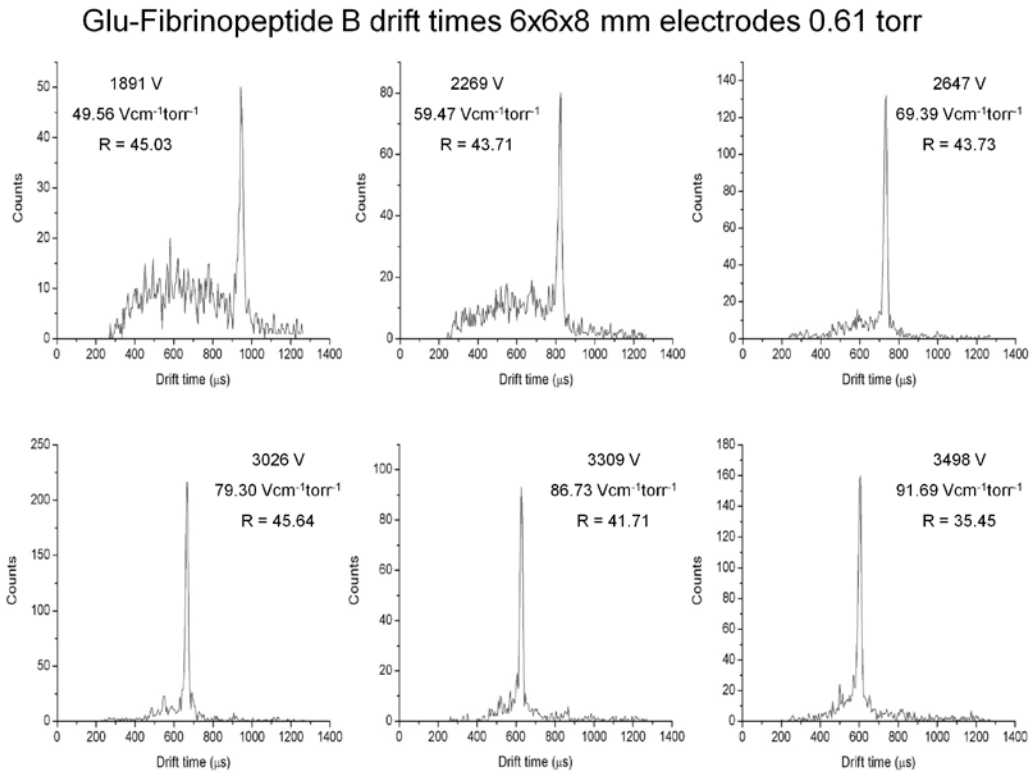

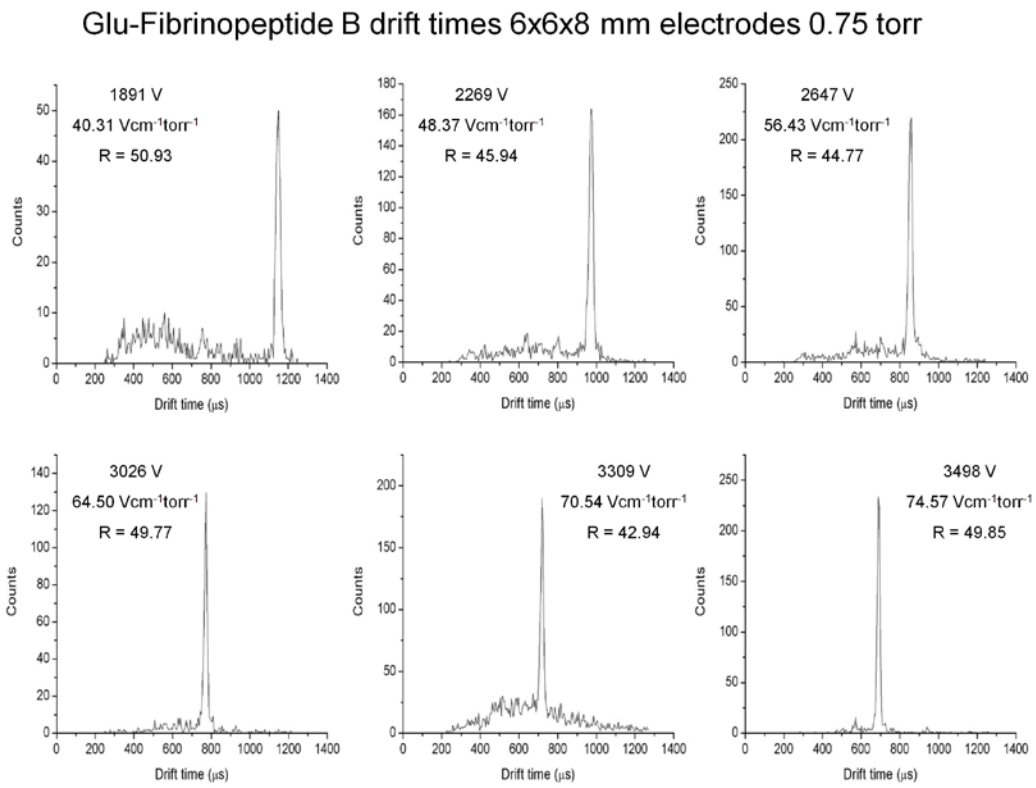
Glu-Fibrinopeptide B drift times 6x6x8 mm electrodes 0.75 torr
1891 V
40.31 Vcm-1torr-1
R = 50.93
2269 V
48.37 Vcm-1torr-1
R = 45.94
2647 V
56.43 Vcm-1torr-1
R = 44.77
3026 V
64.50 Vcm-1torr-1
R = 49.77
3309 V
70.54 Vcm-1torr-1
R = 42.94
3498 V
74.57 Vcm-1torr-1
R = 49.85
Counts
Drift time (μs)

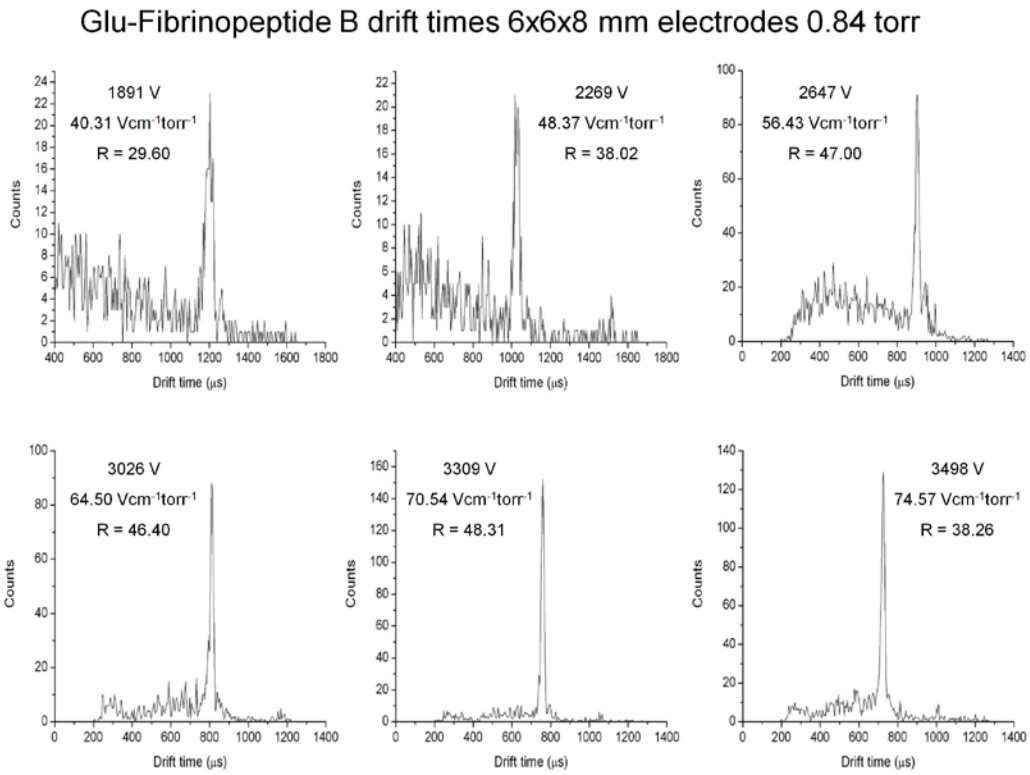
Glu-Fibrinopeptide B drift times 6x6x8 mm electrodes 0.84 torr
1891 V
40.31 Vcm-1torr-1
R = 29.60
2269 V
48.37 Vcm-1torr-1
R = 38.02
2647 V
56.43 Vcm-1torr-1
R = 47.00
3026 V
64.50 Vcm-1torr-1
R = 46.40
3309 V
70.54 Vcm-1torr-1
R = 48.31
3498 V
74.57 Vcm-1torr-1
R = 38.26
Counts
Drift time (μs)

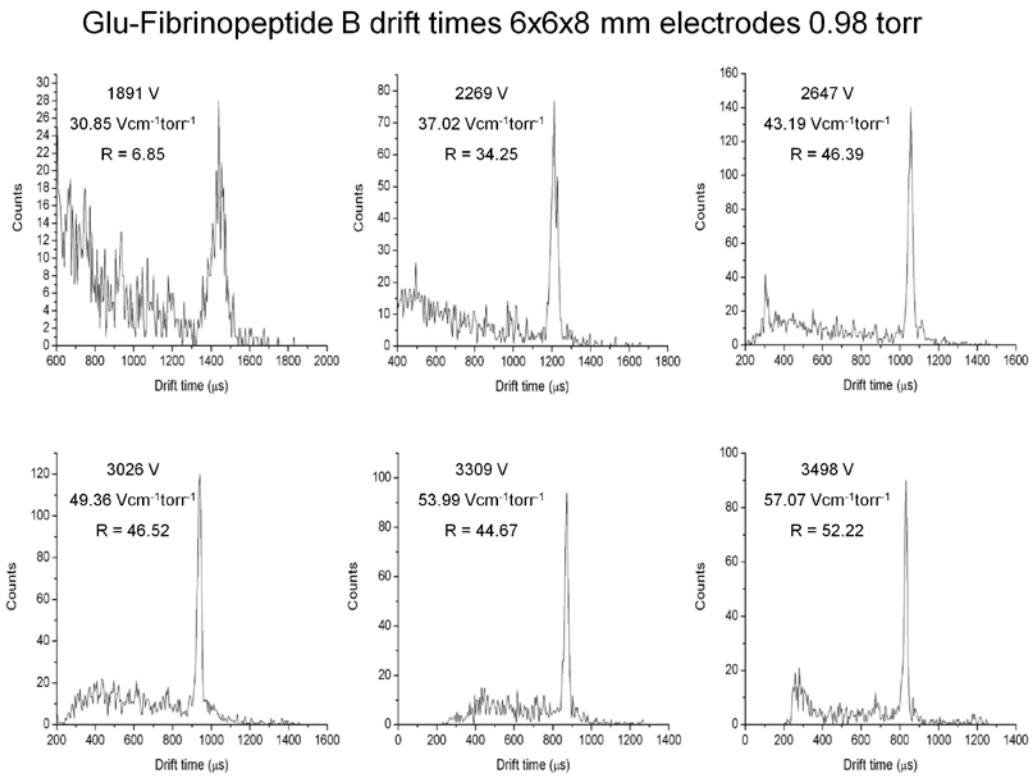
Glu-Fibrinopeptide B drift times 6x6x8 mm electrodes 0.98 torr
1891 V
30.85 Vcm-1torr-1
R = 6.85
2269 V
37.02 Vcm-1torr-1
R = 34.25
2647 V
43.19 Vcm-1torr-1
R = 46.39
3026 V
49.36 Vcm-1torr-1
R = 46.52
3309 V
53.99 Vcm-1torr-1
R = 44.67
3498 V
57.07 Vcm-1torr-1
R = 52.22
Counts
Drift time (μs)

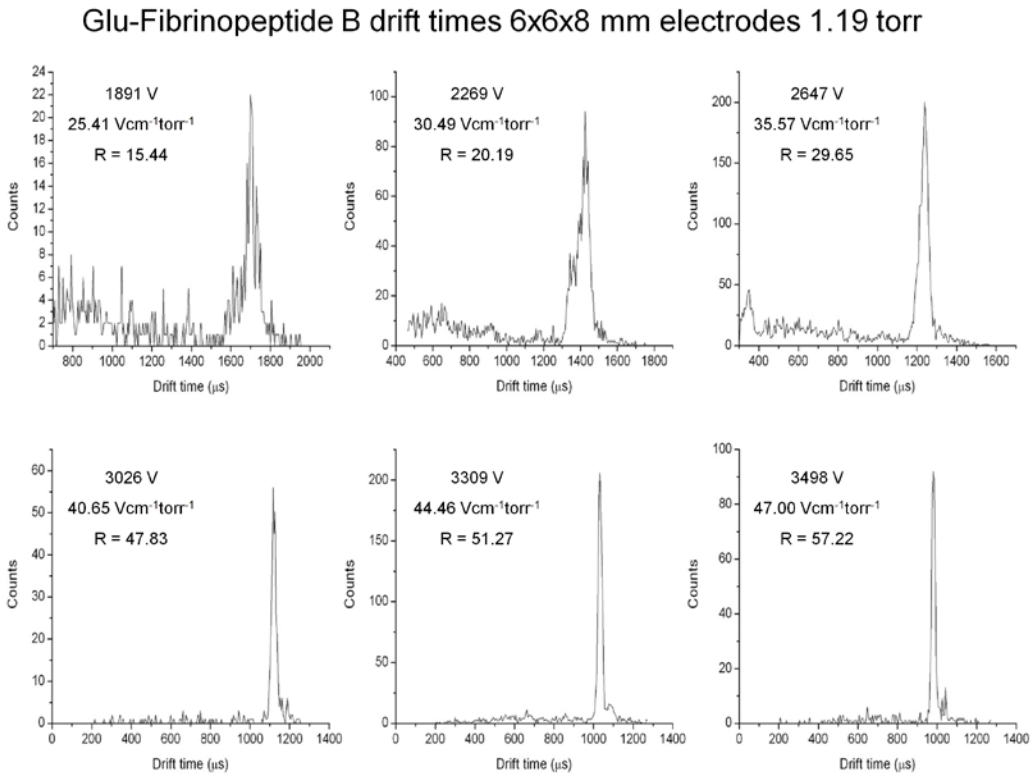
Glu-Fibrinopeptide B drift times 6x6x8 mm electrodes 1.19 torr
1891 V
25.41 Vcm-1torr-1
R = 15.44
2269 V
30.49 Vcm-1torr-1
R = 20.19
2647 V
35.57 Vcm-1torr-1
R = 29.65
3026 V
40.65 Vcm-1torr-1
R = 47.83
3309 V
44.46 Vcm-1torr-1
R = 51.27
3498 V
47.00 Vcm-1torr-1
R = 57.22
Counts
Drift time (μs)

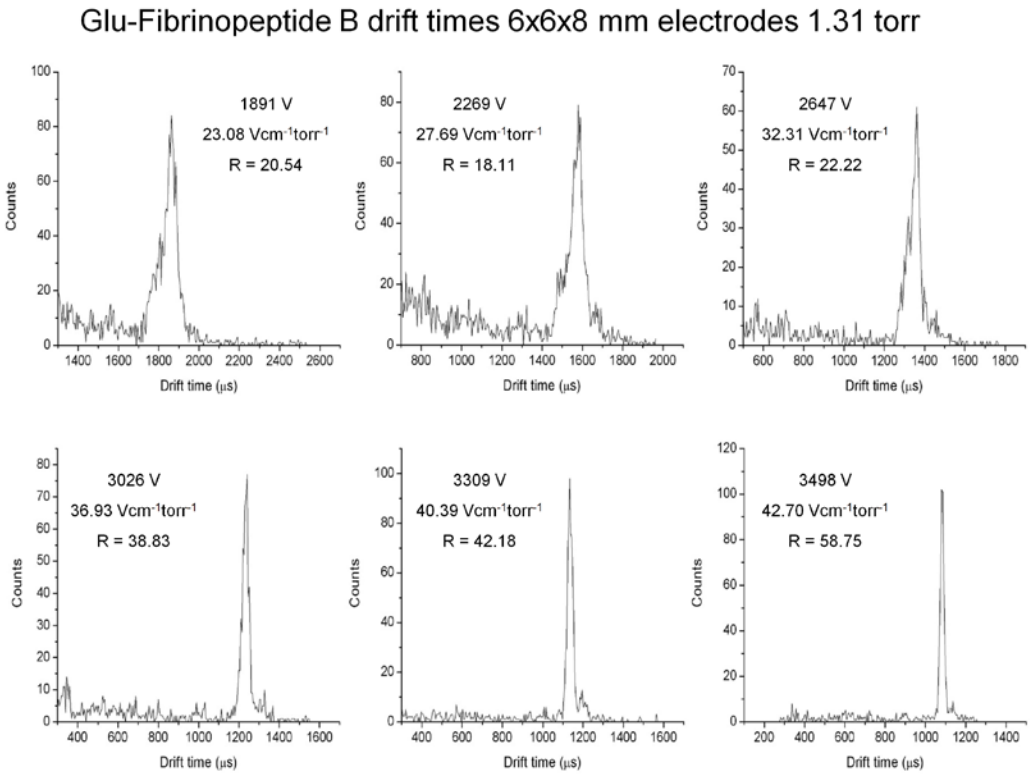
Glu-Fibrinopeptide B drift times 6x6x8 mm electrodes 1.31 torr
1891 V
23.08 Vcm-1torr-1
R = 20.54
2269 V
27.69 Vcm-1torr-1
R = 18.11
2647 V
32.31 Vcm-1torr-1
R = 22.22
3026 V
36.93 Vcm-1torr-1
R = 38.83
3309 V
40.39 Vcm-1torr-1
R = 42.18
3498 V
42.70 Vcm-1torr-1
R = 58.75
Counts
Drift time (μs)

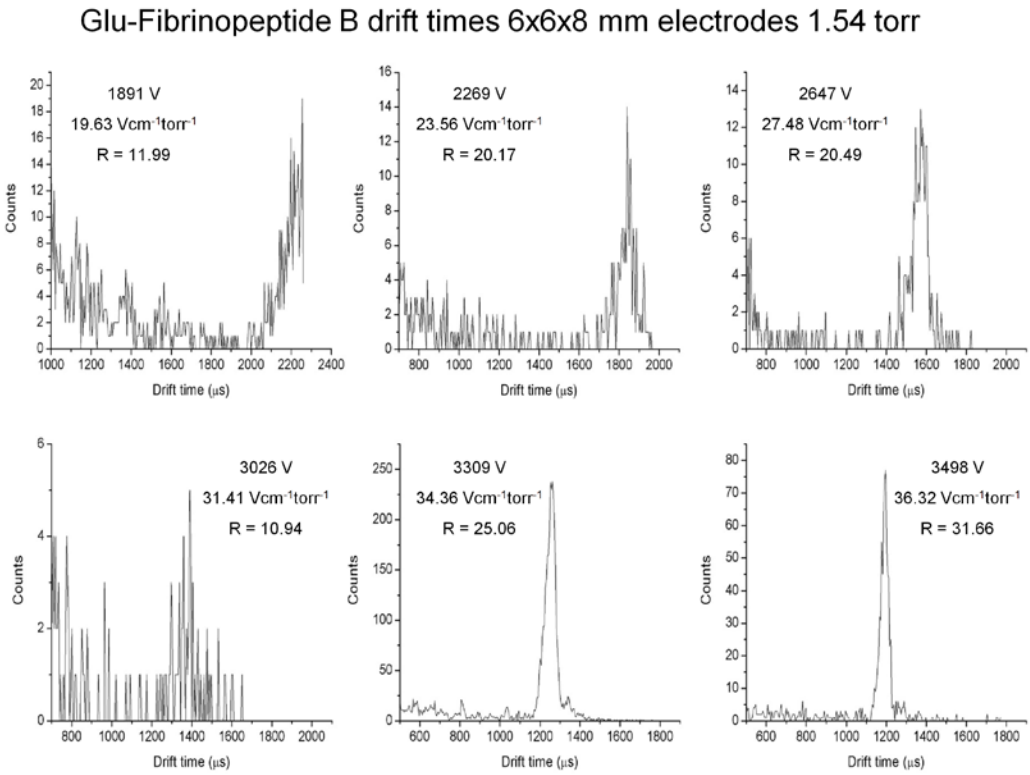
Glu-Fibrinopeptide B drift times 6x6x8 mm electrodes 1.54 torr
1891 V
19.63 Vcm-1torr-1
R = 11.99
2269 V
23.56 Vcm-1torr-1
R = 20.17
2647 V
27.48 Vcm-1torr-1
R = 20.49
3026 V
31.41 Vcm-1torr-1
R = 10.94
3309 V
34.36 Vcm-1torr-1
R = 25.06
3498 V
36.32 Vcm-1torr-1
R = 31.66
Counts
Drift time (µs)

APPENDIX B

125 CENTIMETER PDC IG DRIFT CELL

Note: The center rod for electrode support is removed prior to compressing the electrodes with the threaded rods. Compression is provided from the Rulon source against the first few electrodes of the drift cell. Vacuum is provided by O-ring seals at the Rulon source region and mobility drift cell exit that face seal with the alumina tube.

APPENDIX C

ALUMINUM MOUNTING FLANGE COMPONENTS FOR 15-KV COLLISION DYNODE

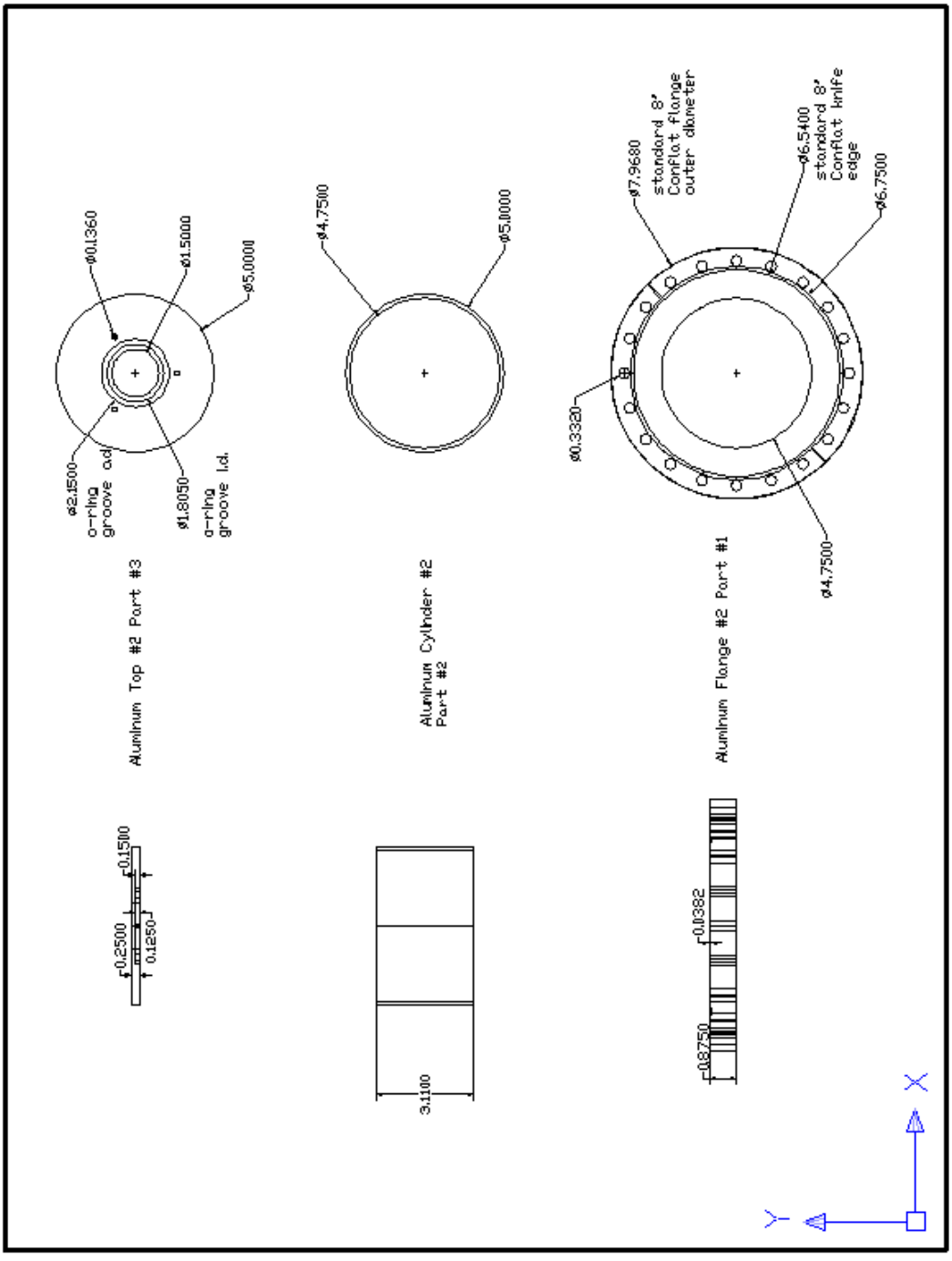

ALUMINUM MOUNTING FLANGE COMPONENTS FOR CONTINUOUS DYNODE ELECTRON MULTIPLIER

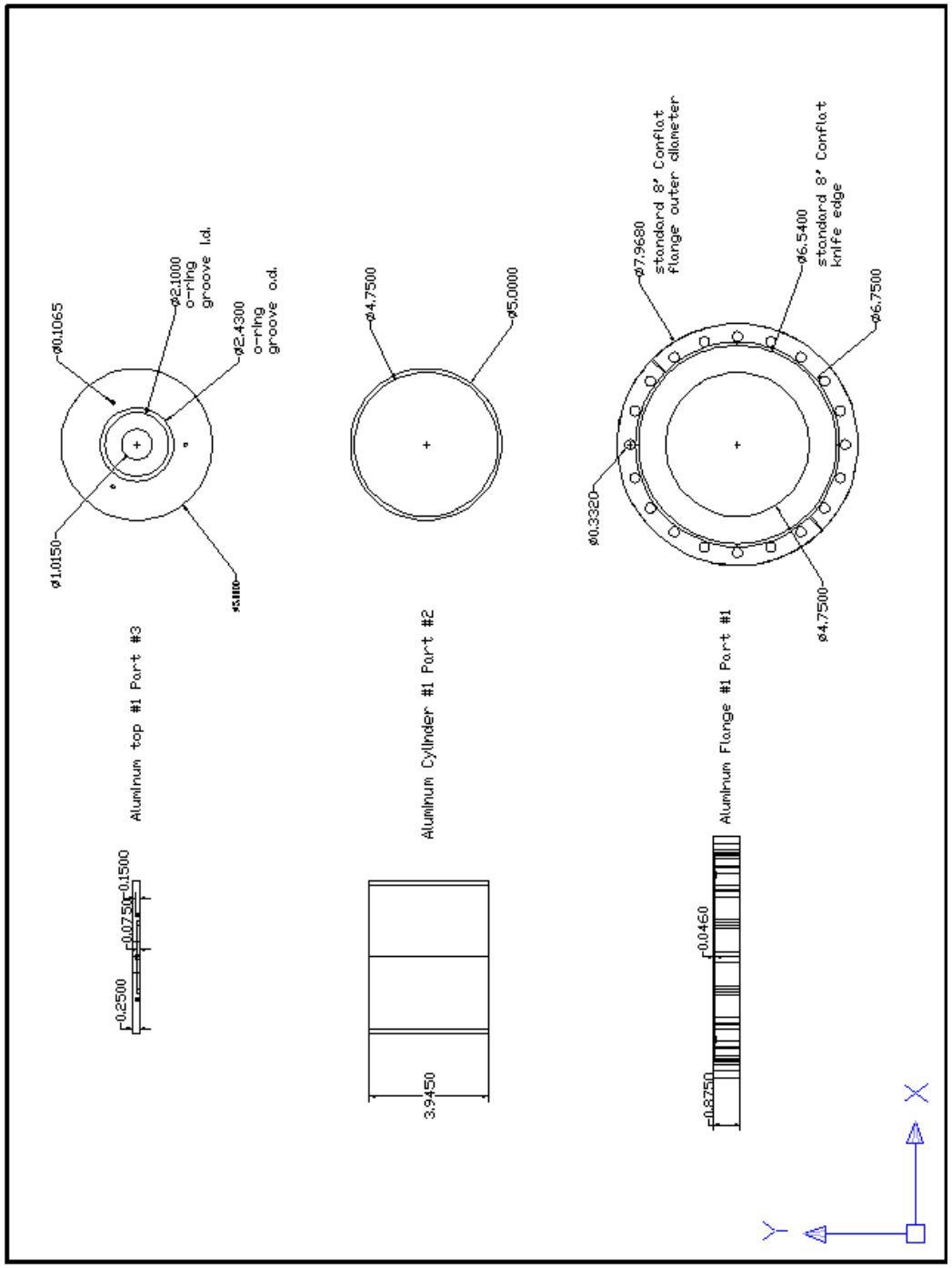

15 kV COLLISION DYNODE AND MOUNTING FLANGE ASSEMBLY

15 kV Collision Dynode and Aluminum Mounting Flange

(a)

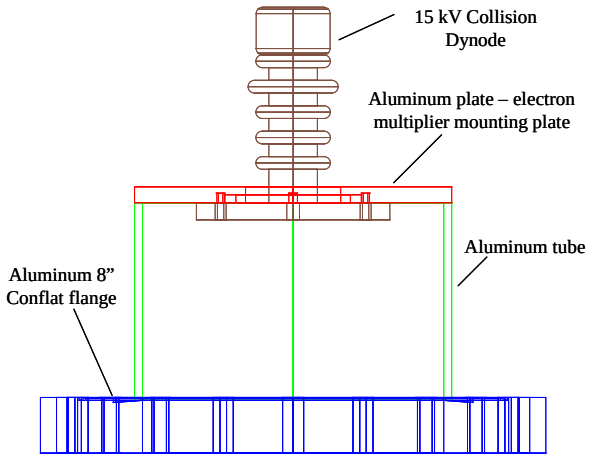

(b)

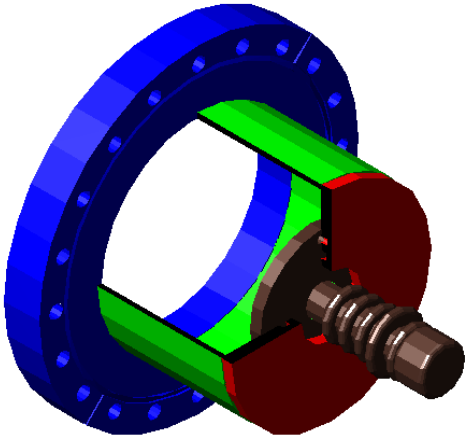

CONTINUOUS DYNODE ELECTRON MULTIPLIER AND MOUNTING FLANGE ASSEMBLY

Continuous Dynode Electron Multiplier and Aluminum Mounting Flange

(a)

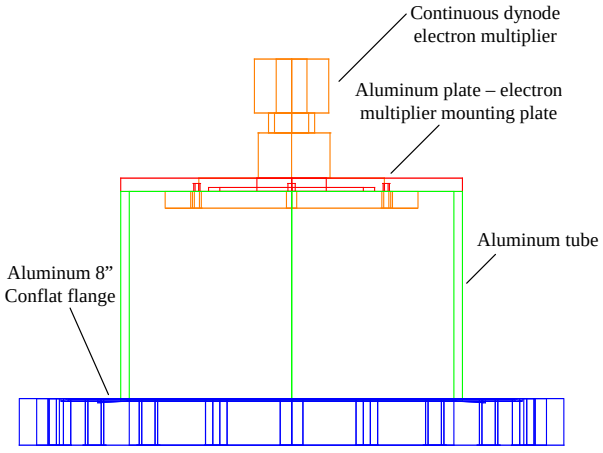

(b)

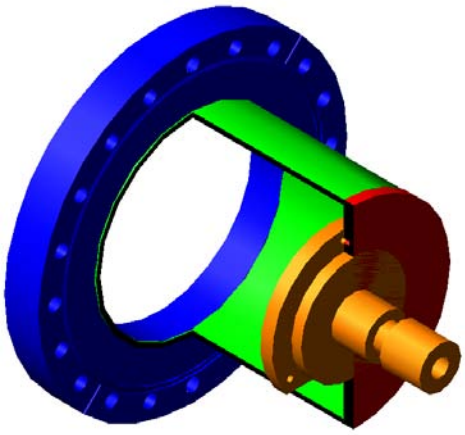

POST-ACCELERATION DETECTOR ASSEMBLED IN VACUUM CHAMBER

Complete Assembly of Post-Acceleration Detector inside 8” Conflat 6-way cross vacuum chamber

(a)

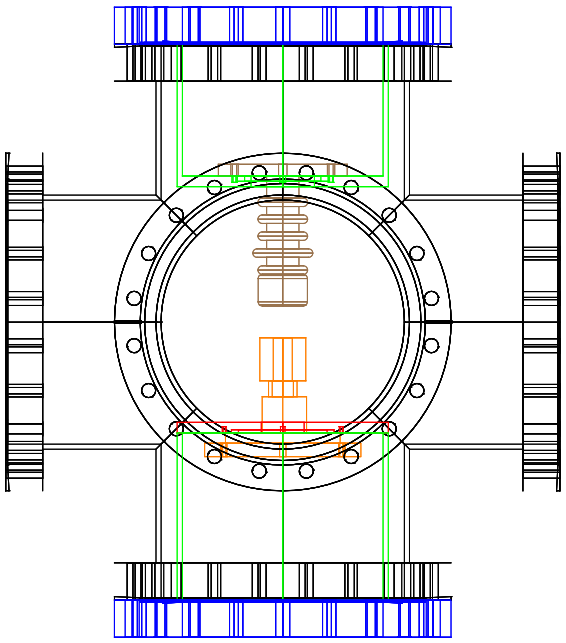

(b)

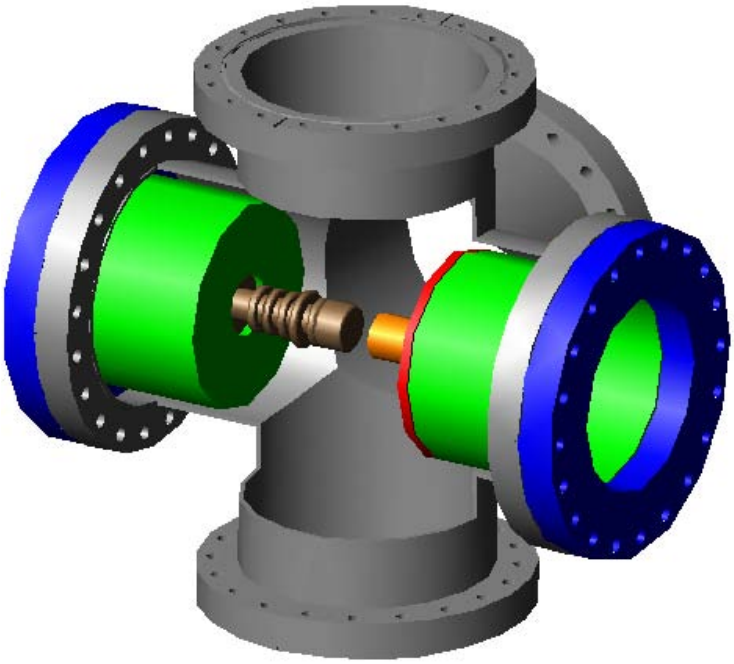

APPENDIX D

BASELINE SHIFT WHILE PULSING THROUGH AN RC CIRCUIT: DETERMINING RESISTORS TO USE IN VOLTAGE CORRECTION FEEDBACK CIRCUIT

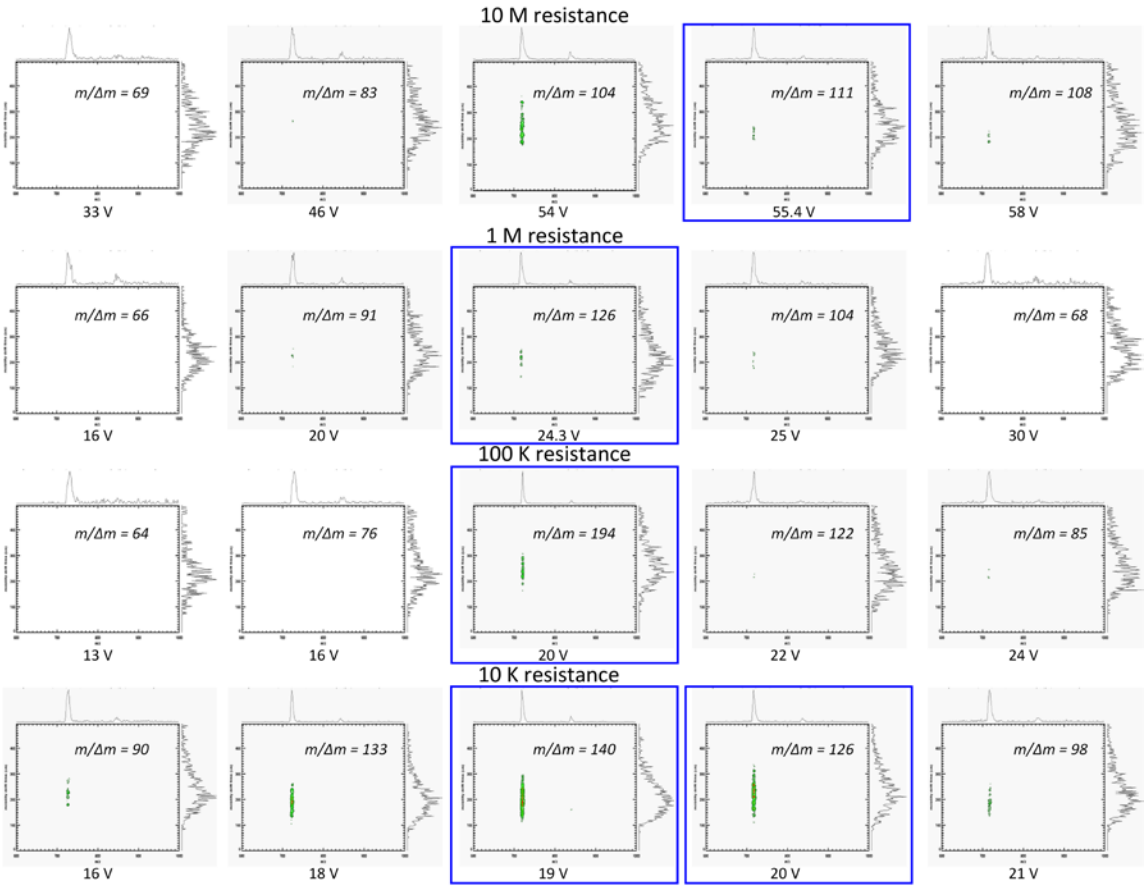

The baseline shift correction voltage for the TOF push electrode was tested with different resistors in the circuit to apply the correction voltage. The TOF parameters for the experiment were as follows: frequency of 40 kHz, pulse width of 2 µs, corresponding to a duty cycle of 8 percent, and pulse amplitude of 275 V with the TOF source at ground potential. For these parameters, the correction voltage for the baseline shift should be approximately 22 volts. For resistors≥ 1 MΩ, the correction voltage applied must be much greater as the resistor acts as a voltage divider in the circuit. For resistors ≤ 100 KΩ, the correction voltage applied to the TOF push plate is essentially the voltage provided from the power supply. For this reason, the 100 KΩ resistor was chosen to be included in the circuit from the output of the power supply to the output of the RC circuit (capacitively coupled pulsing box). Note: when the correction voltage is equal to the amplitude shift in the baseline mass resolution is at a maximum. The maximum mass resolution is boxed in blue for each resistor inserted into the correction voltage circuit.

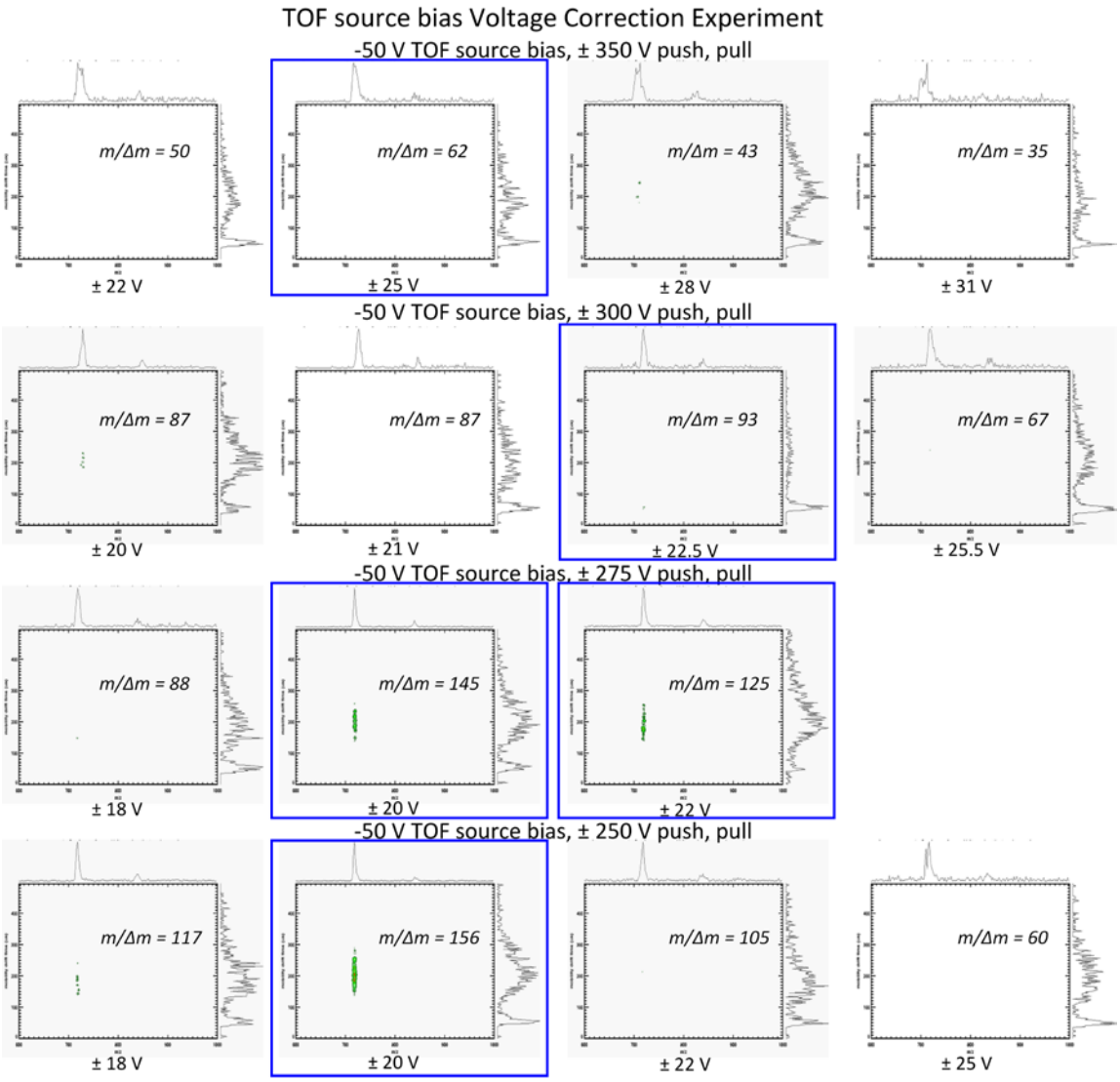

Baseline shift correction experiments utilizing voltage correction on both the push and pull TOF extraction electrodes with the TOF source biased at -50 V. The TOF extraction parameters were as follows: frequency of 40 kHz, pulse width of 2 μs, corresponding to a duty cycle of 8 percent, and varying pulse amplitude. The correction voltages providing the highest mass resolution agree well with the calculated correction voltage required from equation 5.1-2.

APPENDIX E

NOVEL ION OPTICS LENS SYSTEM

TRANSFER ELECTRODES

Schematic Drawings with Dimensions

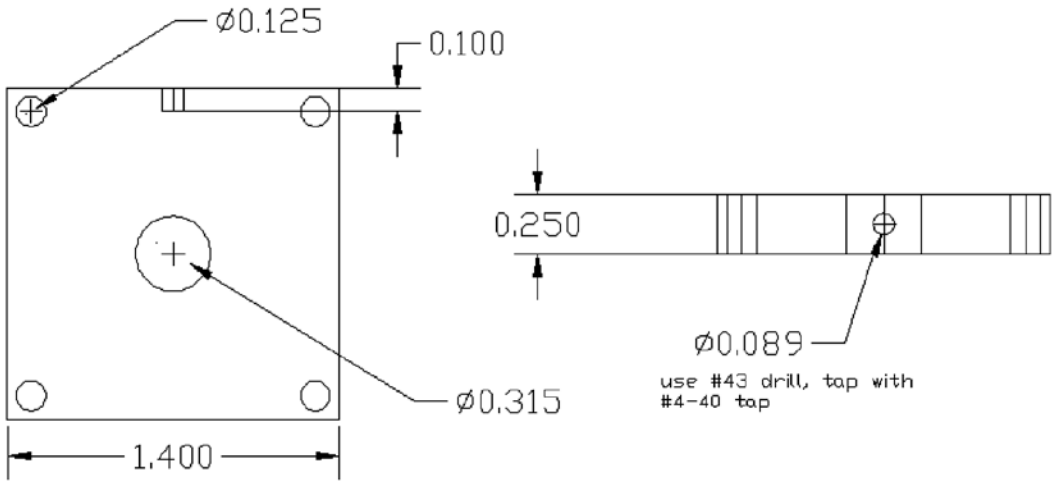

Three-dimensional solid view

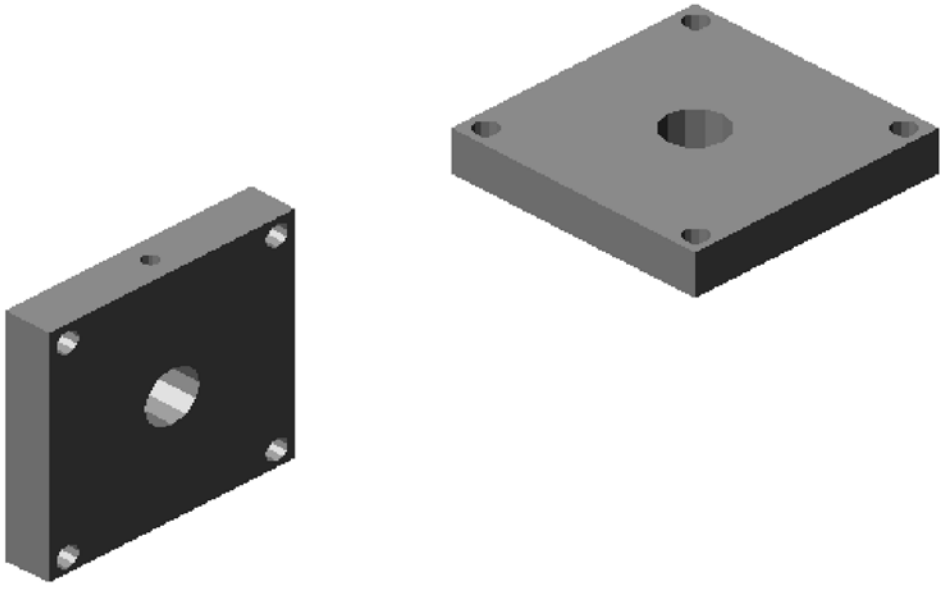

EXPLODED VIEW OF NOVEL ION OPTICS SYSTEM

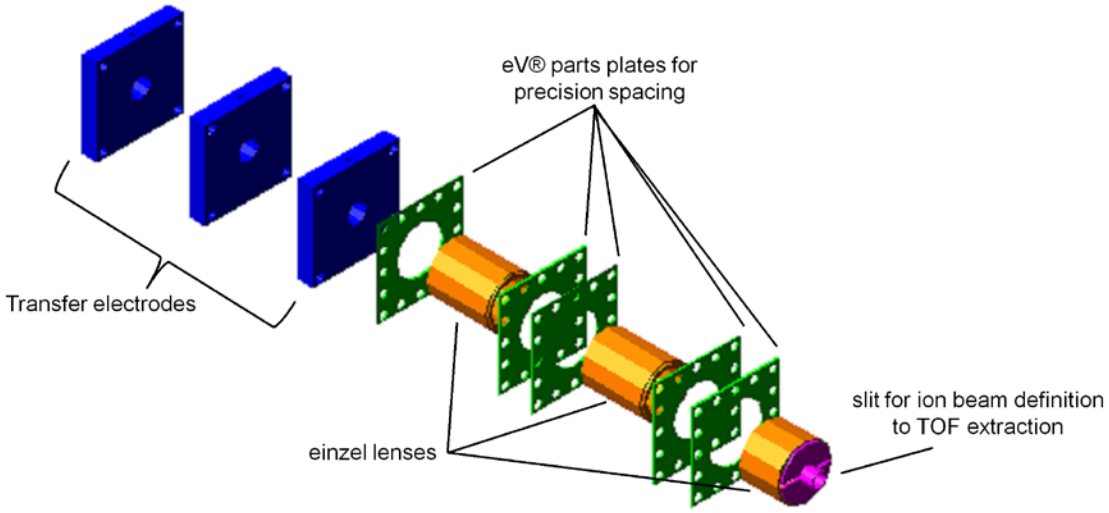

NOVEL ION OPTIC ASSEMBLY WITH MOUNTING PLATE

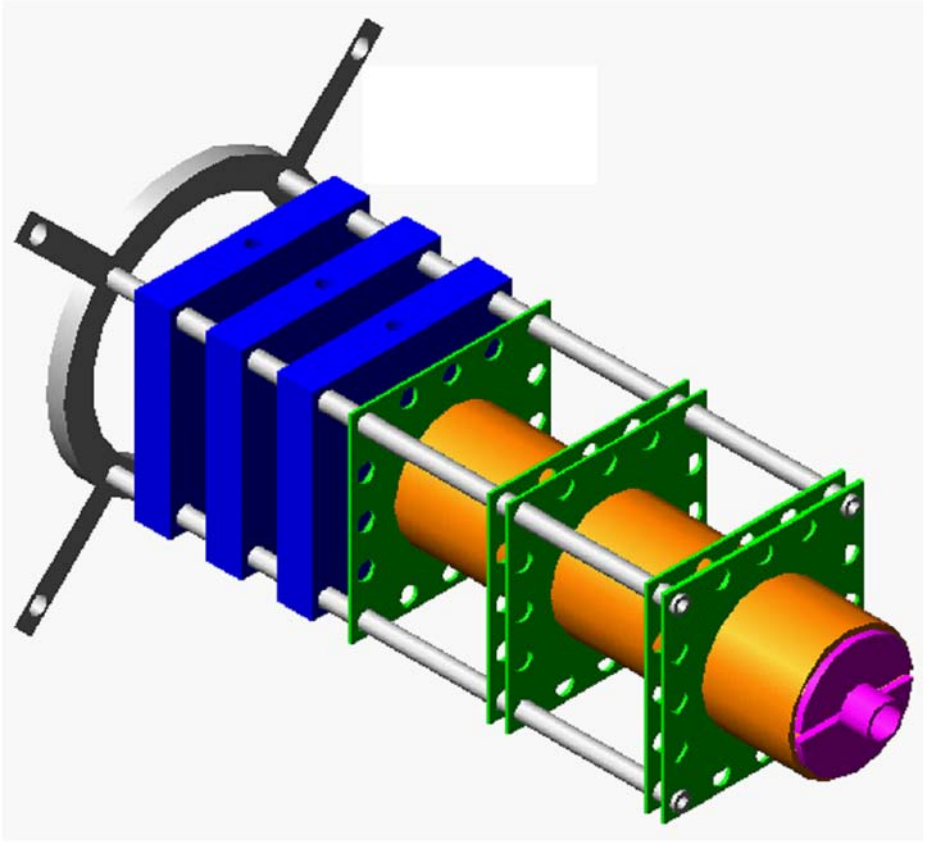

APPENDIX F

DELRIN® MODULAR, PDC IG DRIFT CELL FLANGE

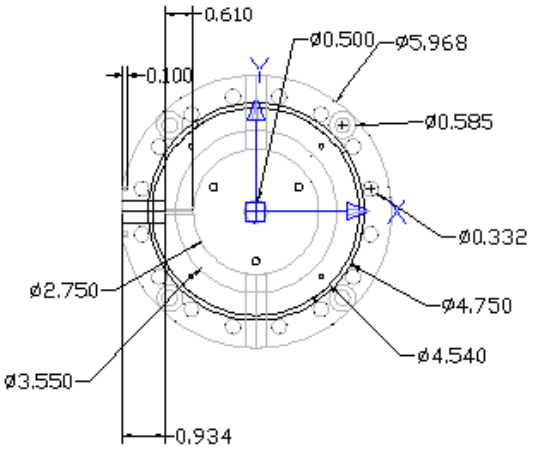

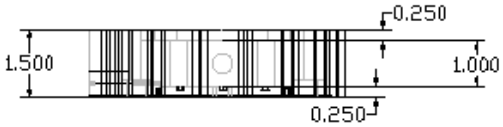

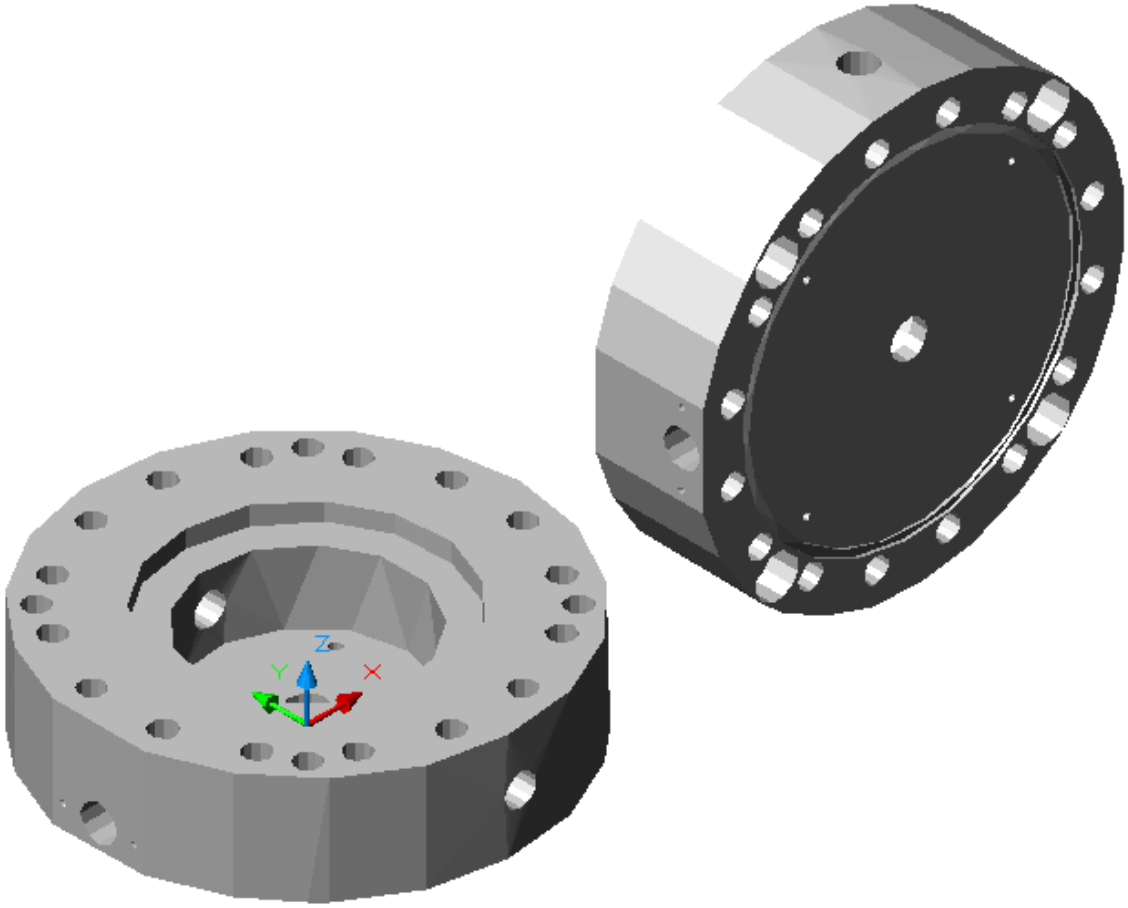

TOP HAT ELECTRODES FOR FIRST AND LAST ELECTRODES OF INDIVIDUAL MODULAR, PDC IG DRIFT CELLS

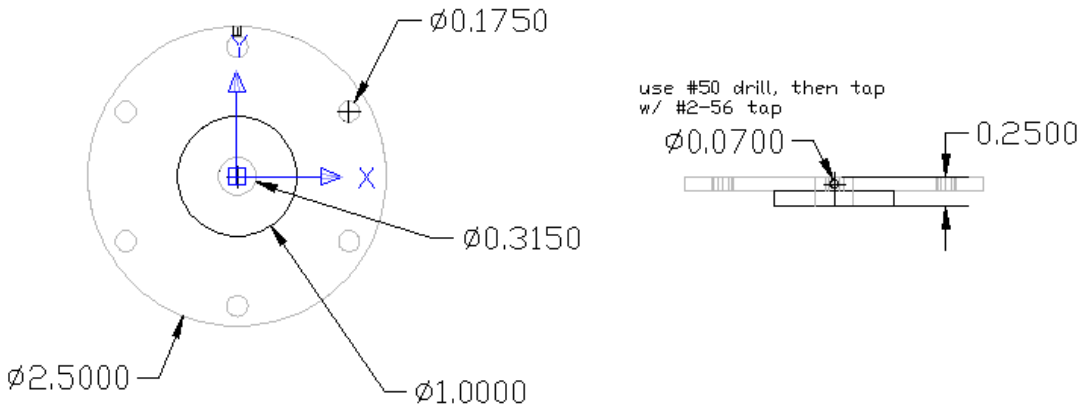

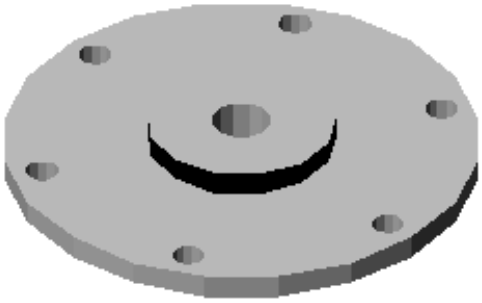

MODULAR, PDC IG DRIFT CELL FULL ASSEMBLY

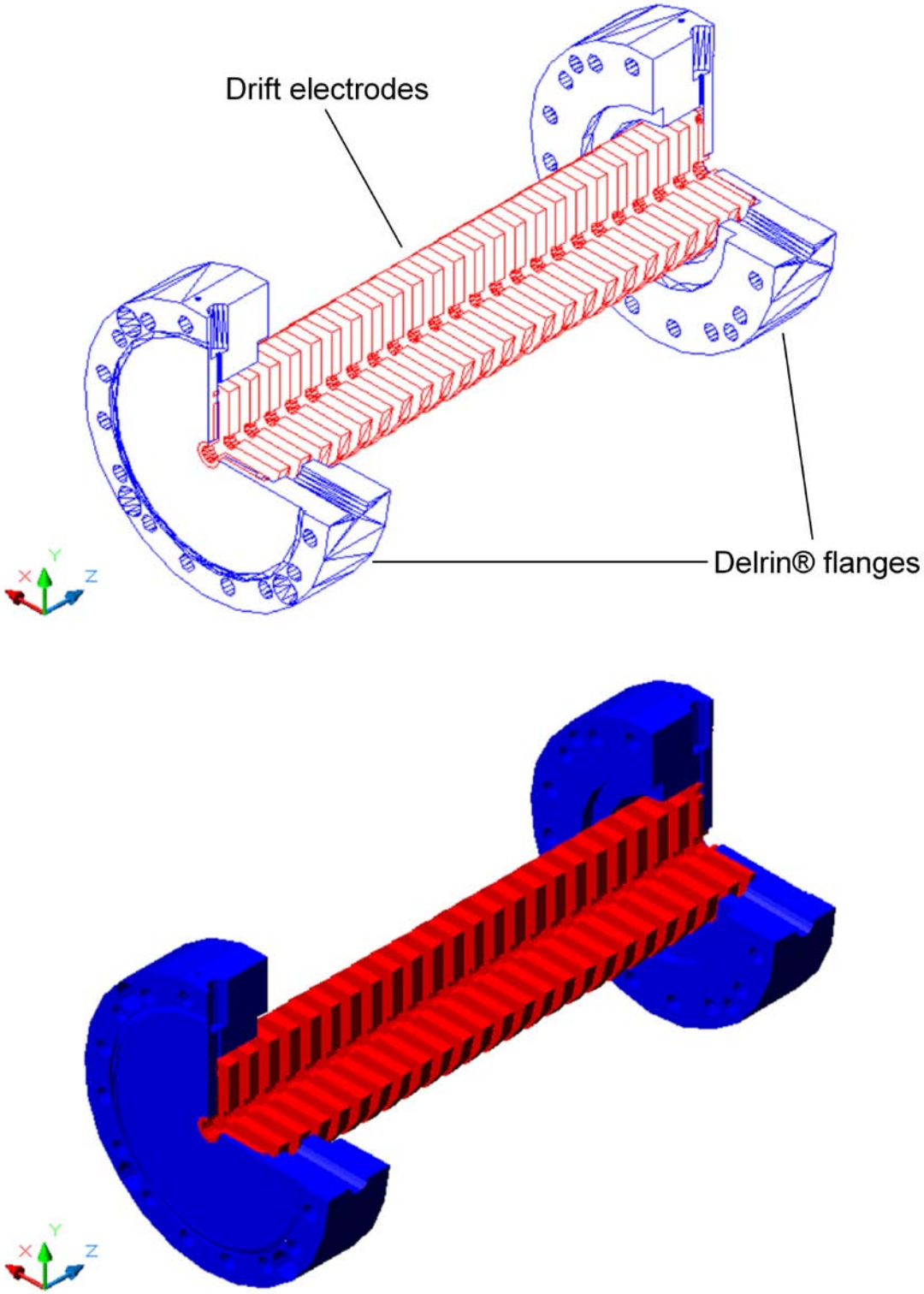

VITA

Ryan Christopher Blase

Department of Chemistry
Texas A&M University, MS 3255
College Station, TX 77843

Email: iamryanblase@hotmail.com Phone: 402-770-1253

Education

December 2010	Ph.D. / Analytical Chemistry Texas A&M University, College Station, TX, December 2010 Dissertation: High Resolution Ion Mobility Spectrometry with increased Ion Transmission: Exploring the Analytical Utility of Periodic-Focusing DC Ion Guide Drift Cells (Prof. David H. Russell)
May 2005	B.S. / Chemistry Truman State University, Kirksville, MO

HONORS

2001-2005	Member of President's List (4.0 GPA) seven of eight semesters
May 2005	Summa Cum Laude, Truman State University
August 2005	Recipient of Texas A&M University Fellowship
2007-present	Member of Phi Lambda Upsilon Honorary Chemistry Society
2008-2009	Texas A&M Beta-Beta Chapter President of Phi Lambda Upsilon

SELECTED PUBLICATIONS

1. Blase, R.C.; Silveira, J.A.; Gillig, K.J.; Gamage, C.M.; Russell, D.H. Increased ion transmission in IMS: A high resolution, periodic-focusing DC ion guide ion mobility spectrometer, Int. J. Mass Spectrom. (2010), doi:10.1016/j.ijms.2010.08.016, in press.

2. Silveira, J.A.; Gamage, C.M.; Blase, R.C.; Russell, D.H. Gas-phase ion dynamics in a periodic-focusing DC ion guide, Int. J. Mass Spectrom. 296 (2010) 36-42.

3. Fernandez-Lima, F.A.; Blase, R.C.; Russell, D.H. A study of ion-neutral collision cross-section values for low charge states of peptides, proteins, and peptide/protein complexes, Int. J. Mass Spectrom. 298 (2010) 111-118.